UNIVERSIDAD DE NAVARRA

ESCUELA SUPERIOR DE INGENIEROS

SAN SEBASTIÁN

A New Robust Motion Reconstruction Method Based on Optimisation with Redundant Constraints and Natural Coordinates

M E M O R I A

que para optar al Grado de Doctor
presenta

SERGIO AUSEJO MUÑOZ

bajo la dirección de

Juan Tomás Celigüeta Lizarza
Ángel Suescun Cruces

San Sebastián, April 2006

Servicio de Publicaciones de la Universidad de Navarra

ISBN 84-8081-152-8

Author: Sergio Ausejo Muñoz
CEIT – Applied Mechanics Department
Paseo de Manuel Lardizabal, 15
P.O. Box 1.555
20018 Donostia-San Sebastian – Spain
email: sausejo@ceit.es

The research described in this book was carried out at CEIT and TECNUN (University of Navarra) in San Sebastian, Spain.

Copyright © 2006 by Sergio Ausejo Muñoz. All rights reserved. No part of this publication may be reproduced or transmitted in any form or by any means, electronic or mechanical, including photocopy, recording, or any information storage and retrieval system, without the written permission of the author.

Legal deposit: SS – 210 – 06

A Magda,
a Hernán y María Santos

AGRADECIMIENTOS

Me gustaría dar las gracias desde estas líneas a todas las personas que han contribuido de una u otra manera a la realización de esta tesis. En primer lugar quiero agradecer a mis padres por empeñarse en que estudiase Ingeniería Industrial en la Universidad de Navarra en lugar de otras opciones. Gracias a esa decisión y a su apoyo durante todos estos años, he acabado haciendo esta tesis doctoral.

Gracias a Magdalena, por quererme, por su apoyo en los malos días y porque la decisión de escribir esta tesis en inglés fue más sencilla gracias a su ayuda.

Gracias a mis directores de tesis, Ángel y Juanto, porque cada uno a su manera me han ayudado para llegar al final. Ángel ha sido el otro padre del método de optimización que se presenta en la tesis y todas las discusiones que hemos tenido a lo largo de varios años han sido fundamentales para mí y para el desarrollo de esta tesis. Juanto me contrató como becario hace ya unos cuantos años, en tiempos difíciles para el departamento con muchos proyectos y poco personal. Quiero agradecerle la oportunidad de hacer esta tesis y las concienzudas y detalladas correcciones de este documento.

A Diego y Leyre por su amistad, por los ratos de cafés y triskis, por todos los buenos y malos ratos que hemos pasado juntos y los que pasaremos. Gracias a Ignacio por estos últimos meses de ayuda mutua y por escuchar mis consejos no pedidos. Gracias a Ana Leiza por nombrarme doctor en el cartel del despacho unas semanas antes de la defensa oficial.

A Abraham y Monika por interesarse siempre por el avance de esta tesis, por la cordura del autor y por aceptar que dos semanas para el final pueden alargarse durante meses.

A Itziar, Arantza y Paloma por el apoyo mutuo durante la realización de nuestras respectivas tesis y los momentos de descanso durante la comida. En especial a Itziar por sus consejos sobre Estadística.

Al profesor Juan Flaquer por su ayuda con el Álgebra y sus consejos sobre los métodos numéricos usados en esta tesis.

A mis excompañeros de despacho con los que pasé la mayor parte del tiempo: Aritz, Mikel Pérez, Iker y Aiert. También a Aitor Cazón y Luis Unzueta por sus contribuciones con algunas partes de esta tesis. Al resto de mis compañeros del CEIT también les quiero agradecer estos años que hemos compartido juntos. Igualmente quiero agradecer a toda mi familia su cariño e interés durante todo este tiempo.

ABSTRACT

The three-dimensional analysis of human movement is of interest in many different fields of life sciences, computer animation and engineering. The elements involved in the analysis of human movement are usually measurement equipments for estimating kinematic, kinetic and myoelectric variables, mathematical models of the human musculoskeletal system, and mathematical methods for calculating the variables which cannot be directly measured.

The aim of this thesis is to advance in the knowledge of four aspects of the three-dimensional analysis of the human movement: 1) the motion reconstruction of human movements using large and medium-size skeletal models with open- and closed-loops, 2) two problems inherent to optoelectronic motion capture systems: the missing marker problem and the impossibility of measuring completely the motion of some bones which move under the skin, 3) the estimation of subject-specific parameters using only a motion capture system, and 4) the development of several human skeletal models suitable for analysing different vehicle-related motions.

The motion reconstruction problem using human skeletal models defined with natural coordinates is formulated as a nonlinear constrained optimisation problem with equality constraint equations. The main contribution of this thesis is a new optimisation method for solving the motion reconstruction problem. The new optimisation method can reconstruct the motion of large-size human skeletal models with open- and closed-loops defined with natural coordinates and it can also handle redundant constraints.

Four new strategies have been proposed for solving the two problems inherent to optoelectronic motion capture systems addressed in this thesis. The four strategies have been evaluated using experimental motion data with satisfactory results. These strategies enable a more robust reconstruction of the human movement.

The subject-specific parameters are estimated using methods based on the measurement of anatomical landmarks. Furthermore, a new measurement protocol for measuring the anatomical landmarks and a new methodology for estimating all subject-specific parameters from the measured anatomical landmarks are proposed.

Three human skeletal models have been developed for studying driving manoeuvres: one upper body model with a detailed model of the shoulder complex and another upper body model with a simplified model of the shoulder complex for studying steering manoeuvres and one right lower limb model for studying braking manoeuvres. Additionally, a human skeletal model of the whole body, based on the RAMSIS model, has been used to study generic arm reaching motions and three types of vehicle-related motions.

CONTENTS

LIST OF FIGURES

LIST OF TABLES

NOTATION

Abbreviations

In the text some abbreviations have a lower case *s* at the end. This is used to denote the plural of a term.

ACP	Anatomical calibration protocol
AL	Anatomical landmark
BSPs	Body segment parameters. They are the inertia properties of each body segment of a human skeletal model.
CAST	Calibrated Anatomical Systems Technique. Protocol introduce by Cappozzo et al. (1995) based on the use of technical coordinate system (TCS) defined by markers and local coordinate system (LCS) defined by anatomical landmarks.
CoM	Centre of mass of a body segment
CP	Convergence profile. See list of symbols below.
DM	Direct method. Type of motion reconstruction method.
DoF	Degree of freedom
EJC	Elbow joint centre
FEM	Finite element method
GCS	Global coordinate system
GHJ	Glenohumeral joint
GHJC	Glenohumeral joint centre
GOM	Global optimisation method. Type of motion reconstruction method.
HJ	Hip joint
HJC	Hip joint centre
ISB	International Society of Biomechanics
JCS	Joint coordinate system
KJ	Knee joint
KJC	Knee joint centre
LCS	Local coordinate system
LCSd	Local coordinate system of a distal body segment
LCSp	Local coordinate system of a proximal body segment
MBS	Multibody system
MoI	Moment of inertia
MoIs	Moments of inertia

NLP	Nonlinear programming
OTM	Optimal tracking method
OTP	Optimal tracking problem
PCSA	Physiological cross-sectional area
QP	Quadratic programming
REV	Revolute (joint)
SD	Standard deviation
SOM	Segmental optimisation method. Type of motion reconstruction method.
SPH	Spherical (joint)
SQP	Sequential quadratic programming
STJ	Scapulothoracic joint
SVD	Singular value decomposition
TCS	Technical coordinate system
UBM	Upper body model without scapula used for motion reconstruction
UBM-INV	Upper body model without scapula used for generating computer-simulated motions.
UBMS	Upper body model with scapula used for motion reconstruction
UBMS-INV	Upper body model with scapula used for generating computer-simulated motions.
UNIV	Universal (joint)

Symbols

α	Step-length parameter which can take any value between 0 and 1. The new iteration point is calculated as $\mathbf{q}^{k+1} = \mathbf{q}^k + \alpha \Delta\mathbf{q}$
λ	Column vector of all Lagrange multipliers
$\lambda_1,\ldots,\lambda_n$	Lagrange multipliers
λ_{ld}	Column vector of Lagrange multipliers associated to the linearly dependent columns of $\mathbf{A}^k$
λ_{li}	Column vector of Lagrange multipliers associated to the linearly independent columns of $\mathbf{A}^k$
$\Psi(\mathbf{q},t)$	Column vector of the r driving constraints which prescribe the motion of a multibody model
Ψ_m	Column vector of driving constraint included in the objective function, whose errors will be minimised
$\Psi_\mathbf{q}$	Jacobian matrix of the driving constraints

Ψ_s	Column vector of driving constraint included in the equality constraints of the optimisation problem OTP, which are satisfied exactly
$\Phi(\mathbf{q})$	Column vector of the m kinematic constraints (rigid body constraints, joint constraints and relative coordinate constraints) that describe a multibody system. Each element $\phi_i(\mathbf{q})$ of $\Phi(\mathbf{q})$ is a constraint equation.
$\Phi_{\mathbf{q}}$	Jacobian matrix of the kinematic constraints, i.e. the matrix of partial derivatives of the kinematic constraints with respect to the vector of dependent coordinates $\mathbf{q}$. The i-th row of $\Phi_{\mathbf{q}}$ is the transposed gradient vector of the i-th kinematic constraint.
$\Phi_{\mathbf{q}}^k$	Jacobian matrix of the kinematic constraints evaluated at $\mathbf{q}^k$
$\mathbf{A}^k$	$\Phi_{\mathbf{q}}^{k\,\mathrm{T}}\Phi_{\mathbf{q}}^k$
$\mathbf{A}_{li}^k$	Matrix whose columns are the linearly independent columns of $\mathbf{A}^k$
$\mathbf{A}_{ld}^k$	Matrix whose columns are the linearly dependent columns of $\mathbf{A}^k$
$\mathbf{B}$	$\begin{bmatrix} \Phi_{\mathbf{q}}^k \\ \mathbf{S} \end{bmatrix}$
$\mathbf{b}^k$	$-\Phi_{\mathbf{q}}^{\mathrm{k}\,\mathrm{T}}\Phi^k$
$\mathbf{C}$	$\begin{bmatrix} \mathbf{H} & \mathbf{A}^k \\ \mathbf{A}^k & 0 \end{bmatrix}$
CP	Convergence profile. It is a bar plot that depicts the quality of the solution found by a solver. The CP shows the CR for one solver and several tolerance values usually 10^{-3}, 10^{-4}, 10^{-5}, 10^{-6} and 10^{-7}
CR	Convergence rate. It is defined as the percentage of frames that converged to the solution for a given tolerance value
$\mathbf{d}$	Column vector of size $r \times 1$ whose i-th element is a given function of time that gives the value of corresponding driven coordinate
${}^G d_{TCS}$	Centroid of the cluster of skin-markers in a given body segment referred to GCS. It is also the origin of the body segment TCS.
${}^T d_L$	Position vector of the LCS origin of a body segment referred to TCS
$({}^G d_T{}^j)^{opt}$	Optimal position vector of the TCS origin referred to GCS for calibration frame j

$\mathbf{e}$	$\begin{bmatrix} -\mathbf{g}^k \\ \mathbf{b}^k \end{bmatrix}$
$f(\mathbf{q})$	Objective function of the optimisation problem OTP. It is a function of the driving constraints: $f(\mathbf{q}) = \frac{1}{2}\,\Psi^{\mathrm{T}}(\mathbf{q},t)\,\Psi(\mathbf{q},t)$
$\mathbf{g}^k$	Gradient vector of the objective function $f(\mathbf{q})$ evaluated at $\mathbf{q}^k$, where $\mathbf{g}^k = \mathbf{S}^{\mathrm{T}}\Psi^k$
$\mathbf{g}_w^k$	Weighted gradient vector. $\mathbf{g}_w^k = \mathbf{S}^{\mathrm{T}}\mathbf{W}\,\Psi^k$. It is similar to the unweighted gradient vector $\mathbf{g}^k$ but each element of the vector is multiplied by the weighting factor associated with each driving constraint
$h(\mathbf{q})$	Objective function of the optimisation problem OTP written in terms of the Hessian matrix $\mathbf{H}^k$ and gradient vector $\mathbf{g}^k$
$\mathbf{H}$	See $\mathbf{H}^k$
$\mathbf{H}^k$	Hessian matrix of objective function $f(\mathbf{q})$ evaluated at $\mathbf{q}^k$. $\mathbf{H}^k$ is a constant diagonal matrix with 0's in the main diagonal except in the positions corresponding to driven coordinates that contain 1's. $\mathbf{H}^k$ is usually denoted simply as $\mathbf{H}$ because it is constant and does not depend on $\mathbf{q}^k$.
$\mathbf{H}_w$	Weighted Hessian matrix. It is a diagonal matrix with 0's in the main diagonal except in the positions corresponding to driven coordinates in which the positive or zero weighting factors associated with each coordinate are located. $\mathbf{H}_w = \mathbf{S}^{\mathrm{T}}\mathbf{W}\mathbf{S}$
${}^{G}JC$	Position vector of a joint centre in GCS
${}^{G}JA$	Coordinates of a joint axis in GCS
${}^{Ld}JC$	Position vector of a joint centre in LCS of the distal body segment
${}^{Ld}JA$	Coordinates of a joint axis in LCS of the distal body segment
${}^{G}L_j$	Position vector of the anatomical landmark j in GCS
${}^{T}L_j$	Position vector of the anatomical landmark j in TCS of the corresponding body segment
${}^{L}L_j$	Position vector of the anatomical landmark j in LCS of the corresponding body segment
m	Number of kinematic constraints of a multibody model
MCR_b	Best mean convergence rate. It is defined as the maximum MCR_i for the studied problem.
MCR_i	Mean convergence rate of solver i. It is defined as the mean CR_i for all

	the studied tolerances
n	Number of dependent coordinates of a multibody model
$nMaxIter$	Maximum number of iterations defined by the user for OTM. Its default value is 25.
${}^{G}PM_1^j$	Position vector in GCS of the pointer-marker located far from the pointer tip
${}^{G}PM_2^j$	Position vector in GCS of the pointer-marker located close to the pointer tip
p	Number of linearly independent columns in $\mathbf{A}^k$
$\mathbf{q}$	Column vector of n dependent coordinates
$\mathbf{q}^0$	Initial approximation for $\mathbf{q}$ in an iterative method
$\mathbf{q}^k$	Iteration point k in an iterative method
$\mathbf{q}^{k+1}$	Iteration point $k + 1$ in an iterative method
$\Delta\mathbf{q}$	Increment between two iteration points in an iterative method
r	Number of driving constraints or driven coordinates
${}^{T}R_L$	Rotation matrix between TCS and LCS of a body segment
${}^{G}R_T{}^j$	Rotation matrix between TCS and GCS in calibration frame j
$({}^{G}R_T{}^j)^{opt}$	Optimal rotation matrix between GCS and TCS for calibration frame j
RCR_i	Relative convergence rate of solver i. It is defined as the difference between the mean convergence rate MCR_i of solver i and the best mean convergence rate MCR_b.
RSR_i	Relative speed rate of solver i. It is defined as the relative speed between solver i and the fastest solver: $RSR_i = 100 \cdot \left(\frac{SR_i - SR_b}{SR_b} \right)$
$\mathbf{S}$	Matrix of size $r \times n$ which defines the relationship between $\mathbf{z}$ and $\mathbf{q}$. The elements of its i-th row are all zero except the one corresponding to the coordinate of $\mathbf{q}$ selected as the i-th driven coordinate. $\mathbf{z} = \mathbf{Sq}$
s	Number of degrees of freedom of a multibody model
${}^{G}SM_i$	Position vector of skin-marker i in GCS
${}^{T}SM_i^j$	Position vector of skin-marker i in calibration frame j referred to TCS of the corresponding body segment.
${}^{T}\overline{SM}_i$	Averaged position vector of skin-marker i referred to TCS of the corresponding body segment. In each calibration frame the coordinates of skin-marker i in TCS are slightly different due to measurement errors.

${}^{L}\overline{SM}_i$	Averaged position vector of skin-marker i in calibration frame j referred to LCS of the corresponding body segment.
SR_b	Best speed rate of solver i. It is defined as the minimum SR_i.
SR_i	Speed rate of solver i. It is defined as the mean T-t for all the studied tolerances.
T-t	Total elapsed time required to reconstruct the motion of all the trials considered in one experiment.
u	Number of effectively driven degrees of freedom
$\mathbf{W}$	Weighting diagonal matrix of size $r \times r$ with positive or zero weighting factors in the main diagonal
$\mathbf{W}_m$	Weighting diagonal matrix associated with Ψ_m. $\mathbf{W}_m$ is similar to $\mathbf{W}$
$\mathbf{W}_s$	Weighting diagonal matrix associated with Ψ_s. The weighting factors of $\mathbf{W}_s$ can be only 0's or 1's
$\mathbf{y}$	$\begin{bmatrix} \Delta\mathbf{q} \\ -\lambda \end{bmatrix}$
$\mathbf{z}$	Column vector of r driven coordinates, which are a subset of $\mathbf{q}$. $\mathbf{z} = \mathbf{Sq}$
$\mathbf{Z}$	Basis for the nullspace of $\mathbf{A}^k$

GLOSSARY

Anatomical position (or posture) or **Standard anatomical position** is defined as a posture where the human body is standing upright on a horizontal surface with arms hanging straight down at the sides of the body, palms turned forward, and head erected. In human anatomy, the body and its parts are always described using the assumption that the body is in the anatomical position.

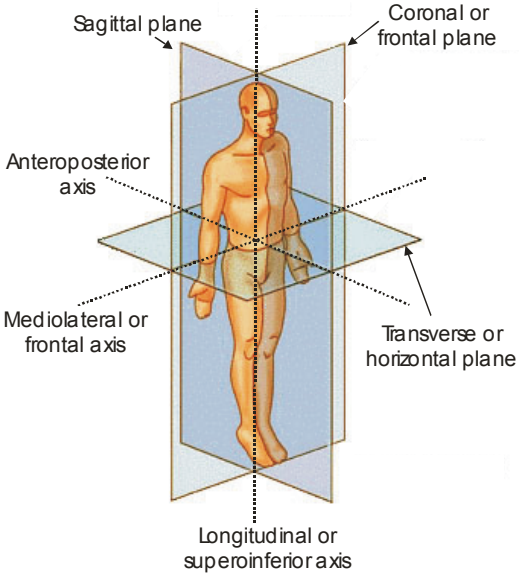

In the anatomical position three anatomical planes and three anatomical axes are defined:

- **Sagittal** or **median plane**: any plane dividing a human body into left and right sections.
- **Transverse** or **horizontal plane**: any plane passing through the body and parallel to the ground.
- **Frontal** or **coronal plane**: plane that goes from side-to-side of the body and is perpendicular to both the transverse and sagittal planes.
- **Anteroposterior axis**: Axis defined by the intersection of the sagittal and transverse planes.
- **Longitudinal** or **superoinferior axis**: Axis defined by the intersection of the sagittal and frontal planes.
- **Mediolateral** or **frontal axis**: Axis defined by the intersection of the frontal and transverse planes.

The following relative terms are used to express the relationship of any given structure to another:

- **Anterior** or **ventral**: towards the front side of the body.
- **Posterior** or **dorsal**: towards the back half of the body.
- **Superior** or **cranial**: closer to the head.
- **Inferior** or **caudal**: farther away from the head, toward the feet.
- **Medial**: toward the sagittal plane
- **Lateral**: away from the sagittal plane

General motions of the human body:

- **Flexion**: bending movement that decreases the angle between two parts. Flexion of the hip or shoulder moves the limb forward (towards the anterior side of the body).
- **Extension**: straightening movement that increases the angle between body parts. The opposite of flexion. Extension of the hip or shoulder moves the limb backward (towards the posterior side of the body).
- **Adduction**: motion that pulls a structure or part towards the midline of the body, or towards the midline of a limb. Adduction of the wrist is called ulnar deviation.
- **Abduction**: motion that pulls a structure or part away from the midline of the body. Abduction of the wrist is called radial deviation.
- **Rotation**: motion that occurs when a part turns on its axis.
- **Elevation**: movement in a superior direction.
- **Depression**: movement in an inferior direction, the opposite of elevation.
- **Pronation**: rotation of the forearm that moves the palm from an anterior-facing position to a posterior-facing position.
- **Supination**: rotation of the forearm that moves the palm from a posterior-facing position to an anterior-facing position. Opposite of pronation.
- **Dorsiflexion**: flexion of the entire foot superiorly, or upwards.
- **Plantarflexion**: flexion of the entire foot inferiorly, or downwards.
- **Eversion**: movement of the foot sole away from the sagittal plane.
- **Inversion**: movement of the sole of the foot towards the sagittal plane.

Distal: farther from the trunk, e.g. the hand is at the distal end of the upper limb.

Proximal: nearer to the trunk, e.g. the thigh is at the proximal end of the leg.

CHAPTER 1

INTRODUCTION

The three-dimensional analysis of human movement is of interest in many different fields of life sciences, animation and engineering. Depending on the application the requirements on accuracy, efficiency and number of variables measured or estimated are different. For example, in biomechanical applications the focus could be at the precise estimation of the muscle forces applied to a body segment, making necessary an accurate measurement and reconstruction of the motion while in computer animation the main interest is at the visual representation of the human movement, making less critical an accurate measurement of the motion.

The human movement analysis (Winter, 1990; Allard et al., 1995) typically starts with the measurement of kinematic and kinetic observable variables of the human musculoskeletal system during the execution of a given motion. Additionally, the electrical activity of muscles can also be measured. The next step consists in defining a mathematical model of the musculoskeletal system suitable for the studied motion. The musculoskeletal model has to be tailored to the subject under investigation by estimating subject-specific parameters. Afterwards, the musculoskeletal model can be used to estimate the kinematic response of the subject (e.g. angles at the articulations) from the measured kinematic variables. Additionally, the kinetic response (e.g. forces at the articulations or forces applied by muscles) can be estimated from the measured kinematic and kinetic variables using inverse dynamics. Finally, the kinematic and kinetic variables can be analysed by the specialist in the field of application. Obviously, not all applications go through the whole process. For example, in computer animation only kinematic variables are typically measured and its output consists in a digital human performing the same measured motion or a modified motion, which uses the original as a reference.

In this thesis muscles are not investigated, therefore they are not included in the mathematical models. Consequently, the human models used are referred to as human skeletal models.

The human movement analysis has been applied to many different problems. Some of its applications are:

- Surgical planning (Delp et al., 1990).
- Gain insight into joints and/or muscles function (van der Helm, 1994b; van der Helm, 1994a).
- Study of work-related joint problems (Högfors et al., 1995).
- Sports performance (Urban, 1995; Celigüeta, 1996).
- Gait analysis (Benedetti et al., 1998; Vaughan et al., 1999).
- Occupant safety (Silva, 2003).
- Computer Animation (Zhao and Badler, 1994; Tolani et al., 2000; Baerlocher and Boulic, 2004).
- Ergonomic studies (Wang and Verriest, 1998; Wang et al., 2005).

The main issues of the human movement analysis investigated in this thesis are: 1) the measurement of the kinematic variables of the subject being studied; 2) the estimation of subject-specific parameters; 3) the development of human skeletal models; and 4) the reconstruction of the motion using the recorded kinematic variables. Next, these four issues are explained in more detail:

1. The kinematic variables measured during the human activity investigated depend on the motion capture technology used. In this thesis, only optoelectronic motion capture systems with passive markers are considered. This technology measures the position of small retro-reflective balls called markers (Figure 1.1-right), which are located on the skin of each body segment. Several cameras (Figure 1.1-left) record the motion of the markers and the three-dimensional coordinates of each marker at each frame are estimated using stereophotogrammetric methods (Medved, 2001). The accuracy and precision of a motion capture system depends on the quality of the hardware as well as on several parameters related to the specific laboratory set-up, such as the number and location of cameras, the lighting or the size of the measurement volume. Typical values for the accuracy and precision are both in the range 1-5 mm, depending on the commercial motion capture system used (Chiari et al., 2005). Two common problems to all optoelectronic

motion capture systems are the missing marker problem and the impossibility of measuring completely the motion of some bones. The missing marker problem appears when a marker is not visible to at least two cameras and its position in the global coordinate system cannot be estimated. The motion of some bones (e.g. vertebrae or scapula) cannot be measured completely using external markers fixed on the skin because of relative skin/bone movement and insufficient number of markers.

Figure 1.1: Left: Vicon MX40 motion capture camera and strobe around the objective. Right: Subject with markers (white spots) on his skin during the REALMAN project.

2. The subject-specific parameters of a human skeletal model for each body segment are joint parameters (Zatsiorsky, 1998), inertia parameters (Zatsiorsky, 2002), position of each marker and anatomical landmark in the local coordinate system. The joint parameters are the magnitudes that define the kinematic characteristics of each joint (e.g. joint axis direction). These joint parameters together with the inertia parameters, which are needed for inverse dynamics, are called generally anthropometric parameters throughout this thesis. The local coordinates of the markers are needed for estimating the position and orientation of each body segment from the measured global marker coordinates. Anatomical landmarks are usually bony palpable landmarks and are used in this thesis for estimating anthropometric parameters and for defining the local coordinate system of each body segment. Anatomical landmarks are not points but surfaces, sometimes large and irregular and their identification by palpation is subject to both intra- and inter-experimenter variability. Furthermore, they are covered by soft tissue of variable thickness which also hinders their identification and accurate measurement.

3. In the human movement analysis, the skeletal system is usually modelled using a multibody system (MBS) approach, although other approaches like the finite element method (FEM) can also be used. In this thesis a multibody approach is used to study the human movement. Several common assumptions like simplified joint models (e.g. fixed joint centres of rotation) or rigidity of the body segments are made.
4. The motion reconstruction consists in estimating the position and orientation of each body segment of the subject at each frame from the measured global marker coordinates. This is a nontrivial problem usually involving a nonlinear optimisation problem.

The main source of error in the human movement analysis is the soft tissue artifact. The soft tissue artefact is due to the relative movement between markers and the underlying bone caused by passive and active soft tissues. Soft tissue artefact is recognised to be the bounding error source in the measurement of human motion by optoelectronic motion capture systems (Alexander and Andriacchi, 2001; Leardini et al., 2005).

1.1 MOTIVATION

This thesis has been developed initially in the frame of two projects, REALMAN and MoDyCo, where the three-dimensional analysis of human movement was a key issue. After the conclusion of the projects further investigations where carried out, achieving significant improvements in the previously developed methods and leading to the methologies presented in this thesis. The projects were an important source of experimental data for evaluating the new enhancements.

1.1.1 REALMAN PROJECT

The REALMAN project (Integrated Technology for Dynamic Simulation and Advanced Visualisation of Human Motion in Virtual Environments) was funded by the European Commission in the context of the Fifth Framework Program under the Information Society Technologies Program (IST-2000-29357). The project aimed at taking into account not only physical aspects but also physio-biomechanical aspects of human motion, controlling the human skeletal model postures and movements through predictive modelling methods, determining new discomfort criteria based on mechanics and biomechanics, and integrating advanced Augmented Reality interfaces for visualisation and force feedback. During the REALMAN project, a number of modelling techniques and simulation technologies were developed, enhanced

and integrated in order to obtain a more intelligent human simulation technology. The following car manufacturers, aerospace companies, universities and research centres participated in the project:

- Renault. Project coordinator, end-user and technology validation.
- PSA Peugeot-Citroën. End-user and technology validation.
- Alenia Spazio. End-user and dissemination.
- Human Solutions GmbH. Technology provider on ergonomic simulation and human models.
- CEIT. Technology provider on modelling and motion reconstruction.
- INRETS-LBMH. Biomechanics and Human Modelling Laboratory. Experiments and discomfort analysis.
- TUM-LfE. Institute of Ergonomics of the Technical University of Munich. Experiments and discomfort analysis.
- UniPatras-LMS. University of Patras. Motion prediction.

The REALMAN methodology is divided in two basic levels: Simulation level and Experimental level (Dufour et al., 2003; Suescun and Pargada, 2003). The Simulation level (Figure 1.2, left hand side) allows an ergonomic designer to evaluate the ergonomic aspects of an existing vehicle package. The designer can choose the virtual environment of the vehicle from a database and can define the subject-specific parameters of the human skeletal model. Finally, the designer defines a task description, which characterises the motion, and starts the REALMAN simulation kernel to predict the motion and to derive discomfort ratings. The kernel makes use of an intelligent access to a motion database, which contains the knowledge about a wide range of motions. The simulated motion and discomfort ratings are visualised in the virtual environment, which allows the user to perform further ergonomic analysis.

In order to extend the knowledge with new motion patterns, the research engineers can define motion experiments during the Experimental level (Figure 1.2, right hand side). The raw data generated in these experiments are processed by the REALMAN data processing tools and converted into high level motion data that are finally included in the motion database. Two different types of experiments were considered in the Experimental level:

- Motion experiments designed to estimate the joint angles of a human skeletal model tailored to a specific subject and the discomfort associated with the motion, during different vehicle-related activities (e.g. door handling, safety belt handling or ingress-egress motions) and generic arm reaches.

- Joint torque experiments designed to measure the maximal and intermediate torques at each joint for several postures and the discomfort associated.

During both types of experiments discomfort questionnaires were filled by the subjects with the help of the experimenter in order to gather discomfort data related to the experiment.

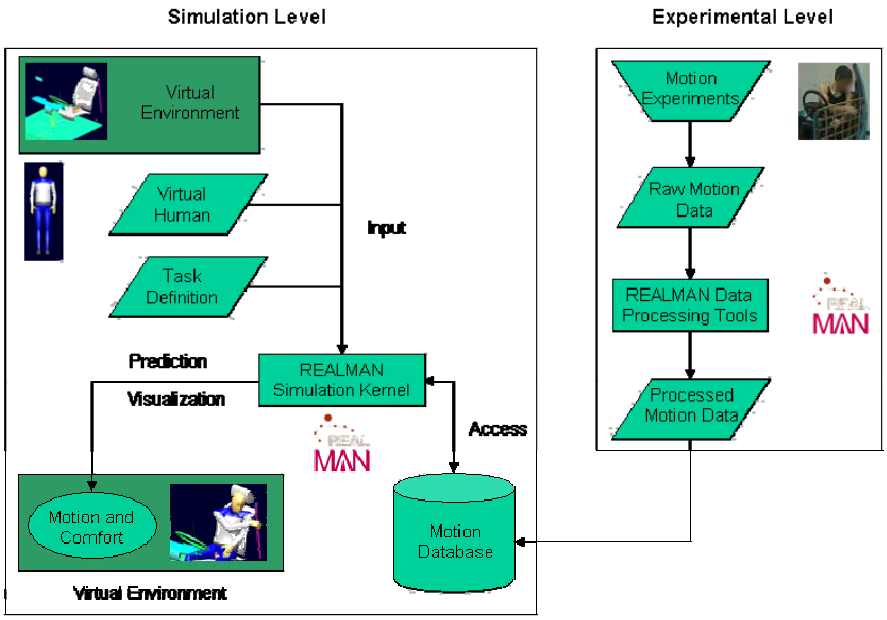

Figure 1.2: REALMAN methodology.

Only the motion experiments are relevant to the objectives of this thesis. The motion experiments were studied following the four steps of the human movement analysis described previously. Due to the limited capabilities for motion reconstruction of the ergonomic software tools initially available to the industrial partners, the main objective of the REALMAN project related to this thesis was the development of efficient software tools for motion reconstruction. The efficiency was a critical necessity as more than 6000 human motions were planned to be analysed. The requirements of the REALMAN project, with regard to the four issues of the human movement analysis considered in this thesis, were:

1. The motion of the subjects had to be measured while performing different vehicle-related activities and generic arm reaches. The motion of most of the body segments was of interest and had to be measured.

2. The subject-specific parameters had to be estimated using an efficient method due to the large number of experiments planned.
3. A whole body model of the skeletal system was needed to analyse the recorded motions.
4. An efficient motion reconstruction method was needed to reconstruct all the recorded motions.

The motion capture system and the software tools adopted to fulfil the requirements of the project were the following:

1. The human motions were measured with Vicon, which is an optoelectronic motion capture system with passive markers (www.viconpeak.com). It was chosen due to availability reasons, its good precision and accuracy compared to other commercial systems (Chiari et al., 2005) and the possibility of using a large number of markers.
2. The subject-specific parameters were estimated using the software PCMAN (Seitz and Bubb, 1999; Seitz et al., 2000; Seitz and Bubb, 2001). It allowed the quick estimation of the subject-specific parameters from a minimum of two simultaneous pictures in two predefined postures. PCMAN gives a first adjustment of the human skeletal model to a specific subject but the user intervention is required to obtain a refined adjustment. This software was specifically designed to estimate the parameters of the human skeletal model used in the project.
3. The RAMSIS whole body model (www.human-solutions.com) was used to analyse all the recorded motions. It was chosen because the ergonomic software tool selected for the project was RAMSIS, which is a CAD tool for the ergonomic design of vehicle interiors and cockpits. According to company that develops RAMSIS, it is used by more than 60% of all vehicle manufacturers world-wide.
4. Compamm was selected as the MBS software tool for performing the motion reconstruction. Compamm is a software tool developed at CEIT for the kinematic and dynamic simulation of mechanical systems based on the natural coordinates concept (García de Jalón and Bayo, 1994). Initially Compamm was equipped with a sport oriented approach (Urban, 1995; Celigüeta, 1996) for motion reconstruction called Compamm HMR (CEIT, 2001), which did not optimally solve the motion reconstruction problem. Therefore, during the REALMAN project a new motion reconstruction method using natural coordinates was developed.

The main contribution to the REALMAN project related to this thesis was the motion reconstruction method implemented in Compamm.

1.1.2 MODYCO PROJECT

The MoDyCo project (Modèle Dynamique de Conducteur) was a bilateral contract between the French car manufacturer PSA Peugeot-Citroën and CEIT. Nowadays, car manufacturers try to improve the comfort and active security of the vehicles by introducing more mechatronic systems. In order to reduce the time-to-market, these systems are designed using simulation tools. These tools require mathematical models of the components of the vehicle (e.g. chassis, suspension, engine or electronic systems) as well as the road and the human driver. The MoDyCo project aimed at improving the current human driver models by taking into account the physiological characteristics of the drivers. The human movement analysis was used in the MoDyCo project as a tool for generating human driver models.

The requirements of the MoDyCo project, with regard to the four issues of the human movement analysis considered in this thesis, were:

1. The motion of the subjects had to be measured while performing several steering and braking manoeuvres. The motion of the upper body had to be measured during the steering manoeuvres and only the right leg had to be measured during braking manoeuvres.
2. The measurement equipment available for the estimation of the subject-specific parameters was a motion capture system and some additional inexpensive instrumentation like measuring tape or anthropometric callipers. Furthermore, as it was planned to study a large number of motions for different subjects, the methods for estimating the parameters had to require a reasonable time compared to the total duration of the experiment.
3. Suitable human skeletal models had to be developed for analysing the human motion during braking and steering manoeuvres.
4. An efficient motion reconstruction method was required.

The motion capture system used in the MoDyCo project was Vicon due to the same reasons explained in the REALMAN project. The solutions adopted for the remaining requirements are the main topics of this thesis. One major requirement of PSA Peugeot-Citroën for the project was the use of Matlab® as development environment. Consequently, both the human skeletal models and the reconstruction method were developed in such a software environment.

1.2 OBJECTIVES

The objectives of this thesis are presented according to the four issues of the human movement analysis mentioned previously. These objectives are related to the goals of the two research projects described before.

1.2.1 MOTION CAPTURE

The Vicon motion capture system was used in both projects. Vicon is an optoelectronic motion capture system, which can suffer from the two problems already mentioned: the missing marker problem and the impossibility of measuring completely the motion of some bones. Both problems are common to all optoelectronic motion capture systems.

The missing marker problem is usually handled by estimating the position of the marker during the frames in which it is missing. Different approaches have been proposed in the literature (Muijtjens et al., 1997; Herda et al., 2001; Desjardins et al., 2002). However, the methods published so far do not solve completely the problem when the marker is missing during a large number of consecutive frames.

In this thesis, the missing marker problem is considered from a different point of view. Instead of estimating the positions of the missing markers, the goal is to use efficiently the information provided by the markers when they are visible. Therefore, the **first objective** of this thesis consists in exploiting the information provided by the marker when it is visible and ignoring it when it is missing. Appropriate strategies have to be devised to include and exclude markers in the solution of the motion reconstruction problem in order to avoid discontinuities on the reconstructed motions.

The second problem related to optoelectronic motion capture systems considered in this thesis is that the motion of some bones cannot be measured completely using external markers fixed on the skin. For example, the motion of the vertebrae cannot be measured completely because markers on the skin cannot provide sufficient information for estimating the three-dimensional motion of each vertebra. Consequently, the **second objective** of this thesis is to develop methods for the approximate estimation of the motion of those bones that cannot be measured completely using markers located on the skin.

1.2.2 SUBJECT-SPECIFIC PARAMETERS

The requirements for estimating subject-specific parameters are different for each project. In the REALMAN project all the parameters were estimated with

the software PCMAN. In the MoDyCo project the subject-specific parameters can be estimated using any method suitable for the measurement equipment available: a motion capture system and some additional inexpensive instrumentation.

The **third objective** consists in selecting the most suitable methods for estimating the subject-specific parameters, taking into account the measurement equipment available and that the total time required by the method has to be reasonable due to the large number of subjects that have to be studied.

The **forth objective** is to develop a detailed protocol for measuring the variables required by the methods used for estimating the subject-specific parameters. Additionally, a methodology for estimating the subject-specific parameters from the measured variables is also required.

1.2.3 HUMAN SKELETAL MODELS

In the REALMAN project the human skeletal model was RAMSIS, due to the ergonomic software tool used in the project. In the MoDyCo project the human skeletal model and the generation of the model equations had to be created only in terms of suitability for the driving manoeuvres investigated. The only constraint was that they had to be developed in Matlab®.

The **fifth objective** consists in creating several human skeletal models appropriate for the analysis of the driving manoeuvres. Additionally, a Matlab® toolbox for generating the equations of the human skeletal models has to be developed.

1.2.4 MOTION RECONSTRUCTION

The **sixth objective** of this thesis is to develop a motion reconstruction method valid for large human skeletal models with open- and closed-loops and with a reasonable efficiency in terms of CPU time. Additionally, the motion reconstruction method has to be specially designed to handle efficiently the strategies devised for the missing marker problem and for estimating the motion of those bones not measured completely by the motion capture system.

Among all possible variables for defining the motion of a mechanical system, natural coordinates were selected due to the following reasons:

- The motion reconstruction problem can be formulated as an optimisation problem and natural coordinates have some potential advantages for optimisation problems, especially for large-size

problems as happened to be the case in the motions addressed in this thesis. This potential advantages are:

a. The objective function of the optimisation problem is quadratic.

b. The Jacobian matrix of the constraint equations is sparse with linear or constant terms.

- Natural coordinates are an important area of expertise of the Applied Mechanics Department of CEIT.

1.3 ORGANISATION OF THE DOCUMENT

This thesis joins the abstract concepts of mechanics and optimisation with the study of the living systems. With the aim of facilitating the reading of this document to people with different backgrounds, simple examples and basic concepts are presented throughout the text. The author hopes that these examples and concept descriptions are explanatory and do not hinder the reading of the document for experts in each specific topic.

The content of this thesis is organised according to the four presented issues of the 3D analysis of human movement, which are treated in chapters 2, 3, 4 and 5. The state-of-the-art of each issue is presented in the corresponding chapter.

Chapter 2 reviews the different methods reported in the literature for estimating the anthropometric parameters, i.e. joint parameters and inertia parameters, of a specific subject. The suitability of the different methods for the problems faced on this thesis is discussed and the most appropriate methods are indicated.

Chapter 3 describes the medium-size models and whole body models published in the literature and relevant to this thesis. The human skeletal models developed for the MoDyCo project for analysing driving manoeuvres are described in detail in this chapter. In addition, the whole body model used in the REALMAN project is also presented.

The main topic of Chapter 4 is the description of a new motion reconstruction method for natural coordinates and valid for open- and closed-loops. The chapter starts with a brief description of natural coordinates and the constraint equations obtained from them. Next, the optimisation problem originated from a motion reconstruction problem formulated with natural coordinates is presented. The state-of-the-art of motion reconstruction methods based on different approaches is reviewed. Also the optimisation

methods suitable for solving the motion reconstruction problem defined with natural coordinates are reviewed. Then, a new motion reconstruction method for natural coordinates is presented in detail. Furthermore, four numerical methods are proposed for solving the problem. Finally, new strategies for dealing with the missing marker problem and for the approximate estimation of the motion of those bones, whose movement cannot be measured completely using optoelectronic motion capture systems, are proposed. These strategies are presented at the end of Chapter 4 because they take advantage of the characteristics of the new motion reconstruction method proposed in this thesis.

Chapter 5 covers the new methodologies developed in this thesis and the experiments to which these methodologies have been applied. Special attention is given to the description of the measurement protocol of the MoDyCo project and the process of estimating the subject-specific parameters from the measured variables.

Chapter 6 is dedicated to validate the methods proposed in this thesis. The performance of the new motion reconstruction method and the suitability of the new strategies proposed for dealing with the missing marker problem and the impossibility of measuring completely the motion of some bones are evaluated. In addition, the errors in the subject-specific parameters associated with the measurement errors during the measurement protocol are also assessed.

Finally, Chapter 7 presents the conclusions of this thesis and recommendations for future work.

CHAPTER 2

ANTHROPOMETRIC PARAMETERS

In order to define a skeletal model of a human subject, anthropometric parameters of the subject must be estimated. These anthropometric parameters are the joint centre location and axes orientation (joint parameters) and inertia properties of each body segment (body segment parameters).

At least two types of skeletal models can be distinguished, generic and subject-specific. Anthropometric parameters for generic skeletal models are usually obtained from anthropometric databases. For example, the parameters of a 50^{th} percentile subject can be used to build a generic skeletal model, whose analysis allows obtaining general conclusions for the problem being studied. Subject-specific skeletal models are built with particular anthropometric parameters estimated for the specific subject under study.

This thesis focuses on the analysis of the movement of specific subjects. Therefore, methods for estimating subject-specific anthropometric parameters are required. In this chapter, different methods reported in the literature for estimating joint parameters (section 2.1) and body segment parameters (section 2.2) of a specific subject are reviewed. The methods used in the MoDyCo and REALMAN projects for estimating joint parameters are presented in section 2.1.15, while the methods for estimating the body segment parameters in the MoDyCo project are discussed in section 2.2.6.

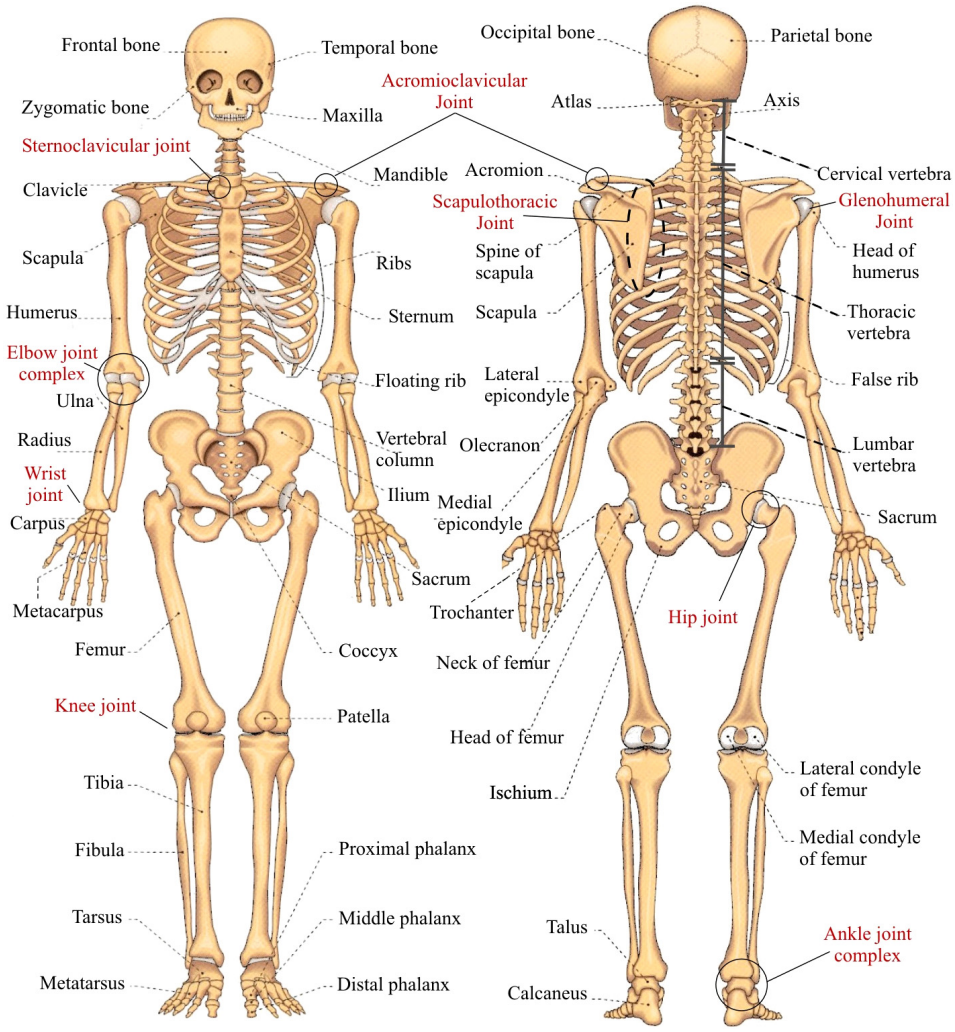

Figure 2.1: Main bones and joints of the human skeleton. Anterior and posterior view. Adapted from (Wang and Doriot, 2001).

2.1 JOINT PARAMETERS

Joint parameters are the variables that define the kinematic characteristics of a joint. In this thesis, natural coordinates (section 4.1) are used to define skeletal models and only spherical, revolute and universal joints are used to model human joints. Using natural coordinates, a spherical joint is defined by a point shared between the two body segments that the joint connects. A revolute joint is defined by a point and a vector shared between the two body segments

connected. In a universal joint one vector of each body segment must remain perpendicular to each other and one point is shared between the two body segments. Joint parameters are defined as the coordinates of the elements (point and/or vectors) shared between the body segments connected by the joint, and referred to the local coordinate system of each body segment.

Real human joint motions cannot be described only by revolute joints, spherical joints or universal joints because joint motions involve complex rotations and translations. The joint centres of rotation are not fixed and the axes of rotations are neither fixed nor orthogonal to each other and may not intersect. When the aim of an investigation is to study the motion of a specific joint, it must be studied in its full complexity. However, when gross motion of the human body involving several body segments and joints is studied, as is the case in this thesis, some assumptions are usually made. In this thesis joint translations are neglected and joint centres of rotation and joint axes are assumed to be fixed. These assumptions are common in most of the biomechanical studies related to gross human motion (van der Helm, 1994b; Högfors et al., 1995; Anderson and Pandy, 1999; Garner and Pandy, 1999; Charlton and Johnson, 2000; Maurel and Thalmann, 2000).

Note that if a joint is not correctly modelled, the muscle forces, ligament forces and the loading of the bones cannot be calculated accurately and they are under- or overestimated. Consider that a joint is modelled as a spherical joint but it behaves approximately as a universal joint. The spherical joint cannot produce reaction torques and it can only generate reaction forces while in reality, the joint can produce a reaction torque and the joint ligaments and joint contact surfaces can transmit torques from one body to another. Therefore, the forces of the muscles crossing the joint are overestimated and the ligament forces and the loading of the bones are underestimated.

The methods for estimating joint parameters for a specific subject *in vivo* can be classified into four groups:

1. Prediction methods, which estimate joint parameters from crude predictions using constant distances with regard to anatomical landmarks (ALs).
2. Regression methods, which estimate joint parameters from coordinates of ALs using regression equations.
3. Functional methods, which estimate joint parameters from recorded motion data.
4. Optimisation methods, which estimate joint parameters of complex joint models or multi-joint models from experimental motion data using optimisation techniques.

There are methods for estimating joint parameters *in vitro* but they are not of interest in this thesis because our goal is to estimate joint parameter in living subjects. Unfortunately, the accuracy of joint parameters estimated *in vivo* is difficult to assess because it is difficult to measure the real values of the joint parameters.

Prediction and regression methods for estimating the main joint centres are presented in sections 2.1.1 and 2.1.2 respectively. Generic functional and optimisation methods for estimating joint parameters are described in sections 2.1.3 and 2.1.4 respectively. Finally, specific methods for estimating joint parameters of the main human joints are presented in sections 2.1.5 to 2.1.13.

2.1.1 PREDICTION METHODS

Prediction methods give the location of fixed joint centres with respect to one or more ALs. Using this approach, Dempster (1955) presented a prediction method for estimating the location of the ankle, knee, hip, glenohumeral, acromioclavicular, sternoclavicular, elbow and wrist joints. For example, the author locates the knee joint centre as the midpoint of a line between the centres of the posterior convexities of the femoral condyles. When distances are used to define a joint centre location, they are not given as a percentage of body segment length with respect to an AL but as a fixed distance.

Plagenhoef (1971) described a prediction method for estimating the location of the ankle, knee, hip, glenohumeral and elbow joints. The prediction methods of Dempster (1955) and Plagenhoef (1971) are summarised in Zatsiorsky (2002).

Chaffin and Snyder (Snyder et al., 1972; Chaffin et al., 1999, p. 68) presented a prediction method for estimating the location of seven joint centres (between two successive vertebrae) of the spine. The location of the joints was referred to the most superior dorsal palpable points on the spinous process of each vertebra (section B.2.3 in Appendix B).

2.1.2 REGRESSION METHODS

Regression methods estimate joint centre location and/or joint axes orientation as a function of a few anthropometric measurements of the subject. The anthropometric measurements are usually body segment lengths defined between two ALs, although the number and type of anthropometric measurements depends on the regression method.

De Leva (De Leva, 1996b) presented a regression method for estimating joint centre location of the 12 main human joints (shoulder, elbow, wrist, hip,

knee and ankle). The joint centre is assumed to lie on the longitudinal axis of the body segment and is given as a percentage of the body segment length with respect to an AL (Figure 2.2). Body segment lengths are defined between two ALs of each body segment. Percentages were calculated from a subset of the anthropometric data of Chandler et al. (1975). Unfortunately the method has not been validated by the author or other studies to date.

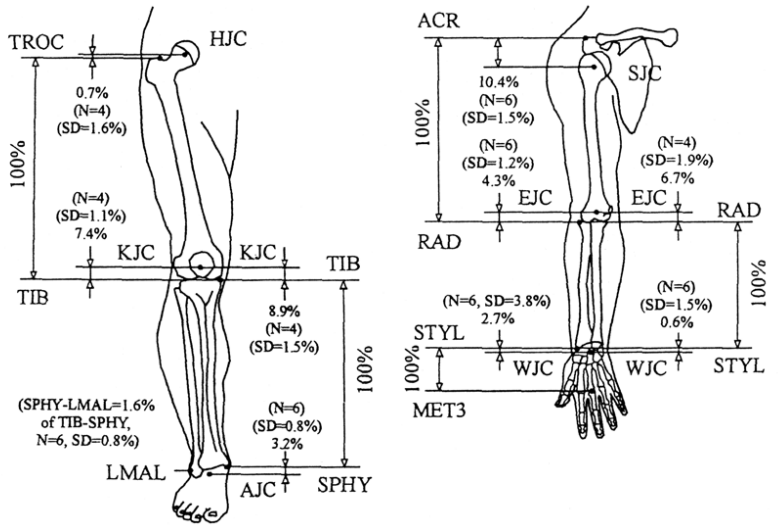

Figure 2.2: Joint centre locations as a percentage of body segment length with regard to an AL (N: number of subjects). Reproduced from De Leva (1996b).

Rab et al. (2002) derived a regression method for estimating the joint centre location of the neck top, neck bottom, wrist, elbow, glenohumeral, and hip joints based on data measured directly on an adult, a pediatric skeleton (six year-old), as well as data from seven cadavers available in the literature (van der Helm et al., 1992). Local coordinate systems for each body segment are defined in the anatomical position, parallel to the anatomical axes. Three-dimensional coordinates of each joint centre are given in the local coordinate system of each body segment as a percentage of body segment length with respect to an AL.

2.1.3 FUNCTIONAL METHODS

Functional methods estimate joint parameters from motion data recorded using different motion capture systems. Unlike prediction and regression methods, functional methods are valid for subjects whose joint parameters have changed due to degeneration of the articular surfaces, or due to an implant. In this situation, prediction and regression methods are not valid

because they are derived from measurements in normal healthy subjects. Several researchers have suggested that functional methods may not give accurate results when the range of motion of a joint is limited in pathological cases (Bell et al., 1990; Seidel et al., 1995; Kirkwood et al., 1999). This issue was investigated by Piazza et al. (2001) for the hip joint (see section 2.1.11).

Woltring (1990) proposed a functional method for estimating joint parameters based on the instantaneous (or finite) helical axes approach. The location of an instantaneous helical axis in three-dimensions is defined by a position vector and an orientation vector. Instantaneous helical axes are estimated between two successive positions for each sample time and a least-squares method is applied to the set of instantaneous helical axis in order to calculate the average centre of rotation (spherical joint) or the average axis of rotation (revolute joint). This method is sensitive to low angular velocities.

A common assumption of several functional methods is that each marker describes a sphere centred at the centre of rotation (spherical joint) or a circle about the axis of rotation (revolute joint). A number of methods have been proposed based on these assumptions for spherical joints (Cappozzo, 1984; Silaghi et al., 1998; Halvorsen et al., 1999; Gamage and Lasenby, 2002) and revolute joints (Halvorsen et al., 1999; Gamage and Lasenby, 2002). These methods find the centre of rotation or axis of rotation from the solution of a least-squares problem or optimisation problem.

2.1.4 OPTIMISATION METHODS

Functional methods fit a simple mathematical model (e.g. a sphere) to the motion data, while optimisation methods estimate all the parameters of complex joint models or multi-joint models from experimental motion data using optimisation techniques. Van den Bogert (1994) proposed an optimisation method for estimating the joint parameters of the talocrural and subtalar joints (see section 2.1.13 for details).

Kecskeméthy et al. (2003) presented an optimisation method for estimating joint parameters of a kinematic model of the lower limb. The model included the pelvis, thigh, shank, and foot and the hip, knee and ankle joints were modelled as spherical joints. The method was applied to data obtained from gait analysis.

Recently, Reinbolt et al. (2005) have proposed a general two-level optimisation method for estimating the joint parameters of any multi-joint kinematic model. The method simultaneously estimates the joint parameters (outer level of optimisation) and calculates the optimal position and orientation

of the kinematic model (inner level of optimisation) from the measured marker coordinates. This optimisation method has been applied successfully to a 3D kinematic model of the lower extremity with 12 DoFs and 27 joint parameters. One drawback of this approach is that it requires a large amount of computation time, making parallel processing necessary in order to complete it in a reasonable amount of time.

2.1.5 STERNOCLAVICULAR JOINT

The sternoclavicular joint (Figure 2.1 and Figure 2.3) is a compound joint in which the clavicle articulates with the manubrium of the sternum and the cartilage of the first rib. The rotation centre translates only a few millimetres and these translations can be neglected (van der Helm et al., 1992). The joint is usually modelled as a spherical joint (Högfors et al., 1987; Engin and Tümer, 1989; van der Helm, 1994b; Garner and Pandy, 1999; Maurel, 1999; Charlton and Johnson, 2000).

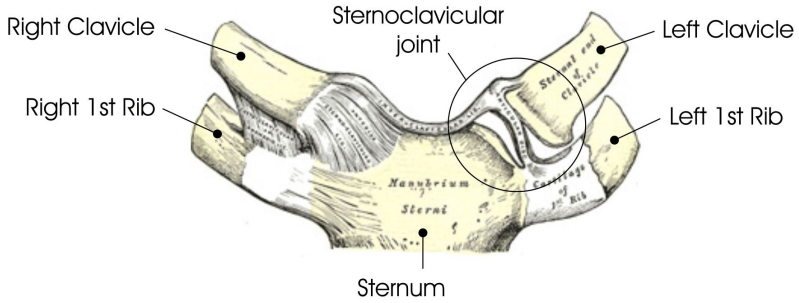

Figure 2.3: Anterior view of the sternoclavicular joint. Adapted from (Gray, 1918).

Methods for estimating the sternoclavicular joint rotation centre from ALs have not been published to date and most authors estimate the joint rotation centre from the geometry of the articular surfaces. The joint rotation centre has been located at the centroid of a plane fitted to the proximal joint surface (van der Helm et al., 1992; van der Helm, 1994b) or near the medial side of the clavicular attachment of the costo-clavicular ligament (Garner and Pandy, 1999).

2.1.6 ACROMIOCLAVICULAR JOINT

The acromioclavicular joint (Figure 2.1 and Figure 2.4), also called the claviculoscapular joint, is formed by the lateral end of the clavicle and the acromion of the scapula. The translations of this joint are restricted to a few millimetres (van der Helm et al., 1992) and it is usually modelled as a spherical

joint (Högfors et al., 1987; Engin and Tümer, 1989; van der Helm, 1994b; Garner and Pandy, 1999; Maurel, 1999; Charlton and Johnson, 2000).

Similarly to the sternoclavicular joint, methods for estimating the acromioclavicular joint rotation centre from ALs have not been published to date and the joint rotation centre is estimated from the geometry of the articular surfaces. For example, van der Helm (1992; 1994b) approximated the joint rotation centre by the centroid of a plane fitted to the proximal joint surface while Garner and Pandy (1999) assumed that the joint rotation centre was located at the middle of the gap between the lateral end of the clavicle and the medial side of the acromion process.

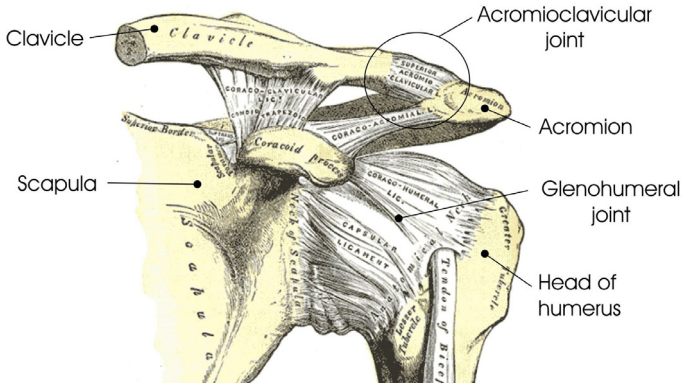

Figure 2.4: Anterior view of the acromioclavicular joint. Adapted from (Gray, 1918).

2.1.7 SCAPULOTHORACIC JOINT

The scapulothoracic joint does not involve articular structures between the scapula and thorax and is not a true joint (Figure 2.1). Although the scapula glides over the thorax due to the dynamic action of the surrounding muscles, the scapula and thorax do not glide directly over each other because they are separated by the subscapularis and serratus anterior muscles.

The scapula, clavicle and thorax form a closed kinematic chain called the shoulder girdle and together with the humerus form the shoulder complex. The bones of the shoulder complex have a conjunct motion called the shoulder rhythm or scapulohumeral rhythm.

Two approaches have been proposed to model the scapulothoracic joint. The first approach is based on the fact that the scapula can be assumed to glide over the thorax and the second is based on the shoulder rhythm.

In the first approach, two points that belong to the scapula are constrained to remain in contact with the thorax, which is approximated by an

ellipsoid. This approach was originally introduced by van der Helm (1994b) who considered two points on the medial border of the scapula (trigonum spinae and angulus inferior) and modelled the thorax with a single ellipsoid. Garner and Pandy (1999) presented a scapulothoracic joint model based on van der Helm's model where each side of the rib cage was approximated by an ellipsoid and the two scapula-fixed points where shifted from the medial border of the scapula so that they could contact with the rib cage. The gap between the medial border of the scapula and the two points is considered in order to take into account the thickness of the muscles between scapula and thorax.

In the second approach, the scapulothoracic joint is not modelled with a kinematic constraint; instead the orientation of the scapula is determined by the shoulder rhythm. The shoulder rhythm defines the kinematic relation between the clavicle, scapula and humerus. If the orientation of the humerus is given, the orientation of the clavicle and scapula can be determined by the shoulder rhythm relationship (Högfors et al., 1991; Karlsson and Peterson, 1992; de Groot and Brand, 2001).

2.1.8 GLENOHUMERAL JOINT

The glenohumeral joint is formed by the humeral head and the glenoid cavity of the scapula (Figure 2.1 and Figure 2.4). The two joint surfaces are almost spherical and the displacement of the instantaneous centre of rotation is minimal. Therefore, the glenohumeral joint can be modelled as a spherical joint (Poppen and Walker, 1976; van der Helm et al., 1989; Veeger et al., 1997; Garner and Pandy, 1999).

The only regression method to date for estimating the glenohumeral joint centre (GHJC) was proposed by Meskers et al. (1998). Multiple linear regression equations were estimated from measurements of the coordinates of five ALs performed on 36 defleshed scapulae (section B.2.1 of Appendix B). A regression equation for each glenohumeral joint coordinate was provided as a function of several AL coordinates and distances between ALs. The root mean-square error between the GHJC location measured and predicted by the regression method was 2.32 mm for the x-coordinate, 2.69 mm for the y-coordinate and 3.04 mm for the z-coordinate.

Stokdijk et al. (2000) presented two functional methods in order to locate the GHJC *in vivo* and compared it with the regression method of Meskers et al. (1998). The motion of the humerus and scapula was recorded with a 3D electromagnetic tracking device (Flock of Birds – Ascension Technology Inc.) using two receivers, one attached on a cuff around the upper

arm and the other on a scapula locator (Figure 2.5). The GHJC was estimated from three different recorded motions using two functional methods: a sphere-fitting method and a helical-axes method. All three methods (one regression method and two functional methods) had a low variability and located the GHJC within 4 mm but the joint centre differed significantly between the methods ($p < 0.001$). The sphere-fitting method and helical-axes method found the GHJC medially (mean -0.74 cm and -0.98 cm respectively) of the acromial angle (AA) and the regression method laterally (mean 0.88 cm). According to previous studies (Poppen and Walker, 1976; Veeger et al., 1997) the GHJC lies medially of AA and the regression method probably mislocates the GHJC. The inter- and intra-observer reliability was adequate for all methods except for the intra-observer reliability of the regression method, which differed significantly ($p < 0.008$). This means that the regression method is very sensitive to AL location errors.

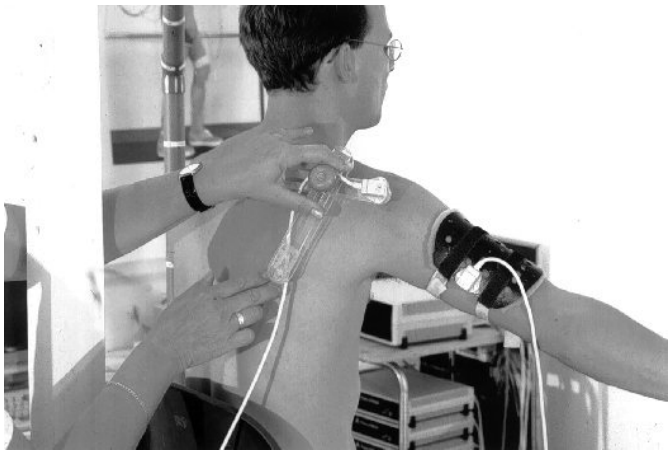

Figure 2.5: Motion recording of the scapula and humerus. A cuff with a receiver is attached to the upper arm and the observer places the scapula locator on the right scapula and follows scapular motion. Reproduced from Stokdijk et al. (2000).

Wang (1996) presented a functional method for estimating the GHJC of a simplified model of the shoulder complex. The model does not include the scapula and the clavicle is connected directly to the humerus through an equivalent glenohumeral joint. Therefore, the centre of rotation of this equivalent glenohumeral joint cannot be compared with the two previous methods. The equivalent GHJC was estimated for 5 subjects (17-47 yr) from three upper arm circumduction movements recorded with an optoelectronic motion capture system (ELITE – BTS: www.bts.it) using a helical-axes method. The mean equivalent GHJC was located with regard to the acromioclavicular joint 37 mm inferiorly, 14 mm laterally and 8 mm anteriorly.

2.1.9 ELBOW JOINT COMPLEX

The elbow joint complex (Figure 2.1) as a whole has two DoFs, flexion-extension about an axis approximately connecting the lateral and medial epicondyles of the humerus, and pronation-supination about an axis approximately connecting the proximal end of the radius and the centre of the distal end of the ulna. The elbow joint complex is composed of the radioulnar joint at the distal end of radius and ulna, and the elbow joint at the proximal end of the forearm. The elbow joint is a compound joint that includes the humeroulnar and humeroradial joints. The humeroradial joint can be modelled as a spherical joint and the humeroulnar joint as a revolute joint (Lemay and Crago, 1996; Zatsiorsky, 1998). The radioulnar joint can be modelled as a revolute joint (van der Helm, 1997b; Garner and Pandy, 1999; Maurel, 1999; Charlton and Johnson, 2000) or as a cylindrical joint (Lemay and Crago, 1996).

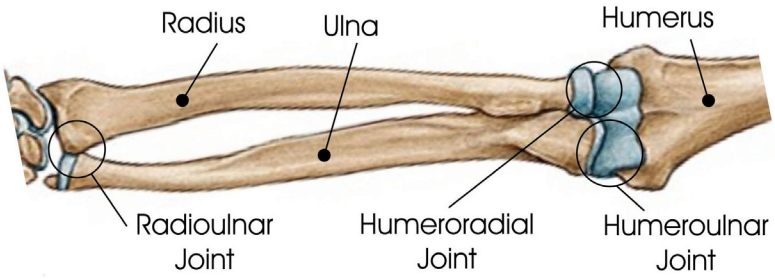

Figure 2.6: Anterior view of the right forearm.

The joint parameters of the three joints that include the elbow joint complex are difficult to measure *in vivo* using functional methods. Regression methods for estimating the joint parameters of the elbow joint complex have not been found in the literature. The methods available only estimate the flexion-extension axis and pronation-supination axis, which are usually considered as fixed axes. During the flexion-extension motion the instantaneous centre of rotation displaces less than 3 mm (Chao and Morrey, 1978).

Wang (1996) estimated the elbow flexion-extension axis and elbow joint centre of 3 subjects using an optoelectronic motion capture system (ELITE – BTS: www.bts.it). One marker was located at the lateral epicondyle of the humerus and a triangle plate with three markers attached to it at the forearm. The flexion-extension axis was estimated using a helical-axes method from recorded flexion-extension movements when the forearm was fully pronated, neutral and fully supinated. The arm plane was defined as a plane formed by GHJC, the centre of the trochlea, and the wrist centre. The elbow joint centre

was approximated by the intersection of the estimated elbow flexion-extension axis and the arm plane. According to the author the average flexion-extension axis can be approximated by an axis normal to the arm plane. This approximation leads to an average deviation from the flexion-extension axis of 9º in pronation and 12º when the forearm is fully supinated. The average elbow joint centre is located 10 mm below the centre of the trochlea along the direction from the GHJC to the centre of the trochlea.

Veeger et al. (1997) used a 3D electromagnetic tracking device (3Space Isotrack – Polhemus: www.polhemus.com) to measure the flexion-extension and pronation-supination axes of 5 fresh cadavers. Three receivers mounted directly onto the humerus, ulna and radius were used to measure three trials of passive flexion-extension and pronation-supination motions. The optimal position and orientation axes in global coordinates were estimated from the recorded motions using a helical-axes method. It was found that the pronation-supination axis is approximately fixed and runs through the radial head and the distal end of the ulna. The mean flexion-extension and pronation-supination axes were approximately perpendicular to each other and about 4 mm away. Only data for one specimen were presented and for this subject the position and orientation errors were 1.27 cm and 4.12º respectively.

Stokdijk et al. (1999) presented a functional method for estimating the position and orientation of the elbow flexion-extension axis *in vivo* using a 3D electromagnetic tracking device (Flock of Birds – Ascension Technology Inc.). One receiver was attached on a circular cuff around the upper arm and the other one was glued to the distal end of the forearm. The position and orientation of the elbow flexion-extension axis was estimated from several cycles of flexion and extension recorded motions (forearm at midposition between supination and pronation) performed by the subject using a helical-axes method. The mean standard deviation of the position and orientation of flexion-extension axis for 10 subjects (5 males, 5 females, 30.8±9.8 yr) was 2.37, 1.36, and 1.19 cm for the position and 1.43, 4.84 and 4.41º for the orientation in the local coordinate system of the humerus, which was defined with the lateral humeral epicondyle, medial humeral epicondyle and GHJC. GHJC was estimated using the regression method of Meskers et al. (1998), and the mean position and orientation of the flexion-extension axis for the 10 subjects was given in the local coordinate system of the humerus. The authors concluded that their results agreed with previous studies and that the inter-individual variability was rather low. Then, the mean values could be used to estimate the flexion-extension axis for a specific subject as a function of GHJC, the lateral humeral epicondyle and the medial humeral epicondyle.

2.1.10 WRIST JOINT

The wrist is an anatomic entity composed of 8 bones called carpal bones or wrist bones (Figure 2.1). The relative motion between the carpal bones is usually neglected in gross motion studies. These bones are considered as a single joint, called the wrist joint. The wrist joint, as a whole, has two DoFs: flexion-extension about an axis approximately through the radial styloid and ulnar styloid, and abduction-adduction (or radio-ulnar deviation) about an axis perpendicular to the flexion-extension axis and the plane of hand palm (Zatsiorsky, 1998). The abduction-adduction axis passes distally with regard to the flexion-extension axis by approximately 5 mm (Zatsiorsky, 1998).

Biryukova et al. (2000) modelled the wrist joint as a skewed-oblique universal joint and estimated the joint parameters from passive wrist motions using a functional method.

Garner and Pandy (1999) modelled the wrist joint as a skew universal joint. They estimated the joint parameters by fitting different geometrical shapes to the three-dimensional articular surfaces of the reconstructed bones for one specific subject (see section 3.2.1.5 and 3.2.1.9 for details).

2.1.11 HIP JOINT

The hip joint is formed by the femoral head and the acetabulum, a concave surface in the hip bone of the pelvis (Figure 2.1). The femoral head is almost spherical and the hip joint is usually modelled as a spherical joint with its centre at the geometric centre of the femoral head. Different functional and regression methods have been used to estimate the hip joint centre (HJC). The pelvic width, pelvic depth and pelvic height are three common parameters used by regression methods for estimating the HJC. Pelvic width is defined as the distance between the left and right ASIS, pelvic depth is the distance between the ASISs and PSISs midpoints and pelvic height is the perpendicular distance from the pubic symphysis to a line passing through the left and right ASIS.

Bell et al. (Bell et al., 1989; Bell et al., 1990) used radiographic measurements for estimating the HJC position, which was located with respect to the ASIS at 14% of pelvic width in the medial direction, 30% of pelvic width in the inferior direction and 22% of pelvic width in the posterior direction. The authors compared their method with two regression methods (Tylkowski et al., 1982; Andriacchi and Strickland, 1983) and Cappozzo's functional method (Cappozzo, 1984) and concluded that their method was the most accurate.

According to Seidel et al. (1995) and Leardini et al. (1999) the correlation of the anteroposterior and superior-inferior coordinates of HJC with pelvic

width is low and the regression equations proposed by Bell et al. (1990) are not justified. Kirkwood et al. (1999) evaluated the accuracy of Bell's method and found that the estimated hip centre is 2.6 cm lateral and 1.0 cm superior to the true hip centre location on average.

Seidel et al. (1995) presented a regression method for estimating HJC location from ALs based on direct measurements performed on defleshed pelves of sixty five cadavers (35 females and 30 males; 75.1 yr SD 12.6). HJC location as a function of ALs was similar for both genders. Its location relative to ASIS is 14% of pelvic width along the medio-lateral axis (SD 3%, r=0.85, mean error 0.58 cm), 34% of pelvic depth along the anteroposterior axis (SD 2%, r=0.54, mean error 0.30 cm) and 79% of pelvic height along the superior-inferior axis (SD 5%, r=0.81, mean error 0.35 cm). The pelvis axes used to define the HJC location can be found from the definition of the frontal plane, which is defined as the plane containing the pubic symphysis and the left and right ASIS.

Leardini et al. (1999) pointed that Seidel's method is not practical since it requires the measurement of the pubic symphysis, which is an awkward AL. Furthermore, they found that the correlation between pelvic width and HJC location in the medio-lateral direction was different (r=0.29) to the one reported by Seidel et al. (r=0.85). Kirkwood et al. (1999) evaluated Seidel's method and found that the estimated hip centre is on average 2.6 cm lateral, 1.0 cm anterior, and 2.107 cm inferior with regard to the true hip centre location.

Leardini et al. (1999) presented and validated a functional method for the estimation of HJC location based on Cappozzo et al. (1984) and compared it with the regression methods of Bell et al. (1990) and David et al. (1991). The accuracy of each method was assessed by comparing the estimated HJC location with the true HJC measured in 11 males (29 yr SD 5.8, 1.796 m SD 0.073) using a roentgen stereo-photogrammetric analysis. The functional method consists in measuring predefined hip motions (flexion-extension, abduction-adduction and circumduction) with an optoelectronic motion capture system. Then, the HJC is estimated as the centre of the optimal spherical surface fitted to the centroid of the markers located on the thigh. This method estimated the HJC location within a root mean square distance of 13 mm on average and did not exhibit a significant bias while both regression methods gave a root mean square distance of 25-30 mm on average and were biased.

Several authors have suggested that the accuracy of functional methods may be compromised for subjects with limited hip range of motion in

pathological cases (Bell et al., 1990; Seidel et al., 1995; Kirkwood et al., 1999). Piazza et al. (2001) studied the effect of a limited range of motion and different variations of the functional method on a mechanical linkage approximating the pelvis and thigh. They found that the HJC location errors increased significantly when the range of motion was limited but the errors were small (< 1 cm) when compared to typical errors of regression methods.

Kirkwood et al. (1999) compared four prediction methods for estimating the HJC location. The compared methods were: Seidel et al. (1995), Bell et al. (1989; 1990), Andriacchi and Strickland (1983), and a modified version of Andriacchi and Strickland. Andriacchi and Strickland (1983) considered that the HJC is located 2 cm distal (inferiorly) from the midpoint of a line connecting the ASIS and the pubic symphysis. The modified version locates the HJC at the midpoint of the line connecting the ASIS and the pubic symphysis. The true 3D location of the HJCs of 10 healthy subjects (6 males and 4 females, 57-73 yr, 51-99 kg) was measured using X-rays in order to compare them with the estimations of the four methods. The method of Andriacchi and Strickland was found to be the most accurate and on average, the HJC was located 0.7 cm medially and 0.8 superiorly from the true location. Bell's method found on average the HJC 2.6 cm laterally, 0.5 cm posteriorly, and 1.0 cm superiorly from the true location. Unfortunately the investigation of Bell et al. (1990) is not in agreement with Kirkwood et al. (1999) because Bell et al. found that Andriacchi and Strickland's approach located the HJC 4.6 distal and 1.7 cm lateral to the true location on average.

Summarising, the studies that compare different methods to locate HJC have failed to demonstrate conclusively which one is the most accurate and their results are contradictory. Nevertheless, functional methods seem to be the most accurate and they are recommended by the ISB (Wu et al., 2002).

2.1.12 KNEE JOINT

The knee joint is composed of two joints: the tibiofemoral joint, which connects the tibia and femur, and the patellofemoral joint, which connects the patella and femur (Figure 2.1). The knee joint motion is determined by the geometry of the internal surfaces and the forces exerted by the muscles and ligaments. The location of the knee joint axes is still a matter of discussion between researchers and there are at least four different points of view in the literature (Zatsiorsky, 1998 pp. 302-303).

In this thesis, the knee joint centre (KJC) is assumed to be fixed but during a normal walk cycle it can move by an average of 7 mm longitudinally, 14.3 mm anteroposteriorly, and 5.6 mm mediolaterally (Lafortune et al., 1992).

The most common approximation in gross motion studies is to locate the KJC at the middle point of a line connecting the centres of the lateral and medial femoral epicondyles (Benedetti et al., 1998; Holden and Stanhope, 1998; Vaughan et al., 1999). The knee joint flexion-extension axis is usually approximated by the line connecting the centres of the lateral and medial femoral epicondyles (Lafortune et al., 1992; Cappozzo et al., 1995; Hagemeister et al., 1999; Piazza and Cavanagh, 2000) and the internal-external rotation axis by the longitudinal axis of the tibia (Hagemeister et al., 1999; Piazza and Cavanagh, 2000). However, the femoral condyles are relatively large and it is not easy to identify their centres repeatably and accurately. Although the KJC and the knee joint axes presented above are assumed to be an approximation of the true KJC and axes, Churchill et al. (1998) have suggested that they are the true KJC and knee joint axes.

2.1.13 ANKLE JOINT COMPLEX

The ankle joint complex is composed of two joints (Figure 2.1). The ankle or talocrural joint connects the talus with the tibia-fibula and the subtalar or talocalcaneal joint connects the talus with the calcaneous.

The talocrural joint can be modelled as a revolute joint whose axis lies approximately between the tips of the lateral and medial malleolus (Zatsiorsky, 1998). When viewed from medial to lateral, the joint axis is directed posteriorly and inclined downward. The angle between the mediolateral direction and the joint axis in the transverse plane is 6º on average according to Inman (1976) and 6.6º±8.1º according to van den Bogert et al. (1994). The angle between the anteroposterior direction and the joint axis in the sagittal plane is 8º on average according to Inman (1976) and 7.0º±5.4º according to van den Bogert et al. (1994).

The subtalar joint is difficult to study because the movement of the talus bone cannot be measured with markers. The subtalar joint can be approximated by a fixed revolute joint (Zatsiorsky, 1998). The angle between the subtalar joint axis and the anteroposterior axis in the transverse plane is on average 23º±11º (range 4º-47º) according to Inman (1976) and 18º±1.6º according to van den Bogert et al. (1994). The angle between the subtalar joint and the anteroposterior axis in the sagittal plane is 49º±9º (range 20.5º-68.5º) according to Inman (1976) and 37.4º±2.7º according to van den Bogert et al. (1994).

Van de Bogert et al. (1994) proposed an optimisation method to locate the talocrural and subtalar joint axes. The talocrural and subtalar joints were modelled with a revolute joint each one and the model of the ankle joint

complex was defined with 12 parameters. Eight different unloaded motions of the ankle joint complex in 14 subjects covering the entire physiological range of joint motion were recorded with a motion capture system using three markers on the shank and three on the foot. The 12 model parameters were estimated from the recorded motions by solving a least-squares optimisation problem.

The talocrural and subtalar joint axes are difficult to locate in a living subject. Furthermore, due to the axes configuration the description of the relative motion between the shank and the foot requires three Euler's angles, although they are not independent. Gross motion studies usually considered a fixed centre of rotation and model the ankle joint complex as a spherical joint (Moseley et al., 1996; Benedetti et al., 1998; Frigo and Rabuffetti, 1998; Vaughan et al., 1999). The ankle joint complex centre is usually approximated by the midpoint between the lateral and medial malleolus. Another option is to use the multiple linear regression equation presented by Vaughan et al. (1999). These regression equations give the location of the ankle joint complex centre with regard to the lateral malleolus as a function of foot length (from heel to the tip of the longest toe), malleolus height (vertical distance from the floor to the lateral malleolus), and malleolus width (distance between the medial and lateral malleolus).

2.1.14 INFLUENCE OF JOINT PARAMETERS IN RESULTS

Only a few papers have been published about the influence of joint parameter errors in the analysis results and most of them are limited to studies of the lower extremity. Notice that the origin of the joint parameter errors could be caused by incorrect estimation of the joint parameters or by movement of the joint centre or joint axes away from their assumed fixed location during the course of the movement.

Delp and Maloney (1993) investigated the effect of the HJC location on the moment arms, maximum isometric muscle forces, and maximum isometric joint moments generated by four muscle groups (hip abductors, hip adductors, hip extensors and hip flexors) using a three-dimensional musculoskeletal model of the human lower extremity. The HJC was displaced ± 2 cm in the three anatomical directions, hip abduction angle was varied in the range (-10, 20) degrees, and hip flexion angle in the range (0, 60) degrees. The authors found that superior-inferior displacement of HJC has the greatest effect on muscle forces, moment arms and moments. A 2 cm superior displacement of HJC decreases abduction force (44%), moment arm (12%), and moment (49%), while a 2 cm inferior displacement increases abduction force (20%), moment

arm (7%) and moment (26%). Similarly, a 2 cm superior displacement decreases flexion force (27%), moment arm (6%), and moment (22%), while a 2 cm inferior displacement increases flexion force (4%), moment arm (8%), and moment (12%).

The influence of the KJC location on knee flexion-extension moments in gait analysis was investigated by Holden and Stanhope (1998). They assumed that the KJC was located at the midpoint between the lateral and medial epicondyle of the femur. Gait data were measured on 18 healthy subjects at five different speeds and KJC was varied by ±10 mm in the anteroposterior direction. The effect of KJC variation on knee flexion-extension moments was similar across subjects and at all five walking speeds. The effect of KJC variation on the first extensor moment peak increased from 14% for the fastest speed up to 123% for the slowest speed, expressed as a percentage of the mean knee flexion-extension moment. The authors concluded that KJC variation is important at low walking speeds when the knee joint moments are small in magnitude.

Stagni et al. (2000) investigated the influence of the HJC mislocation on gait analysis results. Gait data were measured on five subjects (25-29 yr, 54.9-99.5 kg, 1.64-1.83 m) using a motion capture system and one force platform. HJC location was estimated using a functional method (Cappozzo, 1984; Leardini et al., 1999) and errors in the range of ±30 mm were added in the three axes in order to study the effect of HJC mislocation on the angles and moments of the hip and knee joints. The effect of HJC mislocation on knee angles and moments and on the hip angles can be considered negligible. The error in the hip flexion-extension moment is -22% when the HJC is mislocated 30 mm anteriorly. When the HJC is mislocated 30 mm laterally, the error in the hip abduction-adduction moment is -15%. The flexion-to-extension timing is delayed about 25% of the stride duration when the HJC is mislocated 30 mm posteriorly. The authors recommended the use of HJC estimation methods with minimum anteroposterior error because the largest errors appear when the HJC is mislocated in this direction. Based on this recommendation, the functional method should be preferred first and Bell's method in the second place.

The effect of joint centre location and the centre of mass location (see section 2.2.5) on the work output was investigated by Nagano et al. (2000). Data for a vertical jumping were generated with a 2D computer model, which consisted of four body segments representing head-arms-trunk, thighs, shanks and feet. The location of each joint centre (hip, knee and ankle) was varied by ±10% of the length of the proximal body segment. The effect of joint centre variation in the work output was in the range -20% and 20%. When variations

of the joint centre and the centre of mass were combined independently, the errors in the work output ranged between -23% and 28%.

One of the scarce studies on the influence of joint parameters on the upper extremity was presented by Challis and Kerwin (1996). The motion of the upper extremity was measured experimentally with a motion capture system during elbow flexion-extension and pronation-supination motions. Among other parameters, they studied the influence of the elbow joint centre location on the resultant joint moments of the elbow. The location of elbow joint centre was varied ±0.01 m in the three axes and the effect on the resultant joint moments was small, with a maximum absolute difference of 1.4 Nm for the flexion-extension axis (peak-to-peak value of 55 Nm) and 2.5 Nm for the supination-pronation axis (peak-to-peak value of 14 Nm). The resultant elbow joint moments were most sensitive to errors in the estimated velocities and accelerations.

Summarising, the influence of joint parameter errors in the joint moments, muscle forces and work output cannot be neglected and it must be taken into account. However, the influence of joint parameter errors in the joint angles can be considered negligible at least for gait analysis (Stagni et al., 2000).

2.1.15 SELECTION OF METHODS FOR ESTIMATING JOINT PARAMETERS

2.1.15.1 MoDyCo skeletal models

The three skeletal models developed for the MoDyCo project (section 3.3) require the identification of the parameters of 13 joints of the upper body and 3 joints of the right lower extremity. The joints of the upper body are the sternoclavicular, acromioclavicular, scapulothoracic, glenohumeral, elbow, wrist and a fictitious joint connecting the thorax and pelvis. The joints of the right lower extremity model are the hip, knee and ankle joints.

As mentioned in the objectives of this thesis (section 1.2.2), in the MoDyCo project, the measurement equipment available for estimating the joint parameters is the Vicon motion capture system and inexpensive instrumentation like measuring tape. Fortunately, a motion capture system is all that is necessary for applying all the joint parameter estimation methods presented in the previous sections. Vicon can be used for recording motion data for functional and optimisation methods and for measuring global coordinates of ALs using the CAST approach introduced by Cappozzo et al. (1995), which is described in section 5.1.1.

In the MoDyCo project, it is planned to study a large number of motions for different subjects. Therefore, the methods for estimating joint parameters should be relatively fast. The ISB recommendations (Wu et al., 2002) on definitions of local coordinate systems are used in the skeletal models developed for the project (Chapter 3). These recommendations define local coordinate systems as a function of several AL coordinates of each body segment. Hence, the global coordinates of some ALs are already available and this is an advantage for regression methods which require AL positions.

Prediction methods presented in section 2.1.1 are discarded due to their low accuracy. Functional methods require recording several motions for each joint, e.g. Leardini et al. (1999) and Stokdijk et al. (2000) measured three different motions for estimating hip joint centre and glenohumeral joint centre respectively. Then, the trajectories of the markers located on each body segment must be post-processed with the motion capture software. Finally, joint parameters are estimated from marker trajectories using a functional method. If an average of three different motions are recorded for each joint, 48 joint motions are needed for estimating the joint parameters of the 16 joints. Considering that a minimum of 20 subjects will participate in the investigation, the number of motions (960 = 48 motions × 20 subjects) and the total amount of time required seems too large. Another drawback of functional methods is that they may need specific equipment for some joints (e.g. glenohumeral joint in Stokdijk et al. (2000), see section 2.1.8). Also for these reasons functional methods are discarded.

Optimisation methods require the development of complex computer models and recording several motions for each joint like functional methods, which is time consuming. An additional drawback of optimisation methods is that some of them need parallel processing to complete in a reasonable amount of time (Reinbolt et al., 2005).

In the MoDyCo project, regression methods have been selected for joint parameter estimation whenever they exist. If regression methods are not available, methods based on ALs have been used. The specific methods for estimating the parameters of each joint are presented in Chapter 3 for each human skeletal model.

Regression methods estimate joint parameters from a few anthropometric measurements which can be obtained from the global coordinates of some ALs. Most of the required ALs are already available because they must be measured for the ISB recommendations and this can save time in the experimental protocol. A drawback common to all regression methods derived from data measured on defleshed bones is that subcutaneous

tissue thickness is not taken into account in the regression equations. However, when AL positions are measured on a living subject, the subcutaneous tissue thickness is inevitably included in the measurements. Therefore, systematic errors are introduced into the measurements although they are not usually taken into account in most of the investigations.

Some authors suggest that inaccuracies associated with subcutaneous tissue thickness are minimised because ALs are selected in regions of thin subcutaneous tissue (Rab et al., 2002). Other authors consider a given value of tissue thickness while estimating the true location of an AL on the bone, e.g. Bush and Gutowski (2003) considered a tissue thickness of 8 mm for estimating the ASIS and PSIS landmarks on the pelvis. The main drawback of regression methods is that they have been found less accurate than functional methods for several joints (Leardini et al., 1999; Stokdijk et al., 2000). However, the comparative studies of functional and regression methods presented in the previous sections do not take into account subcutaneous tissue thickness and this may have biased the comparison results.

2.1.15.2 RAMSIS whole body model

The approach used in the REALMAN project is different from the methods for estimating joint parameters presented in the previous sections. The basic idea of the REALMAN project was to adjust the RAMSIS whole body model to a specific subject using a minimum of two simultaneous pictures of the subject from two different angles in two different postures.

The RAMSIS whole body model consists of an internal kinematic skeleton and an external body surface (see section 3.4). The software PCMAN (Seitz and Bubb, 1999; Seitz et al., 2000; Seitz and Bubb, 2001) was used to adjust semi-automatically the RAMSIS model to a specific subject. PCMAN is based on the principles of stereophotogrammetry and one of the main advantages is that any camera can be used provided that the pictures can be converted into digital format. PCMAN gives the first adjustment of the RAMSIS model to a specific subject but the user intervention is required to obtain a refined adjustment. The software allows the user to adjust the posture (by specifying joint angles) and the anthropometry of the subject (length and width of the body segments). The standard procedure requires a minimum of two simultaneous pictures in two predefined postures (Figure 2.7) although increasing the number of simultaneous pictures per posture and/or the number of postures increases the accuracy of the adjustment. On these pictures, a calibration corpus must be seen in order to compute the position and orientation of the cameras. The mean measurement errors compared to

conventional measuring methods are 4.2 mm for body height, 8.2 mm for sitting height, and 15.1 mm for waist circumference (Seitz and Bubb, 1999).

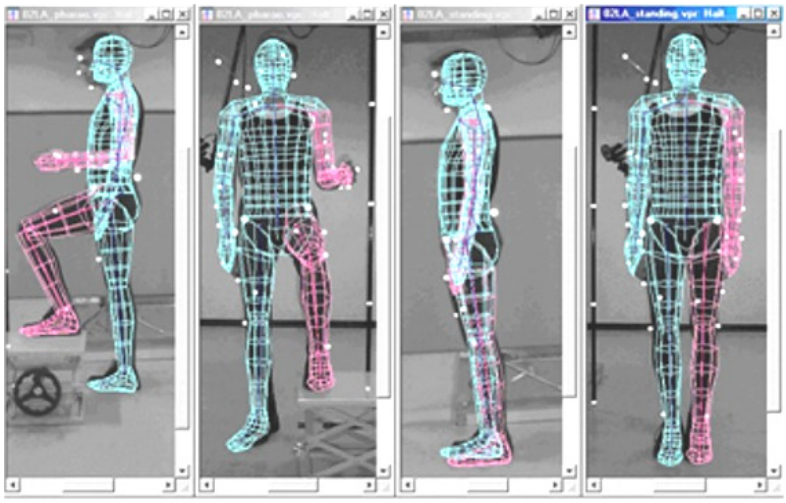

Figure 2.7: Superimposed RAMSIS model adjusted to a subject. PCMAN postures: standing posture (right) and "pharaoh" posture (left), which is a standing posture where the left knee and thigh and the left elbow and upper arm are in a right-angled position.

Measure (mm)	Standing (N=24)			Sitting (N=20)		
	min	max	mean±std	min	max	mean±std
Body height	0.5	39.9	13.7±12.0	0.7	58.9	20.9±15.8
Sitting height	2.1	46.0	19.0±10.6	23.2	75.1	44.1±16.2
Upper arm length	4.0	65.0	28.7±16.9	0	53.9	15.3±14.1
Forearm length	1.0	42.1	14.1±11.3	1.1	41.4	18.1±13.6
Buttock-knee length	1.2	70.5	21.2±17.3	2.1	51.2	21.2±11.4
Knee sitting height	1.5	36.2	10.7±8.0	0.4	40.4	13.7±12.1

Table 2.1: Absolute differences (in mm) between direct and PCMAN measurements. From Wang et al. (2005).

During the REALMAN project the partners Renault and Peugeot-Citroën assessed the joint location accuracy of PCMAN in a wooden manikin. Joint location errors ranged from 10 to 30 mm in the wooden manikin but its accuracy for living subjects was not investigated. INRETS compared direct anthropometric measurements and those obtained by PCMAN in two different postures, a standing posture and a sitting posture (Wang et al., 2005). The differences between direct measurements and PCMAN calculations (Table 2.1) were less than 30 mm in average except for the sitting height in the case of the sitting posture, where the average was 44 mm.

2.2 BODY SEGMENT PARAMETERS

The so-called body segment parameters (BSPs) are the inertia properties of each body segment of a human skeletal model. They are needed for inverse and forward dynamic analyses of skeletal models. Throughout this text, the term BSPs is used to refer to mass, centre of mass (CoM) location and three moments of inertia (MoIs) at the CoM about the anatomical axes. Otherwise, it is specified which inertia parameters are considered.

Two common assumptions are considered in this thesis. First, the body segment CoM is assumed to be located along the longitudinal axis of the body segment. Second, the principal inertia axes are assumed to be coincident with the anatomical axes of each body segment and the products of inertia are considered negligible. Depending on the body segment considered, these assumptions are more or less appropriate but they are made in most of the human movement studies. However, the influence of the errors associated with these assumptions have rarely been investigated (Zatsiorsky, 2002).

Pearsall and Reid (1994) presented a thorough survey paper on methods for estimating BSPs. They reviewed BSPs studies between 1850 and 1993. Other less comprehensive reviews can be found in Cappozzo and Berne (1990), Nigg (1999) and Zatsiorsky (2002). In this section the most representative investigations and methods for estimating BSPs are reviewed. Subject-specific BSPs can be directly estimated on the subject using different measurement techniques (section 2.2.1), scaled from existing BSPs databases (section 2.2.2), or estimated using optimisation techniques (section 2.2.3).

2.2.1 MEASUREMENT TECHNIQUES FOR BSPS ESTIMATION

BSPs have been estimated using different measurement equipments with different levels of complexity. Those methods in which different anthropometric measurements are used to estimate subject-specific BSPs are included in this group. Other methods like proportions methods or regression equations (section 2.2.2) also require anthropometric measurement but they are used to scale BSPs from a database and not to estimate directly BSPs from the measured variables. The measurement techniques for BSPs estimation can be classified into four groups: geometric modelling, 3D whole body scanners, medical imaging techniques and other experimental techniques.

2.2.1.1 Geometric modelling

Geometric methods model body segments as homogeneous solids with geometric forms of varying complexity (e.g. circular cylinder, truncated cones,

stadium solids or elliptical cylinders of small height). The dimensions of the geometric forms are estimated from anthropometric measurements performed on the subject being studied. The anthropometric measurements can be obtained from direct manual measurements using anthropometric callipers and measuring tape or from photogrammetric and computer image processing techniques. The density of each body segment is usually assumed to be uniform and its value is taken from the literature (e.g. Dempster, 1955; Clauser et al., 1969; e.g. Chandler et al., 1975). Then, from the estimated volume and density of each body segment, BSPs can be calculated.

The first elementary geometric method was proposed by Simmons and Gardner (1960), who approximated the human body by 8 body segments, each one modelled with a single geometric form (cylinders and spheres). Whitsett (1963) used 14 body segments to model the human body and increased the type of geometric forms (spheres, ellipsoids, cylinders, truncated cones and rectangular parallelepipeds).

Another simple geometric method was proposed by Hanavan (1964), who modelled the human body with 15 body segments, each one approximated by a single geometric form, which were defined with 25 anthropometric measurements. Wooley (1972) presented a simplified version of the Hanavan model by merging the most distal body segments of the human body (hands, feet, and head) with the adjoining body segment.

Jensen (1978) modelled the human body with 16 body segments, whose volume was approximated by the sum of elliptical cylinders of 2 cm height. The dimensions of the ellipses were estimated using front and side view photographic images of the subject. Uniform density values for each body segment were taken from cadaver studies in the literature (Dempster, 1955; Clauser et al., 1969). The difference between the estimated and measured total mass of the body was less than 2%. The method was also validated with inanimate objects and volume errors ranged from -5.18% to 4.58%. Recently the method has been thoroughly validated in 20 human subjects (Wicke and Lopers, 2003) comparing the volume estimated by the proposed method with the volume measured with a water immersion technique. In the worst case the error in calculating body segment volumes was 4.80%±2.49%. Both studies (Jensen, 1978; Wicke and Lopers, 2003) located the boundary of the body segments on the photographic images by manual digitisation.

A very detailed geometric model with 17 body segments, each one modelled with several geometrical forms, was presented by Hatze (1980). The model requires 242 anthropometric measurements, which according to Hatze can be obtained in less than 80 minutes. It differentiates between male and

female subjects, adjusts the densities of certain body segments based on a special subcutaneous-fat indicator and fully accounts for the specificities of pregnancy and obesity. Density values were taken from the studies by Dempster (1955) and Clauser et al. (1969). The mean error between the estimated and measured total body mass was 0.26% with a maximum error of 0.52%. The overall accuracy of the model compared with experimentally measured BSPs was better than 3% with a maximum error of about 5%. Afterwards, Baca and Hatze (Hatze and Baca, 1992; Baca, 1996) presented a method for estimating the anthropometric measurements required by the Hatze's geometric method from four video images. The edges of the body segments were located automatically with a threshold edge-detector algorithm. The maximum measurement difference between their video-based system and direct manual measurements was 4.6%.

Yeadon (1990) proposed a geometric method that divided the human body in 20 segments. They were modelled with 40 geometric solids (stadium solids, truncated cones and a semi-ellipsoid for the cranium) that required 95 anthropometric measurements (20-30 min. of measurement time) and used the density values of Dempster (1955). The proposed method was applied to three subjects and a maximum error of 2.3% in the total body mass estimation was found.

Sarfaty and Ladin (1993) proposed a method based on photogrammetric and computer image processing techniques for estimating BSPs. Similarly to Jensen (1978), each body segment was approximated by several elliptical cylinders of small width and the dimensions of each elliptical cylinder were estimated from two video images (a frontal view and a lateral view). The edges of the body segments were located automatically with a threshold edge-detector algorithm but the segmentation of the body segments were performed manually. The body segments were assumed to have uniform densities and their numeric values were taken from Dempster (1955). The method gave an average overestimation of 2.51% for the mass, 1.21% for the CoM location and 4.53% for the MoIs.

There are three main concerns about the density values currently available in the literature. First, available density values are obtained on a limited sample of elderly Caucasian cadavers. Second, the density of tissues in cadavers may differ from the density of living tissues. The loss of body fluids in fresh cadavers may vary between 5% and 6% of total body weight (Zatsiorsky, 2002). Third, the generalised assumption of uniform body segment density (with the exception of Hatze (1980)) may affect the estimation of BSPs (Ackland et al., 1988).

In order to evaluate the assumption of uniform body segment density, Wei and Jensen (1995) compared the BSPs estimated by using uniform body segment densities from the literature and the body segment axial density profiles estimated by the authors. The axial density profile gives the body segment density as a function of the percentage of body segment length from the proximal end. Axial density profiles were estimated from CT scans of 50 Chinese young females (18-23 years old) and densities of 17 tissues. They applied the geometric method of Jensen (1978) to five different groups of population (young adult females, young adult males, infants, male children and elderly adults) in order to compare BSPs estimated by using uniform densities and axial density profiles. The effects of using axial density profiles were in general small and the authors could not decide if the axial density profiles produce more accurate estimates of BSPs than uniform density.

2.2.1.2 3D whole body scanners

3D whole body scanning is a relatively new technology to measure body surface geometry (Figure 2.8). A 3D whole body scanner is an optical 3D measuring system that returns a high-density cloud of data points (three-dimensional coordinates and colour) of the whole body. 3D whole body scanners are based on different techniques (e.g. stereo-photogrammetry, laser scanning, infrared scanning, structured light projection) depending on the manufacturer (Daanen and van der Water, 1998). Some manufacturers of 3D whole body scanners are: Cyberware (www.cyberware.com), Vitronic (www.vitronic.de), [TC]² (www.tc2.com), Wicks and Wilson (www.wwl.co.uk) and Hamamatsu (www.hpk.co.jp). 3D whole body scanning has some problems like noise, occlusion (e.g. in the armpits area), areas invisible to sensors (e.g. scalp hair or dark surfaces) or merging data from different sensors, although these problems do not represent a major trouble for its usage.

A surface can be reconstructed from the cloud of data points measured by the scanner. There are different surface reconstruction techniques, which can be classified in mesh-based methods and deformable model methods (Buxton et al., 2000). Once the surface has been reconstructed, it is possible to detect features in the surface and perform measurements between features like AL location or body segment length. Several automatic or semi-automatic techniques have been developed to detect features from the reconstructed surface. They can be classified into three groups: detection of markers placed before scanning, deformable templates with markers on and pattern recognition (Buxton et al., 2000; Suikerbuik et al., 2004). The time required, the resolution, and the accuracy of the scanners varies between manufactures and

techniques. Scanning time can range from less than 1 second (e.g. stereo-photogrammetry) to 10-20 seconds (laser scanning), the resolution can be less than 2 mm and the number of data points can be greater than 1 million.

Figure 2.8: Left: Vitus Pro 3D whole body scanner. Right: Cyberware WB4 3D whole body scanner.

3D whole body scanning was used successfully in the CAESAR project (Robinette et al., 1999; Robinette and Daanen, 2003). A large-scale anthropometric survey was conducted, in which 2500 people in the United States and 2500 people in The Netherlands and Italy participated. Before scanning, 73 small markers were attached to 73 selected anthropometric locations on the body of each individual. All individuals were scanned and the locations of the markers and other anthropometric measurements (e.g. lengths, circumferences) were extracted.

The only published study to date where BSPs have been estimated by using a 3D whole body scanner (Hamamatsu – Bodyline scanner) was conducted by Norton et al. (2002). The mass and the CoM location of 10 human lower limbs (considered as a whole) were calculated using the volume estimated from the lower limb surface measured with the scanner and tissue densities taken from the literature. In order to estimate the mass and CoM location, the lower limb was modelled as composed of two different elements, bone and soft tissue. The volume of the bone of each subject was estimated by scaling bone geometry obtained from the Visible Human Project. The bone geometry was scaled to each subject using distances measured from a lower limb X-ray of the subject. The volume estimated from the scanner was validated with the volume measured using a water displacement method, which gives an averaged percentage error of 0.61% (SD 0.31%).

Pain and Challis (2001a) presented a method for estimating BSPs based on sonic digitisation of the body surface. This study is difficult to classify and is included here because it can be considered as a manual 3D whole body scanning technique. The authors measured surface data points (three-dimensional coordinates) of several human shanks using a sonic digitiser (SAC GP-12XL) and estimated shank volume from them. They calculated BSPs from the estimated shank volume and the uniform density values of Clauser (1969). The accuracy of the method for estimating BSPs was assessed on a wooden test object and an error of 2.5%±1.4% was found. According to the authors the time required to measure surface data points of the whole body is approximately 45 minutes.

3D whole body scanners are fast, non-invasive, and give personalised surface measurements but at present the cost of the scanner is high (40000-410000) and it requires the usage of specialised software to post-process the data.

2.2.1.3 Medical diagnostic technologies

BSPs can be estimated using medical diagnostic technologies like magnetic resonance imaging (MRI), computed tomography (CT), dual energy x-ray absorptiometry (DEXA), gamma-ray scanning (GRS) and biplanar low-dose radiography (BLR). All these methods can provide accurate measurements of BSPs for a specific subject. However, such techniques require specialised and expensive instrumentation and personnel, and involve high radiation levels in CT and GRS.

MRI and CT provide 2D cross-sectional medical images of the human body. The method for estimating BSPs consists in identifying from the 2D images the boundaries of the different tissues manually or automatically. From the estimated boundaries, the 3D surface and volume of each tissue can be reconstructed. Then, from each tissue volume and measured or estimated density values BSPs can be calculated. DEXA and GRS measure the surface density in a single plane, i.e. the mass per unit of surface area which is a 2D measurement, and from this surface density the BSPs can be estimated. BLR records simultaneous low-dose frontal and sagittal X-rays views of a subject and from these data 3D geometric models of the bones and external body surface can be reconstructed. Then, BSPs can be calculated from estimated volumes and tissue density values available in the literature.

One of the first studies for estimating BSPs from CT was conducted by Huang and co-workers (Huang and Suarez, 1983). They measured the density of each tissue (Huang and Wu, 1976) and estimated BSPs of a young porcine

subject and a 3 year-old female specimen. The porcine subject was sacrificed, frozen and sectioned in order to check the accuracy of the method. Zheng et al. (1990) estimated BSPs of fifty Chinese young female university students (18-23 yr) using CT. Densities of 17 tissues measured in 26 cadavers were used to estimate BSPs from the 2D images. Four fresh cadavers were used to validate BSPs estimates in living subjects using CT. Pearsall et al. (1996) investigated BSPs of the trunk in two males and two females using CT. They reported BSPs associated with the different vertebral levels of the trunk and provided a proportion method for estimating BSPs.

Martin and co-workers (1989) performed two investigations to study the validity of MRI for estimating mass, CoM location and moment of inertia (MoI) about a transverse axis through the CoM. In both studies the tissue boundaries of bone, fat and muscle were determined manually. In the first study eight baboon cadaver body segments (four forearms, two upper arms and two lower legs) were used to measure BSPs and tissue densities were measured experimentally. BSPs estimated from MRI were compared with BSPs obtained by other experimental techniques. It was concluded that there was a close agreement for the location of the CoM while the volume (average 6.3%), mass (average 6.7%) and MoIs (average 4.4%) were overestimated. In the second study, 12 lower right legs of adult male distance runners were MRI scanned (Mungiole and Martin, 1990). The density values of muscle, fat and bone were taken from Clauser et al. (1969). BSPs estimated from MRI were compared with other methods from the literature. While the location of the CoM was similar for all methods, mass and MoI estimated from MRI were higher than those from most of the other methods.

Cheng (2000) estimated BSPs of 8 Chinese young males using MRI and provided a proportion method (see section 2.2.2.2) to scale BSPs to different body sizes. Tissue density values were taken from the literature and the human body was segmented in 14 body segments. Significative differences for the upper arm, thigh, and shank were found between some of the BSPs of Chinese subjects and Caucasian subjects from previous studies (Dempster, 1955; Clauser et al., 1969; Hatze, 1980; Martin et al., 1989; Pearsall et al., 1996). The mean error between the estimated and measured total body mass was 3.8%.

Zatsiorsky and co-workers (Zatsiorsky and Seluyanov, 1983; Zatsiorsky and Seluyanov, 1985; Zatsiorsky et al., 1990a; Zatsiorsky et al., 1990b) used GRS to estimate the BSPs of 100 young living Caucasian males and 15 young living Caucasian females. The method gave an error less than 3% for the estimation of BSPs except for the longitudinal MoI which gave an error up to 10%. From the measured BSPs, they derived 4 methods with different levels of complexity for scaling BSPs to a specific male or female (see section 2.2.2).

Durkin et al. (2002) investigated the accuracy of DEXA for estimating BSPs. The maximum error of the whole body mass estimation for 11 young males was 2.79%. The percentage error of a plastic cylinder and a human leg for length, mass, and CoM location were under 1.3%, 3.2% and 2.8% respectively. Currently, the main limitation of the method is that only the MoI in the frontal plane can be estimated due to the two-dimensional nature of the DEXA machine. The main advantages of DEXA are that the equipment cost is less than one-tenth of an MRI or CT equipment and the measurement time is less than 3 minutes.

Ganley and Powers (2004) used DEXA for estimating BSPs in fifty children from 7 to 13 years (33 males and 17 females). Only the mass, CoM location and MoI in the frontal plane of the thigh, shank and foot were measured. A proportion method to scale the measured BSPs to different subjects was derived from these data (see section 2.2.2).

Dumas et al. (2004) investigated the use of BLR for estimating BSPs of 12 thighs (6 young males and 6 young females). Simultaneous low-dose frontal and sagittal X-rays of the 12 thighs were obtained with the EOSTM system (Biospace Instruments - www.biospace.fr). 3D surfaces of the femur, patella and external surface of the thigh were reconstructed using the Non Stereo Corresponding Contour (NSCC) algorithm (Laporte et al., 2003). This algorithm is based on the deformation of 3D generic surface models in order to match 2D radiographic contours. The surface of the femur can be reconstructed with a mean error of less than 1 mm (Le Bras et al., 2003). BSPs are estimated from the reconstructed 3D surfaces and densities of bone and soft tissue taken from the literature. BSPs estimated from BLR were compared with BSPs estimated using GRS (Zatsiorsky et al., 1990b), DEXA (Durkin and Dowling, 2003), MRI (Cheng et al., 2000) and two cadaver studies (Dempster, 1955; Clauser et al., 1969). BLR gave similar results to GRS, DEXA and MRI.

2.2.1.4 Other experimental techniques

In addition to the techniques presented in the two previous sections, there are a number of other experimental techniques for estimating BSPs or related variables. The mass of each body segment can be obtained by dissecting the human body and weighting each body segment on a balance or a force plate but this is only valid for cadaver studies (Dempster, 1955; Clauser et al., 1969; Chandler et al., 1975).

The volume of a body segment can be estimated by introducing the body segment in a water recipient and measuring the water volume displaced. This method is usually referred to as water immersion method and it can be

used to estimate BSPs if a constant density is assumed or to validate the volume estimated with other methods (Norton et al., 2002; Wicke and Lopers, 2003).

The CoM location can be estimated using a balance plate (Winter, 1990. pp. 64-65). The method can be used to estimate the CoM of dissected body segments (Dempster, 1955; Clauser et al., 1969) or distal body segments of living subjects, if measurements are performed with the body segment in different positions and the body segment mass is known (Bernstein, 1931 according to Clauser, 1969). Pataky et al. (2003) proposed a similar method but they used a force plate, assumed a known CoM location and estimated the body segment mass instead of the CoM location.

Another method for estimating the CoM location and MoIs is the incremental water immersion method (Drillis and Contini, 1966). Incremental volumes are measured as a body segment is submerged in water in small equidistant steps. Assuming a constant body segment density the CoM location and MoIs can be estimated.

The MoIs of the body segments can be estimated using a pendulum oscillation method. If a dissected body segment is suspended from one end and the period of oscillation is measured, the MoI around the axis of oscillation can be estimated (Dempster, 1955; Chandler et al., 1975; Durkin et al., 2002). Chandler et al. (1975) evaluated the accuracy of their pendulum oscillation method using a solid aluminium bar with known inertial parameters. They found that the error ranged from -10.4% to 3.8% with a standard deviation of 3%.

The quick release method (Winter, 1990. pp. 65-66) can be used to estimate MoIs of distal body segments (foot, shank, hand and forearm) in living subjects. The basic method consists in applying a sudden force at the distal end of the body segment and measuring the force and the linear acceleration at the distal end of the body segment. The MoI of the body segment can be estimated from the distance between the body segment joint centre and the force application point, the distance between the body segment joint centre and the accelerometer location, the measured force and the measured acceleration. The method assumes that joint friction and antagonistic muscle force are negligible. Different versions of the method have been proposed in the literature (Drillis and Contini, 1966; Bouisset and Pertuzon, 1968; Cavanagh and Gregor, 1974; Stijnen et al., 1983).

2.2.2 SCALING FROM BSPS DATABASES

In the literature several BSPs databases have been presented together with methods to scale BSPs from the database to a specific subject. However, most of the current databases are deficient in four aspects. First, the sample of population investigated is usually too small. Second, several authors (Pearsall and Reid, 1994; Cheng et al., 2000; Zatsiorsky, 2002; Durkin and Dowling, 2003) suggest that differences in BSPs exist between human populations due to differences in age, gender, race and morphology but there is a lack of studies of diverse populations. Most databases are based on data from a limited number of elderly male Caucasian cadavers, although data from young male and female Caucasian living subjects (Zatsiorsky et al., 1990b), young male Chinese living subjects (Cheng et al., 2000), living children (Jensen, 1989; Ganley and Powers, 2004) and living infants (Schneider and Zernicke, 1992) are also available. Third, the assumption that BSPs estimated from cadavers is similar to BSPs of living subjects has been questioned (Mungiole and Martin, 1990; Pearsall and Reid, 1994; Zatsiorsky, 2002). And fourth, the databases are also difficult to compare due to the different segmentation methods used to define each body segment.

The methods reported in the literature to scale BSPs of the databases to a specific subject can be classified into three groups: regression methods, proportions method and geometric scaling. It must be noted that the database used to scale BSPs to a specific subject should be derived from subjects sufficiently similar to the subject being studied, i.e. age, gender, race and morphology must be within the range of the sample population.

2.2.2.1 Regression methods

Regression methods estimate BSPs of a specific subject as a function of a few anthropometric measurements. The number of anthropometric measurements depends on the regression method, which can be linear or nonlinear. Anthropometric measurements range from one or two global measurements (e.g. body height or body weight) to several measurements for each body segment (e.g. body segment length and body segment circumference).

Hinrichs (1985) derived a set of linear regression equations for estimating MoIs, based on the data of Chandler et al. (1975). The human body was segmented into 14 body segments, and one or two anthropometric dimensions per body segment (body segment length or body segment circumference) were used as predictors in each equation. The two transverse MoIs were considered equal for all body segments excluding the torso, i.e. symmetry about the longitudinal axis was assumed. According to Yeadon and

Morlock (1989), the two transverse MoIs differ by less than 5% in Chandler's database. Furthermore, Yeadon and Morlock (1989) and Vaughan (1999) pointed out that the regression equations proposed by Hinrichs (1985) are not dimensionally consistent.

Jensen (1986) studied the effects of growth in BSPs for 12 boys between the ages of 4 and 15 yr. BSPs were estimated using the geometric method of Jensen (1978). Linear regression equations were derived from the measured BSPs using as independent variables age, body mass, body segment length and body segment circumference or width.

Yeadon and Morlock (1989) derived linear and non-linear regression equations, based on the data of Chandler et al. (1975), for estimating MoIs about the CoM. The two transverse MoIs were considered equal for all body segments except for the torso. Using data within the sample range of Chandler et al. (1975) the averaged standard error was 21% for the linear equations and 13% for the nonlinear equations. Outside the sample range of Chandler et al. the regression equations were compared with the geometric method of Yeadon (1990) and the percentage residuals were 286% of the linear equations and 20% for the nonlinear equations. It was concluded that the non-linear approach is better than the linear one, especially outside the sample range of Chandler's data.

Zatsiorsky and co-workers (Zatsiorsky and Seluyanov, 1983; Zatsiorsky and Seluyanov, 1985; Zatsiorsky et al., 1990a; Zatsiorsky et al., 1990b) used gamma-ray scanning to measure the BSPs of 100 young living Caucasian males and 15 young living Caucasian females (see section 2.2.1.3). The human body was modelled with 16 body segments (trunk divided in 3 body segments), and the reference points for the CoM location were ALs. From the measured BSPs, the authors derived 4 methods with different levels of complexity for estimating BSPs of males and females:

1. A proportion method that is described in section 2.2.2.2.
2. Linear multiple regression method for estimating BSPs from total body weight and height.
3. Linear multiple regression method for estimating BSPs from several anthropometric measurements for each body segment.
4. A nonlinear regression method for estimating body segment mass and MoIs from each body segment length and circumference.

The authors concluded that the fourth method gives more accurate results than the second method although numerical results were not reported. Nevertheless, this conclusion has been contradicted recently by Durkin and

Dowling (2003). They also claimed that if the stature of a subject falls in the range of the subjects measured in the study, the fourth method gives less accurate results than the third method.

Schneider and Zernicke (1992) estimated the mass, CoM location, and transverse (mediolateral axis) MoI of 44 infant upper limbs (upper arm, forearm, and hand) and 70 infant lower limbs (thigh, shank, and foot) using a modified version of Hatze's geometric method (Hatze, 1980). The age of the infants ranged from 0.04 to 1.5 year old. From the estimated body segment masses and transverse MoIs, linear regression equations were derived using as independent variables age, body mass, body segment length and circumference or width. The body segment CoM location was reported as a percentage of body segment length measured from the proximal joint because there was no correlation between body segment CoM location and the independent variables used.

Vaughan et al. (1999) presented a method for estimating the BSPs of the thigh, shank and foot, based on the data of Chandler et al. (1975). The method requires 20 anthropometric measurements for estimating BSPs of the left and right legs. Body segment mass is calculated with multiple linear regression equations, MoIs with linear regression equations and CoM location is given as a percentage of body segment length measured from the proximal body segment joint.

Shan and Bohn (2003) measured BSPs of four population groups (25 male Chinese, 25 female Chinese, 25 male Germans and 25 female Germans) using a 3D whole body scanner developed by the authors. The human body was modelled with 16 body segments according to the segmentation used by Zatsiorsky and Seluyanov (1983). Density data of Dempster (1955) were used in the calculations of BSPs, and the difference between the estimated and measured total body mass ranged from -5.38% to 4.52%. Multiple linear regression equations for estimating body segment mass and MoIs were derived from the measured BSPs for the four population groups using only body height and body mass as independent variables. CoM location was given as a percentage of body segment length because the correlation with body height and weight was very low.

Table 2.2 summarises the main characteristics of the nine regression methods presented in this section for estimating the BSPs of all segments of the human body.

Method	Subjects	BSPs	Measures	Type
Hinrichs (1985)	6 Caucasian elderly male cadavers from Chandler et al. (1975)	MoIs	32 in total	linear
Jensen (1986)	12 living boys (4-15 yr)	All	age, TM, SL & SC or SW	linear
Yeadon & Morlock (1989)	6 Caucasian elderly male cadavers from Chandler et al. (1975)	MoIs	32 in total	linear & nonlinear
Zatsiorsky et al. (1983, 1985, 1990a, 1990b)	100 Caucasian living males (24±6 yr, 174±6 cm, 73±9 kg) 15 Caucasian living females (19±4 yr, 173±3 cm, 62±7 kg)	All	TM & TH	linear
Idem	Idem	All	SL & SC	linear
Idem	Idem	All	SL & SC	nonlinear
Schneider & Zernicke (1992)	44 infants arms and 70 infants legs (living subjects)	M, CoM, I_{ML}	age, TM, SL & SC or SW	M linear MoIs linear CoM prop.
Vaughan* (1999)	6 Caucasian elderly male cadavers from Chandler et al. (1975)	All	20 in total (both legs)	M linear MoIs linear CoM prop.
Shan & Bohn (2003)	25 Chinese living males (27-38 yr, 1.59-1.82 m, 52-72 kg) 25 Chinese living females (22-37 yr, 1.52-1.70 m, 43-62 kg) 25 German living males (20-34 yr, 1.70-1.89 m, 69-94 kg) 25 German living females (21-36 yr, 1.59-1.78 m, 56-75 kg)	All	TH, TW for M & MoIs, SL for CoM	M linear, MoIs linear, CoM prop.

Table 2.2: Summary of regression methods for estimating BSPs. Acronyms: M – mass, CoM – centre of mass, MoIs – moments of inertia, I_{ML} – moment of inertia about the mediolateral axis, TM – total body mass, TH - total body height, TW - total body weight, SL – body segment length, SC – body segment circumference, SW – body segment width, CoM prop – proportional method for estimating CoM. *Only the thigh, shank and foot were considered.

2.2.2.2 Proportion methods

Proportion methods give BSPs as a percentage of an anthropometric variable. Typically, the mass of each body segment is given as a percentage of the whole body mass and the CoM location and radii of gyration (or moments of inertia) about the anatomical axes at the CoM are given as a percentage of the body segment length. The CoM location is usually supposed to lie in the body segment longitudinal axis and is referred to an AL or a joint centre. It should be noted that proportion methods corresponds to a regression line constrained to pass through the origin.

Dempster (1955) presented a proportion method based on 8 Caucasian elderly male cadavers. Body segment mass was given as a percentage of total body mass. The CoM location was given as a percentage of body segment length referred to the proximal or distal joint centre. The radius of gyration about the medio-lateral axis was given as a percentage of body segment length. The body was divided in 16 segments (trunk divided in 3 segments) and segment lengths were defined using joint centres.

Clauser et al. (1969) presented a proportion method based on 13 Caucasian elderly male cadavers. The body segment mass was given as a percentage of total body mass and the CoM location as a percentage of body segment length referred to a proximal or distal AL. The body was divided in 14 segments (trunk considered as a single segment) and segment lengths were defined using ALs. Hinrichs (1990) adjusted the CoM proportions of Clauser et al. (1969) referring the CoM location to joint centres.

Chandler et al. (1975) presented a proportion method based on 6 Caucasian elderly male cadavers. The body segment mass was given as a percentage of total body mass and the CoM location as a percentage of body segment length referred to a proximal or distal AL. The inertia tensor of each body segment was calculated but a proportion method or regression equations were not derived. The body was divided in 14 body segments (trunk considered as a single body segment) and body segment lengths were defined using ALs. The study by Chandler et al. (1975) was the first study to determine the three principal axes of inertia. Furthermore, 116 anthropometric measurements were obtained from each cadaver and this allowed other researchers to derive their own regression equations from Chandler's data (e.g. Hinrichs, 1985; or Yeadon and Morlock, 1989). Several authors (Yeadon and Morlock, 1989; Vaughan et al., 1999; Zatsiorsky, 2002) have noticed that the principal moments of inertia of some body segments are wrong and Chandler's inertia data must be used with caution.

Jensen presented a proportion method based on 12 Caucasian male children between 4-20 yr (Jensen, 1986; Jensen, 1989) where the body was divided in 14 body segments. The body segment mass was given as a percentage of total body mass, CoM location as a percentage of body segment length and the radius of gyration about the medio-lateral axis as a percentage of body segment length.

Zatsiorsky and co-workers (Zatsiorsky and Seluyanov, 1983; Zatsiorsky et al., 1990a; Zatsiorsky et al., 1990b) developed a proportion method for males and females based on data from 100 young living Caucasian males and 15 young living Caucasian females using a gamma-ray scanner (see sections 2.2.1.3

and 2.2.2.1). The body segment mass was given as a percentage of total body mass, CoM location as a percentage of body segment length referred to a proximal or distal AL, and the radii of gyration about the three anatomical axes as a percentage of body segment length. The body was divided in 16 segments (trunk divided in 3 body segments) and body segment lengths were defined using ALs. De Leva (1996a) adjusted the CoM location and radii of gyration proportions reported by Zatsiorsky and co-workers referring them to joint centres and other commonly used ALs.

Cheng (2000) presented a proportion method based on 8 Chinese young males using MRI. The body segment mass was given as a percentage of total body mass and the CoM location as a percentage of body segment length referred to the proximal joint centre. Furthermore, three dimensionless MoI (MoI divided by the body segment mass and the square of the body segment length) about the three anatomical axes were presented. The human body was divided in 14 segments following Dempster's method (Dempster, 1955).

Durkin and Dowling (2003) measured BSPs of four population groups of varying racial backgrounds (25 young males, 25 young females, 25 elderly males and 25 elderly females) using DEXA and developed a proportion method for each population group. The body segment mass was given as a percentage of total body mass, the CoM location as a percentage of body segment length referred to an AL or joint centre, and the radii of gyration about the anteroposterior anatomical axis as a percentage of body segment length. The proportion method proposed predicted only the mass of five body segments (forearm, hand, thigh, shank and foot) and the CoM location and radii of gyration of three body segments (forearm, thigh and shank).

Ganley and Powers (2004) presented a proportion method based on 55 children from 7 to 13 years and estimated the BSPs using DEXA. The body segment mass was given as a percentage of total body mass, the CoM location as a percentage of body segment length referred to a proximal AL, and the radii of gyration about the anteroposterior anatomical axis as a percentage of body segment length. Only the foot, shank and thigh were considered and body segment lengths were defined using ALs.

Table 2.3 summarises the main characteristics of the nine proportion methods presented in this section for estimating the BSPs of the body segments of the human body.

Method	Subjects	BSPs	Type
Dempster (1955)	8 Caucasian elderly male cadavers (52-83 yr, 1.55-1.86 m, 49-72 kg)	SM as %TM CoM as %L referred to JC I_{ML} as %L	A
Clauser et al. (1969)	13 Caucasian elderly male cadavers (49.3±13.7yr, 1.72±5.9m, 66.5±8.7kg)	SM as %TM CoM as %L referred to AL	B
Chandler et al. (1975)	6 Caucasian elderly male cadavers (54.3±7.4yr, 1.72±5.7m, 65.2±13.2kg)	SM as %TM CoM as %L referred to AL	B
Jensen (1986; 1989)	12 Caucasian male children (4-20 yr)	SM as %TM CoM as %L referred to JC I_{ML} as %L	B
Zatsiorsky et al. (1983, 1990a, 1990b)	100 Caucasian living males (24±6 yr, 174±6 cm, 73±9 kg) 15 Caucasian living females (19±4 yr, 173±3 cm, 62±7 kg)	SM as %TM CoM as %L referred to AL MoIs as %L	A
De Leva (1996a)	Adjusted the CoM location and I proportions reported by Zatsiorsky referring them to JCs and other commonly used ALs		A
Cheng (2000)	8 Chinese young living males (26±4 yr, 173±4 cm, 64±6 kg)	SM as %TM CoM as %L referred to JC dimensionless MoIs	B
Durkin and Dowling (2003)	25 young living males (19-27 yr, 1.55-1.85 m, 55.5-97.7 kg) 25 young living females (19-30 yr, 1.50-1.80 m, 47-70.5 kg) 25 elderly living males (55-78 yr, 1.63-1.88 m, 59-107.7 kg) 25 elderly living females (56-82 yr, 1.52-1.70 m, 50.9-86.4 kg)	SM as %TM CoM as %L referred to JC or AL I_{ML} as %L	Only forearm, hand, thigh, shank & foot
Ganley and Powers (2004)	55 living children (ages 7-8, n=21; ages 9-10, n=16; ages 11-13, n=13)	SM as %TM CoM as %L referred to AL I_{AP} as %L (only foot, thigh & shank)	Only foot, shank, thigh

Table 2.3: Summary of proportion methods for estimating BSPs. Acronyms: M – body segment mass, CoM – centre of mass, MoIs – moments of inertia, I_{ML} – moment of inertia about the mediolateral axis , I_{AP} – moment of inertia about the anteroposterior axis, L – body segment length, TM – total body mass, JC – joint centre, AL – anatomical landmark. Type A: body divided in 14 body segments (trunk is a single segment). Type B: body divided in 16 body segments (trunk is divided in 3 segments).

2.2.2.3 Geometric scaling

Isometric scaling assumes complete proportionality among all linear dimensions. Consequently, body segments can be assumed to be geometrically similar and differ only in size. In order to obtain subject-specific BSPs each BSP of the database must be multiplied by a scaling factor, which is the same for all body segments.

In isometric scaling, body segment masses are considered proportional to total body mass and then, the scaling factor is the quotient between the subject total body mass and the mean total body mass of the database. The CoM location of each body segment is scaled by the ratio between the standing height of the specific subject and the mean standing height of the database. The scaling factor S_I for the MoIs is calculated as

$$S_I = \frac{m_s h_s^2}{m_d h_d^2} \tag{2.1}$$

where m_s is the subject total body mass, h_s is the subject standing height, m_d is the mean total body mass of the database and h_d is the mean standing height of the database.

If the subject-specific body segment lengths and masses are available, a different scaling factor can be obtained for each body segment. For example, Silva (2003) estimated the BSPs of a human skeletal model composed of 16 body segments using a different scaling factor for each body segment.

2.2.3 OPTIMISATION METHODS

Optimisation methods estimate BSPs from the position, velocity and acceleration of body segments and the external efforts acting on the human body, measured during a predefined motion. The objective function is based on the difference between measured and calculated external efforts, while the equality constraints are based on the motion equations of the model. The goal of these methods is to find the BSPs that minimise the objective function and satisfy the constraint equations during the whole human motion.

One of the first methods for estimating BSPs using optimisation techniques was proposed by Vaughan et al. (1982). The whole human body was modelled with 14 rigid body segments. Three motions with a single support leg were measured: running, long jumping takeoff and kicking. The motions were considered two-dimensional and only the motion equations in the sagittal plane were used. Then, mass, CoM location and MoI about the transverse axis of each body segment were considered as the unknown variables and lower and upper bounds were set for them. Kinematic data were measured with a motion capture system and ground reaction forces with a force plate. BSPs estimated with the proposed optimisation method were different for the three motions and different from BSPs data in the literature.

Nagano (2004) presented a method for estimating the mass and CoM location of body segments of the lower extremities using simulated annealing

optimisation. Data for two different jumping motions were generated by simulation with a 3D musculoskeletal model. The optimisation method minimised the difference between the vertical component of the simulated ground reaction force and the calculated ground reaction force, which is a function of the unknowns (mass and CoM location of body segments). The average error found for the mass and the CoM location was less than 1% and 6% respectively. However, the method was not validated with experimental data and the error reported should be considered cautiously.

Kodek and Munich (2004) presented an optimisation method for estimating the mass and CoM location of the hand, forearm and upper arm using an industrial robot. The robot was connected to the subject hands and imposed a slow motion of the arms in the sagittal plane. The arm was modelled with a 2D model in the sagittal plane using three rigid bodies connected by three revolute joints. Arm motion was recorded with a motion capture system and forces and moments at the contact points were measured with a force sensor. The method was tested on humans and on a mechanical device with known BSPs. The maximum error was greater than 50% showing the method requires further improvements.

2.2.4 COMPARISON OF BSPS METHODS

To evaluate the accuracy of a BSP estimation method, most studies compare the estimated and measured total body mass (Jensen, 1978; Hatze, 1980; Yeadon, 1990; Cheng et al., 2000; Durkin et al., 2002) or the estimated and measured volume of a body segment or inanimate object. However, these two comparisons do not give a direct measure of the accuracy of the estimated BSPs.

The main problem when comparing different methods for estimating BSPS is the difficulty to accurately estimate the real BSPs on a living subject. For this reason most studies compare the different methods published among them but the error of the methods with respect to the true BSPs is usually not assessed. The methods are also difficult to compare due to the different segmentation methods used to define each body segment.

The differences between BSPs estimation methods can be large: the magnitude of the percentage maximal differences between methods can be up to 48% for body segment mass, 25% for CoM location and 90% for the sagittal MoI (Cappozzo and Berme, 1990).

2.2.5 INFLUENCE OF BSPS IN RESULTS

Very few quantitative investigations on the influence of BSPs in analysis results have been published. Pearsall and Costigan (1999) investigated the influence of BSPs errors on forces and moments on the hip joint during human walking motion using a 2D model of the lower limb. The studied BSPs included mass, CoM location, and transverse MoI for the thigh and shank. BSPs were varied independently between -40% and +40% at intervals of 10%, but changes of this magnitude only produced small changes in forces and moments about the hip joint. Although statistically significant differences were found on kinetic variables due to BSPs variation, most effects were less than 1% of body weight. One reason is that thigh and shank BSPs variations are small in absolute terms.

The effect of CoM location and joint centre location (see section 2.1.14) on the work output was investigated by Nagano et al. (2000). The data for a vertical jumping were generated with a 2D computer model, which consisted of four body segments representing head-arms-trunk, thighs, shanks and feet. The location of the CoM of each body segment was varied by ±10% of the body segment length, and its effect in the variation of the work output was in the range -4% and 6%.

Several authors have indicated that the influence of BSPs in the analysis results depends on the human motion investigated (Challis and Kerwin, 1996; Kingma et al., 1996; Lenzi et al., 2003). The influence of BSPs would increase for human motions in which larger body segment accelerations are involved. This suggests that the influence of BSPs on analysis results must be evaluated for each specific human motion investigated.

2.2.6 SELECTION OF METHODS FOR ESTIMATING BSPS

Of the two projects considered in this thesis only the MoDyCo project performs an inverse dynamic analysis and therefore requires the estimation of BSPs. The measurement equipment available in the MoDyCo project is the Vicon motion capture system, although some additional inexpensive instrumentation like measuring tape or an anthropometric calliper can be used. Therefore, the available measurement equipment limits the BSPs estimation methods that can be used.

As it is planned in the project to study a large number of motions for different subjects, the methods for estimating BSPs have to be relatively fast. Furthermore, some AL positions are already available and this is an advantage for geometric, regression and proportion methods. These AL positions are

measured for joint parameter estimation methods and for the ISB recommendations (Wu et al., 2002) on definitions of local coordinate systems.

Medical diagnostic technologies and 3D whole body scanners are discarded because of their high cost, the large amount of time needed to produce a set of BSPs for one subject and the unavailability of this type of equipment in the MoDyCo project.

Optimisation methods are not considered because the methods published to date do not provide all BSPs of the human body. They require the development of additional computer models and recording several human motions, which is time consuming. Moreover, BSPs obtained by optimisation methods depend on the measurement errors of the motion capture system and force sensors, estimation errors of the velocities and accelerations, and estimation errors of joint parameters.

Geometric methods can be used to estimate BSPs with the equipment available in the MoDyCo project. Lengths can be estimated using anthropometric callipers or from the distances between the ALs measured with Vicon and circumferences can be measured with a measuring tape. Geometric methods that calculate anthropometric measurements using photogrammetric techniques (Jensen, 1978; Hatze and Baca, 1992; Sarfaty and Ladin, 1993; Baca, 1996) cannot be used because the equipment and software needed are not available. Therefore, only the geometric methods proposed by Hanavan (1964), Hatze (1980) and Yeadon (1990), which are based on manual measurements, can be used. Recall that Hanavan's method needs 25 anthropometric measurements, Yeadon's method requires 30 minutes to obtain 95 measurements and Hatze's method requires 80 minutes to obtain 242 measurements. The measuring time needed by Hatze's method seems excessive for estimating BSPs of a large number of subjects while Hanavan's and Yeadon's methods require a more reasonable measuring time. Thus, the two latter methods are considered appropriate for the MoDyCo requirements. Furthermore, some of the anthropometric measurements can be estimated from the AL positions already measured for the ISB recommendations and for the joint parameter estimation methods.

The regression and proportion methods have been criticised because the sample of population used to derive the equations is usually too small, there is a lack of studies of diverse population (Pearsall and Reid, 1994; Cheng et al., 2000; Zatsiorsky, 2002; Durkin and Dowling, 2003) and the assumption that BSPs of cadavers are similar to BSPs of living subjects is questionable (Mungiole and Martin, 1990; Pearsall and Reid, 1994; Zatsiorsky, 2002). The regression and proportion methods proposed by Zatsiorsky and co-workers

(Zatsiorsky and Seluyanov, 1983; Zatsiorsky and Seluyanov, 1985; Zatsiorsky et al., 1990a; Zatsiorsky et al., 1990b) are considered the best regression and proportion methods because they are based on BSPs measured on living subjects, the number of subjects measured (100 young males and 15 young females) is the biggest published to date, the methods provide different equations for females and males, and all the segments of the human body are included in their methods.

In summary, there are six methods which can be considered suitable for the requirements of the MoDyCo project: Hanavan's and Yeadon's geometric methods and Zatsiorsky's regression and proportion methods.

Recently, Durking and Dowling (2003) have compared BSPs measured using DEXA, which were considered the true values, with five BSPs estimation methods:

1. Hanavan's geometric method (Hanavan, 1964).
2. Dempster's proportion method (Dempster, 1955).
3. Zatsiorsky's nonlinear regression method (section 2.2.2.1).
4. Zatsiorsky's linear multiple regression method based on the total body weight and height (section 2.2.2.1).
5. A proportion method developed by the authors for only five body segments (forearm, hand, thigh, shank and foot).

The BSPs studied were the mass of the forearm, hand, thigh, shank and foot, and the CoM location and the radii of gyration about the anteroposterior axis of the forearm, thigh and shank. The proportion method developed by Durking and Dowling performed best overall when compared to the other four methods. The methods were tested with the same data used to generate the proportion method proposed by the authors and this biased the comparison results. However, none of the methods provided the best estimations for all body segments and population groups. The authors concluded that since their method can only estimate the mass of five segments and CoM location and the radii of gyration about the anteroposterior axis of three segments, Zatsiorsky's linear multiple regression method provided the best complete set of equations for BSPs estimation. The performance of the remaining methods, ordered from best to worse performance, was: Zatsiorsky's nonlinear regression method, Hanavan's geometric method and finally Dempster's proportion method.

From the six BSPs methods suitable for the requirements of the MoDyCo project, Hanavan's geometric method is discarded due to its poor performance compared to Zatsiorsky's method according to Durkin and

Dowling (2003). Yeadon's method needs at least 70 additional measurements, which cannot be estimated from the available data, and is also discarded. From the four methods proposed by Zatsiorsky, the proportion method requires only three additional measurements, the nonlinear regression method needs 16 additional measurements, the linear multiple regression method based on several measurements per body segment needs 28 additional measurements, and the linear multiple regression method based on the total body weight and height needs only two measurements.

Comparative studies have not been published in order to decide which of the four Zatsiorsky's methods is best. Even contradictory results have been found. For example Zatsiorsky recommended the use of the nonlinear regression method for subjects outside the range of the database (Zatsiorsky et al., 1990a) and found this method more accurate than the linear regression method based on total body height and weight, even for subjects within the database range. However, Durkin and Dowling (2003) contradicted this result and found the opposite to be true.

At the time of writing this document, real experiments have not been recorded in the MoDyCo project and the anthropometric features of the subjects that will participate in the experiments are unknown. However, BSPs methods must be applied to subjects with the same anthropometric features as the subjects database used to generate the BSPs methods. For this reason, two different methods are selected: Zatsiorsky's proportion method for subjects with features similar to the database and Zatsiorsky's linear regression method based on total body height and weight for subjects outside the database range.

Zatsiorsky's proportion method is selected because it requires only three additional anthropometric measurements and it uses segment-specific measurements for estimating BSPs. Zatsiorsky's linear regression method based on total body height and weight is selected because it only requires two additional anthropometric measurements and according to Durkin and Dowling (2003) it is more accurate than Zatsiorsky's nonlinear regression method for subjects outside the database range.

CHAPTER 3

HUMAN SKELETAL MODELS

A skeletal model of the human body can be developed using different mathematical approaches depending on the aim of research. The two main approaches are the multibody system (MBS) analysis and the finite element method (FEM). MBS analysis is used when the aim of the research is to study large and complex displacements of the human body including interactions with the environment. This type of analysis is applied for example in ergonomic studies, gait analysis, surgical planning or determination of muscle forces during different activities. FEM is used when the main objective is to study the stresses and deformations on the body (e.g. bone stress or brain stress during impact). It is applied for example to occupant dynamic analysis for crashworthiness, or design and analysis of prosthesis.

Another approach is to use hybrid models combining multibody and finite element models. This hybrid approach has been applied among others to realistic visualisation of human models (Maurel, 1999) and software applications for crashworthiness and safety systems development (MADYMO – TNO: www.automotive.tno.nl).

Depending on the detail and level of complexity of a human skeletal model, it can be classified into three groups: detailed partial models, medium-size models and whole body models.

Detailed partial models are used to study specific elements of the human body, which are modelled with a high level of detail, using few simplifications. For example a detailed partial model of the knee could include all knee ligaments, a detailed model of the articular surfaces of the femur and tibia, and all six degrees of freedom (DoFs) of the joint (Hefzy and Abdel-Rahman, 2000; Caruntu and Hefzy, 2004).

Medium-size models include several body segments of the human body, usually consider simplified models of the joints (e.g. fixed joint centres of rotation), and optionally include muscle lines of action and some ligaments. The anthropometric parameters are obtained from cadavers or living subjects using different methods (see sections 2.1 and 2.2). These models are used for many different applications like surgical planning (Delp et al., 1990), gait analysis (Benedetti et al., 1998), gain insight into joints and/or muscles function (van der Helm, 1994b; van der Helm, 1994a) or study of work-related joint problems (Högfors et al., 1995).

Whole body models consider the complete human body, although the number of body segments and the level of detail of the model depend on the application. They are used for example in ergonomic studies (Wang et al., 2005), sports performance (Celigüeta, 1996) or occupant safety (Silva, 2003).

In this thesis, a MBS approach is used to study different human motions. These human motions have been produced in the frame of two projects: in the MoDyCo project three medium-size models are used to analyse different driving manoeuvres; in the REALMAN project one whole body model is used for ergonomic analysis of several vehicle-related motions and generic arm reaching movements.

The assumptions considered in this thesis are discussed in section 3.1. The medium-size models and whole body models presented in the literature and relevant to this thesis are reviewed in section 3.2. The human skeletal models developed in the frame of the MoDyCo project are described in detail in section 3.3 and the RAMSIS whole body model used in the REALMAN project is presented in section 3.4.

3.1 ASSUMPTIONS

The human skeletal system is a very complex mechanism thus requiring that several assumptions be made for modelling it in order to develop an adequate and manageable model. The assumptions considered depend on the purpose of the analysis and the level of detail required in the investigation. Some of the assumptions considered in this thesis have initially been presented in Chapter 2. In this section, the assumptions previously presented are restated and additional ones are introduced.

3.1.1 RIGID BODY ASSUMPTION

The human skeletal system is modelled as a multibody model and each body segment is considered as a rigid body. A body segment is composed by one or

several bones and soft tissues. The bones can be considered as rigid bodies in the range of forces applied during the activities studied in this thesis. The soft tissues of each body segment are not rigid and they can change their configuration due to muscle activation or external forces. However, the effect of soft tissue in the results is neglected in most biomechanical studies. The rigid body assumption has been questioned when the goal of the investigation is the analysis of impacts. Some authors (Gruber et al., 1998; Pain and Challis, 2001b) found a dramatic influence of the soft tissue on joint forces and torques during impacts.

Most of the body segments can be approximated by rigid bodies but some concerns arise for some body segments like the foot or trunk. The implications of the rigid body assumption on these body segments are discussed for each skeletal model in the corresponding section.

3.1.2 MARKER ASSUMPTIONS

The rigid body assumption has some implications for the motion capture system. The motion of the human body is recorded using small retro-reflective balls called markers that are located on the skin of each body segment. It is assumed that the motion of each bone is described by the markers over the bone. Unfortunately there are two sources of inaccuracies (Cappozzo et al., 1996):

1. Instrumental errors, due to the motion capture system. These errors are systematic and random with high- and low-frequency content.
2. Skin movement artifact, due to the relative movement between markers and the underlying bone caused by passive and active soft tissues. Marker relative motion can be decomposed into:
    a. Deformation of the cluster of markers located on a body segment. Markers move with respect to each other.
    b. Rigid movement of the cluster of markers relative to the underlying bone.

In this thesis it is assumed that the markers are rigidly attached to the underlying bone. The errors associated with this assumption are minimised due to specialised mathematical methods developed for estimating body segment position and orientation from recorded marker trajectories. In Chapter 4, these mathematical methods are reviewed and a new one is proposed.

3.1.3 BODY SEGMENT PARAMETERS ASSUMPTIONS

Body segment parameters (BSPs) are constant when the body segments are considered as rigid bodies, i.e. the inertia properties of each body segment are constant. The methods for estimating BSPs have been presented in section 2.2. Although some methods measure the three-dimensional coordinates of the body segment CoM, most of the methods assume that it is located along the longitudinal axis. Another common assumption is that the principal inertia axes are coincident with the anatomical axes of the body segment and the products of inertia are zero. These assumptions are based on the fact that the trunk and the head are approximately symmetric about the mid-sagittal plane, and the upper arm, forearm, thigh and shank are approximately symmetric in the sagittal and frontal planes. These assumptions do not always hold but the errors have been rarely investigated and there is insufficient experimental evidence to either accept or reject them (Zatsiorsky, 2002).

These BSPs assumptions are considered only in the MoDyCo project. They are not required in the REALMAN project as only kinematic analysis is performed.

3.1.4 JOINT PARAMETERS ASSUMPTIONS

Human joints do not have a fixed centre of rotation or fixed axis of rotation and their motion is a combination of translations and rotations with pressure between the contact areas. In this thesis joint translations are neglected because they are considered to be very small with respect to the large rotations in the joints. Furthermore, joint translations are difficult to differentiate from the measurement errors in most of the joints due to their small magnitude. Therefore, the human joints are modelled with fixed joint centres of rotation and fixed joint axes. Consequently, only revolute, spherical and universal joints are used. These assumptions are common in most of the biomechanical studies related to gross human motion (Glitsch and Baumann, 1997; van der Helm, 1997b; Anderson and Pandy, 1999; Garner and Pandy, 1999; Charlton and Johnson, 2000).

The previous assumptions have different implications for each joint. The most common joint models and the range of joint translations for the main human joints have been presented from section 2.1.5 to 2.1.13.

If a joint does not have translational motions, some joint elements must exist so that they constraint these translations and generate joint reaction forces. A common assumption is to consider that joint reaction forces are counteracted by joint structures as ligaments and articular surfaces. This is not

always true so additional muscle forces are required to maintain the joint stability as some authors have pointed for the glenohumeral joint (van der Helm, 1994b; Högfors et al., 1995). In this thesis it is assumed that joint reaction forces are counteracted by joint structures. Consequently, muscles forces will be underestimated to unknown extent. To the best knowledge of the author the implication of this assumption has been investigated only for the glenohumeral joint. Van der Helm (1994b) found out that this assumption affected mainly the force generated by muscles of the rotator cuff. Therefore, the forces estimated for these muscles cannot be considered reliable.

3.2 MUSCULOSKELETAL MODELS IN THE LITERATURE

In this thesis only human skeletal models are used to study different human motions. However, musculoskeletal and skeletal models are closely related and both are reviewed in this section for the sake of completeness.

3.2.1 UPPER LIMB MODELS

The upper limb models presented in the literature are difficult to classify due to the different levels of complexity and the number of body segments considered. Some models include the whole upper limb while others only consider a specific region, e.g. the forearm and hand in order to study the wrist joint and the muscles that cross the joint. No attempt has been made to classify the existing upper limb models and they are presented in chronological order. The first sections introduce models of the shoulder complex, which is the most difficult region to model. Models of the whole upper limb are also included in these first sections but with special focus on the modelling of the shoulder complex. The forearm and wrist models are described in section 3.2.1.8 and 3.2.1.9 respectively.

3.2.1.1 Initial shoulder complex models

Earlier attempts of modelling the shoulder complex were restricted to two-dimensional models or partial three-dimensional models. They modelled only a few muscles, just those expected to be the most active, and only certain motion patterns were studied (Inman et al., 1944; De Luca and Forrest, 1973; Poppen and Walker, 1978; Dul, 1988).

Some three-dimensional models were proposed (Wood et al., 1989b; Wood et al., 1989a; Bassett et al., 1990) but from the nature of the geometrical

measurements performed, i.e. centroid line assessment for muscle function, these models were restricted to static analysis in one position.

In these studies only a part of the three-dimensional movement of clavicle, scapula and humerus was considered. However, to gain insight into the role of each morphological structure in the functioning of the total mechanism, all structures should be included.

3.2.1.2 Engin shoulder model (1980-1989)

Engin and co-workers started in 1980 a research program to study and model the shoulder complex (Engin, 1980). In a first approach, the shoulder complex was simplified as a single spherical joint between thorax and humerus. The passive resistance properties beyond the shoulder complex sinus, which is defined as the range of the upper arm circumduction motion, were measured on three subjects (Engin et al., 1984b; Engin et al., 1984a). They presented a database of the passive resistance properties of the shoulder complex that was measured *in vivo* on a male population with ages raging from 18 to 32 years. Afterwards, spherical coordinates were used to express the passive resistance torque as a function of two spherical angular variables (Engin and Chen, 1986a; Engin and Chen, 1986b). The voluntary resistance beyond the shoulder complex sinus were also measured on three male subjects (Engin and Peindl, 1987; Peindl and Engin, 1987).

In a second approach, Engin and co-workers modelled the shoulder complex as an open chain composed of three rigid bodies (the clavicle, scapula, and humerus) connected by three spherical joints (sternoclavicular, acromioclavicular, and glenohumeral) without considering the scapulothoracic joint (Engin and Tümer, 1989). They measured the joint boundaries of each joint, modelling the joint boundary as a cone with an elliptic base. The joint boundaries were supposed to be independent of the joint axial (twist) motion range. This model did not define the simultaneous relative motion of the shoulder bones. The authors estimated the joint rotations using numerical optimisation by minimising the summed joint rotations (Tümer and Engin, 1989).

3.2.1.3 Swedish shoulder model (1987-1999)

Högfors and co-workers initiated in 1987 a long-term research program to study the shoulder complex under static working situations where the load is low or moderate. The shoulder static model (Högfors et al., 1987) included the thorax (fixed body), clavicle, scapula, humerus and forearm (only flexion-extension), which were modelled as rigid bodies. A bone-fixed coordinate

system was defined for each bone based on anatomical landmarks (ALs) measured on each bone. BSPs were not considered in the model because the effect of inertia forces was neglected.

The joints considered were the sternoclavicular, acromioclavicular, and glenohumeral joints and were all modelled as spherical joints. The contact between the thorax and the scapula was modelled with two contact forces perpendicular to the thorax, which was modelled using a cylinder. These two contact forces were applied at two points on the medial border of the scapula. The scapulothoracic joint was not included in the model as a kinematic constraint; instead a shoulder rhythm was introduced. The shoulder rhythm defines the kinematic relation between the clavicle, scapula and humerus, i.e. given the orientation of the humerus, the orientation of the clavicle and the scapula is determined by the shoulder rhythm relationship. The shoulder rhythm was derived from motions recorded on three subjects using low dose roentgen-stereophotogrammetry (Högfors et al., 1991). Afterwards, the range of applicability of the shoulder rhythm was extended (Karlsson and Peterson, 1992). The extrapolated shoulder rhythm covered the range of humeral elevation from 0 to 120º in planes from -10 to 90º from a sagittal one. Although a personalised shoulder rhythm can be used for each subject, the same shoulder rhythm was used for all subjects which is a limitation of the model. The methods used to estimate joint parameters were not reported.

The model included 21 muscles of the shoulder complex measured on three human male cadavers (55-71 years). Some broad muscles were split into several parts based only on anatomic and functional considerations. Muscle path was modelled as a straight line between origin and insertion. When the muscle path was constrained by some structure, the constraint was modelled with simple geometrical forms (point, line, curve, sphere or cylinder).

A submodel of the shoulder model that included only the glenohumeral joint was used to calculate the muscle and contact forces using optimisation techniques (Karlsson and Peterson, 1992). BSPs were considered in the shoulder model and were taken from the literature (Pheasant, 1986). The physiological cross-sectional area (PCSA) of the muscles was taken from a previous unpublished study of the authors. Theoretical force results were compared with data from EMG studies in the literature concluding that the model required further development.

In a subsequent study (Högfors et al., 1995), the direction of the glenohumeral contact force was constrained to be directed within a cone of a given angle, which represented the glenoid cavity. The sensitivity of the model to assumptions and parameters, and the consistency of the shoulder model

were also investigated. It was found that the model was not sensitive to small variations of the assumptions and the parameter values, and that the shoulder rhythm was not in conflict with other assumptions.

A comparison between EMG measurements and the shoulder model predictions was performed by Palmerud et al. (1998) for 10 shoulder muscles. This study indicated that muscles PCSA should be adjusted in order to achieve a good agreement with EMG measurements. The muscle PCSA data of the shoulder model were adjusted by Makhsous et al. (1999). Strength profiles of the shoulder were experimentally measured on seven male subjects and calculated with the Swedish shoulder model. The muscle PCSA data were adjusted in such a way that the experimental and calculated strength profiles became similar.

3.2.1.4 Delft upper limb model (1988-1997)

In 1988 van der Helm, Pronk and Veeger started an extensive cadaver study for the collection of morphological data in order to develop a musculoskeletal model of the human shoulder. In a first paper (Veeger et al., 1991), the methodology and the measurement device used to measure both shoulders of seven cadavers (five males and two females) were presented (Figure 3.1). Elements attached to the thorax, clavicle, scapula and humerus were included in this cadaver study. The measured parameters were the relevant body dimensions for derivation of the inertia parameters, positions of ALs for each bone, shape and position of relevant articular surfaces, locations of muscle and ligament insertions, shape and position of bony contours determining the muscle path, muscle mass and muscle PCSA. A total of 16 muscles and 3 ligaments were measured on each cadaver.

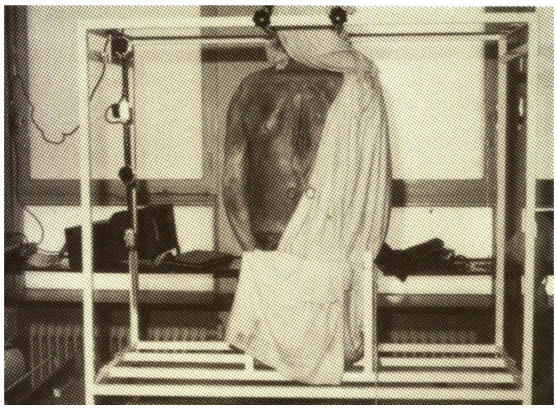

Figure 3.1: Fixation frame for cadaver measurements. Back view of the cadaver with the measuring device fixed on the frame on its left-hand side (Veeger et al., 1991).

Van der Helm and Veenbass (1991) presented a general theory for representing muscles with large attachment sites. The method allows to determine the number of lines of action, their origin and insertion coordinates that best represent the mechanical effect of a muscle with a large attachment site. The main feature of the method is that the complete attachment site is described mathematically, and a map of the muscle fibre distribution from origin to insertion is derived.

Van der Helm et al. (1992) presented the methods used to estimate the musculoskeletal parameters from the cadaver measurements and a complete set of parameters for one cadaver. Morphological structures were described mathematically by simple geometrical forms (plane, line, sphere, cylinder or ellipsoid), which were fitted to measured datapoints on the morphological structures using a least-squares criterion. The joint rotation centres were estimated from the geometrical forms that model the articular surfaces (e.g. the glenohumeral rotation centre was estimated from the sphere fitted to the glenoid cavity). Muscle paths were modelled either as a straight line from origin to insertion or as a curved line wrapping a geometrical form when there was a morphological structure between origin and insertion.

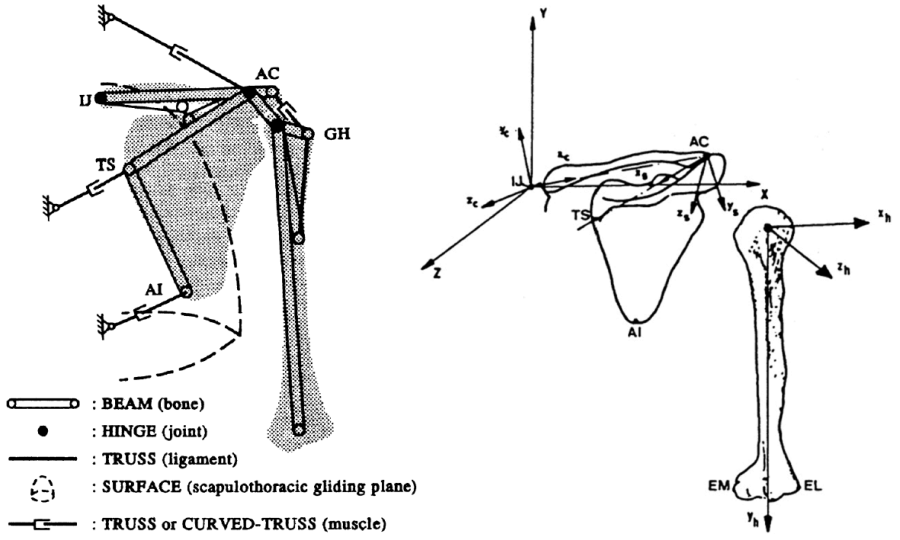

Figure 3.2: Left – Finite element model of the shoulder complex (van der Helm, 1994b). Right – LCS of each bone (van der Helm and Pronk, 1995).

A finite element model of the shoulder mechanism was built by van der Helm (1994a; 1994b) with the musculoskeletal parameters estimated previously. The model included the thorax (fixed body), clavicle, scapula and humerus, which were modelled as rigid elements (Figure 3.2). The LCS of each

bone was defined using only ALs. Body segment mass and CoM location were taken from Clauser et al. (1969) and moments of inertia from Hinrichs (1985). The joints considered were the sternoclavicular, acromioclavicular, glenohumeral and scapulothoracic. The first three joints were considered as spherical and were modelled with three perpendicular revolute joints. The scapulothoracic joint was modelled using two contact points between the medial border of the scapula and the thorax, which was modelled as an ellipsoid. Only compression forces were possible at these two contact points. Additionally, the glenohumeral contact force was constrained to point from the rotation centre of the joint to the glenoid cavity. The mechanism has seven DoFs: four at the shoulder girdle and three for the humerus. The model can be used for kinematic, dynamic, and inverse dynamic analyses but only static simulations were analysed due to lack of dynamic data on shoulder motions. The muscle forces were calculated using optimisation techniques and surface EMG data recorded at 12 locations in 12 subjects were compared with the calculated muscle forces in order to validate the model.

In a second cadaver study, five upper extremity specimens (one left and four right arms) were measured (Veeger et al., 1997). Elements attached to the scapula, humerus, ulna and radius were measured in this cadaver study. The parameters measured were the same as in the previous cadaver study. Additionally, muscle volumes, muscle lengths, pennation angles and joint parameters of the humeroulnar and radioulnar joints were measured. Muscle path and attachment sites were modelled as in the previous cadaver study (van der Helm and Veenbass, 1991). The joint parameters were estimated from recorded passive arm motions using an algorithm described by Woltring (1990). Body segment mass and CoM location were taken from Clauser et al. (1969) and moments of inertia from Yeadon and Morlock (1989).

In a third cadaver study, additional muscle parameters were measured in one specimen to allow more reliable muscle force predictions (Klein Breteler, 1997; Klein Breteler et al., 1999). The body segments considered and elements measured were the same as in the first cadaver study and additionally optimum muscle length and tendon length for each muscle. Muscles with large attachment sites were divided in several parts based on anatomic and functional considerations but not according to the method proposed by van der Helm and Veenbass (1991) and the centroid of muscle origins and insertions were visually estimated. Body segment mass and CoM location were taken from Clauser et al. (1969) and moments of inertia from Hinrichs (1985).

Using the morphological data measured in the second and third cadaver studies, the Delft shoulder model was improved with the muscle optimum length parameters and extended with the elbow and wrist joints (van der Helm,

1997b). The humeroulnar and radioulnar joints were modelled as revolute joints (see section 3.2.1.8 for details) and the wrist joint as a spherical joint due to the lack of data about the joint axes. The shoulder complex was actuated by 17 muscles and the elbow joint by 7 muscles. The model was implemented in the FEM software SPACAR© (Laboratory of Mechanical Automation, University of Twente) and SIMM (Musculographics Inc., IL, USA) was used as visualisation tool.

Applications of the Delft shoulder model have included standardised arm motions (van der Helm, 1994a), analysis of a glenohumeral arthrodesis (van der Helm and Pronk, 1994), goal-directed arm motions (Happee and van der Helm, 1995), manual wheelchair propulsion (van der Helm and Veeger, 1996) and sensitivity analysis of an glenohumeral endoprosthesis design and operation technique (De Leest et al., 1996).

3.2.1.5 Garner upper limb model (1999-2003)

Garner and Pandy presented a musculoskeletal model of the right upper limb (Figure 3.3) based on the Visible Human Project Dataset of the U.S. National Library of Medicine (Spitzer and Whitlock, 1998). The musculoskeletal parameters were estimated from high-resolution 2D medical images (Color-cryosection images, MR images, and CT images) of a human male cadaver from the Visible Human Project. Surface boundaries of the bones and muscles from the right side of the body were identified using a color-thresholding formula, and their 3D surfaces were reconstructed in the form of triangular meshes using the Marching Cubes algorithm (Lorensen and Cline, 1987).

The model included the thorax (fixed body), clavicle, scapula, humerus, ulna, radius, carpal bones, and hand, which were modelled as rigid elements (Garner and Pandy, 1999). The LCS of each bone was defined using ALs and bone surfaces. The sternoclavicular, acromioclavicular and glenohumeral joints were considered as spherical joints. The humeroulnar and radioulnar joints were modelled as revolute joints. Although the humeroradial joint was not included in the model, it was taken into account implicitly (see section 3.2.1.8 for details). The radiocarpal (wrist flexion-extension), and radiocarpal radial-ulnar deviation (wrist pronation-supination) joints were each modelled as a revolute joint (see section 3.2.1.9 for details). The scapulothoracic joint was modelled approximately as in the Delft shoulder model. Two points fixed on the medial border of the scapula were constrained to remain in contact with the exterior surface of the right side of the rib cage, whose shape was approximated by an ellipsoid. Because of the thickness of the underlying muscles, these two points do not actually make contact with the rib cage.

Therefore, they were shifted to the surface of the ellipsoid while remaining fixed to the scapula. The Delft shoulder model approximated both sides of the rib cage with a single ellipsoid but in this model the ellipsoid was fitted to the shapes of ribs 1-9 only on the right side of the body.

The joint centres of rotation and joint axes of rotation were calculated, based on the anatomical descriptions reported in the literature, by fitting different geometrical shapes (plane, sphere, ellipsoid or variable-radius cylinder) to the three-dimensional articular surfaces of the reconstructed bones, e.g. the humeroulnar joint axis was found by fitting a variable-radius cylinder to the curvature of the articulating surfaces of the trochlea and capitulum.

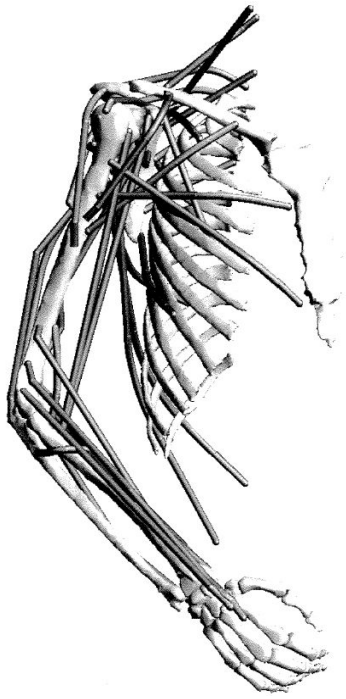

Figure 3.3: Garner upper limb model showing the muscles (Garner and Pandy, 2001).

The model included 26 muscles of the upper limb (Garner and Pandy, 2001). They were modelled with one or several muscle parts according to the muscle part definitions reported by Johnson (1996). The muscle origins and insertions were estimated from the centroid of the muscle attachment sites on the reconstructed surfaces of the bones. The path of each muscle was described using the Obstacle-set method (Garner and Pandy, 2000). Muscle pennation angles were based on experimental data reported in the literature. Maximum isometric muscle force, optimum fiber length and tendon slack

length for each muscle were calculated using a two-stage optimisation method (Garner and Pandy, 2003) by matching the maximum isometric joint torques of the model to the maximum isometric joint torques measured on three human subjects.

3.2.1.6 Maurel shoulder and elbow model (1999)

Maurel developed a musculoskeletal model of the left shoulder and elbow in the frame of the EU ESPRIT project CHARM based on the Visible Human Project Dataset (Maurel et al., 1996; Maurel, 1999; Maurel and Thalmann, 2000). Bones and muscles 3D surfaces were estimated from high-resolution 2D medical images of a human male cadaver from the Visible Human Project (Spitzer and Whitlock, 1998).

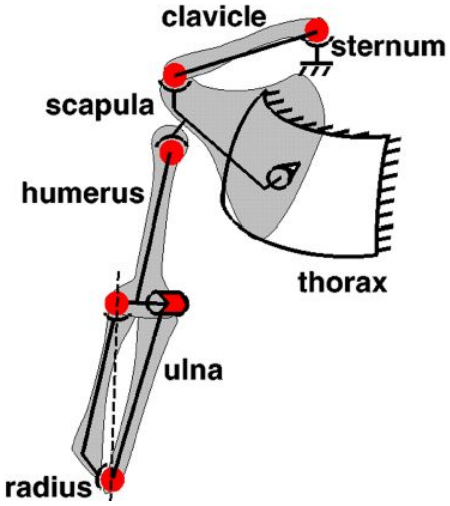

Figure 3.4: Maurel upper limb model.

The model included the thorax (fixed body), clavicle, scapula, humerus, ulna and radius, which were modelled as rigid elements (Figure 3.4). The LCS of each bone was not defined using ALs. BSPs were estimated by approximating the body segments as homogeneous cylinders. The sternoclavicular, acromioclavicular and glenohumeral joints were considered as spherical joints and modelled with three perpendicular revolute joints. The humeroulnar and radioulnar joints were modelled as revolute joints. Although the humeroradial joint was not included in the model it was taken into account implicitly (see section 3.2.1.8 for details). The scapulothoracic joint was modelled using one contact point between the medial border of the scapula and the thorax, which was modelled as an ellipsoid. Consequently, the closed-loop formed by the thorax, clavicle and scapula has 5 DoFs. The joint centres

and axes of rotations were visually estimated using a 3D graphic software interface.

The model included 22 muscles divided in 34 muscle parts based on anatomical considerations only. The muscle origins and insertions were estimated from the centroid of the muscle attachments on the reconstructed surfaces of the bones. The muscle path was defined as the line connecting the origin and insertion through via points fixed on the bone. Muscle PCSA data were taken from Veeger et al. (1991).

3.2.1.7 Newcastle shoulder and elbow model (2000)

The University of Newcastle developed a musculoskeletal model of the upper extremity (Charlton and Johnson, 2000) using the software SIMM (Musculographics Inc., IL, USA) and a MBS toolbox for Matlab® (Barker and Kirtley, 1997). The model included the thorax (fixed body), clavicle, scapula, humerus, radius and ulna, which were modelled as rigid elements. The LCS of each bone was defined using only ALs. BSPs were estimated from the regression equations of De Leva (1996a). The sternoclavicular, acromioclavicular and glenohumeral joints were considered as spherical joints. Additionally, the glenohumeral reaction force was constrained to pass through the glenoid cavity, which was approximated as an ellipse. The scapulothoracic joint was modelled similarly as in the Delft shoulder model but the motion of the clavicle and scapula was not directly measured. Instead, the motion of the clavicle and scapula was obtained from the orientation of the humerus using regression equations (Barnett, 1996), i.e. a shoulder rhythm. The forearm joints, humeroulnar and radioulnar joints were modelled as revolute joints. Although the humeroradial joint was not included in the model it was taken into account implicitly (see section 3.2.1.8 for details).

The model was based on the musculoskeletal parameters from Johnson et al. (1996), van der Helm et al. (1992) and Veeger et al. (1997). The main difference between the three sets of muscle parameters is that the first study divided muscles with large attachment sites based on anatomic considerations and the other two studies based on mechanical principles (van der Helm and Veenbass, 1991). The bone surface data were derived from medical images available through the Visible Human Project (Spitzer and Whitlock, 1998). The obtained bone geometry was used to define the muscle wrapping conditions for each bone (Charlton and Johnson, 2001).

The main limitation of the model is the range of validity for the regression equations of the shoulder rhythm, which is valid for the anterior portion of the cone of circumduction below shoulder level. Furthermore, the

data from four different studies were combined representing a potential source of incoherencies.

3.2.1.8 Forearm models

Different forearm models with varying complexity have been published in the literature. Forearm models previously presented in the preceding sections are described in more detail here and new forearm models are introduced. The forearm joints receive many different names; in this thesis humeroulnar joint, humeroradial joint, and radioulnar joint are used. The humeroulnar joint is also named elbow joint or elbow flexion-extension joint and the radioulnar joint is also named forearm joint, elbow pronation-supination joint or forearm pronation-supination joint.

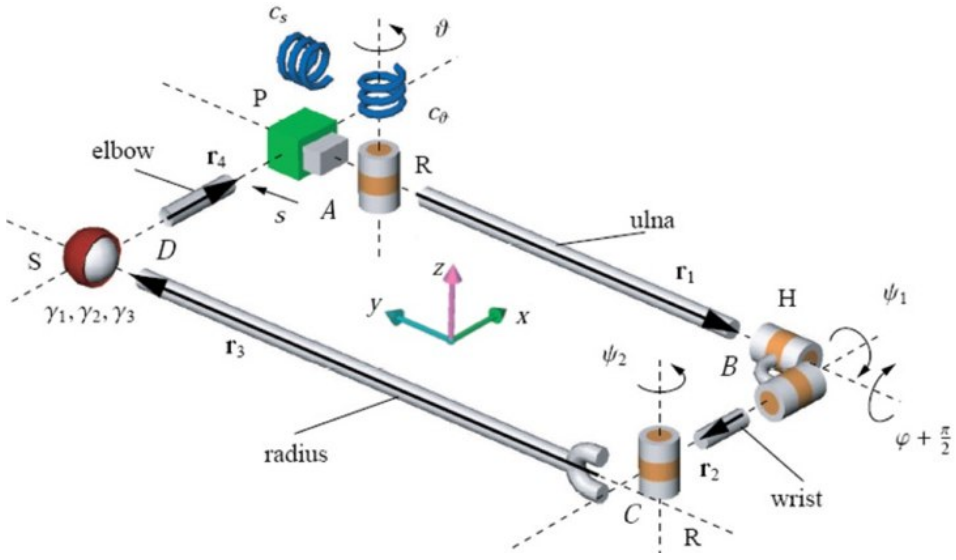

Figure 3.5: Forearm model for pronation and supination with 2 DoFs. Reproduced from (Kecskeméthy and Weinberg, 2003).

Weinberg et al. (2000) developed a kinematic model of pronation-supination of the forearm for medical diagnosis of the ulna and radius fractures. The model was developed and validated using a database of MRI-scans measured in 30 healthy forearms for several pronation-supination angles. The kinematic model has a spherical joint on the proximal end of the radius, a revolute joint on the distal end of the radius, a universal joint on the distal end of the ulna and a prismatic joint on the proximal end of the ulna. The mechanism has one DoF: the pronation-supination angle. In a subsequent study the model was modified and improved (Kecskeméthy and Weinberg,

2003). The prismatic joint on the proximal end of the ulna was substituted by one revolute joint plus a prismatic joint and two virtual springs (Figure 3.5). Model parameters were estimated from static X-ray and MRI scans in living subjects and *in vitro* measurements in one cadaver. The measurements performed between 90º pronation and 90º supination showed that the translation and rotation in the prismatic and revolute joints respectively, on the proximal end of the ulna are small (maximum translation of 0.6 mm at 85º pronation and maximum angle of 7.5º at 90º pronation).

A dynamic musculoskeletal model of the upper arm, forearm and hand including only the elbow and wrist joints was presented by Lemay and Crago (1996). The motion of the model was controlled by muscles, which were modelled with a Hill-type muscle model (Zajac, 1989). The model included the humerus (fixed body), ulna, radius and hand, which were modelled as rigid elements (Figure 3.6). The LCS of each bone was defined in the anatomical position and was parallel to the anatomical axes. Masses and CoM locations were taken from Seireg and Arvikar (1989) and the moments of inertia were estimated using the regression equations of Hinrichs (1985). BSPs of the forearm were divided equally between the ulna and radius. This division was arbitrary due to lack of knowledge but it served to consider that not all the forearm mass moves during pronation-supination.

Lemay and Crago (1996) considered the humeroradial joint as a spherical joint whose centre of rotation coincides with the centre of the capitulum. The humeroulnar joint was modelled as a revolute joint whose axis of rotation passes through the centre of the capitulum and the centre of the trochlea. The distal radioulnar joint was modelled as a cylindrical joint whose axis of rotation passes through the centre of the capitulum and the distal end of the ulna. This arrangement of the forearm joints makes the radius slide and rotate on the fixed ulna. The wrist joint was modelled as a universal joint and was attached to the radius only. The model included 20 muscles of the upper limb. Instead of describing muscle path with origins, insertions and via or wrapping points, muscle actions were defined using moment arms as a function of joint angle. Muscle moment arms were obtained from several sources in the literature. A muscle force model similar to Zajac's (1989) was used and muscle force parameters were taken from several sources in the literature. The model was implemented with the multibody software ADAMS® (MSC.Software Corporation).

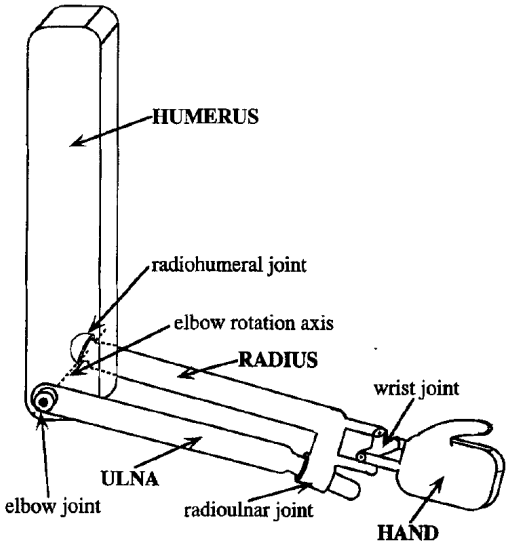

Figure 3.6: Forearm model propose by Lemay and Crago (1996).

Several authors have adopted a simplified forearm model (Murray et al., 1995; Gonzalez et al., 1996; Garner and Pandy, 1999; Maurel, 1999; Charlton and Johnson, 2000). The humeroulnar and radioulnar joints are modelled as revolute joints. Although the humeroradial joint is not included in the model, it is taken into account implicitly in the modelling of the radioulnar joint. The humeroulnar joint represents the elbow flexion-extension motion and its axis of rotation passes through the centres of the capitulum and trochlea. The radioulnar joint represents the elbow pronation-supination motion and its axis of rotation passes through the centre of the radial head, which approximates the humeroradial joint centre, and the distal end of the ulna. Some authors consider that the radioulnar joint axis passes through the centre of the capitulum (e.g. Garner and Pandy, 1999) instead of the centre of the radial head but the differences are minimum (Figure 3.7).

Other authors consider a forearm model with a kinematic structure similar to the preceding model but they are not comparable because the joint parameters are estimated differently. The preceding forearm models derive joint parameters from bone geometry assuming that the joint axes and joint centres location are completely determined by bone geometry. Delft upper limb model (section 3.2.1.4) or Biryukova et al. (2000) estimate joint parameters from passive forearm motions using a functional method. Therefore, in these two latter models joint parameters are not exclusively determined by the geometry of the bones.

The radioulnar joint axis is also approximated in some forearm models by the line connecting the humeroulnar joint centre and the wrist joint centre (Schmidt et al., 1999). This is a common assumption in ergonomic software tools like RAMSIS, SAFEWORK or JACK (section 3.2.3).

3.2.1.9 Wrist models

The wrist joint has been modelled as a universal joint (Brumbaugh et al., 1982; Lemay and Crago, 1996; Rab et al., 2002), skew universal joint (Garner and Pandy, 1999), and skewed-oblique universal joint (Sommer and Miller, 1980; Buchanan et al., 1993; Biryukova et al., 2000). These three different wrist joint models are presented next using a representative paper of each modelling option.

Buchanan et al. (1993) modelled the wrist joint as a skewed-oblique universal joint. The two wrist joint axes did not intersect and were separated a few millimetres, the abduction-adduction axis being more distal than the flexion-extension axis. Furthermore, the wrist joint axes were assumed to be nonorthogonal and this was defined with an oblique angle between the two joint axes. The distance between the two wrist joint axes was varied from 0.0 to 2.0 cm and the oblique angle from 60º to 120º. However, muscle forces were found to be insensitive to variations of these two parameters. This finding was attributed to deficiencies in the muscle force estimation method and it was not clear if muscle forces are insensitive to distance between wrist joint axes and the oblique angle.

Lemay and Crago (1996) proposed a dynamic musculoskeletal model of the upper arm, forearm and hand including the elbow and wrist joints. According to previous studies in the literature they assumed that the flexion-extension and abduction-adduction axes intersect. Then, the wrist joint was modelled as a universal joint with the joint centre at the head of the capitate bone and attached only to the radius.

Garner and Pandy (1999) presented a musculoskeletal model of the right upper limb based on the Visible Human Project Dataset (Spitzer and Whitlock, 1998). The wrist joint was modelled with two independent revolute joints, whose joint axes were perpendicular to each other but did not intersect (skew universal joint). The wrist flexion-extension axis passed through the centre of the proximal end of the capitate bone (Figure 3.7). The wrist abduction-adduction axis was assumed to be perpendicular to the wrist flexion-extension axis and the long axis of the third metacarpal. According to previous studies in the literature, the distance between the two wrist axes was set to 5 mm, the abduction-adduction axis being more distal.

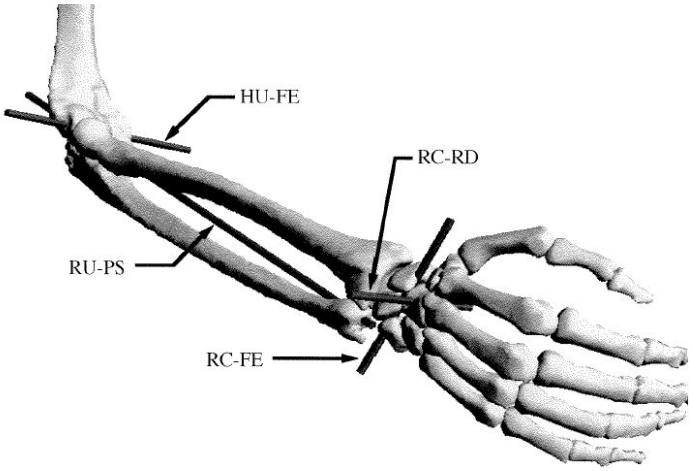

Figure 3.7: Wrist and elbow model of Garner and Pandy (1999) showing the wrist flexion-extension axis (RC-FE), wrist abduction-adduction axis (RC-RD), elbow flexion-extension axis (HU-FE) and elbow pronation-supination axis (RU-PS).

3.2.2 LOWER LIMB MODELS

The lower limb has been modelled with different levels of detail depending on the purpose of the investigation. Complex models of the joints of the lower limb have been published (van den Bogert et al., 1994; Caruntu and Hefzy, 2004) but they have been applied to studies of one specific joint. Musculoskeletal models of the whole lower limb usually consider simple models of the joints instead of using state-of-the-art models. The main three-dimensional models of the lower limb are summarised in this section.

Brand et al. (1982) presented a musculoskeletal kinematic model of the lower limb. The model included the pelvis, femur and tibia, which were modelled as rigid elements. The patella and foot were included in the model but they were considered as rigid extensions of the tibia. The LCS of each bone was defined using ALs. The hip, knee and ankle joints were considered but details about how they were modelled were not provided. The model included the main muscles of the lower limb. Three-dimensional coordinates of muscles origins and insertions were measured in six lower limbs of three fresh cadaver specimens. Muscle origin and insertion were visually estimated as the centroid of the muscle attachment sites. Some broad muscles were split into several parts (up to 3) based only on anatomic and functional considerations. Muscle path was modelled as a straight line between origin and insertion. Delp et al. (1990) investigated the muscle paths reported by Brand and found out that several muscles passed through the bones or deeper muscles.

Delp et al. (1990) described an interactive graphic-based musculoskeletal model of the lower limb to study how surgical changes in musculoskeletal geometry and musculotendon parameters affect muscle force and joint moments. The model included the pelvis, femur, patella, tibia-fibula, talus, foot (calcaneous, navicular, cuboid, cuneiforms, and metatarsals), and toes (phalanges), all modelled as rigid elements. Bone surface data were measured on actual bones using a three-dimensional digitiser. The relative motion between the body segments was defined with five joints: hip, knee, ankle, subtalar and metatarsophalangeal. The hip was modelled as a spherical joint, while the knee model had one DoF and was based on the knee planar model of Yamaguchi and Zajac (1989). The knee model accounts for the kinematics of the tibiofemoral and patellofemoral joints. The ankle, subtalar and metatarsophalangeal were modelled as revolute joints. Joint parameters were taken from several sources in the literature. Muscle path was defined as the line connecting the origin and insertion through via points fixed on the bones. Some via points were considered as a function of the joint angle and they were activated or deactivated depending on the joint angle value. Muscle path was not measured directly on cadavers but it was estimated from digitised bone geometry and validated visually and with moment arm data measured on cadavers by the authors and obtained from the literature. Muscle force parameters were taken from several sources in the literature except for the tendon slack length that was estimated by the authors. The complete musculoskeletal model is publicly available at the International Society of Biomechanics web page (www.isbweb.org).

An inverse-dynamic model of the lower extremity for determining internal loads was presented by Glitsch and Baumann (1997). The model included the pelvis, thigh, shank and foot, which were modelled as rigid elements. The LCS of each bone was defined using ALs. BSPs were based on Chandler et al. (1975) but with some modifications. The hip joint was modelled as a spherical joint. The knee and ankle joints were modelled using three types of joints: revolute, spherical and "intermediate". The authors concluded that "intermediate" joints give more realistic results. Muscle path parameters and Muscle PCSA data were taken from Brand et al. (1982). Kinematic, kinetic, and EMG data were measured on a subject during walking and running. From these data, muscle forces and joint reactions were estimated using a static optimisation approach and compared with EMG data measured in 8 muscles.

Benedetti et al. (1998) developed an inverse dynamic model of the lower limb in order to analyse gait data of 20 subjects. The model included the pelvis, thigh, shank and foot, which were modelled as rigid bodies. The LCS of each bone was defined using ALs. BSPs were not considered in the model because

the effects of inertia on the results were neglected. The hip, knee and ankle joints were modelled as spherical joints. The ankle joint centre was approximated by the midpoint between the lateral and medial malleolus and the knee joint centre by the midpoint between the two femoral epicondyles. The hip joint centre was estimated with a functional method (Cappozzo, 1984). Muscles were not included in the model.

Anderson and Pandy (1999) presented a musculoskeletal forward-dynamic model of the lower limb used to calculate the pattern of muscle excitations needed to produce a maximal vertical jump. The model included the head-arms-torso, pelvis, thighs, shanks, hindfeet and toes. The head, arms and torso were modelled as a single rigid body. The LCS of each bone was defined in the anatomical position and was parallel to the anatomical axes. The origin of each LCS was located at the CoM of the body segment. BSPs of the model were calculated by averaging BSPs estimated on five male subjects using the methods reported by McConville et al. (1980).

In this model the head-arms-torso body segment was connected to the pelvis through a spherical joint, which was located approximately at the third lumbar vertebra. Each hip was modelled as a spherical joint, and each knee was modelled as a revolute joint. The shank was connected to the hindfoot via a universal joint, which represented the ankle and subtalar joints. The metatarsal joint, between the hindfoot and toes, was modelled as a revolute joint. Some joint parameters were taken from the literature and others were estimated from recorded kinematic data using functional methods. The contact between foot and ground was modelled using five spring-damper units distributed over the sole of each foot.

The motion of this model was controlled by muscles, which were modelled with a Hill-type muscle model (Zajac, 1989). Each lower limb was actuated by 24 muscles and the head-arms-torso body segment was actuated by 6 muscles. Muscle path was based on data reported by Delp et al. (1990) but some modifications were considered. The path of some muscles was defined using via cylinders to model wrapping around some elements. Muscle force parameters were based on data reported by Delp et al. except for the tendon slack length that was estimated by the authors.

3.2.3 WHOLE BODY MODELS

A large number of whole body models have been developed for many different applications. Most of the whole body models are skeleton models without musculotendon actuators but they include a graphic representation of the human skin and even clothes. Whole body models usually consider simplified

models of joints with fixed centres of rotation and fixed joint axes. Whole body models are used in many different fields like ergonomic applications (Monnier et al., 2003; Wang et al., 2005), sports performance (Gutierrez, 1990; Alvarez et al., 1993b; Urban, 1995; Celigüeta, 1996), occupant safety (Silva, 2003), or computer animation (Baerlocher and Boulic, 2004) among others.

A number of CAD tools are available in the market for the ergonomic design of vehicle interiors, cockpits and workplaces. The kernel of all these tools is a model of the whole human body. The main CAD tools for ergonomic design are RAMSIS (Human Solutions GmbH), JACK (UGS Corp.), and SAFEWORK (Safework Inc.).

The RAMSIS model (Figure 3.8) has 53 joints with 104 DoFs (see section 3.2.3). The spine is modelled with 6 body segments and two different hand models are available: simplified and detailed. The JACK model has 69 bodies connected by 68 joints with 135 DoFs. The spine is modelled with 17 body segments and the hand with 16 body segments. The SAFEWORK model (Figure 3.8) has 100 body segments with 148 DoF and fully articulated models of the spine and hands.

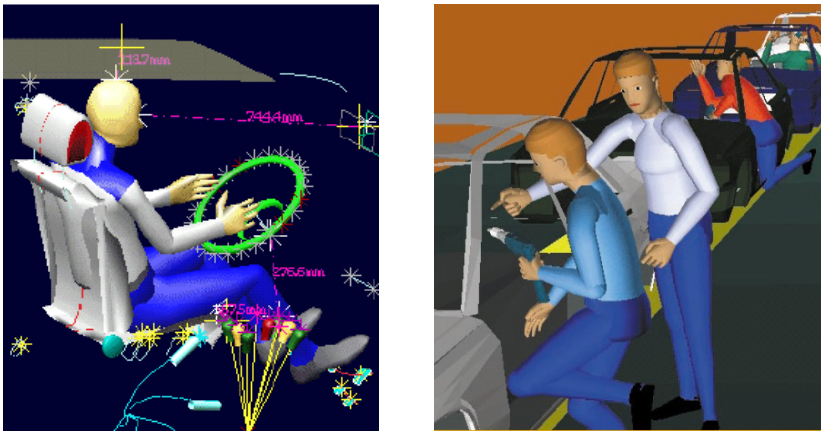

Figure 3.8: RAMSIS model seated in a vehicle (left). SAFEWORK model in a manufacturing application (right).

At the Applied Mechanics department of CEIT several whole body models have been developed for sports and space applications:

- A whole body model developed by Gutiérrez (1990) was used in the ABAT project in Barcelona '92 Olympic games (Alvarez et al., 1993a; Alvarez et al., 1993b). The model was defined using natural coordinates (see section 4.1) and composed of 33 bodies connected by 15 revolute joints and 2 universal joints.

- In the frame of the DYNAMAN project for the European Space Agency, two kinematic whole body models were developed. The first model had 26 points, 21 unitary vectors and 39 DoFs. The second model had also 26 points but only 19 unitary vectors and 36 DoFs.
- Urban (1995) proposed a more detailed whole body model with 32 bodies connected by 32 joints: 28 revolute joints located at the main articulation, 2 universal joints at the ankles, 1 universal joint at the throat and a floating joint (3 translations and 3 rotations) between the lower trunk and the ground. The model was used to analyse sport activities of elite athletes (Celigüeta, 1996).

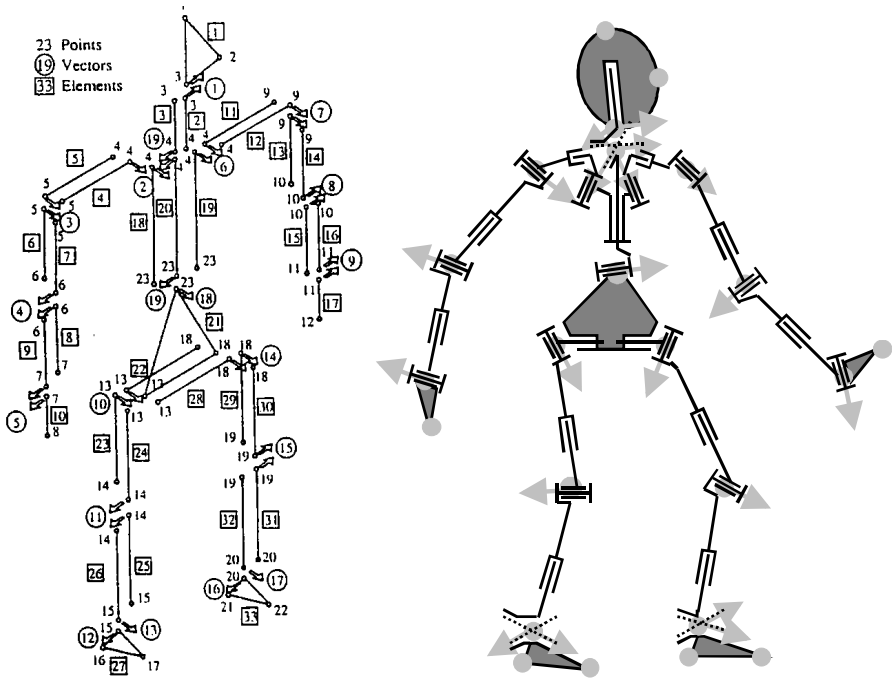

Figure 3.9:Whole body model of Gutiérrez (1990) (left) and whole body model of Urban (1995) (right). Both models were defined with natural coordinates.

A whole body model based on Urban's model has been used recently by Silva et al. (Silva, 2003; Silva and Ambrósio, 2003) in gait analysis and injury biomechanics application cases. These are just a few examples from the large number of whole body models and applications published in the literature.

3.3 MODYCO SKELETAL MODELS

Three human skeletal models have been developed in the frame of the MoDyCo project, and two types of common driving manoeuvres have been analysed with them: braking and steering manoeuvres. Braking manoeuvres have been studied with a skeletal model of the right lower extremity (section 3.3.3) that includes the pelvis, right thigh, right shank and right foot. Two different skeletal models of the upper body have been used to analyse steering manoeuvres. Both models include left and right arms, thorax and pelvis and the difference between them is the model of the shoulder complex. One model considers a simplified shoulder complex without scapula in which the clavicle is connected directly to the humerus through an equivalent glenohumeral joint (section 3.3.2). The other model includes the clavicle, scapula and humerus, with the scapula connected to the thorax through the scapulothoracic joint forming a closed-loop mechanism (section 3.3.1). The three human skeletal models of the MoDyCo project are based on ALs, which are used to estimate joint parameters and BSPs, and to define the LCSs of each body segment.

3.3.1 UPPER BODY MODEL WITH SCAPULA

The upper body model with scapula (UBMS) is used to study steering manoeuvres. The following table summarises the ALs (see section B.1 of Appendix B for a detailed description) required for the UBMS.

Number	Acronym	Body segment	Name	Origin
L1	C7	Thorax	7th cervical vertebra	B/L
L2	T8	Thorax	8th thoracic vertebra	L
L3	IJ	Thorax	Incisura jugularis	B/L
L4	PX	Thorax	Processus xiphoideus	L
L5	LSC	Thorax Left clavicle	Left sternoclavicular joint	J/L
L6	RSC	Thorax Left clavicle	Right sternoclavicular joint	J/L
L7	LAC	Left clavicle Left scapula	Left acromioclavicular joint	J/L
L8	LTS	Left scapula	Left trigonum spinae scapulae	J/L
L9	LAI	Left scapula	Left angulus inferior	J/L
L10	LAA	Left scapula	Left angulus acromialis	J/L
L11	LPC	Left scapula	Left processus coracoideus	J
L12*	LGHJC*	Left scapula Left upper arm	Left glenohumeral joint centre	B/L
L13	LLEH	Left upper arm	Left lateral epicondyle of humerus	J/L
L14	LMEH	Left upper arm	Left medial epicondyle of humerus	J/L

Number	Acronym	Body segment	Name	Origin
L15*	LEJC*	Left upper arm Left forearm	Left elbow joint centre	B/L
L16	LRS	Left forearm	Left radial styloid	J/L
L17	LUS	Left forearm	Left ulnar styloid	J/L
L18*	LWJC*	Left forearm Left hand	Left wrist joint centre	B/L
L19	LDAC3	Left hand	Left 3rd dactylion	B
L20	RAC	Right clavicle Right scapula	Right acromioclavicular joint	J/L
L21	RTS	Right scapula	Right trigonum spinae scapulae	J/L
L22	RAI	Right scapula	Right angulus inferior	J/L
L23	RAA	Right scapula	Right angulus acromialis or acromion	J/L
L24	RPC	Right scapula	Right processus coracoideus	J
L25*	RGHJC*	Right scapula Right upper arm	Right glenohumeral joint centre	B/L
L26	RLEH	Right upper arm	Right lateral epicondyle of humerus	J/L
L27	RMEH	Right upper arm	Right medial epicondyle of humerus	J/L
L28*	REJC*	Right upper arm Right forearm	Right elbow joint centre	B/L
L29	RRS	Right forearm	Right radial styloid	J/L
L30	RUS	Right forearm	Right ulnar styloid	J/L
L31*	RWJC*	Right forearm Right hand	Right wrist joint centre	B/L
L32	RDAC3	Right hand	Right 3rd dactylion	B
L33	LPSIS	Pelvis	Left posterior superior iliac spine	J/L
L34	RPSIS	Pelvis	Right posterior superior iliac spine	J/L
L35	LASIS	Pelvis	Left anterior superior iliac spine	J/L
L36	RASIS	Pelvis	Right anterior superior iliac spine	J/L
L37	PS	Pelvis	Pubic symphysis	J
L38*	RHJC*	Pelvis Right thigh	Right hip joint centre	B
L49	OMPH	Thorax / Pelvis	Omphalion or navel	B
L50*	LV3*	Thorax / Pelvis	3rd lumbar vertebra	J
L51	VERT	Head	Vertex	B

Table 3.1: ALs of the UBMS. 'Origin' defines the purpose of the AL: J- joint parameters estimation, B- BSPs estimation, L- local coordinate system definition. *Joint rotation centres estimated from ALs, i.e. they cannot be found by palpation.

3.3.1.1 Body segments

The UBMS model includes the pelvis, thorax, clavicles, scapulas, upper arms, forearms and hands (Figure 3.10). The motion of the head is not considered in the model but its BSPs are included in the thorax. All the body segments are considered as rigid bodies with constant BSPs, as the soft tissue motion is

neglected. However, some concerns arise for the spine, thorax, forearm and hand because they are composed by more than one bone.

The spine, which is not included in the UBMS, is formed by 24 vertebrae and its motion originates from the relative motion between the vertebrae. The subject is measured in a seated position during the steering manoeuvres studied with this model, so it is assumed that the motion of the spine is very small and can be neglected. Then, the pelvis and the thorax are connected by a single fictitious spherical joint between the 2nd and 3rd lumbar vertebra following the approach of Anderson and Pandy (1999).

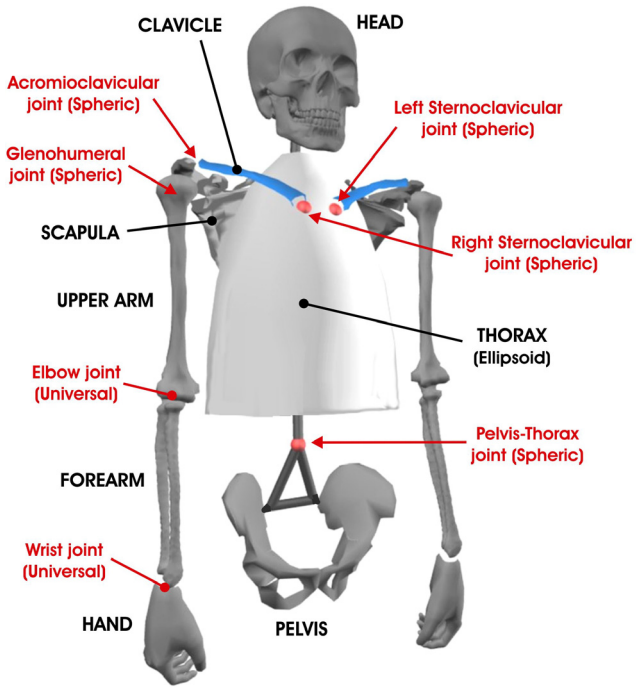

Figure 3.10: Upper body model with scapula.

The thorax deforms during inspiration and expiration and also due to the relative motion of the thoracic vertebrae. Some authors record the motion of the subject after exhaling in order to prevent thorax deformations but this is not always possible. Van der Helm and Pronk (1995) measured humeral abduction and flexion after exhalation and estimated thorax deformation from the angle between the lines through IJ-PX and C7-T8. Standard deviation of this angle ranged between 1.6 and 2.7 deg (10 subjects) which was within the measurement error. In our study it is not possible to record the subject motion after exhalation due to the duration of the experiments. Then, the thorax

deforms during inhalation-exhalation but this effect is considered small compared to measurement errors and is neglected.

The forearm has two bones, the ulna and the radius. During flexion-extension the relative motion between ulna and radius is small and the forearm can be approximated as a rigid body if the soft tissue motion is neglected. During pronation-supination the ulna and radius move relative to each other and the BSPs change. However, its effect on the results is assumed to be small and is neglected.

The skeleton of the hand is subdivided into three bone groups: the carpus or wrist bones (8 bones), the metacarpus or bones of the palm (5 bones), and the phalanges or bones of the digits (14 bones). The motion between the forearm and the wrist bones is considered in this thesis but the motion of the remaining bones of the hand is not considered relevant to our analysis. During steering manoeuvres both hands must hold firmly the steering wheel, so the wrist bones are approximated as a single rigid body and the motion of the other hand bones is neglected.

3.3.1.1.1 Local coordinate systems

In the field of biomechanics for human movement, for many years there were no standard local coordinate systems (LCSs) for each body segment or joint rotation conventions. Different researches used different LCSs and joint rotation conventions, which made comparison among various studies difficult and sometimes impossible. Since November 1993, the Standardisation and Terminology Committee (STC) of the International Society of Biomechanics (ISB) started a project for developing a set of standards for reporting data. Not until recently a first generic recommendation (Wu and Cavanagh, 1995) and the first specific recommendations for the hip, ankle, and spine (Wu et al., 2002) have been published. Also specific recommendations for the shoulder, elbow, wrist, and hand (Wu et al., 2005) have been published lately.

The LCSs of each body segment of UBMS have been defined taking into account the recommendations of the ISB. Pelvis LCS is defined according to the ISB recommendations (Wu et al., 2002) but the remaining body segments of the model do not follow ISB recommendations (Wu et al., 2005) because they were published after the realisation of this thesis. However, the ALs recommended by the ISB and the ones used in UBMS are the same, and therefore it is straightforward to give the results using the ISB recommendations.

The LCS of the thorax, clavicles, scapulas and humerus follow the draft recommendations proposed by van der Helm (1997a), while the LCS of the forearm and hand have been defined by the author. The LCSs of each body segment of the UBMS are presented in Table 3.2 to Table 3.7 and in Figure 3.11 to Figure 3.20.

Body segment	**Local coordinate system definition**	
Thorax	Origin	IJ (L3)
	Y_{Thor}	The line connecting the midpoint between PX (L4) and T8 (L2) and the midpoint between IJ (L3) and C7 (L1), pointing upward.
	X_{Thor}	The line perpendicular to the plane formed by IJ (L3), C7 (L1) and the midpoint between PX (L4) and T8 (L2), pointing to the right.
	Z_{Thor}	The common line perpendicular to the X_{Thor}- and Y_{Thor}-axis.
Pelvis	Origin	Midpoint between RASIS (L36) and LASIS (L35)
	Z_{Pel}	The line parallel to a line connecting the RASIS (L36) and LASIS (L35), and pointing to the right.
	X_{Pel}	The line parallel to a line lying in the plane defined by the RASIS (L36), the LASIS (L35), and the midpoint between RPSIS (L34) and LPSIS (L33), orthogonal to the Z_{Pel}-axis, and pointing anteriorly.
	Y_{Pel}	The line perpendicular to both X_{Pel}- and Z_{Pel}-axis, pointing cranially.

Table 3.2: Definition of thorax and pelvis LCSs.

Body segment	**Local coordinate system definition**	
Right clavicle	Origin	RSC (L6)
	X_{Clav}	The line connecting RSC (L6) and RAC (L20), pointing to RAC.
	Z_{Clav}	The line perpendicular to X_{Clav}-axis and Y_{Thor}-axis, pointing backward.
	Y_{Clav}	The common line perpendicular to the X_{Clav}- and Z_{Clav}-axis
Left clavicle	Origin	LSC (L5)
	X_{Clav}	The line connecting LAC (L7) and LSC (L5), pointing to LSC.
	Z_{Clav}	The line perpendicular to X_{Clav}-axis and Y_{Thor}-axis, pointing backward.
	Y_{Clav}	The common line perpendicular to the X_{Clav}- and Z_{Clav}-axis.

Table 3.3: Definition of right and left clavicle LCSs.

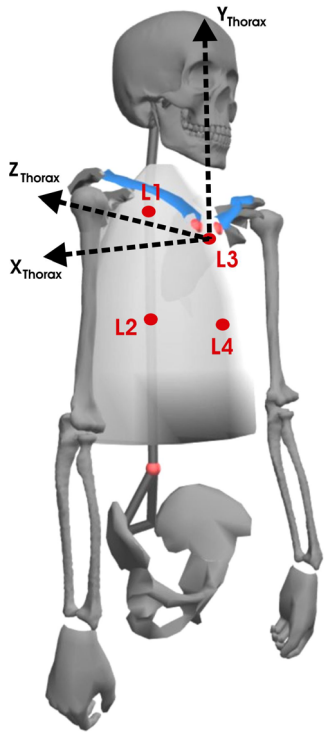

Figure 3.11: Thorax LCS

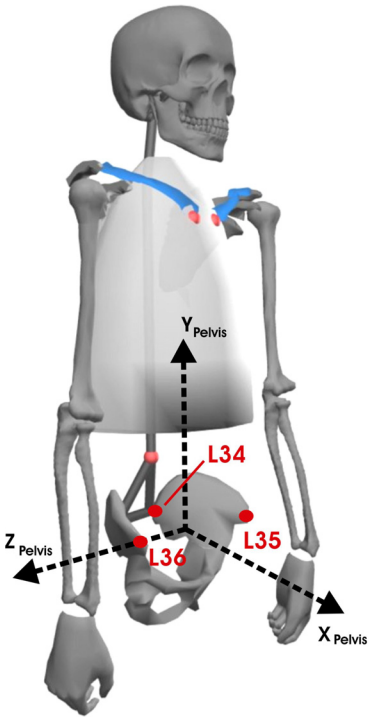

Figure 3.12: Pelvis LCS

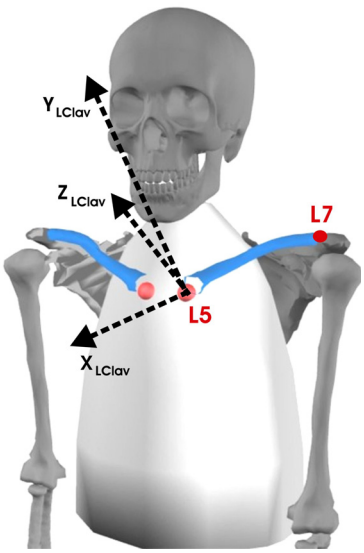

Figure 3.13: Left clavicle LCS

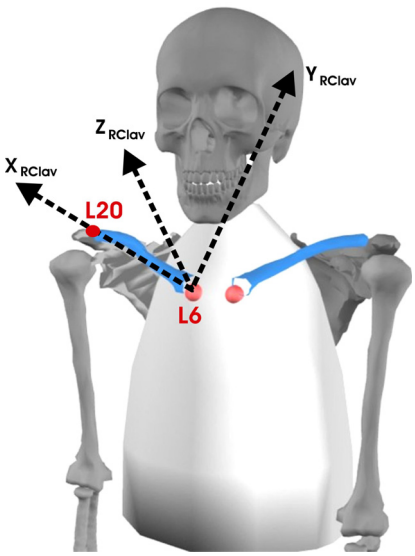

Figure 3.14: Right clavicle LCS

Body segment	Local coordinate system definition	
Right scapula	Origin	RAA (L23)
	X_{Scap}	The line connecting RTS (L21) and RAA (L23), pointing to RAA.
	Z_{Scap}	The line perpendicular to the plane formed by RAI (L22), RAA (L23) and RTS (L21), pointing backward (i.e. perpendicular to scapular plane).
	Y_{Scap}	The common line perpendicular to the X_{Scap}- and Z_{Scap}-axis.
Left scapula	Origin	LAA (L10)
	X_{Scap}	The line connecting LAA (L10) and LTS (L8), pointing to LTS.
	Z_{Scap}	The line perpendicular to the plane formed by LAI (L9); LAA (L10), and LTS (L8), pointing backward (i.e. perpendicular to scapular plane).
	Y_{Scap}	The common line perpendicular to the X_{Scap}- and Z_{Scap}-axis.

Table 3.4: Definition of right and left scapula LCSs.

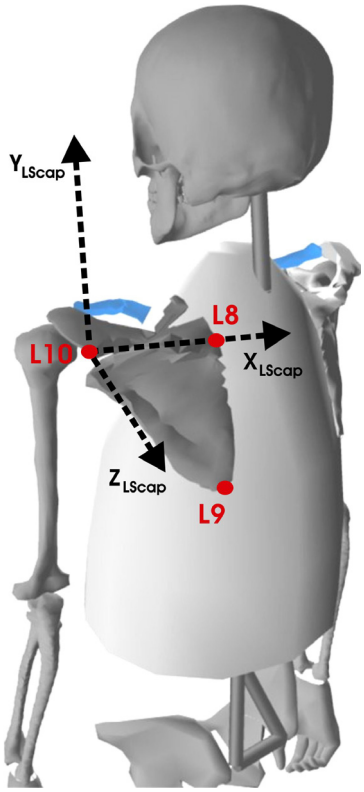

Figure 3.15: Left scapula LCS

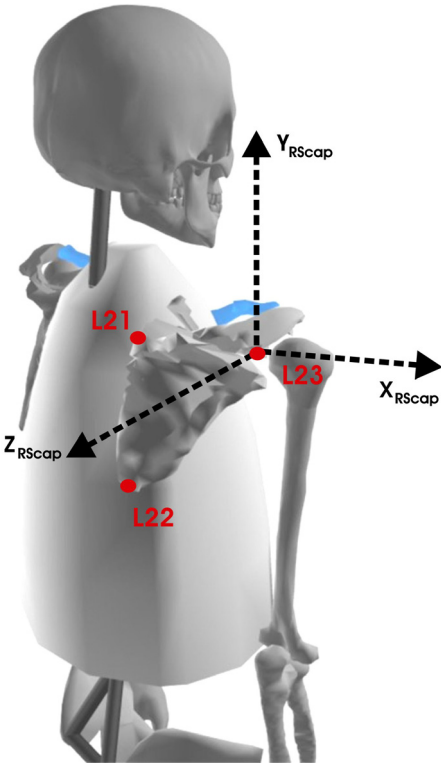

Figure 3.16: Right scapula LCS

Body segment	Local coordinate system definition	
Right Upper arm	Origin	RGHJC (L25)
	Y_{Uarm}	The line connecting RGHJC (L25) and the midpoint between RLEH (L26) and RMEH (L27), pointing distally.
	Z_{Uarm}	The line perpendicular to the plane formed by RGHJC (L25); RLEH (L26), and RMEH (L27), pointing backward.
	X_{Uarm}	The common line perpendicular to the Y_{Uarm}- and Z_{Uarm}-axis.
Left Upper arm	Origin	LGHJC (L12)
	Y_{Uarm}	The line connecting LGHJC (L12) and the midpoint between LLEH (L13) and LMEH (L14), pointing distally.
	Z_{Uarm}	The line perpendicular to the plane formed by LGHJC (L12); LLEH (L13), and LMEH (L14), pointing backward.
	X_{Uarm}	The common line perpendicular to the Y_{Uarm}- and Z_{Uarm}-axis.

Table 3.5: Definition of right and left upper arm LCSs.

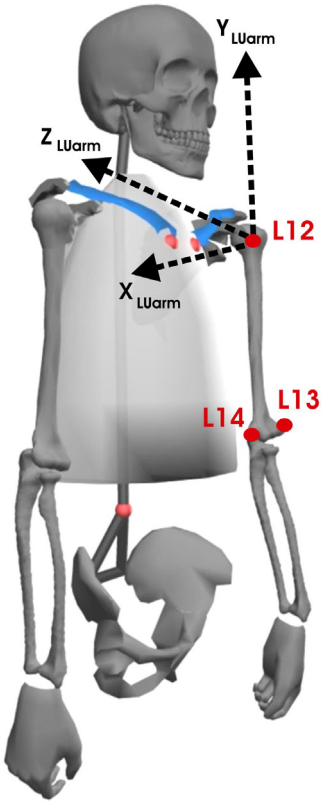

Figure 3.17: Left upper arm LCS

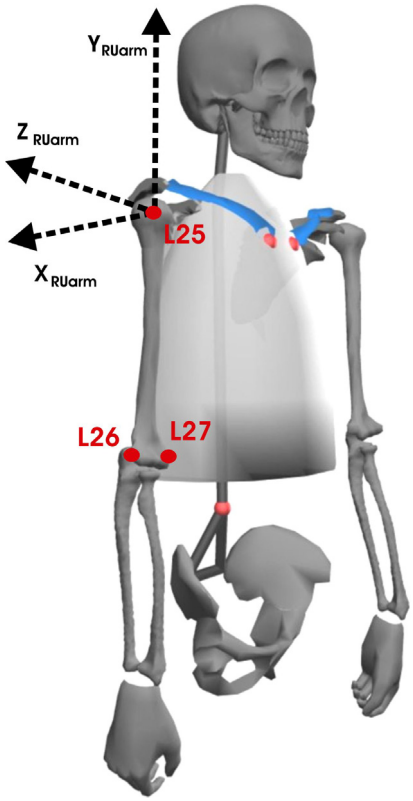

Figure 3.18: Right upper arm LCS

Body segment	Local coordinate system definition	
Right Forearm	Origin	The midpoint between RRS (L29) and RUS (L30).
	Y_{Farm}	The line connecting the midpoint between RRS (L29) and RUS (L30), and REJC (L28), pointing to REJC.
	Z_{Farm}	The line perpendicular to the plane formed by RRS (L29), RUS (L30) and REJC (L28), pointing backward when the subject is in the anatomical position.
	X_{Farm}	The common line perpendicular to the Y_{Farm}- and Z_{Farm}-axis.
Left Forearm	Origin	The midpoint between LRS (L16) and LUS (L17).
	Y_{Farm}	The line connecting the midpoint between LRS (L16) and LUS (L17), and LEJC (L15), pointing to LEJC.
	Z_{Farm}	The line perpendicular to the plane formed by LRS (L16), LUS (L17) and LEJC (L15), pointing backward when the subject is in the anatomical position.
	X_{Farm}	The common line perpendicular to the Y_{Farm}- and Z_{Farm}-axis.

Table 3.6: Definition of right and left forearm LCSs.

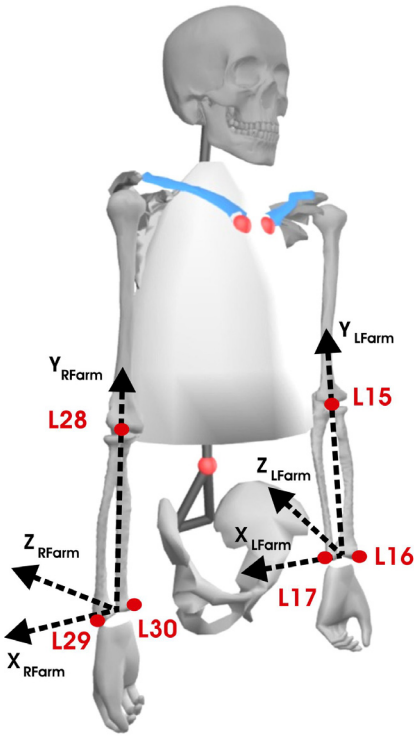

Figure 3.19: Left and right forearm LCS

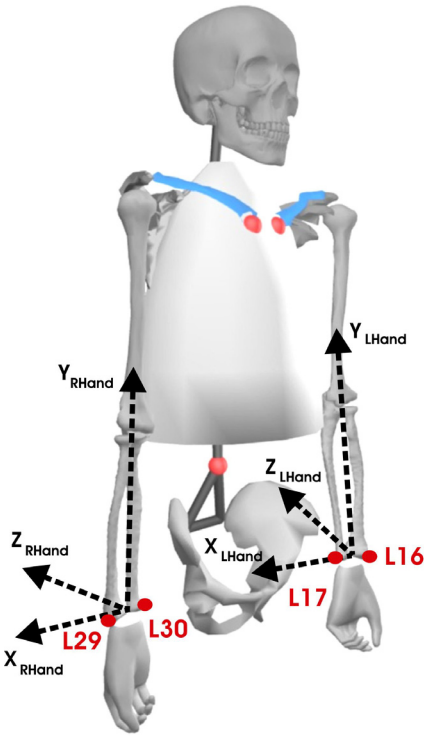

Figure 3.20: Left and right hand LCS

Body segment	Local coordinate system definition	
Right Hand	Origin	The midpoint between RRS (L29) and RUS (L30).
	Y_{Hand}	The line coincident with the Y_{Farm}-axis in the anatomical position.
	Z_{Hand}	The line coincident with the Z_{Farm}-axis in the anatomical position.
	X_{Hand}	The common line perpendicular to the Y_{Hand}- and Z_{Hand}-axis.
Left Hand	Origin	The midpoint between LRS (L16) and LUS (L17).
	Y_{Hand}	The line coincident with the Y_{Farm}-axis in the anatomical position.
	Z_{Hand}	The line coincident with the Z_{Farm}-axis in the anatomical position.
	X_{Hand}	The common line perpendicular to the Y_{Hand}- and Z_{Hand}-axis.

Table 3.7: Definition of right and left hand LCSs.

3.3.1.1.2 Body segment parameters

The method for estimating BSPs must be applied to subjects with the same anthropometric features as the subjects database used to generate it. For this reason, two different methods are selected:

- Zatsiorsky's proportion method (Zatsiorsky et al., 1990a) adjusted by De Leva (1996a) for subjects with features similar to the database.
- Zatsiorsky's linear regression method based on total body height and weight (Zatsiorsky and Seluyanov, 1983) for subjects outside the database range.

The suitability of these two methods for the requirements of the MoDyCo project has been discussed in section 2.2.6.

The clavicles and scapulas move under the skin and it is difficult to estimate their BSPs. Furthermore, the influence of BSPs of the clavicles and scapulas is considered small comparing to other body segments, and therefore they are neglected. Zatsiorsky segmented the trunk in 3 parts: upper, middle and lower trunk. BSPs of the upper and middle trunk segments are associated to the thorax body segment and BSPs of the lower trunk segment are associated to the pelvis body segment. The remaining body segments have a direct equivalent in the segmentation of Zatsiorsky. The details of the method are presented in section B.3 of Appendix B.

3.3.1.2 Joint parameters and joint rotation order

UBMS includes the sternoclavicular, acromioclavicular, scapulothoracic, glenohumeral, elbow, wrist and thorax-pelvis joints. The human joints are modelled with fixed joint centres of rotation and fixed joint axes and only revolute, spherical and universal joints are used. In section 2.1.15, it was

discussed that the methods based on ALs for estimating joint parameters are the most appropriate for the requirements of the MoDyCo project. Table 3.8 summarises the methods selected for estimating joint parameters for UBMS.

The sternoclavicular joint (SCJ) is modelled as a spherical joint (Högfors et al., 1987; Engin and Tümer, 1989; van der Helm, 1994b; Garner and Pandy, 1999; Maurel, 1999; Charlton and Johnson, 2000). Methods for estimating the sternoclavicular joint rotation centre from ALs have not been published to date and such a rotation centre is estimated by palpation as the most inferior point on the proximal end of the clavicle in contact with the sternum.

The acromioclavicular joint (ACJ) is modelled as a spherical joint (Högfors et al., 1987; Engin and Tümer, 1989; van der Helm, 1994b; Garner and Pandy, 1999; Maurel, 1999; Charlton and Johnson, 2000) and similarly to the SCJ, the ACJ rotation centre is estimated by palpation. The ACJ rotation centre is approximated by the middle point between the lateral end of the clavicle and the medial side of the acromion process.

The glenohumeral joint (GHJ) is considered as a spherical joint (Poppen and Walker, 1976; van der Helm et al., 1989; Veeger et al., 1997; Garner and Pandy, 1999) and its joint rotation centre is estimated with the regression method of Meskers et al. (1998) (see section 2.1.8).

The model of the scapulothoracic joint (STJ) is based on the approach of van der Helm (1994b) (see section 3.2.1.4). In this approach, the thorax is approximated by an ellipsoid and two points fixed on the medial border of the scapula are constrained to remain in contact with the ellipsoid. The ellipsoid is determined by fitting it to the ALs measured on the thorax using a least-squared method. Similarly to van der Helm, the trigonum spinae and the angulus inferior ALs are selected as the two points fixed on the scapula.

The elbow joint complex is formed by three joints: humeroulnar, humeroradial and radioulnar. The humeroulnar joint is modelled as a revolute joint (Murray et al., 1995; Gonzalez et al., 1996; Lemay and Crago, 1996; Garner and Pandy, 1999; Maurel, 1999; Charlton and Johnson, 2000), which defines the flexion-extension motion of the elbow. The joint axis and joint rotation centre are estimated according to Stokdijk et al. (1999). The humeroradial and radioulnar joints define the pronation-supination motion of the elbow (see section 3.2.1.8). The humeroradial joint has been approximated by a spherical joint (Lemay and Crago, 1996; Zatsiorsky, 1998) and the radioulnar joint by a revolute joint (Murray et al., 1995; Gonzalez et al., 1996; Garner and Pandy, 1999; Maurel, 1999; Charlton and Johnson, 2000) or a cylindrical joint (Lemay and Crago, 1996). The kinematic behaviour of humeroradial and radioulnar joints can be represented by a single revolute

joint, whose joint axis passes through the centre of the radial head and the distal end of the ulna (Murray et al., 1995; Gonzalez et al., 1996; Garner and Pandy, 1999; Maurel, 1999; Charlton and Johnson, 2000).

In this thesis, the elbow complex is modelled with a universal joint with nonorthogonal axes, assuming that the two revolute joint axes (humeroulnar and humeroradial/radioulnar) intersect at the humeroradial joint centre. The humeroradial joint centre is approximated by the joint rotation centre given by Stokdijk's method and it is denominated elbow joint centre (EJC).

The wrist joint (WJ) is modelled as a universal joint (Brumbaugh et al., 1982; Lemay and Crago, 1996; Rab et al., 2002). The abduction-adduction axis is assumed to be perpendicular to the hand palm and the flexion-extension axis is assumed to be perpendicular to the abduction-adduction axis and parallel to the hand palm. The joint rotation centre is located at the midpoint between the radial styloid and the ulnar styloid.

The thorax-pelvis joint (TPJ) is a fictitious joint between the thorax and pelvis and is modelled as a spherical joint. The joint centre is assumed to lie between the 2nd and 3rd lumbar vertebra following the approach of Anderson and Pandy (1999) and is estimated according to Snyder et al. (1972).

Joint name	type	Joint parameter methods
Sternoclavicular joint	SPH	Directly by palpation of the landmarks RSC (L6) or LSC (L5) for the right and left side of the human body respectively.
Acromioclavicular joint	SPH	Directly by palpation of the landmarks RAC (L20) or LAC (L7) for the right and left joints respectively.
Scapulothoracic joint	STJ	Thorax: ellipsoid fitted to ALs measured on the thorax. Scapula: The trigonum spinae and the angulus inferior are two ALs fixed on the scapula, which are constrained to remain in contact with the thorax (ellipsoid).
Glenohumeral joint	SPH	Joint centre estimated with the regression method of Meskers et al. (1998).
Elbow joint	SPH	Joint centre: optimal pivot point given by Stokdijk et al. (1999). Flexion-extension joint axis: method of Stokdijk et al. (1999). Pronation-supination axis: axis through the universal joint centre and the ulnar styloid.
Wrist joint	UNI	Joint centre: midpoint between ulnar styloid and radial styloid. Abduction-adduction axis: perpendicular to the palm hand. Flexion-extension axis: perpendicular to the abduction-adduction axis and parallel to the palm hand.
Thorax-Pelvis joint	SPH	Joint centre between the 2nd and 3rd lumbar vertebrae estimated according to Snyder et al. (1972) (section 2.1.1).

Table 3.8: Methods selected for estimating the joint parameters of UBMS. SHP – Spherical joint; UNI – Universal joint; STJ – Scapulothoracic joint.

The relative rotation between two body segments is described using Euler angles. A joint rotation sequence for each joint is required in order to define unambiguously the motion between the two body segments. Joint rotation sequences for the sternoclavicular, acromioclavicular, and glenohumeral joints follow the draft recommendations proposed by van der Helm (1997a) because ISB recommendations (Wu et al., 2005) for these joints were published after the realisation of this work. Joint rotation sequences for the elbow, wrist and thorax-pelvis joints are defined by the author. Table 3.9 summarises the joint rotation sequences for UBMS.

Acronym	Joint Name	Base Follower	Joint Type	Joint rotation sequence
PelThor	Pelvis-Thorax Joint	Pelvis Thorax	SPH	Z: Flexion-Extension X: Lateral-Medial rotation Y: Axial rotation
RSterClav	R. Sternoclavicular Joint	Thorax Clavicle	SPH	Y: Retraction-Protraction Z: Elevation-Depression X: Axial rotation
RAcroClav	R. Acromioclavicular Joint	Clavicle Scapula	SPH	Y: Retraction-Protraction Z: Lateral-Medial rotation X: Anterior-Posterior tilt
RScapThor	R. Scapulothoracic Joint	Scapula Thorax	STJ	-
RGlenHum	R. Glenohumeral Joint	Scapula Upper arm	SPH	X: Flexion-Extension Z: Abduction-Adduction Y: Axial rotation
RElbow	R. Elbow Joint	Upper arm Forearm	UNI	Flexion-Extension Pronation-Supination
RWrist	R. Wrist Joint	Forearm Hand	UNI	Flexion-Extension Abduction-Adduction
LSterClav	L. Sternoclavicular Joint	Thorax Clavicle	SPH	Y: Retraction-Protraction Z: Elevation-Depression X: Axial rotation
LAcroClav	L. Acromioclavicular Joint	Clavicle Scapula	SPH	Y: Retraction-Protraction Z: Lateral-Medial rotation X: Anterior-Posterior tilt
LScapThor	L. Scapulothoracic Joint	Scapula Thorax	STJ	-
LGlenHum	L. Glenohumeral Joint	Scapula Upper arm	SPH	X: Flexion-Extension Z: Abduction-Adduction Y: Axial rotation
LElbow	L. Elbow Joint	Upper arm Forearm	UNI	Flexion-Extension Pronation-Supination
LWrist	L. Wrist Joint	Forearm Hand	UNI	Flexion-Extension Abduction-Adduction

Table 3.9: Joint rotation sequences for UBMS.

3.3.2 UPPER BODY MODEL WITHOUT SCAPULA

Similarly to UBMS, the upper body model without scapula (UBM) has been used to study steering manoeuvres. The only difference between both models is located at the shoulder complex model. UBM considers a simplified model of the shoulder complex in which the scapula is not included. Then, the thorax is connected to the humerus through a single body segment equivalent to clavicle and scapula. This body segment is called ClSc and connects the sternoclavicular joint with the glenohumeral joint.

All definitions, methods and conventions presented for UBMS are valid for UBM. In this section, only the new body segment ClSc, and its relation with the thorax and humerus is described. The same ALs presented in Table 3.1 are required for UBM.

3.3.2.1 Body segments

UBM includes the pelvis, thorax, right and left ClSc, upper arms, forearms, and hands (Figure 3.21). All the body segments are considered as rigid bodies with constant BSPs.

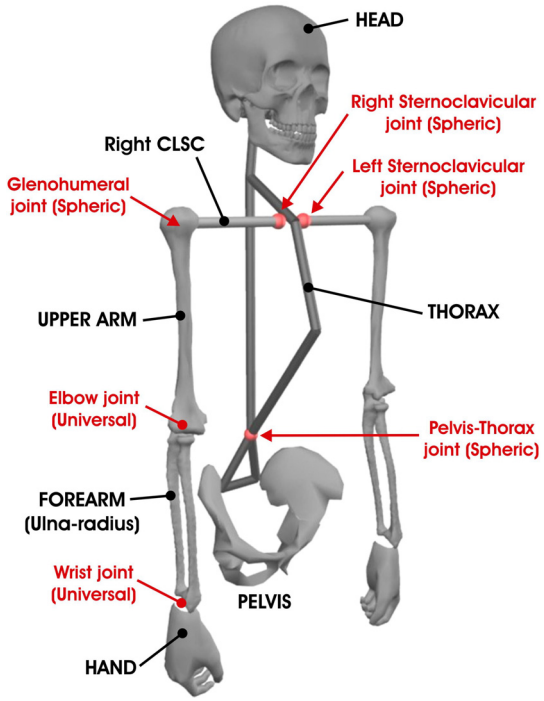

Figure 3.21: Upper body model without scapula.

3.3.2.1.1 Local coordinate systems

The LCSs of each body segment are defined taking into account the recommendations of the ISB (see section 3.3.1.1.1). The definition of the LCS of left and right ClSc are presented in Table 3.10, Figure 3.22 and Figure 3.23.

Body segment	Local coordinate system definition	
Right ClSc	Origin	RSC (L6)
	X_{ClSc}	The line connecting RSC (L6) and RGHJC (L25), pointing to L25.
	Z_{ClSc}	The line perpendicular to X_{ClSc}-axis and Y_{Thor}-axis, pointing backward.
	Y_{ClSc}	The common line perpendicular to the X_{ClSc}- and Z_{ClSc}-axis
Left ClSc	Origin	LSC (L5)
	X_{CSc}	The line connecting LGHJC (L12) and LSC (L5), pointing to LSC.
	Z_{ClSc}	The line perpendicular to X_{ClSc}-axis and Y_{Thor}-axis, pointing backward.
	Y_{ClSc}	The common line perpendicular to the X_{ClSc}- and Z_{ClSc}-axis.

Table 3.10: Definition of right and left ClSc LCSs.

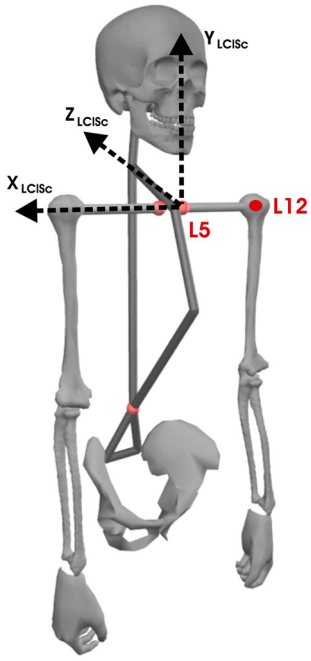

Figure 3.22: Left ClSc LCS

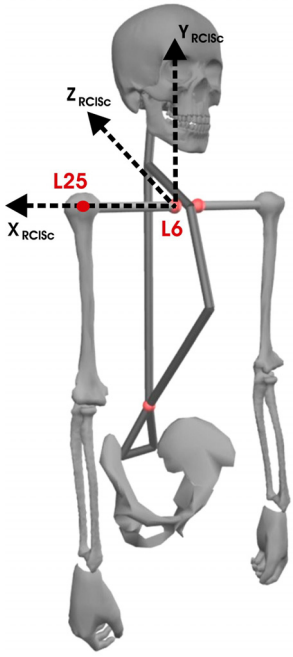

Figure 3.23: Right ClSc LCS

3.3.2.1.2 Body segment parameters

The same two methods for estimating BSPs of the UBMS model are used for the UBM model (see section 3.3.1.1.2). The influence of BSPs of ClSc is considered small comparing to other body segments and it is neglected.

3.3.2.2 Joint parameters and joint rotation order

UBM considers the sternoclavicular, glenohumeral, elbow, wrist and thorax-pelvis joints. The body segment ClSc connects the thorax with the humerus. Similarly to UBMS, the joint between the thorax and ClSc is named sternoclavicular joint and is modelled as a spherical joint. The joint between ClSc and humerus is called glenohumeral joint and is modelled as a spherical joint. Joint parameters for these two joints are estimated using the methods already mentioned for UBMS.

Joint rotation sequences are defined taking into account the ISB recommendations as close as possible (see section 3.3.1.2). Joint rotation sequences for the sternoclavicular and glenohumeral joints of UBM (Table 3.11) follow the same conventions as for UBMS.

Acronym	Joint Name	Base Follower	Joint Type	Joint rotation sequence
RSterClav	R. Sternoclavicular Joint	Thorax ClSc	SPH	Y: Retraction-Protraction Z: Elevation-Depression X: Axial rotation
RGlenHum	R. Glenohumeral Joint	ClSc Upper arm	SPH	X: Flexion-Extension Z: Abduction-Adduction Y: Axial rotation
LSterClav	L. Sternoclavicular Joint	Thorax ClSc	SPH	Y: Retraction-Protraction Z: Elevation-Depression X: Axial rotation
LGlenHum	L. Glenohumeral Joint	ClSc Upper arm	SPH	X: Flexion-Extension Z: Abduction-Adduction Y: Axial rotation

Table 3.11: Joint rotation sequences of the sternoclavicular and acromioclavicular joints of UBM. The remaining joint rotation sequences of UBM can be found in Table 3.9.

3.3.3 LOWER LIMB MODEL

The lower limb model has been used to study braking manoeuvres. The model is based on the use of ALs for estimating joint parameters and BSPs, and for defining the LCSs of each body segment. Table 3.12 summarises the ALs (see

section B.1 of Appendix B for a detailed description) required for the lower limb model.

Number	Acronym	Body segment	Name	Origin
L33	LPSIS	Pelvis	Left posterior superior iliac spine	J/L
L34	RPSIS	Pelvis	Right posterior superior iliac spine	J/L
L35	LASIS	Pelvis	Left anterior superior iliac spine	J/L
L36	RASIS	Pelvis	Right anterior superior iliac spine	J/L
L37	PS	Pelvis	Pubic symphysis	J
L38*	RHJC*	Pelvis R. Thigh	Right hip joint centre	B/L
L39	RLEF	R. Thigh	Right lateral epicondyle of the femur	J/L
L40	RMEF	R. Thigh	Right medial epicondyle of the femur	J/L
L41*	RKJC*	R. Thigh R. Shank	Right knee joint centre	B
L42	RLC	R. Shank	Right lateral condyle of tibia	L
L43	RMC	R. Shank	Right medial condyle of tibia	L
L44	RLM	R. Shank	Right lateral malleolus	J/L
L45	RMM	R. Shank	Right medial malleolus	J/L
L46*	RAJC*	R. Shank R. Foot	Right ankle joint centre	B/L
L47	RHEEL	R. Foot	Right pterion or pternion	B
L48	RTTIP	R. Foot	Right acropodion	B
L49	OMPH	Thorax Pelvis	Omphalion or navel	B
L50*	LV3*	Thorax Pelvis	3rd lumbar vertebra	J

Table 3.12: ALs of the lower limb model. 'Origin' defines the purpose of the ALs: J- joint parameters estimation, B- BSPs estimation, L- local coordinate system definition. *Joint rotation centres estimated from ALs. They cannot be found by palpation.

3.3.3.1 Body segments

The lower limb model includes the pelvis, right thigh, right shank and right foot (Figure 3.24). If the soft tissue motion is neglected, the pelvis and thigh can be approximated by rigid bodies but some concerns arise for the shank and foot because they are composed by more than one bone.

The shank is composed of two bones, the fibula and tibia connected in a highly rigid way that does not permit the relative motion between them. Then, the two bones can be considered as a single rigid body segment.

The skeleton of the foot is subdivided into three bone groups: the tarsal bones (7 bones), metatarsal bones (5 bones), and the phalanges (14 bones).

During braking manoeuvres the foot is inside a shoe which is in contact with the brake pedal. It is assumed that the relative motion between the foot bones is small due to the type and range of motion investigated, and therefore the foot is modelled as a rigid body.

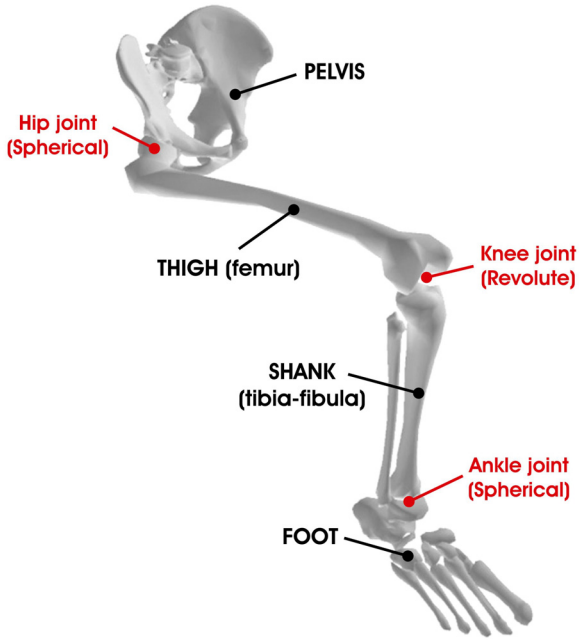

Figure 3.24: Lower limb model.

3.3.3.1.1 *Local coordinate systems*

The LCSs of each body segment of lower limb model are defined according to the ISB recommendations (Wu et al., 2002). They are presented in Table 3.14 to Table 3.13 and in Figure 3.25 to Figure 3.26.

Joint rotation	Definition of neutral configuration
Neutral dorsiflexion/plantarflexion	Zero degrees between the long axis of the tibia/fibula and the line perpendicular to the plantar aspect of the foot projected onto the sagittal plane of the tibia/fibula
Neutral inversion/eversion	Zero degrees between the long axis of the tibia/fibula and the line perpendicular to the plantar aspect of the foot projected onto the frontal plane of the tibia/fibula.
Neutral internal/external rotation	Zero degrees between the line perpendicular to the frontal plane of the tibia/fibula and the long axis of the 2nd metatarsal, projected onto the transverse plane of the tibia/fibula.

Table 3.13: Definition of the neutral configuration of the ankle joint.

Body segment	Local coordinate system definition	
Pelvis	Origin	Midpoint between RASIS (L36) and LASIS (L35)
	Z_{Pel}	The line parallel to a line connecting the RASIS (L36) and LASIS (L35), and pointing to the right.
	X_{Pel}	The line parallel to a line lying in the plane defined by the RASIS (L36), the LASIS (L35), and the midpoint between RPSIS (L34) and LPSIS (L33), orthogonal to the Z_{Pel}-axis, and pointing anteriorly.
	Y_{Pel}	The line perpendicular to both X_{Pel}- and Z_{Pel}-axis, pointing cranially.
Right Thigh	Origin	RHJC (L38)
	Y_{Thigh}	The line connecting the midpoint between RMEF (L40) and RLEF (L39) and RHJC (L38), pointing upward (cranially).
	Z_{Thigh}	The line perpendicular to the y-axis, lying in the plane defined by RHJC (L38), RMEF (L40) and RLEF (L39), pointing to the right.
	X_{Thigh}	The common line perpendicular to the Y_{Thigh}- and Z_{Thigh}-axis.

Table 3.14: Definition of pelvis and right thigh LCSs.

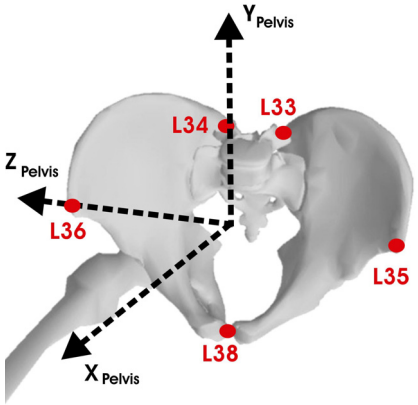

Figure 3.25: Pelvis LCS

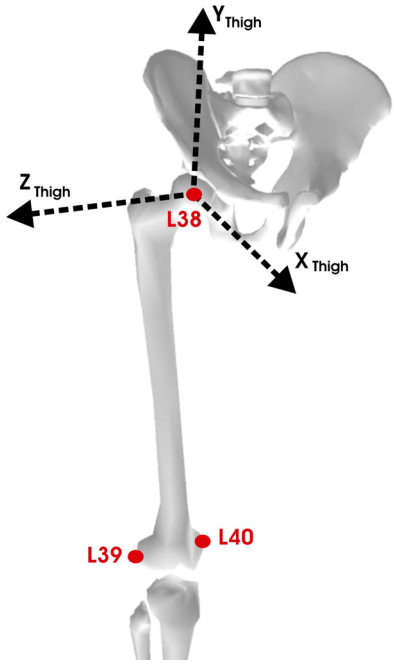

Figure 3.26: Right thigh LCS

Body segment	Local coordinate system definition	
Right Shank	Origin	RAJC (L46)
	Z_{Shank}	The line connecting RMM (L45) and RLM (L44), pointing to the right (laterally).
	X_{Shank}	The line perpendicular to the plane formed by RMM (L45), RLM (L44) and the midpoint between RLC (L42) and RMC (L43), pointing anteriorly.
	Y_{Shank}	The common line perpendicular to the X_{Shank}- and Z_{Shank}-axis.
Right Foot	Origin	RAJC (L46)
	Y_{Foot}	The line coincident with the Y_{Shank}-axis in the neutral configuration (Table 3.13) of the ankle joint.
	X_{Foot}	The line coincident with the X_{Shank}-axis in the neutral configuration (Table 3.13) of the ankle joint.
	Z_{Foot}	The common line perpendicular to the X_{Foot}- and Y_{Foot}-axis.

Table 3.15: Definition of right shank and right foot LCSs.

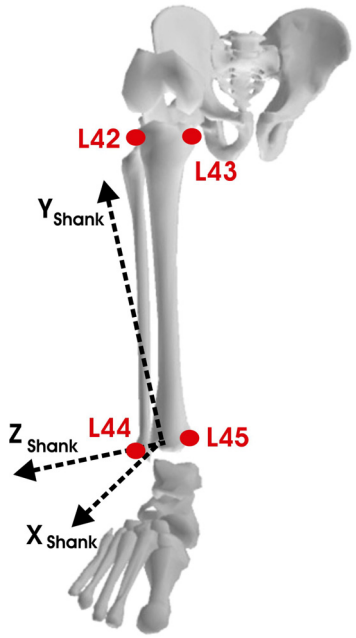

Figure 3.27: Right shank LCS

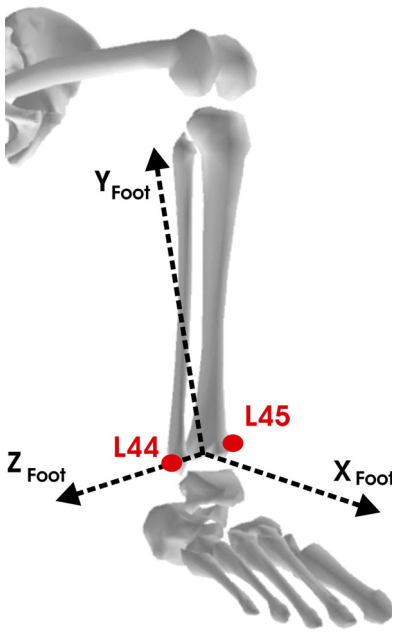

Figure 3.28: Right foot LCS

3.3.3.1.2 Body segment parameters

The same two methods for estimating BSPs of the UBMS model are used for the lower limb model (see section 3.3.1.1.2).

3.3.3.2 Joint parameters and joint rotation order

The lower limb model includes the hip, knee and ankle joints. The hip joint (HJ) is modelled as a spherical joint (Delp et al., 1990; Benedetti et al., 1998; Anderson and Pandy, 1999), whose joint rotation centre is estimated using the regression method of Seidel et al. (1995) (see section 2.1.11).

The knee joint (KJ) is modelled as a revolute joint (Delp et al., 1990; Anderson and Pandy, 1999), whose joint centre is approximated by the midpoint between the lateral and medial epicondyles of the femur. The revolute knee joint axis is approximated by the line connecting the lateral and medial epicondyles of the femur (see section 2.1.12).

The ankle joint complex (AJ) is modelled as a spherical joint (Moseley et al., 1996; Benedetti et al., 1998; Frigo and Rabuffetti, 1998; Vaughan et al., 1999), whose joint rotation centre is approximated by the midpoint between the lateral and medial malleolus (see section 2.1.13).

Table 3.16 summarises the methods selected for estimating joint parameters of the lower limb model in the MoDyCo project.

Joint name	Joint type	Joint parameter methods
Hip joint	SPH	Seidel et al. (1995) method (section 2.1.11)
Knee joint	REV	Joint centre: Midpoint between RLEF (L39) and RMEF (L40). Joint axis: The line connecting RMEF (L40) and RLEF (L39), pointing laterally.
Ankle joint complex	SPH	Midpoint between RLM (L44) and RMM (L45)

Table 3.16: Methods selected for estimating the joint parameters of the lower limb model.

The relative rotation between two body segments is described using Euler angles. Joint rotation sequences are defined according to ISB recommendations of the hip, knee and ankle joints (Wu et al., 2002). Table 3.17 summarises joint rotation sequences for the lower limb model.

Acronym	Joint Name	Base Follower	Joint Type	Rotation Order
RHip	Right Hip Joint	Pelvis Thigh	SPH	Z: Flexion-Extension X: Adduction-Abduction Y: Internal-External rotation
RKnee	Right Knee Joint	Thigh/Shank	REV	Flexion-Extension
Rankle	Right Ankle Joint	Shank Foot	SPH	Z: Dorsiflexion-Plantarflexion X: Inversion-Eversion Y: Internal-External rotation

Table 3.17: Joint rotation sequences for the lower limb model.

3.4 RAMSIS WHOLE BODY MODEL

The development of the RAMSIS whole body model (www.human-solutions.com) started in 1988 and was a collective project between the automotive industry (Audi, BMW, Ford, Mercedes-Benz, Opel, Porsche, and Volkswagen), car seats manufacturers (Keiper-Recaro and Naue/Johnson Controls), Human Solutions GmbH (formerly Tecmath AG), Universität Eichstädt, and the Lehrstuhl für Ergonomie at the Technische Universität München. RAMSIS was developed with the aim of creating a CAD tool for the ergonomic design of vehicle interiors and cockpits.

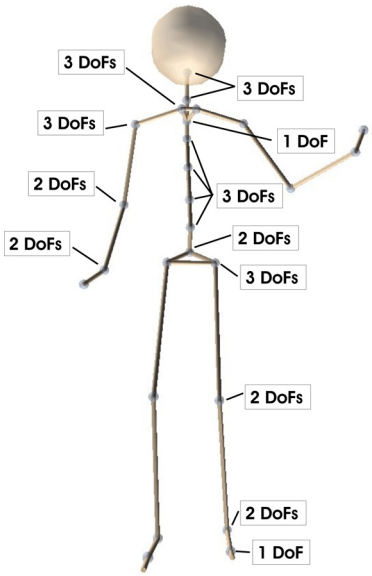

Figure 3.29: RAMSIS internal model.

Figure 3.30: RAMSIS external model.

The structure of the RAMSIS whole body model is divided into an internal model or kinematic model (Figure 3.29) and an external model or skin model (Figure 3.30). The kinematic model includes 25 body segments:

- The spine is modelled with 6 body segments: upper cervical vertebrae, lower cervical vertebrae, upper thoracic vertebrae, lower thoracic vertebrae, upper lumbar vertebrae and lower lumbar vertebrae.
- The shoulder complex is modelled with a simplified model similar to UBM, in which the thorax and humerus are connected directly through a body segment. This body segment is called clavicle although it is not a real clavicle because it connects directly the sternoclavicular and glenohumeral joints.

- The lower cervical vertebrae segment and the clavicles are connected through a body segment called chest. The joint between the chest body segment and the clavicle is called sternoclavicular joint.
- The arm is modelled with 3 body segments: the upper arm, forearm and hand.
- The leg is modelled with 4 body segments: the thigh, shank, hindfoot and toes.
- The remaining body segments are the head and pelvis.

The 25 rigid bodies are connected by 1 floating joint (3 translations and 3 rotations) between the pelvis and ground, 12 spherical joints, 9 universal joints and 3 revolute joints (Table 3.18). The model has 63 DoFs.

Joint	Type	Joint	Type
sternoclavicular	SHP	head-upper cervical vertebrae	SPH
glenohumeral	SPH	upper cervical vertebrae - lower cervical vertebrae	SPH
elbow	UNIV	lower cervical vertebrae - upper thoracic vertebrae	SPH
wrist	UNIV	upper thoracic vertebrae - lower thoracic vertebrae	SPH
hip	SPH	lower thoracic vertebrae - upper lumbar vertebrae	SPH
knee	UNIV	upper lumbar vertebrae - lower lumbar vertebrae	SPH
ankle	UNIV	lower lumbar vertebrae-pelvis	UNIV
hindfoot-toes	REV	lower cervical vertebrae-chest	REV

Table 3.18: Joints of the RAMSIS model.

CHAPTER 4

MOTION RECONSTRUCTION

In this chapter, a new motion reconstruction method for estimating the joint angles of a human skeletal model from motion capture data is proposed. The new method, called Optimal Tracking Method (OTM), is valid for open- and closed-loop multibody systems modelled with natural coordinates. Furthermore, new strategies are proposed for dealing with the missing marker problem and for the approximate estimation of the motion of those bones, whose movement cannot be measured completely using optoelectronic motion capture systems. These new strategies enable a more robust reconstruction of the human movement.

The human skeletal models are modelled with natural coordinates using a multibody system approach. The constraint equations that define a multibody model using natural coordinates are a key feature of OTM. Therefore, a brief description of the constraint equations originated from natural coordinates is presented in section 4.1.

The problem of obtaining the position and orientation of each body segment or the joint angles of a human skeletal model starting from motion capture data is usually called *Inverse Kinematic problem* or *Motion Reconstruction problem*. As opposed to the Inverse Kinematic problem, a *Forward Kinematic problem* consists in calculating the configuration of the model given all the joint angles. This classification of kinematic problems is common in Robotics and Computer Animation where relative coordinates are used to define the models (Zhao and Badler, 1994; Tolani et al., 2000; Rubí, 2002; Baerlocher and Boulic, 2004). When natural coordinates and a global formalism are used, the kinematic problem has always a similar structure, independently of the multibody topology (open- or closed-loop) or the type of problem to solve

(forward or inverse). Consequently, in this chapter the problem of obtaining joint angles of a human skeletal model from motion capture data is referred to simply as the kinematic problem or motion reconstruction problem. In section 4.2, the structure of the kinematic problem obtained from a multibody system modelled with natural coordinates is presented. The solution of the kinematic problem is proposed using an optimisation approach. Furthermore, a classification of kinematic problems according to the number of degrees of freedom and the number of guided coordinates is presented.

The state-of-the-art of mathematical methods for estimating joint angles from motion capture data is reviewed in section 4.3. Moreover, other issues related to joint angle estimation from motion capture data are also reviewed. In section 4.4 the available optimisation methods for solving the particular kinematic problem proposed in section 4.2 are reviewed.

OTM is presented in section 4.5 and some of its main features are discussed. In section 4.6, a weighted OTM is proposed and several strategies for dealing with the missing marker problem and handling the lack of motion data for some body segments are discussed. These strategies take advantage of the especial structure of the weighted OTM. Finally, in section 4.7 the relationship between OTM and the Sequential Quadratic Programming method is shown.

4.1 MULTIBODY SYSTEMS

A multibody approach is used to model human skeletal systems in this thesis. In the following subsections a brief introduction to the subject is presented.

A multibody system can be defined as an assembly of two or more rigid bodies interconnected by joints (or kinematic pairs) which permit certain degrees of freedom (DoFs) of relative motion and restrict others. The most common joints are revolute, prismatic, cylindrical, spherical and universal. Bodies can be connected via force transmission elements (springs, shock absorbers or dampers) and/or acted upon by external applied forces. The relative motion between rigid bodies can be prescribed using driving actuators.

Multibody systems are classified as open-loop or closed-loop systems. If a system is composed of bodies without closed branches (or loops), then it is called an open-loop system; otherwise, it is called a closed-loop system. For example, a double pendulum is an open-loop system (Figure 4.1) and a four-bar articulated quadrilateral (Figure 4.2) is a closed-loop system.

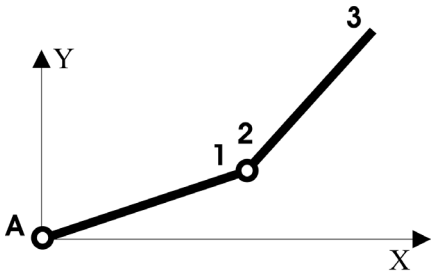

Figure 4.1: An open-loop multibody system (double pendulum).

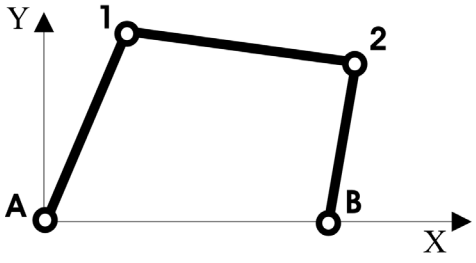

Figure 4.2: A closed-loop multibody system (four-bar articulated quadrilateral).

4.1.1 COORDINATES

A multibody system can be described with different types of coordinates. An adequate set of coordinates must allow to define unequivocally the position, velocity and acceleration of the multibody. It is important to choose the most appropriate type of coordinates to our problem because different types of coordinates lead to different computational efficiency and simplicity of implementation.

A system of coordinates can be classified into dependent coordinates and independent coordinates. The number of *independent coordinates* that describe a multibody system coincides with its number of DoFs. This means that the number of independent coordinates required to describe the multibody system is minimal. However, studies tend to conclude that independent coordinates are not a suitable solution for a general purpose analysis because they do not define unequivocally the position of the multibody system (García de Jalón and Bayo, 1994).

Dependent coordinates can describe the position of a multibody system unequivocally but its number is greater than the number of DoFs. Therefore, these coordinates are not independent but interrelated through certain equations known as *constraint equations*. The number of constraint equations is equal to the difference between the number of dependent coordinates and the number of DoFs. Three major types of dependent coordinates have been proposed in the literature: relative coordinates, reference point coordinates (also called Cartesian coordinates), and natural coordinates (also called fully Cartesian coordinates). The three types of coordinates have both advantages and drawbacks (García de Jalón and Bayo, 1994).

Natural coordinates have been used throughout this work. They were originally introduced by García de Jalón et al. (1981) and Serna et al. (1982) for

planar cases, and García de Jalón et al. (1986; 1987) for spatial systems. *Natural coordinates* describe the position and orientation of bodies through the Cartesian components of points and vectors located at the mechanism joints. Natural coordinates are used because of some advantages that are presented in the following sections.

As it is explained in section 4.2.2.3 some kinematic problems require relative coordinates to define appropriately the problem. Natural coordinates do not include relative coordinates but mixed coordinates can solve this problem. If angular or linear relative coordinates corresponding to the DoFs of the system joints are added to the natural coordinates describing the multibody system, *mixed coordinates* are obtained. The same number of relative coordinates and constraint equations must be added if the number of DoFs is not modified. The constraint equations arising from relative coordinates are called relative coordinate constraints throughout this text.

4.1.2 CONSTRAINT EQUATIONS

Dependent coordinates are related by algebraic constraint equations in a number equal to the difference between the number of dependent coordinates and the number of DoFs. Different types of dependent coordinates lead to different constraint equations. Constraint equations are generally nonlinear and play the main role in the kinematic and dynamic analysis of multibody systems.

When modelling a multibody system with natural coordinates there are four types of constraint equations to be considered: *rigid body constraints* that originate from the rigid body conditions for each element; *joint constraints* that originate from the kinematic pairs; *relative coordinate constraints* that originate from the additional relative coordinates added to natural coordinates; and *driving constraints* that are used to prescribe the motion of the multibody system. In this thesis, rigid body constraints, joint constraints and relative coordinate constraints are referred to as *kinematic constraints*.

Two simple examples modelled with natural coordinates (Figure 4.3) and mixed coordinates (Figure 4.4) are presented to illustrate the different constraint equations.

The double pendulum in Figure 4.3 is modelled with natural coordinates, i.e. with the Cartesian coordinates of points 1, 2 and 3 (point A is fixed). Points A and 1 define the first bar and points 2 and 3 define the second bar of the double pendulum. The double pendulum is modelled with six dependent coordinates (x_1, y_1, x_2, y_2, x_3, y_3) and it has two DoFs. Therefore, there must be four kinematic constraints. Two kinematic constraints arise from imposing a

constant distance condition between points A and 1, and 2 and 3. These are rigid body constraints:

$$\begin{aligned}(x_1 - x_A)^2 + (y_1 - y_A)^2 - L_{A1}^2 = 0\\ (x_3 - x_2)^2 + (y_3 - y_2)^2 - L_{23}^2 = 0\end{aligned} \tag{4.1}$$

where L_{A1} and L_{23} are the lengths of bar A1 and bar 23 respectively. Two other constraints arise from imposing the condition that point 1 and point 2 must remain together during the motion. These are joint constraints:

$$\begin{aligned}x_1 - x_2 = 0\\ y_1 - y_2 = 0\end{aligned} \tag{4.2}$$

Points 1 and 2 are included in this example in order to illustrate joint constraints. However, constraints (4.2) are not included in practical implementations. Instead points 1 and 2 are considered as a single point and equations (4.2) are automatically satisfied.

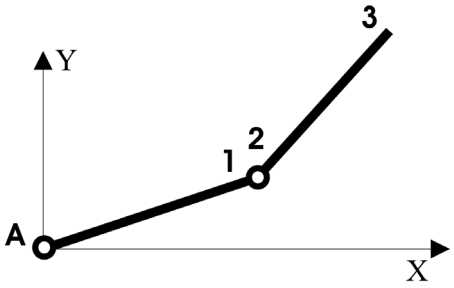

Figure 4.3: Double pendulum modelled with natural coordinates.

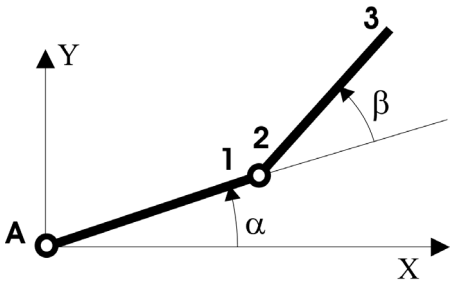

Figure 4.4: Double pendulum modelled with mixed coordinates.

This multibody system has six dependent coordinates, four kinematic constraints and two DoFs. In order to determine the position of the multibody system the value of the two DoFs must be prescribed. The motion of the multibody can be defined with two additional driving constraints. If the dependent coordinates $x1$ and $x3$ are chosen as DoFs, and $f(t)$ and $g(t)$ are two given functions of time, the driving constraints can be formulated as follows

$$\begin{aligned}x_1 - f(t) = 0\\ x_3 - g(t) = 0\end{aligned} \tag{4.3}$$

The dependent coordinates whose motion is prescribed by driving constraints are called *driven coordinates*. For a given value of time, the six

dependent coordinates can be obtained from the solution of the six previous nonlinear constraint equations (equations (4.1), (4.2) and (4.3)).

Another option for imposing the value of the two DoFs is to remove the two variables chosen as DoFs from the unknown variables and substitute their value directly in the four kinematic constraints (equations (4.1) and (4.2)). Then, four equations in four unknowns are obtained. This last option seems to be better than using driving constraints, however, there are situations where the driving constraints are useful as it is explained in section 4.2.

The double pendulum in Figure 4.4 is modelled with mixed coordinates, i.e. with the Cartesian coordinates of points 1, 2 and 3; and the relative coordinates α and β. There are eight dependent coordinates (x_1, y_1, x_2, y_2, x_3, y_3, α, β) and the mechanism has two DoFs. Therefore, two additional kinematic constraints coming from the two relative coordinates must be added to the six kinematic constraints of the previous example. The two additional relative coordinate constraints originate from the scalar product of vectors V_x and V_{A1}, and V_{A1} and V_{23} respectively. These vectors are defined as follows

$$V_x = \begin{bmatrix} 1 \\ 0 \end{bmatrix}, \quad V_{A1} = \begin{bmatrix} x_1 - x_A \\ y_1 - y_A \end{bmatrix}, \quad V_{23} = \begin{bmatrix} x_3 - x_2 \\ y_3 - y_2 \end{bmatrix} \tag{4.4}$$

The two relative coordinate constraints can be written as follows

$$\begin{aligned} (x_1 - x_A) - L_{A1}\cos(\alpha) &= 0 \\ (x_1 - x_A)(x_3 - x_2) + (y_1 - y_A)(y_3 - y_2) - L_{A1}L_{23}\cos(\beta) &= 0 \end{aligned} \tag{4.5}$$

An advantage of natural coordinates is that rigid body constraints, joint constraints and driving constraints are always quadratic or linear. Mixed coordinates include more complex equations because relative coordinate constraints involve transcendental functions.

In this thesis, the human movement of a subject is measured with a motion capture system using markers and the measured marker coordinates are used to prescribe the motion of the multibody model. The following example shows how markers can be added to a multibody model and how the motion of the model can be prescribed with the measured marker coordinates.

Consider the double pendulum of Figure 4.3 and suppose that one marker is added to each bar (Figure 4.5). One point representing each marker is added to each bar and the associated rigid body constraints must be included in the kinematic constraints of the model. The rigid body constraints for marker M1 are

$$
\begin{aligned}
(x_{M1} - x_A)^2 + (y_{M1} - y_A)^2 - L_{AM1}^2 = 0 \\
(x_{M1} - x_2)^2 + (y_{M1} - y_2)^2 - L_{2M1}^2 = 0
\end{aligned}
\tag{4.6}
$$

The rigid body constraints for marker M2 are

$$
\begin{aligned}
(x_{M2} - x_2)^2 + (y_{M2} - y_2)^2 - L_{2M2}^2 = 0 \\
(x_{M2} - x_3)^2 + (y_{M2} - y_3)^2 - L_{3M2}^2 = 0
\end{aligned}
\tag{4.7}
$$

The variables L_{AM1}, L_{2M1}, L_{2M2} and L_{3M2} are the constant lengths between point A and M1, 2 and M1, 2 and M2, and 3 and M2 respectively. These lengths are usually estimated in a static posture and depend on the location of the markers on each body segment. The kinematic constraints (4.6) and (4.7) are used in this example only for illustrative purposes. However, in practical implementations linear constraints equations are generally used to include the markers in the model.

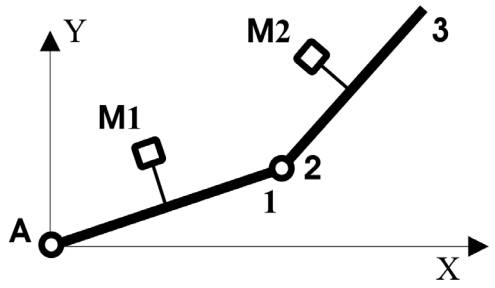

Figure 4.5: Double pendulum with 2 markers modelled with natural coordinates.

The double pendulum of Figure 4.5 is defined by kinematic constraints (4.1), (4.2), (4.6) and (4.7). This multibody model has ten dependent coordinates (x_1, y_1, x_2, y_2, x_3, y_3, x_{M1}, y_{M1}, x_{M2}, y_{M2}), eight kinematic constraints and two DoFs.

In order to determine the position of the multibody system the value of the two DoFs must be prescribed. When motion capture data are used to define the motion of a multibody system, the data available to prescribe the motion are the measured global coordinates of the markers. For the double pendulum of Figure 4.5 four driving constraints can be formulated:

$$
\begin{aligned}
x_{M1} - x_{M1}(t) = 0 \\
y_{M1} - y_{M1}(t) = 0
\end{aligned}
\tag{4.8}
$$

$$\begin{aligned} x_{M2} - x_{M2}(t) &= 0 \\ y_{M2} - y_{M2}(t) &= 0 \end{aligned} \tag{4.9}$$

where x_{M1}, y_{M1}, x_{M2} and y_{M2} are the Cartesian coordinates of the points representing the markers in the multibody model and $x_{M1}(t)$, $y_{M1}(t)$, $x_{M2}(t)$ and $y_{M2}(t)$ are the measured global coordinates of the markers. The first are sometimes referred to as *model-determined marker coordinates* and the second as *measured marker coordinates*.

This multibody system has ten dependent coordinates, eight kinematic constraints and four driving constraints, i.e. ten unknowns and twelve equations. The problem is overdetermined because there are more equations than unknowns. Note that the values of the driven coordinates x_{M1}, y_{M1}, x_{M2} and y_{M2} may be or may not be *consistent* with the kinematic constraints of the multibody system due to measurement errors of the motion capture system. This means that if the values of the driven coordinates are substituted in the kinematic constraints, they can (consistent values) or cannot satisfy the kinematic constraints (non-consistent values). In section 4.3, the mathematical methods proposed in the literature to solve this type of problems are reviewed.

4.1.2.1 Redundant kinematic constraints

In the previous section it has been shown that a multibody system with s DoFs can be described with n dependent coordinates and m $(= n - s)$ independent kinematic constraints. In practice, there are situations where an excess of kinematic constraints is obtained. This means that some of the kinematic constraints are not independent from the remaining ones. The kinematic constraints that are not independent are called *redundant constraint equations*. If a multibody system is described with $m > n - s$ kinematic constraints, which must be consistent, there must be $l = m - (n - s)$ redundant constraint equations.

There are two ways in which redundant constraint equations arise (García de Jalón and Bayo, 1994):

1. Due to convenience of implementation. For example, instead of switching between the kinematic constraints coming from the dot product or the cross product when the angle is close to 0º/180º or ±90º respectively, both kinematic constraints can be included (see example A.1 in Appendix A).
2. In over-constrained multibody systems that are exceptions to the Grübler criterion.

In this thesis, due to the human skeletal models considered and the implementation used, only the first type of redundant constraint equations arises. Redundant constraints are only associated with relative coordinate constraints. Therefore, when natural coordinates are used, there are not redundant constraints in the problem and when mixed coordinates are used, redundant constraints appear in the kinematic constraints.

4.2 KINEMATIC ANALYSIS FOR MOTION RECONSTRUCTION

Kinematic analysis studies the motion of a multibody system independently of the forces and reactions that generate it. Kinematic problems are problems of a purely geometrical nature. Therefore, they can be solved independently not only of the forces and reactions but also of the inertial properties of the bodies.

To perform a kinematic analysis the motion of the multibody system must be prescribed. The motion of some dependent coordinates, called driven coordinates, must be prescribed and this can be done using driving constraints as it is explained in section 4.1.2. When an optoelectronic motion capture system is used to record the human motion using markers, the driven coordinates are the marker coordinates of the model.

In general, any dependent coordinate of the model can be selected as a driven coordinate. For example, an electromagnetic motion capture system gives the position and orientation of each electromagnetic sensor located on the human body. The orientation of a sensor can be defined with the global coordinates of three unitary vectors that define the sensor local coordinate system. Then, these measured global vector coordinates can be use to prescribe the motion of three vectors of the model.

The set of m kinematic constraints (rigid body constraints, joint constraints and relative coordinate constraints) can be expressed in matrix form as follows:

$$\mathbf{\Phi(q)} = 0 \tag{4.10}$$

where $\mathbf{q}$ is the column vector of n dependent coordinates and each element $\phi_i(\mathbf{q})$ is a constraint equation. The r driven coordinates are a subset of $\mathbf{q}$ and they can be expressed in matrix form as follows.

$$\mathbf{z} = \mathbf{Sq} \tag{4.11}$$

where $\mathbf{z}$ is the column vector of r driven coordinates. $\mathbf{S}$ is an $r \times n$ matrix and the elements of its i-th row are all zero except the one corresponding to the

coordinate of **q** selected as the *i*-th driven coordinate. The set of *r* driving constraints can be expressed in matrix form as follows:

$$\Psi(\mathbf{q}, t) = \mathbf{S}\mathbf{q} - \mathbf{d}(t) = 0 \tag{4.12}$$

where **d** is a column vector of size $r \times 1$ whose *i*-th element is a given function of time $g_i(t)$ that gives the value of corresponding driven coordinate.

In this thesis, only the initial position problem and the finite displacement problem are considered. The initial position problem consists in determining **q**, given the value of the driven coordinates. The finite displacement problem consists in finding **q**, given an initial estimate of the multibody position consistent with the kinematic constraints and a known finite displacement for the driven coordinates. The finite displacement problem is easier to solve because the initial position of the multibody is known and the mathematical methods can use it to solve the problem more efficiently.

Fortunately, in the MoDyCo project a good initial approximation for the initial position problem can be estimated using the method of Söderkvist (1993) provided that each body segment has three markers (see section 4.3.3.2). For bodies with less than three markers a good initial approximation can also be obtained from the markers on the body segment and the data obtained from the adjacent bodies. In general, the estimated initial approximation for the initial position problem is not consistent with the kinematic constraints. In the REALMAN project, the software PCMAN (section 2.1.15.2) provides an initial approximation for the initial position problem consistent with the kinematic constraints. The quality of the initial approximation of PCMAN depends on how close the calibration posture is to the initial position of the subject during the recorded motion.

The goal of the kinematic analysis is to calculate the joint angles of a human skeletal model, given the global marker coordinates measured by the motion capture system at each frame. This means that an initial position problem with a good initial approximation must be solved the first frame and a repetition of finite displacement problems the following frames. The solution of the initial position problem or the finite displacement problem is always obtained from the nonlinear kinematic constraints (4.10) and the linear driving constraints (4.12) that describe the multibody system. Mathematical methods required to solve the equations (4.10) and (4.12) are presented in section 4.2.2.

The solution of the kinematic problem is **q**, which contains coordinates of points and vectors of the model. Joint angles can be calculated easily from the points and vectors of the model. Joint angles can also be included in **q** and their value obtained directly from the solution of the kinematic problem. This

second option is less efficient for the type of kinematic problems studied in this thesis and is not considered. Nevertheless, for one type of the kinematic problems considered (section 4.2.2.3) a few joint angles must be included in $\mathbf{q}$ in order to define the problem properly.

4.2.1 CLASSIFICATION OF KINEMATIC PROBLEMS ACCORDING TO THE NUMBER OF EFFECTIVELY DRIVEN DREGREES OF FREEDOM

In a generic kinematic problem there are m kinematic constraints (Φ), n dependent coordinates ($\mathbf{q}$), r driving constraints (Ψ) or equivalently r driven coordinates, and s DoFs. The kinematic problems can be classified into three groups according to the following two definitions:

- An *effectively driven DoF* can be defined as a degree of freedom whose value can be calculated directly from the given data.
- A *driven coordinate* can be defined as a coordinate whose motion is prescribed for instance through a driving constraint.

Then, according to these two definitions three different types of kinematic problems can be defined:

1. *Exactly-guided kinematic problem*, when the number of effectively driven DoFs (u) is equal to the number of DoFs of the multibody system and equal to the number of driven coordinates ($u = s = r$).
2. *Over-guided kinematic problem*, when the number of effectively driven DoFs is equal to the number of DoFs of the multibody system but the number of driven coordinates is greater than the number of DoFs ($u = s < r$). The values of the driven coordinates may be or may not be consistent with the kinematic constraints of the multibody system.
3. *Under-guided kinematic problem*, when the number of effectively driven DoFs is less than the number of DoFs of the multibody system ($u < s$). The number of driven coordinates can be less, equal or greater than the number of DoFs ($r < s$, $r = s$, $r > s$).

To illustrate these three types of kinematic problems the double pendulum of Figure 4.4 is used:

1. If the coordinates α and β are chosen as driven coordinates the two DoFs of the multibody are effectively guided and the number of

driven coordinates is equal to the number of DoFs. This is an exactly-guided kinematic problem.

2. If the coordinates x_1, y_1, x_3 and y_3 are chosen as driven coordinates the two DoFs of the multibody are effectively guided because the position of the mechanism is unequivocally defined but there are more driven coordinates than DoFs. This is an over-guided kinematic problem. The values of the driven coordinates may be or may not be consistent with the kinematic constraints.
3. There are three possible cases for an under-guided kinematic problem:

   3a. When $r > s$. If the coordinates x_1, y_1 and α are chosen as driven coordinates, only one DoF of the multibody system is prescribed. The position of the bar 23 is not defined. There are 3 driven coordinates and the system has two DoFs but there is only one effectively driven DoF.

   3b. When $r = s$. If the coordinates x_1 and y_1 are chosen as driven coordinates, only one DoF is prescribed. There are 2 driven coordinates and the multibody system has two DoFs but only one DoF is effectively driven.

   3c. When $r < s$. If the coordinate α is chosen as the driven coordinate, only one DoF is prescribed. There is one driven coordinate and the multibody system has two DoFs. Therefore, there is only one effectively driven DoF.

4.2.2 MATHEMATICAL METHODS FOR KINEMATIC PROBLEMS

There are different mathematical methods to solve each of the three types of kinematic problems defined in the previous section. A generic multibody system described by m kinematic constraints (Φ), r driving constraints (Ψ), n dependent coordinates ($\mathbf{q}$) and s DoFs is considered in the next three subsections. For each kinematic problem two cases are considered, when the kinematic constraints are independent and when they contain redundant constraint equations.

4.2.2.1 Exactly-guided kinematic problems

First, we consider that only independent kinematic constraints exist. In an exactly-guided kinematic problem, the number of effectively driven DoFs is equal to the number of DoFs of the multibody system and equal to the number

of driving constraints ($u = s = r$). Therefore, we have a nonlinear system of n equations ($n = m + r$) in n unknowns:

$$\begin{bmatrix} \Phi(\mathbf{q}) \\ \Psi(\mathbf{q},t) \end{bmatrix} = \mathbf{0} \tag{4.13}$$

This system of nonlinear equations can be solved with any method suitable for nonlinear equations (Nocedal and Wright, 1999). One possible option is the Newton-Raphson method. This method has quadratic convergence in the neighbourhood of the solution. It is based on the linearisation of the system of equations (4.13) and consists in replacing this system of equations with its expansion in a Taylor series around a certain approximation $\mathbf{q}^k$ to the desired solution. The linearised system (4.13) becomes

$$\begin{bmatrix} \Phi(\mathbf{q}) \\ \Psi(\mathbf{q}) \end{bmatrix} \cong \begin{bmatrix} \Phi(\mathbf{q}^k) \\ \Psi(\mathbf{q}^k) \end{bmatrix} + \begin{bmatrix} \Phi_{\mathbf{q}}(\mathbf{q}^k) \\ \Psi_{\mathbf{q}}(\mathbf{q}^k) \end{bmatrix} (\mathbf{q} - \mathbf{q}^k) + \ldots = 0 \tag{4.14}$$

Note that (4.14) does not depend on the time variable because the problem is solved for a given time. The time is a parameter of the equations and it is not a variable of the problem. $\Phi_{\mathbf{q}}$ is the Jacobian matrix of the kinematic constraints, i.e. the matrix of partial derivatives of the kinematic constraints with respect to the dependent coordinates. The i-th row of $\Phi_{\mathbf{q}}$ is the transposed gradient vector ($\nabla\phi_i^{\mathrm{T}}$) of the i-th kinematic constraint. Likewise, $\Psi_{\mathbf{q}}$ is the Jacobian matrix of the driving constraints.

The Jacobian matrix $\Phi_{\mathbf{q}}$ of the kinematic constraints is a linear or constant function of the natural coordinates. When mixed coordinates are considered, transcendental functions appear in the elements of the Jacobian matrix. Considering the first two terms of the Taylor series (4.14) and neglecting higher order terms, the following iterative process can be obtained:

$$\begin{bmatrix} \Phi_{\mathbf{q}}^k \\ \Psi_{\mathbf{q}}^k \end{bmatrix} \Delta\mathbf{q}^k = -\begin{bmatrix} \Phi^k \\ \Psi^k \end{bmatrix} \tag{4.15}$$

$$\mathbf{q}^{k+1} = \mathbf{q}^k + \Delta\mathbf{q}^k$$

where $\mathbf{q}^{k+1}$ is an approximation to the solution of equation (4.13). The notation $\Psi^k = \Psi(\mathbf{q}^k)$, $\Phi^k = \Phi(\mathbf{q}^k)$, etc., is used for quantities derived from $\mathbf{q}^k$. The iteration (4.15) is used repeatedly until the error in the linear system of equations is insignificant, or until the difference between the results of two successive iterations is smaller than a predefined tolerance. As mentioned

previously, a good initial approximation $\mathbf{q}^0$ for the iterative process is available both for the initial position problem and the finite displacement problem.

When redundant constraints exist in equation (4.13) the nonlinear system of equations is compatible but not all the equations are independent. The redundant constraints can induce an excess of linearly independent equations in system (4.15), and this could make the linear system of equations (4.15) overconstrained and incompatible (see example A.1 in Appendix A). A reliable algorithm to solve the redundant system of linear equations is the least-square method (Strang, 1988):

$$\left[\boldsymbol{\Phi}_{\mathbf{q}}^{k\,\mathrm{T}}\,\boldsymbol{\Phi}_{\mathbf{q}}^{k}+\boldsymbol{\Psi}_{\mathbf{q}}^{k\,\mathrm{T}}\,\boldsymbol{\Psi}_{\mathbf{q}}^{k}\right]\Delta\mathbf{q}^{k}=-\left[\boldsymbol{\Phi}_{\mathbf{q}}^{k\,\mathrm{T}}\,\boldsymbol{\Phi}^{k}+\boldsymbol{\Psi}_{\mathbf{q}}^{k\,\mathrm{T}}\,\boldsymbol{\Psi}^{k}\right] \qquad (4.16)$$

$$\mathbf{q}^{k+1}=\mathbf{q}^{k}+\Delta\mathbf{q}^{k}$$

The linear system of equations (4.16), which are known as *normal equations*, is always compatible. This least-square method is also valid when there are not redundant constraints. Therefore, for the convenience of implementation it can be used in both situations. There is no need to either detect if there are redundant constraints or switch to iteration (4.16).

4.2.2.2 Over-guided kinematic problems

In an over-guided kinematic problem, the number of effectively driven DoFs is equal to the number of DoFs of the multibody system but the number of driven coordinates is greater than the number of DoFs of the multibody ($u = s < r$). This means that the motion of more coordinates than DoFs is prescribed and there is an excess of driving constraints. Furthermore, the values of the driven coordinates may be or may not be consistent with the kinematic constraints of the multibody system.

Suppose that the multibody system and its motion are defined with m independent kinematic constraints and r driving constraints ($r > s$) respectively. As the kinematic problem is over-guided, there are more equations than unknowns ($m + r > n$). One possibility is to solve the nonlinear overdetermined system of $m + r$ equations in n unknowns using the least-square method presented in the previous section. The shortcoming is that if the values of the driven coordinates are not consistent, the kinematic constraints are not satisfied because the error is minimised but distributed over both kinematic and driving constraints.

Another possibility is to satisfy the kinematic constraints and minimise the quadratic error of the driving constraints. In this way the multibody integrity is fulfilled while the prescribed motion of the system is satisfied with minimum error in a least-squared sense. If the driving constraints are consistent with the kinematic constraints, the prescribed motion of the multibody is completely fulfilled and the error is zero.

Mathematically the problem described above is a nonlinear constrained optimisation problem or nonlinear programming (NLP) problem. The NLP problem to be solved is:

$$\begin{aligned} \underset{\mathbf{q}\in\Re^n}{\text{minimize}} \quad & f(\mathbf{q}) = \frac{1}{2}\,\Psi^{\mathrm{T}}(\mathbf{q},t)\,\Psi(\mathbf{q},t) \\ \text{subject to:} \quad & \Phi(\mathbf{q}) = 0 \end{aligned} \tag{4.17}$$

Using the optimisation terminology, $f(\mathbf{q})$ is the *objective function* ($f:\Re^n \to \Re$) and $\Phi(\mathbf{q})$ are the nonlinear *equality constraint equations* ($\Phi:\Re^n \to \Re^m$). The NLP problem (4.17) can be solved with different optimisation algorithms. Note that objective function does not depend on the time variable because the problem is solved for a given time. If a motion reconstruction problem is considered, one NLP problem has to be solved for each frame.

When $\Phi(\mathbf{q})$ has only independent equality constraint equations several NLP algorithms and software are available, but when $\Phi(\mathbf{q})$ contains redundant equality constraints, most of the existing NLP algorithms may have difficulties to solve the NLP problem (4.17). In section 4.4, a survey of the current algorithms and software available to solve the NLP problem (4.17) when the equality constraints are independent or redundant is presented. In section 4.5, a new method, called the Optimal Tracking Method, valid to solve over-guided kinematic problems both with independent and redundant equality constraints is proposed.

NLP algorithms may also be used to solve exactly-guided kinematic problems but in general they are less efficient than the method presented in the previous section. However, due to convenience of implementation, it could be advantageous to solve both exactly-guided and over-guided kinematic problems with NLP algorithms. In this case, the minimum of the objective function should be zero for exactly-guided kinematic problems.

When a motion capture system is used to record the human movement using a large number of markers, the kinematic problem is usually over-guided because the number of dependent coordinates driven by the measured marker

coordinates is greater than the number of DoFs. Nevertheless, a large number of markers does not guarantee an over-guided kinematic problem because it also depends on the topology of the multibody model considered and the configuration of the markers. There are situations where a large number of markers are used but not all DoFs of the model are effectively guided. Then, the kinematic problem is under-guided. This situation is studied in the next section.

4.2.2.3 Under-guided kinematic problems

In an under-guided kinematic problem, the number of effectively driven DoFs is less than the number of DoFs of the multibody system ($u < s$). This means that the position of the system is not completely defined and there is at least one DoF whose motion is not prescribed. On the other hand, the number of driven coordinates can be less, equal or greater than the number of DoFs of the multibody model ($r < s$, $r = s$, $r > s$) as it has been explained in section 4.2.1.

An under-guided kinematic problem has an infinite number of solutions. This type of problem appears for example in Computer Animation (Zhao and Badler, 1994; Tolani et al., 2000; Baerlocher and Boulic, 2004), Ergonomics (Wang and Verriest, 1998) and Robotics (Rubí, 2002). As stated in the introduction of the chapter this problem is usually called Inverse Kinematic problem in these areas.

In Computer Animation a human model usually contains many DoFs making it difficult and tedious for the animator to manipulate each DoF to define a posture of the model. Inverse Kinematic methods are used to facilitate the animation process. The animator defines the location of certain points of the model and additional constraints and the Inverse Kinematics method automatically computes a set of joint angles that satisfy the constraints. In Ergonomics, Inverse Kinematics methods can also be used for example to analyse the workspace of a cockpit, i.e. which objects in the environment are reachable. In Robotics, the Inverse Kinematic problem is usually to find the joint angles of a robot given the position and orientation of the end-effector. For conventional robots this problem is determined but for redundant robots (Rubí, 2002) it is underdetermined.

In Computer Animation and Robotics the values of the DoFs which are not defined with the available data are selected in such a way that they minimise a given objective function. In this thesis, the motion of the DoFs of the multibody system that are unknown is prescribed with additional driven coordinates. One possible option is to fix the not guided DoFs to an

appropriate value. For example, suppose that in the double pendulum of Figure 4.4 only the value of angle α is known for each instant of time. Then, the position of bar 23 is not defined. The angle β can be fixed to zero for each instant of time and the problem solved as an exactly-guided kinematic problem.

Another possibility, when the multibody system represents a human body, is to apply a *relative preservation posture condition*. This consists in imposing the condition that the relative movement between bodies whose motion is not defined must preserve as close as possible a given reference posture. The reference posture is represented by a set of joint angles which define the relative position between the bodies. This concept is introduced in the formulation of the kinematic problem by adding the relative coordinates of the joints connecting the bodies and prescribing the motion of these new relative coordinates using additional driving constraints. Then, the relative coordinates can be set to the values corresponding to the desired reference posture. The new additional driving constraints are included in the objective function of the NLP problem (4.17). Note that the relative preservation posture condition adds relative coordinates to the model. Thus, mixed coordinates are used when a relative preservation posture condition is included.

For a human motion the reference posture can be selected on the basis of a priori knowledge of the motion being studied. For example, suppose that the markers located on a subject are sufficient to define the position of all body segments of the RAMSIS whole body model (section 3.4) except those modelling the spine. The spine is modelled with six rigid bodies whose position is not defined producing an under-guided kinematic problem. The relative angles between each body segment of the spine could be added to the model and set through driving constraints to a "normal" spine position for the human motion investigated.

This approach is an approximation to the real posture of the subject and it cannot guarantee a true solution, especially when the range of motion is large. A detailed description of the relative preservation posture conditions used for each human motion investigated in this thesis is presented in Chapter 5 for each experiment. The relative preservation posture condition is one of the possible strategies for defining the motion of a multibody model. Other possible strategies are presented in section 4.6.2.

After adding a relative preservation posture condition, the new resulting problem is exactly-guided or over-guided depending on the sum of the number of initially driven coordinates and the new ones. The new exactly-guided or over-guided problem can be solved with the mathematical methods presented in the two previous sections.

4.3 JOINT ANGLE ESTIMATION FROM MOTION CAPTURE DATA

In the previous sections it has been explained how natural coordinates can be used to estimate joint angles from motion capture data. However, only the generation of the multibody model and the formulation of the kinematic problem (or motion reconstruction problem) were studied. In this section the problem is considered with a broader view; the whole process from motion capture data to joint angles estimation is studied.

Our goal is to estimate the joint angles of a human skeletal model tailored to a subject from the recorded global marker trajectories. In the process of estimating joint angles two sources of inaccuracies are instrumental errors and skin movement artifacts (see section 3.1.2). Two possible ways of enhancing the estimation of joint angles from measured marker trajectories are to improve experimental procedures in order to reduce the instrumental errors, and to improve the methods for estimating the joint angles in order to reduce the influence of the skin movement artifacts.

High-frequency contents of instrumental errors can be dealt with by using smoothing methods. However, skin movement artifact, which has a similar frequency content as the body segment movement, cannot be removed by smoothing methods. Smoothing methods can be classified into two groups: automatic and non-automatic. Automatic smoothing methods estimate an optimal amount of filtering or cut-off frequency for each x, y and z coordinates of the markers automatically. According to Giakas and Baltzopoulus (1997), there is not an automatic method that performs best in all situations for gait data. Non-automatic smoothing methods consider the same fixed cut-off frequency for all marker coordinates. A typical non-automatic smoothing method is a fourth-order Butterworth filter with zero phase lag at an effective cut-off frequency between 5 and 6 Hz (Kingma et al., 1996; Holden and Stanhope, 1998; Stagni et al., 2000; Reinbolt et al., 2005).

In this section, smoothing methods are not considered and only methods designed to deal with skin movement artifact are studied. The influence of skin movement artifact in the joint angles can be reduced at least in three ways:

- The markers can be placed in locations with minimum skin movement artifact.
- If the skin movement artifact for each marker can be measured or estimated, it can be compensated.

- Joint angles can be estimated using mathematical methods that calculate the optimal joint angles (in some sense) reducing the errors originating from the skin movement artifacts.

4.3.1 OPTIMAL MARKER LOCATION

Several authors place markers over anatomical landmarks (ALs) and define the local coordinate system (LCS) of each body segment from the ALs. Unfortunately, skin movement artifact is usually larger over ALs (Cappozzo et al., 1996) affecting the estimation of LCS and subsequently the joint angles.

Cappozzo et al. (1995) proposed the use of technical coordinate systems and the concept of AL calibration. A technical coordinate system (TCS) is an intermediate coordinate system between the global coordinate system (GCS) and LCS of the body segment, which allows positioning markers at any desired location in a body segment. The coordinates of skin-makers and ALs in TCS and LCS of the body segment are estimated with the so-called CAST protocol. A modified version of this method was used in the frame of the MoDyCo project and it is described in section 5.1.1.1.

4.3.2 SKIN MOVEMENT ARTIFACT COMPENSATION

Cappello et al. (1997) improved the method of Cappozzo et al. (1995), presented in the previous section, by means of a deformable model of the cluster of markers located on a body segment. Cappozzo's method considers that the coordinates of markers and ALs in TCS are constant, while Cappello's method estimates the coordinates of markers and ALs in TCS as a linear interpolation between two reference postures. The method of Cappello et al. (1997) was validated with the help of an external fracture fixation device during a cycling motion. The selection of the reference postures for cyclic motions seems feasible but for noncyclic motions it is not clear. The root mean square error of the orientation and position of the femur decreased respectively from about 5 deg and 7 mm with Cappozzo's method to less than 4 deg and 4.5 mm with Cappello's method.

Lucchetti et al. (1998) proposed a method for compensation of the skin movement artifact. Unlike Cappello's method, this method estimates the skin movement artifact for any position of the body segments instead of interpolating between two reference postures. The skin movement artifact for each AL was assessed during several predefined motions, which makes the compensation motion-dependent.

The method of Cappozzo et al. (1995) allows positioning markers at any desired location in a body segment and the methods of Cappello et al. (1997) and Lucchetti et al. (1998) compensate the skin movement artifact. These methods minimise skin movement artifact, which nevertheless cannot be removed unless bone-pins directly attached to the bone are used (Lafortune et al., 1992; Karduna et al., 2001).

4.3.3 MATHEMATICAL METHODS FOR JOINT ANGLES ESTIMATION

An additional way of enhancing the estimation of joint angles is to use mathematical methods that calculate the optimal joint angles by reducing the errors originating from the skin movement artifact. These mathematical methods do not exclude the previous methods but are complementary.

The mathematical methods proposed in the literature estimate joint angles or body segment poses (position and orientation) from measured marker trajectories for each frame. If a method gives body segment poses, but joint angles are required, they can be calculated easily and the opposite is also true. Mathematical methods can be classified into three groups according to Lu and O'Connor (1999):

- Direct methods (DMs).
- Segmental optimisation methods (SOMs).
- Global optimisation methods (GOMs).

DMs and SOMs require a minimum of three noncollinear markers on each body segment. GOMs require in general fewer markers than DMs and SOMs but the minimum number of markers required on each body segment depends on the type of joints and the topology of the model. Only over-guided kinematic problems, as defined in section 4.2.1, are considered in this section.

4.3.3.1 Direct methods

DMs calculate the pose of each body segment or the joint angles directly from the measured marker coordinates without taking into account the errors introduced by the skin movement artifact. DMs can be classified into two groups: DMs without joint constraints and DMs with joint constraints.

The first type of DMs estimate the pose of the LCS of each body segment in GCS directly from the measured global coordinates of three noncollinear markers without taking into account skin movement artifact or joint constraints (Apkarian et al., 1989; Kadaba et al., 1990; Chèze et al., 1995). For example, suppose a body segment with three noncollinear markers. The

first marker can be selected as the origin of the LCS, LCS x-axis points from the first marker to the second one, LCS y-axis is perpendicular to the plane defined by the three markers and LCS z-axis is obtained from the cross product of LCS x-axis and LCS y-axis. From this definition the pose of LCS of the body segment in GCS can be obtained for each frame.

These types of DMs do not impose any joint constraint and the relative motion between two adjacent body segments is defined by a relative rotation and a relative translation. The joint angles can be estimated from the relative rotation matrix between the two body segments. As the joint constraints are not considered, the joint may dislocate in the reconstructed motion, i.e. the relative translation is different from zero.

A possible strategy to maintain the joint integrity and avoid joint dislocation is to estimate the joint angles of the model from the relative rotation matrices and then, apply the estimated joint angles to the model and neglect the relative translations. The result depends on the order in which joint angles are applied and more than one strategy can be used (Lu and O'Connor, 1999). If the goal is to study the detailed kinematic behaviour of a joint, then the relative translation cannot be neglected because it describes the kinematics of the joint (Andriacchi et al., 1998).

The second type of DMS estimate the joint angles directly from the measured marker coordinates without taking into account the errors introduced by the skin movement artifact but imposing joint constraints (Urban, 1995; Celigüeta, 1996; Silva and Ambrósio, 2002; Silva, 2003). This type of DM has been proposed only for human skeletal models defined with natural coordinates. The method is divided into three steps:

- Points and vectors of the model are defined as a function of the markers. Averaged coordinates of the points and vectors of the model referred to each body segment LCS are estimated from the measured marker coordinates of the whole motion.
- Joint angles are estimated directly from the measured marker coordinates at each frame using joint angles definitions, which are a function of the markers. Joint angles are interpolated with cubic splines making it possible to evaluate the human skeletal model posture at any intermediate time step. Unlike the first type of DM, this second type of DM does not require a minimum of three noncollinear markers on each body segment. The number of markers required is usually smaller than for DMs without joint constraints and depends on the definitions of joint angles, points and vectors.

- A subject-specific multibody model is created with the data estimated in the first step and the motion of the multibody model is prescribed at each frame using the joint angles estimated in the second step. In this way an exactly-guided kinematic problem (section 4.2.1) for each frame is obtained and the pose of each body segment can be obtained from its solution. The data obtained are kinematically consistent because they satisfy the kinematic constraints of the model but the skin movement artifact is not considered in the estimation of the joint angles.

4.3.3.2 Segmental optimisation methods

SOMs calculate the pose of each body segment independently without considering joint constraints but skin movement artifact is minimised in a least-square sense at a body segment level (Spoor and Veldpaus, 1980; Veldpaus et al., 1988; Söderkvist and Wedin, 1993; Challis, 1995). SOMs estimate the optimal rigid body transformation between a reference coordinate system and a second coordinate system by minimising the deformation of the cluster of markers on a body segment in a least-squares sense. SOMs require a minimum of three noncollinear markers on each body segment. The method is formulated as an optimisation problem:

$$\min \ f = \sum_{i=1}^{n} \left\| R \cdot x_i + d - y_i \right\|^2 \ \text{subject to} \ R^T R = I; \det(R) = 1 \qquad (4.18)$$

where x_i and y_i are the position vector of marker i in the reference coordinate system (e.g. body segment LCS) and the second coordinate system (e.g. GCS) respectively and d is the optimal translation vector of the origin of the reference coordinate system referred to the second coordinate system. The optimal rotation matrix R is constrained to be a proper orthogonal matrix (i.e. $R^T R = I$ and $\det(R) = 1$).

Equation (4.18) only gives the optimal rigid body transformation between the position of the skin-makers in a reference coordinate system and another coordinate system. The reference position can be any position of the markers without taking into account the skin movement artifact. Chèze et al. (1995) proposed a method for estimating the least-deformed shape of the markers based on the data recorded during the whole motion. The least-deformed shape was used as the reference position for equation (4.18). Another option is to estimate the position vectors of the markers in the body segment LCS in a static calibration posture and use them as the reference position (Cappozzo et al., 1995; Wang et al., 2005).

The previous authors assumed that the marker coordinates in the reference coordinate system are constant. However, a deformable model of the cluster of markers, as proposed by Cappello et al. (1997) and Lucchetti et al. (1998), can also be considered.

Andriacchi et al. (1998) proposed a SOM for estimating the body segment pose based on the minimisation of the eigenvalue norm of the inertia tensor of a cluster of markers. A large number of markers are uniformly distributed on each body segment and each marker is assigned an arbitrary mass, which is used as a weighting factor and can be varied at each time step. The LCS of each body segment is defined by the eigenvectors of the inertia tensor of the discrete cluster of markers. The body segment pose is obtained by minimising the norm of the three eigenvalues. The method is formulated as a nonlinear unconstrained optimisation problem with a single variable, which determines the distribution of weighting factors. The method employs an overabundance of markers on each body segment (eight markers on each body segment in the example presented by the authors) which can be a drawback for some applications.

Alexander and Andriacchi (2001) extended the previous method assuming that the coordinates of the markers in the body segment LCS can be modelled as a functional form plus additive noise. The functional form and the noise function that define the local coordinates of each marker must be defined for the entire motion investigated and can be selected on the basis of a priori knowledge of the activity being studied. For a step-up activity, a Gaussian function was selected as the functional form for the local marker coordinates. The noise functions were modelled as normal distributions with different standard deviations for each marker coordinate.

Similarly to DMs without joint constraints, SOMs do not impose joint constraints between body segments and their relative motion is defined by a relative rotation and a relative translation. The joint angles can be estimated from the relative rotation matrix between adjacent body segments. The relative translation and possible joint dislocation can be treated similarly to DMs without joint constraints (section 4.3.3.1).

In general, the errors in the joint angles or equivalently the orientation and position errors in the body segment pose are bigger for DMs than for SOMs (Chèze et al., 1995; Lu and O'Connor, 1999), although errors in DMs can be reduced by selecting an adequate definition for the body segment LCS. The performance of DMs can be very poor compared to SOMs if an inappropriate definition of the body segment LCS is made (Chèze et al., 1995).

4.3.3.3 Global optimisation methods

As opposed to DMs and SOMs, GOMs calculate the joint angles of a multibody system from measured marker trajectories by imposing joint constraints and minimising the global measurement error introduced by the skin movement artifact. Usually the global measurement error is defined as the sum of squared distances between the measured and model-determined marker positions. GOMs are useful when joint constraints are considered (e.g. fixed joint rotation centres) but SOMs are preferable when the goal of the investigation is to measure the detailed kinematic behaviour of a joint (3 translations and 3 rotations). Only GOMs for over-guided kinematic problems, as defined in section 4.2.1, are considered in this section.

GOMs require in general fewer markers than DMs and SOMs but the minimum number of markers required on each body segment depends on the type of joints connecting the bodies and the topology of the model. For example, consider the double pendulum of Figure 4.5. DMs without joint constraints and SOMs require a minimum of six markers, three on each bar. GOMs require a minimum of two markers, one on each bar because the mechanism has two DoFs.

The term "global optimisation methods" must not be confused with the term "global optimisation" used in optimisation theory. In this section the term "global optimisation methods" does not mean that a global minimiser of the problem is calculated. It only means that measurement errors are minimised at a global level considering all the body segments at once, as opposed to body segment level in SOMs. In fact, all GOMs presented in this section are only able to find local minimisers.

Zhao and Badler (1994) proposed one of the first GOMs. They applied their GOM in the context of interactive manipulation of human skeletal models where joint constraints must be satisfied. The human skeletal model was defined with relative coordinates and only open loops were considered. Joint constraints were considered implicitly in the definition of the human skeletal model and they were automatically fulfilled. Their method was designed to satisfy spatial constraints, e.g. the hand must be located at a certain point, the orientation of the hand must satisfy a predefined orientation or the elbow joint must be constrained to move in a plane. Different weighting factors could be used for each spatial constraint. The problem was formulated as a nonlinear programming problem subject to linear equality and linear inequality constraints on the variables of the problem, i.e. joint angles.

Although Zhao and Badler did not design their method for estimating the joint angles of the human skeletal model from the measured marker trajectories, it can be used for this type of problem without any additional modification. The spatial constraints can be used directly to prescribe the motion of the human skeletal model with the measured marker coordinates.

Bodenheimer et al. (1997) presented a GOM where joint constraints were considered, although in general they were not satisfied. An open-loop multibody system defined with relative coordinates was used to model the human body. Joint constraints were included explicitly in the optimisation problem reducing joint dislocations but not eliminating them completely. The motion of a human skeletal model was prescribed with electromagnetic sensors, which give their position and orientation in GCS. The motion reconstruction problem was formulated as a nonlinear unconstrained optimisation problem where the joint constraints were included. The method was used to produce a number of motions for various commercial games.

Lu and O'Connor (1999) presented a GOM based on the minimisation of the weighted sum of squared distances between measured and model-determined marker positions for each frame. An open-loop multibody system modelled with relative coordinates was considered. Joint constraints were considered implicitly in the definition of the multibody model and they were automatically fulfilled. The method was formulated as a nonlinear unconstrained optimisation problem:

$$\min f(\mathbf{q}) = \left[\mathbf{P} - \mathbf{P}'(\mathbf{q})\right]^{\mathrm{T}} \mathbf{W} \left[\mathbf{P} - \mathbf{P}'(\mathbf{q})\right] \tag{4.19}$$

where $\mathbf{q}$ is the column vector of relative coordinates, $\mathbf{P}$ is the column vector with the measured global coordinates of all markers in a given frame, $\mathbf{P}'(\mathbf{q})$ is a column vector with the global coordinates of all skin-makers given by the multibody model as a function of the relative coordinates and $\mathbf{W}$ is a weighting matrix. Given the measured marker coordinates at a certain time, the goal is to find a vector of relative coordinates $\mathbf{q}$ such that the objective function (4.19) is minimised.

Lu and O'Connor compared a DM, a SOM similar to equation (4.18) and their GOM for a lower limb model using computer generated data and introducing artificial noise into each marker coordinate to simulate skin movement artifact. As expected, the proposed GOM estimated body segment poses more accurately than DM and SOM.

Roux et al. (2002) evaluated the GOM proposed by Lu and O'Connor for the kinematics of the upper limb. Upper arm movements were simulated

and computer-generated measurement noise and skin movement artifacts were added to the marker coordinates. It was concluded that GOM significantly reduce the errors and the variability introduced by skin movement artifact.

Riley et al. (2000) proposed a GOM similar to Lu and O'Connor (1999) but a weighting matrix was not considered and twist coordinates instead of relative coordinates were used to define a kinematic human skeletal model. Their GOM considered joint constraints implicitly in the definition of the kinematic model and it was formulated as a nonlinear unconstrained optimisation problem.

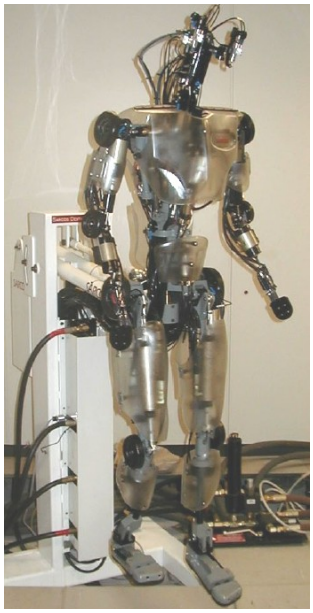

Figure 4.6: Sarcos humanoid robot with 26 DoFs + 4 DoFs at the eyes. Reproduced from Riley et al. (2000).

The method was applied to a motion generation problem for a humanoid robot with 26 DoFs (Figure 4.6). Firstly, the motion of a human dancer was recorded with an optoelectronic motion capture system using 22 markers. Secondly, a kinematic model of the human dancer similar to the robot topology was used to estimate joint angles from the motion capture data using the proposed GOM. Finally, the estimated joint angles were used to prescribe the motion of the humanoid robot.

The four GOMs presented above use objective functions which are nonlinear functions of the coordinates used to define the multibody model and they are applied only to open-loop models. Open-loop multibody systems modelled with relative coordinates or twist coordinates do not require

kinematic constraints for their definition. Then, the resultant optimisation problems can be classified as nonlinear unconstrained optimisation problems. The method of Zhao and Badler (1994) is an exception. Only open-loop multibodies modelled with relative coordinates were studied by the authors but their GOM was formulated as a nonlinear constrained optimisation problem subject only to linear equality and inequality constraints. The linear equality and inequality constraints do not originate from kinematic constraints but from other additional conditions considered by the authors.

A closed-loop multibody system modelled with relative coordinates or twist coordinates requires at least one nonlinear kinematic constraint to define the model. Consequently, as explained in section 4.2.2.2, the kinematic constraint or constraints must be satisfied to fulfil the model integrity and the objective function must be minimised. This is a nonlinear constrained optimisation problem with nonlinear equality constraints. None of the four GOMs presented can solve this type of optimisation problem. Therefore, the four GOMs presented are only valid for open-loop mechanisms.

Furthermore, the four previous GOMs are not valid for open-loop multibody systems modelled with natural coordinates because natural coordinates lead to a nonlinear constrained optimisation problem with nonlinear equality constraints independently of the topology of the multibody system (open- or closed-loop).

In this thesis a new GOM valid for open- and closed-loop multibody systems modelled with natural coordinates is proposed in section 4.5. The basic idea of the proposed GOM is the same presented for the previous GOMs, i.e. minimise the sum of squared distances between measured and model-determined marker positions while maintaining the multibody integrity. The proposed GOM is formulated as the NLP problem (4.17) presented in section 4.2.2.2. This NLP problem requires the satisfaction of the kinematic constraints and the minimisation of the sum of squared errors of the driving constraints. Using natural coordinates, the optimisation problem is the same for open- and closed-loop models because with natural coordinates kinematic constraints always exist. The proposed GOM is valid for over-guided and exactly-guided kinematic problems but under-guided kinematic problems related to human motion can be converted to over-guided ones by adding a relative preservation posture condition (section 4.2.2.3).

In summary, it can be concluded that when fixed joint centres are assumed, GOMs are the most appropriate methods as they estimate joint angles or equivalently body segment poses more accurately than DMs and SOMs. Unfortunately, the four GOMs reviewed in this section are neither valid

for closed-loop multibody system nor natural coordinates. This limitation can be overcome with the new GOM proposed in section 4.5, which is valid for open- and closed-loop systems modelled with natural coordinates.

4.4 OPTIMISATION METHODS FOR NLP PROBLEMS

In this thesis a new GOM valid for open- and closed-loop multibody systems modelled with natural coordinates is proposed. The new GOM is formulated as the NLP problem (4.17) presented in section 4.2.2.2. In this section, the optimisation methods available in the literature to solve the NLP problem (4.17) are reviewed.

The subject of *optimisation* is extremely broad and has applications in almost every branch of science and technology. Optimisation is also referred to as *mathematical programming* or *numerical optimisation*. As indicated in section 4.2.2.2, an over-guided kinematic problem can be formulated as an optimisation problem and solved with optimisation methods. Two cases are considered, optimisation problems with independent equality constraints (section 4.4.1) and optimisation problems with redundant equality constraints (section 4.4.2). The optimisation problem (4.17) arising in over-guided kinematic problem has the following features:

- The objective function is quadratic.
- It is constrained (as opposed to unconstrained), with only nonlinear equality constraints, i.e. inequality constraints are not considered.
- The Jacobian matrix of the equality constraints is sparse.
- It is a large-scale problem.

An optimisation problem with a quadratic objective function and nonlinear equality constraints falls into the category of nonlinear constrained optimisation problems or NLP problems. The Jacobian matrix of the equality constraints is sparse because natural coordinates have been used to model the multibody system (García de Jalón and Bayo, 1994).

There is not a common definition of a large-scale problem. According to Benson et al. (2003), an optimisation problem can be classified as large-scale if the number of variables plus the number of constraints is at least 1000. The number of variables (dependent coordinates) plus the number of constraints (kinematic constraints) of the human skeletal models used in this thesis is greater than 1000 (Chapter 6). Therefore, the NLP problem (4.17) can be considered as a large-scale optimisation problem according to Benson et al. (2003).

In order to solve the NLP problem (4.17), the first decision is to choose between global optimisation algorithms (Neumaier, 2004) or local optimisation algorithms (Conn et al., 1997; Gould and Leyffer, 2003).

Global optimisation is the task of finding the best absolute set of admissible conditions to achieve an objective under some given constraints, assuming that both are formulated in mathematical terms (Neumaier, 2004). In general there can be solutions that are optimal locally but not globally. The main drawback of global optimisation problems is that they are much more difficult to solve. In general, global optimisation algorithms require global information about the problem structure. They need much more computation time than local optimisation algorithms and the algorithms available are not well-suited for large-scale problems. The advantage of global optimisation algorithms is that they can find the global optimum.

Local optimisation is the task of finding a set of admissible conditions to achieve an objective under some given constraints. The main drawback of local optimisation algorithms is that they cannot guarantee convergence to the global optimum. In many practical applications finding the global optimum is desirable but not essential, since a local optimum may be enough. An advantage of local optimisation algorithms is that they require much less time to find a local optimum than global optimisation algorithms to find the global optimum. Furthermore, they do not require information about the problem structure and there are suitable algorithms for large-scale problems.

A global optimisation algorithm can find the *global minimiser* of the NLP problem (4.17), which seems to be the best solution. But the question is whether our goal is to find the global solution to this NLP problem or if a local solution could be enough.

In general, a local optimisation algorithm finds the local solution which is closer to the initial approximation. If the sampling rate of the motion capture system is suitable for the motion being studied, the current position of the multibody system is close to the previous one. Then, the solution in the previous frame can be used as a good initial approximation for the current frame. Therefore, it seems reasonable to find a *local minimiser* of the NLP problem (4.17) using a local optimisation algorithm and the previous position of the multibody as the initial approximation.

Furthermore, a global minimiser can exist in any position of the feasible region. This means that the global solution could be far away from the previous position, and therefore it could give an unrealistic result despite being a global minimum.

4.4.1 INDEPENDENT CONSTRAINTS

Most local NLP algorithms require that the constraint equations are independent. The major local optimisation algorithms for NLP problems with independent constraints are the following:

- Sequential Quadratic Programming (SQP) methods (Boggs and Tolle, 1995).
- Interior-point methods (Forsgren et al., 2002; Wright, Margaret H., 2004a).
- Augmented Lagrangian methods (or the method of multipliers) (Bertsekas, 1982; Bertsekas, 1999).
- Generalised Reduced Gradient (GRG) methods (Smith and Lasdon, 1992; Drud, 1994).

It must be emphasised that most optimisation methods are not a single algorithm, but rather a conceptual method from which numerous specific algorithms have evolved.

The SQP method is an iterative method in which, at a current iterate $\mathbf{q}^k$, the step to the next iterate is obtained through information generated by solving a quadratic programming (QP) subproblem. The QP subproblem is an approximation of the NLP problem (with linear constraints and a quadratic objective function). There are many modification of this basic idea. The softwares SNOPT (Gill et al., 1997; Gill et al., 2002) and filterSQP (Fletcher and Leyffer, 1998) implement SQP methods valid for large-scale problems.

Interior-point methods receive this name because all iterates must remain strictly feasible with respect to the inequality constraints (otherwise the problem is not defined). Although interior-point methods are relevant only to inequality constraints they can be extended to equality constraints also. One common feature of interior-point methods is the existence of continuously parameterised families of approximate solutions that asymptotically converge to the exact solution. Classical barrier methods provide the foundation for modern interior-point methods. The logarithmic barrier function is the predominant barrier function used. There are different software implementations of interior-point methods suitable for large-scale problems: LOQO (Vanderbei and Shanno, 1999) implements a primal-dual approach and KNITRO (Byrd et al., 2000) a trust-region SQP approach of the interior-point method.

Augmented Lagrangian methods are based on the transformation of the NLP problem in a sequence of unconstrained problems that converge to the

exact solution. The objective function of the unconstrained problem is called the augmented Lagrangian function. The softwares LANCELOT (Conn et al., 1992) and MINOS (Murtagh and Saunders, 1998) implement the augmented Lagrangian method and are valid for large-scale problems.

GRG methods use a formulation in which only bounds and equality constraints are present (but an inequality can be transformed to this form). Two software packages for GRG methods are CONOPT (Drud, 1994; ARKI Consulting & Development A/S, 2004) and LSGRG2 (Smith and Lasdon, 1992). Both are well-suited for large-scale problems. However, their performance is often slower than competing codes based on SQP and Augmented Lagrangian algorithms (Wright, Stephen J., 1999).

There are some comparative studies of several state-of-the-art optimisation codes on large-scale NLP problems. Different criteria have been proposed to evaluate the performance of the optimisation software but there is no consensus on the best method. The choice of the best test problem set is also a source of disagreement. The four comparative studies presented next use the performance profiles proposed by Dolan and Moré (2002). When a solver is said to outperform the other, this does not imply that the solver is faster on every problem or that it solves all the problems. It means that the solver is the fastest solver on most of the problems and solves the most problems to optimality.

Dolan and Moré (2002) evaluated the performance of four optimisation codes (MINOS, SNOPT, LANCELOT and LOQO) on the COPS test set (Dolan and Moré, 2000). This study showed that LANCELOT was not competitive with the other solvers tested. LOQO was the best solver for the problem set of the study but this does not imply that LOQO was faster on every problem. LOQO was the fastest solver on 58% of the problems and solved the most problems (87%) to optimality.

Benson et al. (2003) compared three algorithms (LOQO, KNITRO and SNOPT) using test problems from three sources: the CUTE suite (Bongartz et al., 1995), the COPS suite and several engineering problems formulated by Vanderbei (2001). If only the NLP problems with equality constraints are considered, KNITRO outperforms LOQO but the difference is small. SNOPT showed a poor performance when compared with the other two algorithms.

Morales et al. (2001) evaluated the performance of four algorithms (LOQO, KNITRO, SNOPT and filterSQP) on a subset of the CUTE suite (small, medium-sized and moderately large problems). If only the solutions of NLP problems with equality constraints are considered, KNITRO outperforms the other solvers. But if general nonlinear optimisation problems (with

equalities and inequalities) are considered, SNOPT performance is close to KNITRO and better than LOQO or filterSQP.

Mittelmann and Pruessner (2004) compared four solvers (CONOPT3 (Drud, 2002), KNITRO, IPOPT (Wächter, 2002) and SNOPT) on the COPS test set. The fastest solver was KNITRO, which was the fastest in roughly 45% of the problems, followed by CONOPT3 in 25% of the problems. SNOPT had the highest probability of success even though it had the lowest profile for efficiency.

The comparative studies tend to conclude that there is not a best optimisation software for all the problems. It must be emphasised that the results of each study are only valid for the problem set used in that study and it cannot be extrapolated to a different problem set. In addition, most of the software packages are regularly being updated and their performance could change significantly after a new release.

4.4.2 REDUNDANT CONSTRAINTS

Most NLP algorithms make an assumption on the constraint equations called *constraint qualification* (CQ). The most common CQs are the linear independence constraint qualification (LICQ) and the Mangasarian-Fromovitz constraint qualification (MFCQ). In the case of a NLP problem with only equality constraints both CQs are equivalent and are reduced to the condition that the Jacobian matrix $\mathbf{\Phi_q}$ of the nonlinear equality constraints $\mathbf{\Phi(q)}$ should have full row rank, i.e. the gradient vectors (rows of $\mathbf{\Phi_q}$) of the equality constraints must be linearly independent.

When redundant constraints exist in $\mathbf{\Phi(q)}$ neither LICQ nor MFCQ are satisfied because the redundant constraints can induce linearly dependent constraints in $\mathbf{\Phi_q}$ and most NLP algorithms cannot be applied. Two possible ways to handle redundant constraints are:

- One possible approach is to detect and eliminate linearly dependent constraints in $\mathbf{\Phi_q}$. Then, only linearly independent constraints are included in the optimisation problem and standard NLP algorithms can be used. This approach is discussed in section 4.5.2 for the NLP problem (4.17).
- Another approach is to let the optimisation algorithm the responsibility of dealing with the redundant constraints. This approach is followed by the new method proposed in this thesis and the two algorithms presented next.

Recently two new algorithms (Izmailov and Solodov, 2004; Wright, Stephen J., 2004b) valid for redundant equality constraints, which do not assume any CQ, have been presented. The algorithm proposed by Izmailov and Solodov (2004) is not practical for large-scale problems because it requires a singular value decomposition (SVD) of the Jacobian matrix of the constraint equations. The SVD yields a dense matrix in general even when the Jacobian matrix of the constraints is sparse and the time required for computing the SVD is high for large-scale problems. The algorithm presented by Wright (2004b) is valid for large-scale problems and it is based on the SQP method. Unfortunately, there is not a public software implementation of this method available and it cannot be compared with the new optimisation method proposed in the next section.

4.5 OPTIMAL TRACKING METHOD

A new optimisation method to solve over-guided and exactly-guided kinematic problems with and without redundant kinematic constraints is presented in this section. The new optimisation method is called Optimal Tracking Method (OTM) and the formulation of the motion reconstruction problem as the NLP problem (4.17) is named Optimal Tracking Problem (OTP).

Unlike most of the optimisation methods presented in the previous section, OTM does not assume any constraint qualification. It solves OTP, which has a quadratic objective function and nonlinear equality constraints. OTM has not been tested for more complex objective functions or inequality constraints.

4.5.1 INTRODUCTION

The main features of OTP have been introduced in section 4.4. Recall that OTP was defined in section 4.2.2.2 as

$$\begin{aligned} \underset{\mathbf{q}\in\Re^n}{\text{minimize}} \quad & f(\mathbf{q}) = \frac{1}{2}\,\Psi^{\mathrm{T}}(\mathbf{q},t)\,\Psi(\mathbf{q},t) \\ \text{subject to}: \quad & \Phi(\mathbf{q}) = 0 \end{aligned} \tag{4.17}$$

where $\mathbf{q}$ is the vector of n dependent coordinates, $\Phi(\mathbf{q})$ is the vector of m kinematic constraints and $\Psi(\mathbf{q},t)$ is the vector of r driving constraints. Note that objective function does not depend on the time variable because the problem is solved for a given time.

The key idea of OTM is to solve OTP using a Newton-Raphson iteration (section 4.2.2.1) of the kinematic constraints $\Phi(\mathbf{q})$ where at each step the change in coordinates $\Delta\mathbf{q}$ is such that it minimises the objective function.

Consider a generic kinematic problem with m nonlinear kinematic constraints (Φ), n dependent coordinates ($\mathbf{q}$), r driving constraints (Ψ) or equivalently r driven coordinates, and s DoFs. Suppose that there are exactly $m = n - s$ independent nonlinear kinematic constraints, i.e. there are not redundant constraints. Then, the Newton-Raphson iteration of the kinematic constraints is

$$\mathbf{\Phi}_{\mathbf{q}}^{k}\,\Delta\mathbf{q} = -\,\mathbf{\Phi}^{k} \tag{4.20}$$

The linear system of equations (4.20) is underdetermined because there are m linearly independent constraints and n ($>m$) unknown dependent coordinates in $\Delta\mathbf{q}$. This means that infinite column vectors $\Delta\mathbf{q}$ exist that satisfy the linear system of equations (4.20). The column vector $\Delta\mathbf{q}$ that minimises the objective function in (4.17) is chosen as the solution of (4.20) at each iteration step.

The objective function f of OTP is quadratic. At an intermediate iteration point $\mathbf{q}^k + \Delta\mathbf{q}$ it can be written as

$$f(\mathbf{q}) = f(\mathbf{q}^k + \Delta\mathbf{q}) = \frac{1}{2}\,\mathbf{\Psi}^{\mathrm{T}}(\mathbf{q}^k + \Delta\mathbf{q})\,\mathbf{\Psi}(\mathbf{q}^k + \Delta\mathbf{q}) \tag{4.21}$$

For a given $\mathbf{q}^k$ the objective function is only a function h of $\Delta\mathbf{q}$. This objective function h can be written using its Hessian matrix $\mathbf{H}^k$ and gradient vector $\mathbf{g}^k$ as follows

$$h(\Delta\mathbf{q}) = f(\mathbf{q}^k + \Delta\mathbf{q}) = \frac{1}{2}\,\Delta\mathbf{q}^{\mathrm{T}}\mathbf{H}^k\Delta\mathbf{q} + \mathbf{g}^{k\,\mathrm{T}}\Delta\mathbf{q} + f^k \tag{4.22}$$

where

$$\mathbf{g}^k = \nabla f^k = \mathbf{S}^{\mathrm{T}}(\mathbf{S}\mathbf{q}^k - \mathbf{d}) = \mathbf{S}^{\mathrm{T}}\mathbf{\Psi}^k \tag{4.23}[1]$$

$$\mathbf{H}^k = \nabla^2 f^k = \mathbf{S}^{\mathrm{T}}\mathbf{S} \tag{4.24}[2]$$

[1] The symbol ∇ is used frequently in the optimisation literature to denote the first derivative of a real-valued function of n independent variables.

[2] The symbol ∇^2 is used here to denote the Hessian matrix of a real-valued function of n independent variables. It must no be confused with the Laplace operator or Laplacian.

Note that equation (4.22) is not an approximation of the objective function f but the actual objective function because it is quadratic. Matrix $\mathbf{H}^k$ is a constant diagonal matrix with 0's in the main diagonal except in the positions corresponding to driven coordinates that contain 1's. Therefore, $\mathbf{H}^k$ is $n \times n$ and in general positive semidefinite with sparse structure, because the number of driven coordinates is usually less than the number of dependent coordinates. From now on, $\mathbf{H}^k$ is denoted simply as $\mathbf{H}$ because it is constant and does not depend on $\mathbf{q}^k$.

At each Newton-Raphson iteration step, the linearised kinematic constraints (4.20) must be satisfied and the quadratic objective function (4.22) must be minimised. This can be formulated as a QP problem. Thus, the method could also be thought as a sequence of QP subproblems. Each QP subproblem can be written as

$$\begin{aligned} \underset{\Delta\mathbf{q} \in \Re^n}{\text{minimize}} \quad & h(\Delta\mathbf{q}) = \frac{1}{2}\Delta\mathbf{q}^{\mathrm{T}}\mathbf{H}\,\Delta\mathbf{q} + \mathbf{g}^{k\,\mathrm{T}}\Delta\mathbf{q} + f^k \\ \text{subject to} \quad & \boldsymbol{\Phi}_{\mathbf{q}}^k \Delta\mathbf{q} = -\boldsymbol{\Phi}^k \end{aligned} \tag{4.25}$$

4.5.2 INCOMPATIBILITY OF THE LINEARISED KINEMATIC CONSTRAINTS

When redundant constraints exist within the m nonlinear kinematic constraints $\Phi(\mathbf{q})$, a new problem arises. At a solution point $\mathbf{q}^*$ of (4.17), the linear system of equations (4.20) is compatible underdetermined; the number of linearly independent constraints in $\Phi_{\mathbf{q}}{}^k$ is $(n - s)$, and there are $m - (n - s)$ linearly dependent constraints coming from the $m - (n - s)$ nonlinear redundant constraints in $\Phi(\mathbf{q})$. But the problem is that at an intermediate iteration point $\mathbf{q}^k$, the redundant constraints can induce in (4.20) more linearly independent constraints than required. Therefore, at intermediate iteration points, $\Phi_{\mathbf{q}}{}^k$ can contain linearly independent and linearly dependent constraints coming from the redundant constraints.

The number of redundant constraints in $\Phi(\mathbf{q})$ depends on the algorithm implementation and the multibody model used but in general they can take any number, even their number can be greater than the number of dependent coordinates ($m > n$). However, the maximum number of linearly independent constraints induced in $\Phi_{\mathbf{q}}{}^k$ by the redundant constraints is s.

In this situation, there are three potential difficulties with the QP subproblem (4.25) (see examples A.2 and A.3 in Appendix A):

1. The linear system of equations (4.20) could become incompatible. Therefore, the QP subproblem does not have a solution because a feasible region does not exist.
2. The system of equations (4.20) could be compatible determined. This means that the number of linearly independent equations induced by the redundant equations in $\Phi_{\mathbf{q}}^{k}$ is s. Therefore, the feasible region of the QP subproblem is a single point, which is obtained from the solution of the compatible determined system of equations (4.20).
3. The system of equations (4.20) could be compatible underdetermined with the rank of $\Phi_{\mathbf{q}}^{k}$ greater than $(n - s)$ but less than n. Then, there is an excess of linear constraints and the multibody loses some DoFs but the QP subproblem (4.25) can be solved.

During the sequence of iteration points $\mathbf{q}^{k}$ the three situations described above can be found. Generally, the rank of $\Phi_{\mathbf{q}}^{k}$, i.e. the number of linearly independent constraints, decreases as the solution $\mathbf{q}^{*}$ is approached because the excess of linearly independent constraints induced by the redundant constraints decreases (see section 6.3.2.1).

OTM deals with the incompatibility of linear system of equations (4.20) by modifying the linearised kinematic constraints. Instead of (4.20) consider the following linear constraints

$$\Phi_{\mathbf{q}}^{k\,\mathrm{T}}\Phi_{\mathbf{q}}^{k}\Delta\mathbf{q} = -\Phi_{\mathbf{q}}^{k\,\mathrm{T}}\Phi^{k} \tag{4.26}$$

that corresponds to the normal equations of (4.20). The linear system of equations (4.26) is always compatible. Thus, the problem of incompatible linear constraints coming from the nonlinear redundant constraints is eliminated. Equation (4.26) can be rewritten as follows

$$\mathbf{A}^{k}\Delta\mathbf{q} = \mathbf{b}^{k} \tag{4.27}$$

where

$$\mathbf{A}^{k} = \Phi_{\mathbf{q}}^{k\,\mathrm{T}}\Phi_{\mathbf{q}}^{k} \tag{4.28}$$

$$\mathbf{b}^{k} = -\Phi_{\mathbf{q}}^{\mathrm{k}\,\mathrm{T}}\Phi^{k} \tag{4.29}$$

$\mathbf{A}^{k}$ is a $n \times n$ sparse symmetric matrix and usually positive semidefinite. Its rank at the solution is $(n - s)$ but at intermediate iteration points is

$$n - s \leq rank(\mathbf{A}^k) \leq n \tag{4.30}$$

Similarly to $\Phi_{\mathbf{q}}{}^k$, the rank of $\mathbf{A}^k$ depends on the number of linearly independent constraints induced by the nonlinear redundant constraints. Therefore, the linear system of equations (4.27) has always n linear constraint equations but some of them can be linearly dependent.

It can be argued that the linear system of equations (4.20) is preferable to (4.27) because $\Phi_{\mathbf{q}}{}^k$ is in general smaller, has less nonzero elements and has better conditioning than $\mathbf{A}^k$. Unfortunately, as mentioned above the system (4.20) could become incompatible rarely (example A.2 in Appendix A) or for any column vector $\mathbf{q}^k$ which does not satisfy the kinematic constraints (example A.3 in Appendix A). Then, the QP subproblem (4.25) does not have a solution, the iterative process cannot find the next iteration point and consequently, it fails to find a solution.

Instead of the QP subproblem (4.25) OTM considers the following QP subproblem with the new linear constraint equations (4.27).

$$\begin{aligned} \underset{\Delta\mathbf{q} \in \Re^n}{\text{minimize}} \quad & h(\Delta\mathbf{q}) = \frac{1}{2}\Delta\mathbf{q}^{\mathrm{T}}\mathbf{H}\,\Delta\mathbf{q} + \mathbf{g}^{k\,\mathrm{T}}\Delta\mathbf{q} + f^k \\ \text{subject to} \quad & \mathbf{A}^k\Delta\mathbf{q} = \mathbf{b}^k \end{aligned} \tag{4.31}$$

The linear system of equations of the QP subproblem (4.31) can be determined or underdetermined but it is always compatible. If it is determined, the column vector of unknowns $\Delta\mathbf{q}$ is given by the solution of the linear system of equations and the objective function has no influence on $\Delta\mathbf{q}$. If it is underdetermined, $\Delta\mathbf{q}$ is given by the solution of the QP subproblem.

The question of the linearly dependent constraints induced by the redundant constraints in the linear system of equations (4.27) has not been addressed yet. Two possible approaches to handle linearly dependent constraints have been suggested in section 4.4.2. Firstly, eliminate the linearly dependent constraints in $\mathbf{A}^k$ and secondly, let the optimisation algorithm deal with the linearly dependent constraints.

The first approach can be applied but it has to be performed at each iteration step because the number of linearly dependent constraints induced by the redundant constraints could change at each iteration step. Firstly, a factorisation of $\mathbf{A}^k$ has to be performed at each iteration step to detect and eliminate the linearly dependent constraints. Secondly, the QP subproblem (4.31), free of linearly dependent constraints, must be solved.

OTM uses the second approach and the optimisation method must handle the linearly dependent constraints. In the next section, it is described how linearly dependent constraints are handled theoretically within OTM and in section 4.5.6 practical numerical methods are presented. It will be shown that this approach is more efficient because the factorisation of $\mathbf{A}^k$ is not required and the linearly dependent constraints are detected directly during the solution of the QP subproblem.

4.5.3 LAGRANGE'S THEOREM

Consider the following column partitioning of matrix $\mathbf{A}^k$

$$\mathbf{A}^k = \begin{bmatrix} a_1^k & \dots & a_n^k \end{bmatrix} \tag{4.32}$$

where a_i^k is the i-th column of matrix $\mathbf{A}^k$. This matrix is symmetric and then, its i-th row is ${a_i^k}^{\mathrm{T}}$.

The Lagrange's theorem (Bartle, 1976) for the QP subproblem (4.31) can be formulated as follows. Consider the quadratic objective function $h(\Delta\mathbf{q})$ and the n linear constraints

$$c_i(\Delta q) = {a_i^k}^{\mathrm{T}} \Delta q - b_i^k = 0, \quad i = 1,\dots,n \tag{4.33}$$

that are once continuously differentiable, and assume that $\Delta\mathbf{q}^*$ is a solution of the QP subproblem (4.31). Then, there exist $n + 1$ real numbers $\mu, \lambda_1,\dots, \lambda_n$ not all zero such that

$$\mu \nabla h^* = \lambda_1 \nabla c_1^* + \dots + \lambda_n \nabla c_n^* \tag{4.34}$$

The variables $\lambda_1,\dots,\lambda_n$ are called Lagrange multipliers. The gradient vector of the i-th linear constraint evaluated at $\Delta\mathbf{q}^*$ is a constant column vector

$$\nabla c_i = a_i^k \tag{4.35}$$

The linear constraint equations in (4.31) contain linearly dependent equations and the gradient vectors of the constraints ∇c_i are not linearly independent. Then, μ can be zero and the situation requires further study.

Suppose that the first p gradient vectors are linearly independent and the last $(n - p)$ are linearly dependent. Equation (4.34) can be written in terms of the linearly independent and dependent gradient vectors of the constraints and their associated multipliers as follows

$$\mu \nabla h^* = \lambda_1 a_1^k + ... + \lambda_p a_p^k + \lambda_{p+1} a_{p+1}^k + ... + \lambda_n a_n^k \tag{4.36}$$

If the Lagrange multipliers associated with the dependent gradient vectors of the constraints, $\lambda_{p+1},\ldots, \lambda_n$ are set to zero, then (4.36) becomes

$$\mu \nabla h^* = \lambda_1 a_1^k + ... + \lambda_p a_p^k \tag{4.37}$$

The gradient vectors of the constraints in (4.37) are linearly independent. If μ is zero, this implies that $\lambda_1,\ldots, \lambda_p$ must be all zero. Then, $\lambda_1,\ldots,\lambda_p$ and $\lambda_{p+1},\ldots,\lambda_n$ are all zero which is contrary to the hypothesis of the Lagrange's theorem. Hence μ must be distinct from zero so equation (4.37) can be divided by μ and each λ_i/μ replaced by a normalised Lagrange multiplier λ_i. Then, there are p real numbers $\lambda_1,\ldots, \lambda_p$ not all zero such that

$$\nabla h^* = \lambda_1 a_1^k + ... + \lambda_p a_p^k \tag{4.38}$$

Equation (4.38) can be written in matrix form as follows:

$$\nabla h^* = \mathbf{A}_{li}^{k\,\mathrm{T}} \lambda_{li} \tag{4.39}$$

where $\mathbf{A}_{li}^{k\,\mathrm{T}}$ is a matrix whose columns are the independent gradient vectors and λ_{li} the column vector of the associated Lagrange multipliers. This result can be expressed in the following equivalent form

$$\nabla h^* = \mathbf{A}_{li}^{k\,\mathrm{T}} \lambda_{li} + \mathbf{A}_{ld}^{k\,\mathrm{T}} \lambda_{ld} \tag{4.40}$$

$$\lambda_{ld} = 0 \tag{4.41}$$

where $\mathbf{A}_{ld}^{k\,\mathrm{T}}$ is a matrix whose columns are the dependent gradient vectors and λ_{ld} the column vector of the associated Lagrange multipliers. The gradient vector of the objective function of the QP subproblem (4.31) is

$$\nabla h^* = \mathbf{H}\,\Delta\mathbf{q}^* + \mathbf{g}^k \tag{4.42}$$

When there are only linearly dependent gradient vectors, the solution to the QP subproblem (4.31) must satisfy both equation (4.39) and the linearly independent constraints

$$\mathbf{H}\,\Delta\mathbf{q} + \mathbf{g}^k = \mathbf{A}_{li}^k \lambda_{li} \tag{4.43}$$

$$\mathbf{A}_{li}^k \Delta\mathbf{q} = \mathbf{b}_{li}^k \tag{4.44}$$

These two equations can be written as

$$\begin{bmatrix} \mathbf{H} & \mathbf{A}_{li}^{k\,\mathrm{T}} \\ \mathbf{A}_{li}^{k} & 0 \end{bmatrix} \begin{bmatrix} \Delta\mathbf{q} \\ -\lambda_{li} \end{bmatrix} = \begin{bmatrix} -\mathbf{g}^{k} \\ \mathbf{b}_{li}^{k} \end{bmatrix} \tag{4.45}$$

The linear system of equations (4.45) is always compatible because the assumptions of the Lagrange's theorem are satisfied and the linear constraints (4.44) come from the normal equations of (4.20), which are always compatible. However, the linear system of equations (4.45) can be determined or underdetermined depending on the type of objective function. Furthermore, equation (4.45) is only a necessary condition for a solution of (4.31). This condition is satisfied by a minimum, a maximum and a saddle point.

The linearly dependent equations in (4.27) can be added to (4.45) because the algorithm that solves the linear system of equations can easily discard them (see section 4.5.6). The new equivalent system of equations is

$$\begin{bmatrix} \mathbf{H} & \mathbf{A}_{li}^{k\,\mathrm{T}} \\ \mathbf{A}^{k} & 0 \end{bmatrix} \begin{bmatrix} \Delta\mathbf{q} \\ -\lambda_{li} \end{bmatrix} = \begin{bmatrix} -\mathbf{g}^{k} \\ \mathbf{b}^{k} \end{bmatrix} \tag{4.46}$$

The linear system of equations (4.46) is also always compatible because only linearly dependent equations have been added to (4.45). If instead of equation (4.39), the equivalent equations (4.40) and (4.41) are used, another equivalent and compatible linear system of equations is obtained

$$\begin{bmatrix} \mathbf{H} & \mathbf{A}^{k} \\ \mathbf{A}^{k} & 0 \end{bmatrix} \begin{bmatrix} \Delta\mathbf{q} \\ -\lambda \end{bmatrix} = \begin{bmatrix} -\mathbf{g}^{k} \\ \mathbf{b}^{k} \end{bmatrix} \tag{4.47}$$

$$\lambda_{ld} = 0$$

The three previous linear systems of equations (4.45), (4.46) and (4.47) are equivalent, i.e. they all have the same set of solutions and can be used to derive different implementations of OTM. In a strict sense, the linear system of equations (4.47) is not equivalent to (4.45) and (4.46) because it has $(n - p)$ more unknowns (λ_{ld}). The term equivalent is used in the sense that once λ_{ld} is set to zero, the set of solutions for $\Delta\mathbf{q}$ and λ_{li} is the same for the three linear systems of equations.

These systems of equations are only necessary conditions for a minimum of the QP subproblem (4.31). A maximum and a saddle point also satisfy these equations.

It has been demonstrated that the linear systems of equations (4.45), (4.46) and (4.47) are compatible and equivalent but the uniqueness of the solution has still not been studied.

4.5.4 GLOBAL ISOLATED MINIMUM

In this section, it is demonstrated that under certain conditions, the solution of the linear system of equations (4.47) or its equivalents is unique. Furthermore, this unique solution is a global isolated minimum of the QP subproblem (4.31) at any iteration point $\mathbf{q}^k$, including the solution $\mathbf{q}^*$.

Suppose that $\mathbf{Z}$ is a basis for the nullspace of $\mathbf{A}^k$ and assume that the column vectors $\Delta\mathbf{q}^*$ and λ^* satisfy equation (4.47) (necessary condition) and the reduced-Hessian matrix

$$\mathbf{Z}^T\mathbf{H}\,\mathbf{Z} \tag{4.48}$$

is positive definite, then $\Delta\mathbf{q}^*$ is a global isolated minimum of the QP subproblem (4.31). The positive definiteness of the reduced-Hessian matrix $\mathbf{Z}^T\mathbf{H}\mathbf{Z}$ is a sufficient condition for a global isolated minimum of (4.31). This can be proved in three steps:

1. Firstly, for over-guided and exactly-guided kinematic problems, it can be demonstrated that the reduced-Hessian matrix $\mathbf{Z}^T\mathbf{H}\mathbf{Z}$ is positive definite at any iteration point $\mathbf{q}^k$.
2. Secondly, suppose that the reduced-Hessian matrix $\mathbf{Z}^T\mathbf{H}\mathbf{Z}$ is positive definite, then the solution of the linear system of equations (4.47) is unique.
3. Thirdly, suppose that the reduced-Hessian matrix $\mathbf{Z}^T\mathbf{H}\mathbf{Z}$ is positive definite, then the unique solution of (4.47) is a global isolated minimum of the QP subproblem (4.31).

The proofs presented for the second and third points are based on Nocedal and Wright (1999). Note that the only requirement for a global isolated minimum of (4.31) is that the kinematic problem must be exactly-guided or over-guided and the other conditions derive from this one.

4.5.4.1 Positive definiteness of $\mathbf{Z}^T\mathbf{H}\mathbf{Z}$

If a kinematic problem is over-guided or exactly-guided, then the reduced-Hessian matrix $\mathbf{Z}^T\mathbf{H}\mathbf{Z}$ is positive definite at any iteration point $\mathbf{q}^k$. This can be proved in two steps; firstly, suppose that the kinematic problem is over-guided

or exactly-guided, then the matrix $(\mathbf{A}^k+\mathbf{H})$ is positive definite at any iteration point $\mathbf{q}^k$; secondly, suppose that $(\mathbf{A}^k+\mathbf{H})$ is positive definite, then $\mathbf{Z}^T\mathbf{H}\mathbf{Z}$ is positive definite.

Note that taking into account (4.24) and (4.28), matrix $(\mathbf{A}^k+\mathbf{H})$ can be written as follows

$$(\mathbf{A}^k + \mathbf{H}) = \begin{bmatrix} \boldsymbol{\Phi}_{\mathbf{q}}^{k\,\mathrm{T}} & \mathbf{S}^{\mathrm{T}} \end{bmatrix} \begin{bmatrix} \boldsymbol{\Phi}_{\mathbf{q}}^{k} \\ \mathbf{S} \end{bmatrix} \tag{4.49}$$

Consider an exactly-guided kinematic problem without redundant constraints, that has m $(= n - s)$ independent nonlinear kinematic constraints Φ and r $(=s)$ driving constraints Ψ. This problem can be solved with the Newton-Raphson method presented in section 4.2.2.1. The Jacobian matrix of the driving constraints (see equation (4.12)) at any iteration point $\mathbf{q}^k$ is constant

$$\boldsymbol{\Psi}_{\mathbf{q}}^{k} = \mathbf{S} \tag{4.50}$$

Then, equation (4.15) can be written as

$$\begin{bmatrix} \boldsymbol{\Phi}_{\mathbf{q}}^{k} \\ \mathbf{S} \end{bmatrix} \Delta\mathbf{q}^k = -\begin{bmatrix} \boldsymbol{\Phi}^{k} \\ \boldsymbol{\Psi}^{k} \end{bmatrix} \tag{4.51}$$

This equation is compatible determined at any iteration point because an exactly-guided kinematic problem is being considered. This means that the matrix

$$\mathbf{B} = \begin{bmatrix} \boldsymbol{\Phi}_{\mathbf{q}}^{k} \\ \mathbf{S} \end{bmatrix} \tag{4.52}$$

has full rank, otherwise the equation (4.51) would be underdetermined which is contrary to the hypothesis of an exactly-guided kinematic problem. The rank of $\boldsymbol{\Phi}_{\mathbf{q}}^{k}$ is $(n - s)$ and the rank of $\mathbf{S}$ is always r $(=s)$. Hence, $\mathbf{S}$ must be such that it complements the rank of $\boldsymbol{\Phi}_{\mathbf{q}}^{k}$ to n. From a physical point of view this means that the driven coordinates must be chosen in such a way that the motion of all DoFs is prescribed.

If the exactly-guided kinematic problem has some redundant constraints, the matrix $\mathbf{B}$ has some additional dependent rows but its column rank is n. If

the kinematic problem is over-guided with or without redundant constraints, the matrix **B** has also full column rank because only dependent rows are added.

Note that, as explained in the previous sections, exactly-guided problems with redundant constraints and over-guided kinematic problem are not solved with equation (4.51) which is used here only for the purpose of the analysis of the matrix **B**.

It can be concluded that when a kinematic problem is exactly-guided or over-guided with or without redundant constraint, the column rank of matrix **B** is always n. Then, the matrix $\mathbf{B}^{\mathrm{T}}\mathbf{B}$ has also rank n and is positive definite, i.e. $(\mathbf{A}^k+\mathbf{H})$ is positive definite, hence

$$\Delta\mathbf{q}^{\mathrm{T}}(\mathbf{A}^k+\mathbf{H})\Delta\mathbf{q}>0,\quad \forall\Delta\mathbf{q}\in\Re^n,\ \Delta\mathbf{q}\neq 0 \tag{4.53}$$

Suppose now that **Z** is a basis for the nullspace of $\mathbf{A}^k$, then a column vector $\Delta\mathbf{q}_h$ that belongs to the nullspace of $\mathbf{A}^k$ ($\mathbf{A}^k\Delta\mathbf{q}_h=0$) can be written as a linear combination of the columns of **Z** for some vector $\mathbf{y}\in\Re^{n-p}$ as follows

$$\Delta\mathbf{q}_h=\mathbf{Z}\,\mathbf{y} \tag{4.54}$$

If only the column vectors $\Delta\mathbf{q}_h$ are considered, relation (4.54) can be substituted in (4.53) giving

$$(\mathbf{Z}\mathbf{y})^{\mathrm{T}}(\mathbf{A}^k+\mathbf{H})\mathbf{Z}\,\mathbf{y}=\mathbf{y}^{\mathrm{T}}\mathbf{Z}^{\mathrm{T}}\mathbf{A}^k\mathbf{Z}\,\mathbf{y}+\mathbf{y}^{\mathrm{T}}\mathbf{Z}^{\mathrm{T}}\mathbf{H}\,\mathbf{Z}\,\mathbf{y}>0,\quad \forall\,\mathbf{y}\neq 0 \tag{4.55}$$

The basis **Z** of the nullspace satisfies $\mathbf{A}^k\mathbf{Z}=0$, then

$$\mathbf{y}^{\mathrm{T}}\mathbf{Z}^{\mathrm{T}}\mathbf{H}\,\mathbf{Z}\,\mathbf{y}>0,\quad \forall\,\mathbf{y}\neq 0 \tag{4.56}$$

From (4.56) it can be concluded that the reduced-Hessian matrix $\mathbf{Z}^{\mathrm{T}}\mathbf{H}\mathbf{Z}$ is positive definite.

4.5.4.2 Uniqueness of the solution

Assume that the reduced-Hessian matrix $\mathbf{Z}^{\mathrm{T}}\mathbf{H}\mathbf{Z}$ is positive definite, then the solution of the linear system of equations (4.47) is unique. This can be proved as follows. Suppose that there are column vectors $\Delta\mathbf{q}_h$ and λ, both different from zero, such that

$$\begin{bmatrix}\mathbf{H} & \mathbf{A}^k\\ \mathbf{A}^k & 0\end{bmatrix}\begin{bmatrix}\Delta\mathbf{q}_h\\ -\lambda\end{bmatrix}=\begin{bmatrix}0\\0\end{bmatrix} \tag{4.57}$$

$$\lambda_{ld}=0$$

Since $\mathbf{A}^k\Delta\mathbf{q}_h=0$ from (4.57), it can be written that

$$0 = \begin{bmatrix}\Delta\mathbf{q}_h^{\mathrm{T}} & -\boldsymbol{\lambda}^{\mathrm{T}}\end{bmatrix}\begin{bmatrix}\mathbf{H} & \mathbf{A}^k \\ \mathbf{A}^k & 0\end{bmatrix}\begin{bmatrix}\Delta\mathbf{q}_h \\ -\lambda\end{bmatrix} = \begin{bmatrix}\Delta\mathbf{q}_h^{\mathrm{T}}\mathbf{H}\,\Delta\mathbf{q}_h \\ 0\end{bmatrix} \qquad (4.58)$$
$$\lambda_{ld} = 0$$

Since the column vector $\Delta\mathbf{q}_h$ belongs to the nullspace of $\mathbf{A}^k$, it can be written as a linear combination of the columns of $\mathbf{Z}$ as in (4.54). Then, from (4.58)

$$0 = \Delta\mathbf{q}_h^{\mathrm{T}}\,\mathbf{H}\,\Delta\mathbf{q}_h = \mathbf{y}^{\mathrm{T}}\mathbf{Z}^{\mathrm{T}}\mathbf{H}\,\mathbf{Z}\,\mathbf{y} \qquad (4.59)$$

Then, the column vector $\mathbf{y}$ must be zero because $\mathbf{Z}^{\mathrm{T}}\mathbf{H}\mathbf{Z}$ is positive definite. Therefore, $\Delta\mathbf{q}_h$ must be zero and from (4.57) it can be written that

$$\begin{aligned}\mathbf{A}^k\lambda &= 0 \\ \lambda_{ld} &= 0\end{aligned} \qquad (4.60)$$

The Lagrange multipliers (λ_{ld}) associated with the dependent columns of $\mathbf{A}^k$ must be zero, so

$$\mathbf{A}_{li}^k\,\lambda_{li} = 0 \qquad (4.61)$$

The columns of $\mathbf{A}_{li}^k$ are linearly independent, which implies that λ_{li} is zero and then, λ must be zero. It can be concluded that (4.57) is satisfied only if $\Delta\mathbf{q}_h$ and λ are zero. Consequently, the linear system of equations (4.57) has a unique solution.

4.5.4.3 Global isolated minimum of the QP subproblem

Suppose that the column vectors $\Delta\mathbf{q}^*$ and λ^* satisfy equation (4.47) and the reduced-Hessian matrix $\mathbf{Z}^{\mathrm{T}}\mathbf{H}\mathbf{Z}$ is positive definite, then $\Delta\mathbf{q}^*$ is a global isolated minimum of the QP subproblem (4.31). This can be proved as follows. Assume that $\Delta\mathbf{q}$ is a column vector that satisfies the linear constraint equations of the QP subproblem (4.31). Then

$$\mathbf{A}^k\Delta\mathbf{q}^* = \mathbf{b}^k \qquad (4.62)$$

$$\mathbf{A}^k\Delta\mathbf{q} = \mathbf{b}^k \qquad (4.63)$$

Consider a column vector $\mathbf{u}$ defined as

$$\Delta\mathbf{q}^* = \Delta\mathbf{q} + \mathbf{u} \qquad (4.64)$$

Subtracting (4.62) and (4.63) we obtain

$$\mathbf{A}^k(\Delta\mathbf{q}^* - \Delta\mathbf{q}) = \mathbf{A}^k\,\mathbf{u} = 0 \tag{4.65}$$

Substituting the column vector $\Delta\mathbf{q}$ expressed as $(\Delta\mathbf{q}^* - \mathbf{u})$ in the objective function in (4.31) gives

$$\begin{aligned} h(\Delta\mathbf{q}) &= \frac{1}{2}\left(\Delta\mathbf{q}^* - \mathbf{u}\right)^{\mathrm{T}}\mathbf{H}\left(\Delta\mathbf{q}^* - \mathbf{u}\right) + \mathbf{g}^{k\,\mathrm{T}}\left(\Delta\mathbf{q}^* - \mathbf{u}\right) + f^k \\ &= \frac{1}{2}\mathbf{u}^{\mathrm{T}}\mathbf{H}\,\mathbf{u} - \mathbf{u}^{\mathrm{T}}\mathbf{H}\,\Delta\mathbf{q}^* - \mathbf{g}^{k\,\mathrm{T}}\mathbf{u} + h(\Delta\mathbf{q}^*) \end{aligned} \tag{4.66}$$

The second equation in (4.47) is

$$\mathbf{H}\,\Delta\mathbf{q}^* = -\mathbf{g}^k + \mathbf{A}^k\lambda \tag{4.67}$$

Multiplying this relation by $\mathbf{u}^{\mathrm{T}}$ and considering (4.65), we obtain

$$\mathbf{u}^{\mathrm{T}}\mathbf{H}\,\Delta\mathbf{q}^* = \mathbf{u}^{\mathrm{T}}(-\mathbf{g}^k + \mathbf{A}^k\lambda) = -\mathbf{u}^{\mathrm{T}}\mathbf{g}^k \tag{4.68}$$

Substituting relation (4.68) in (4.66) gives

$$h(\Delta\mathbf{q}) = \frac{1}{2}\mathbf{u}^{\mathrm{T}}\mathbf{H}\,\mathbf{u} + h(\Delta\mathbf{q}^*) \tag{4.69}$$

Since $\mathbf{u}$ lies in the nullspace of $\mathbf{A}^k$, it can be written as a linear combination of the columns of $\mathbf{Z}$ as in (4.54), so that

$$h(\Delta\mathbf{q}) = \frac{1}{2}\mathbf{y}^{\mathrm{T}}\mathbf{Z}^{\mathrm{T}}\mathbf{H}\,\mathbf{Z}\,\mathbf{y} + h(\Delta\mathbf{q}^*) \tag{4.70}$$

Considering the positive definiteness of $\mathbf{Z}^{\mathrm{T}}\mathbf{H}\mathbf{Z}$, it can be concluded that $h(\Delta\mathbf{q}) > h(\Delta\mathbf{q}^*)$ except when $\mathbf{y} = 0$, that is, when $\Delta\mathbf{q} = \Delta\mathbf{q}^*$. Therefore, $\Delta\mathbf{q}^*$ is the unique global isolated minimum of the QP subproblem (4.31).

It has been demonstrated that if a kinematic problem is over-guided or exactly-guided, according to the definitions in section 4.2.1, the solution of the linear system of equations (4.47) or its equivalents is a global isolated minimum of the QP subproblem (4.31). In other words, all points $\mathbf{q}^k$ in the sequence that converge to the solution are global isolated minima of the QP subproblem (4.31). Therefore, the last point in the sequence is a global isolated minimum of OTP.

The linear system of equations (4.47) can be used in practice to solve QP subproblem (4.31) only if the variables in λ_{ld} can be identified and then, set to

zero. In the next section we demonstrate that this is possible and how it can be achieved.

4.5.5 ANALYSIS OF THE UNDERDETERMINACY OF THE SOLUTION

An a priori difficulty to solve the linear system of equations (4.47) is how to detect the Lagrange multipliers λ_{ld} associated with the linearly dependent gradient vectors of the constraints and set them to zero. In this section, we show that for exactly-guided and over-guided kinematic problems the free variables of the linear system of equations (4.47) are always in the column vector λ. Therefore, the free variables in λ are λ_{ld} and they can be set to zero.

Section 4.5.4.2 demonstrates that for exactly-guided and over-guided kinematic problems the solution of the linear system of equations (4.47) is unique. Then, the solution of the equivalent linear system of equations (4.45) is also unique. Therefore, matrix in (4.45) has full rank and its columns are linearly independent.

In (4.46) only linearly dependent rows are added to the matrix, then its columns are still linearly independent. In (4.47) linearly dependent columns are added to the matrix of the linear system of equations and the associated variables λ_{ld} are included in the column vector of unknowns. The linearly dependent columns added to the matrix in (4.47) are only linear combinations of the columns of $\mathbf{A}_{li}^{k}$. Therefore, the free variables are associated only to the column vector of Lagrange multipliers λ, i.e. the free variables are always in the column vector of Lagrange multipliers λ and they cannot be exchanged with variables of $\Delta\mathbf{q}$.

Note that the different matrix factorisation algorithms can select different columns in $\mathbf{A}^{k}$ as dependent columns. Therefore, the selection of Lagrange multipliers λ_{ld} associated with $\mathbf{A}_{ld}^{k}$ will depend on the matrix factorisation algorithm used. The column vector λ will be different for each matrix factorisation but $\Delta\mathbf{q}$ will be always the same because equivalent linear constraints are used provided that λ_{ld} is set to zero.

The underdeterminacy of the solution can also be investigated using the nullspace of matrix in (4.47). The general solution of (4.47) can be written as

$$\begin{bmatrix} \Delta\mathbf{q} \\ \lambda \end{bmatrix} = \begin{bmatrix} \Delta\mathbf{q}_0 \\ \lambda_0 \end{bmatrix} + \begin{bmatrix} \mathbf{M} \\ \mathbf{N} \end{bmatrix} \mathbf{k} \tag{4.71}$$

where the first column vector in the right-hand side is a particular solution of (4.47) and the second term is the general solution of the homogeneous system associated with (4.47). The matrix

$$\begin{bmatrix} \mathbf{M} \\ \mathbf{N} \end{bmatrix} \tag{4.72}$$

is a basis of the nullspace of matrix in (4.47). Therefore, its size is $2n \times (n-p)$ and has full column rank. Both matrices $\mathbf{M}$ and $\mathbf{N}$ are $n \times (n-p)$. The column vector $\mathbf{k}$ is $(n-p) \times 1$ and contains the free variables. The nullspace must satisfy that

$$\mathbf{H}\,\mathbf{M} + \mathbf{A}^k \mathbf{N} = 0 \tag{4.73}$$

$$\mathbf{A}^k \mathbf{M} = 0 \tag{4.74}$$

From (4.74) it can be stated that each column of $\mathbf{M}$ belongs to the nullspace of $\mathbf{A}^k$. $\mathbf{M}$ can range from a zero matrix to a basis of the nullspace of $\mathbf{A}^k$. Suppose that $\mathbf{Z}$ is a basis for the nullspace of $\mathbf{A}^k$. Then, $\mathbf{M}$ can be written as

$$\mathbf{M} = \mathbf{Z}\,\mathbf{F} \tag{4.75}$$

where $\mathbf{Z}$ is $n \times (n-p)$ and has full column rank and $\mathbf{F}$ is $(n-p) \times (n-p)$ and can range from a zero matrix to a change of basis matrix. Substituting the relationship (4.75) into (4.73) and multiplying (4.73) by $\mathbf{Z}^T$ gives

$$\mathbf{Z}^T\mathbf{H}\,\mathbf{Z}\,\mathbf{F} + \mathbf{Z}^T\mathbf{A}^k\mathbf{N} = 0 \tag{4.76}$$

Since $\mathbf{A}^k$ is symmetric and $\mathbf{Z}$ satisfies that $\mathbf{A}^k\mathbf{Z}=0$, then

$$\mathbf{Z}^T\mathbf{H}\,\mathbf{Z}\,\mathbf{F} = 0 \tag{4.77}$$

But matrix $\mathbf{Z}^T\mathbf{H}\mathbf{Z}$ is positive definite for the kinematic problems studied in this thesis (see section 4.5.4.1), so $\mathbf{F}$ must be a zero matrix to satisfy (4.77). Therefore, from (4.75) we have that $\mathbf{M}$ is a zero matrix. Furthermore, since matrix (4.72) must have full column rank, then from (4.73) it can be concluded that $\mathbf{N}$ must be a basis for the nullspace of $\mathbf{A}^k$. Substituting these results in (4.71) yields

$$\begin{bmatrix} \Delta\mathbf{q} \\ \lambda \end{bmatrix} = \begin{bmatrix} \Delta\mathbf{q}_0 \\ \lambda_0 \end{bmatrix} + \begin{bmatrix} 0 \\ \mathbf{N} \end{bmatrix} \mathbf{k} \tag{4.78}$$

From this equation it can be concluded that the underdeterminacy of the linear system of equations (4.47) is located only in the column vector $\boldsymbol{\lambda}$.

4.5.6 NUMERICAL METHODS FOR OTM

In this section, different numerical methods to solve the linear system of equations (4.47) are proposed. The linear system in (4.47) can be written as

$$\mathbf{C}\,\mathbf{y} = \mathbf{e} \tag{4.79}$$

where $\mathbf{C}$ is the coefficient matrix, $\mathbf{y}$ is the vector of unknowns and $\mathbf{e}$ is the vector of independent terms. The matrix $\mathbf{C}$ is composed of matrices $\mathbf{A}^k$ and $\mathbf{H}$. Recall that $\mathbf{H}$ is an $n \times n$ constant sparse positive semidefinite diagonal matrix (section 4.5.1) and $\mathbf{A}^k$ is a $n \times n$ sparse symmetric positive semidefinite matrix with rank p where $(n - s) \leq p \leq n$ (section 4.5.2). Then, $\mathbf{C}$ is sparse, symmetric and in general singular. Furthermore, it can demonstrated that $\mathbf{C}$ is indefinite (Fletcher, 1987; Nocedal and Wright, 1999). Both matrices $\mathbf{A}^k$ and $\mathbf{C}$ are singular and their condition number is infinite. Therefore, stable numerical methods are required in order to detect the linearly dependent constraints and to set their associated variables λ_{ld} to zero.

Three classical methods for solving (4.47) when $\mathbf{A}^k$ is $m \times n$ with $m \leq n$ and has full row rank are the direct solution method, the nullspace method and the range space method (Nocedal and Wright, 1999). The range space method is not valid for solving (4.47) because it requires $\mathbf{H}$ to be positive definite. The direct solution method and the nullspace method can be used for solving (4.47) but they must be modified in order to take into account the condition that λ_{ld} must be set to zero.

The direct solution method consists in performing a factorisation of $\mathbf{C}$ involving triangular matrices and solving (4.47) using forward and/or back-substitution. The factorisation can be performed with a direct method or an iterative method. Iterative methods provided in Matlab® 7.0.1 have been tested but have not converged probably due to the bad conditioning of $\mathbf{C}$. Two direct methods based on a QR factorisation of $\mathbf{C}$ are proposed in this thesis, the direct QR method (section 4.5.6.1) and the two-step QR method (section 4.5.6.2).

The nullspace method requires knowledge of a basis of the nullspace of $\mathbf{A}^k$ and it exploits the block structure of $\mathbf{C}$ to decouple (4.47) into two smaller systems. A nullspace method, conveniently modified to take into account the condition that λ_{ld} must be set to zero, is proposed in section 4.5.6.3.

An additional method which does not solve (4.47) is also proposed. This method, called two-step LU method, is based on the LU decomposition of **C** and solves the QP subproblem (4.25). It is included for testing the incidence on practical problems of the incompatibility issue described in section 4.5.2 and for comparison with the three previous methods.

Summarising, four methods for solving (4.47) are considered: direct QR method, two-step QR method, nullspace method and two-step LU method. These methods are presented in this section but their efficiency is analysed in Chapter 6. The four methods have been implemented in Matlab® 7.0.1.

4.5.6.1 Direct QR method

The direct QR method is based on a QR factorisation of **C**, which has the form

$$\mathbf{C} = \mathbf{QR} \tag{4.80}$$

where **Q** is a $2n \times 2n$ orthogonal matrix and **R** is $2n \times 2n$ upper triangular matrix. This factorisation can be used to compute the solution of (4.47) using the following procedure:

1. Set $\mathbf{e}_0 = \mathbf{Q}^T\mathbf{e}$.
2. Solve $\mathbf{Ry} = \mathbf{e}_0$ for **y** by performing back-substitution.

If **Q** is not required for further computations, $\mathbf{e}_0$ can be computed directly and efficiently without computing **Q** explicitly. In this thesis, the Q-less QR factorisation implemented in Matlab® is used to calculate **R** and $\mathbf{e}_0$.

The matrix **R** computed by Matlab® does not have its pivots in the main diagonal and a permutation matrix **P** must be built in order to reorder **R** and relocate its pivots in the main diagonal. By introducing **R**, **P** and $\mathbf{e}_0$ into equation (4.79) it can be rewritten as follows

$$\mathbf{R}_0\,\mathbf{y}_0 = \mathbf{e}_0 \tag{4.81}$$

where $\mathbf{R}_0 = \mathbf{RP}$ and $\mathbf{y}_0 = \mathbf{P}^T\mathbf{y}$. The upper triangular matrix $\mathbf{R}_0$ has its pivots in the main diagonal. $\mathbf{R}_0$ and $\mathbf{e}_0$ have the following structure

$$\mathbf{R}_0 = \begin{bmatrix} \mathbf{R}_1 & \mathbf{D}_1 \\ 0 & 0 \end{bmatrix}, \quad \mathbf{e}_0 = \begin{bmatrix} \mathbf{e}_1 \\ 0 \end{bmatrix} \tag{4.82}$$

where $\mathbf{R}_1$ is $(n + p) \times (n + p)$ and upper triangular, $\mathbf{D}_1$ is $(n + p) \times (n - p)$ and $\mathbf{e}_1$ is $(n + p) \times 1$.

Section 4.5.5 demonstrates that the underdeterminacy in the linear system of equations (4.47) is only in λ. Then, the free variables in $\mathbf{y}_0$ form the column vector λ_{ld}, which must be set to zero. The column vector of unknowns $\mathbf{y}_0$ can be written as

$$\mathbf{y}_0 = \begin{bmatrix} \mathbf{y}_1 \\ 0 \end{bmatrix} \tag{4.83}$$

where $\mathbf{y}_1$ is $(n + p) \times 1$ and can be obtained using back-substitution from the following upper-triangular system of linear equations

$$\mathbf{R}_1 \, \mathbf{y}_1 = \mathbf{e}_1 \tag{4.84}$$

The column vector $\mathbf{y}$ can be obtained as follows

$$\mathbf{y} = \mathbf{P} \begin{bmatrix} \mathbf{y}_1 \\ 0 \end{bmatrix} \tag{4.85}$$

4.5.6.2 Two-step QR method

The two-step QR method is also based on the QR factorisation. The linear system of equations (4.47) can be written as

$$\mathbf{E}\,\Delta\mathbf{q} + \mathbf{F}\,\lambda = \mathbf{e} \tag{4.86}$$

where $-\lambda$ has been substituted for λ and

$$\mathbf{E} = \begin{bmatrix} \mathbf{H} \\ \mathbf{A}^k \end{bmatrix}, \quad \mathbf{F} = \begin{bmatrix} \mathbf{A}^k \\ 0 \end{bmatrix}, \quad \mathbf{e} = \begin{bmatrix} -\mathbf{g}^k \\ \mathbf{b}^k \end{bmatrix} \tag{4.87}$$

Matrix $\mathbf{E}$ is $2n \times n$ and has full column rank, and matrix $\mathbf{F}$ is $2n \times n$ with rank p, where $(n - s) \le p \le n$. Computing the Q-less QR factorisation of $\mathbf{E}$ with Matlab®, which gives $\mathbf{R}$ and $\mathbf{e}_0$, equation (4.86) can be rewritten as

$$\mathbf{R}\,\Delta\mathbf{q} + \mathbf{F}_0\,\lambda = \mathbf{e}_0 \tag{4.88}$$

where

$$\mathbf{F}_0 = \mathbf{Q}^{\mathrm{T}}\mathbf{F}, \quad \mathbf{e}_0 = \mathbf{Q}^{\mathrm{T}}\mathbf{e} \tag{4.89}$$

$\mathbf{F}_0$ and $\mathbf{e}_0$ are obtained efficiently without computing $\mathbf{Q}$ by using the Q-less QR factorisation implemented in Matlab®. Equation (4.88) has the following structure

$$\begin{bmatrix} \mathbf{R}_1 \\ 0 \end{bmatrix} \Delta\mathbf{q} + \begin{bmatrix} \mathbf{F}_1 \\ \mathbf{F}_2 \end{bmatrix} \lambda = \begin{bmatrix} \mathbf{e}_1 \\ \mathbf{e}_2 \end{bmatrix} \tag{4.90}$$

where $\mathbf{R}_1$ is $n \times n$ and upper triangular with full rank, $\mathbf{F}_2$ is $n \times n$ with rank p, and $\mathbf{F}_1$ is $n \times n$. The Q-less QR factorisation of $\mathbf{F}_2$, where $\mathbf{F}_2 = \mathbf{Q}_2\mathbf{R}_2$, gives a matrix $\mathbf{R}_2$ and a vector $\mathbf{e}_3$. The matrix $\mathbf{R}_2$ is $n \times n$ and upper triangular and $\mathbf{e}_3 = \mathbf{Q}_2^{\mathrm{T}}\mathbf{e}_2$.

The matrix $\mathbf{R}_2$ does not have its pivots in the main diagonal and a permutation matrix $\mathbf{P}_2$ must be built in order to reorder $\mathbf{R}_2$ and relocate its pivots in the main diagonal. By introducing $\mathbf{R}_2$, $\mathbf{P}_2$ and $\mathbf{e}_3$ into the second equation in (4.90), we obtain

$$\mathbf{R}_3 \, \lambda_3 = \mathbf{e}_3 \tag{4.91}$$

where $\mathbf{R}_3 = \mathbf{R}_2\mathbf{P}_2$ and $\lambda_3 = \mathbf{P}_2^{\mathrm{T}}\lambda$. The upper triangular matrix $\mathbf{R}_3$ has its pivots in the main diagonal. $\mathbf{R}_3$ and $\mathbf{e}_3$ have the following structure

$$\mathbf{R}_3 = \begin{bmatrix} \mathbf{R}_4 & \mathbf{D}_4 \\ 0 & 0 \end{bmatrix}, \quad \mathbf{e}_3 = \begin{bmatrix} \mathbf{e}_4 \\ 0 \end{bmatrix} \tag{4.92}$$

where $\mathbf{R}_4$ is $p \times p$ and upper triangular with full rank, $\mathbf{D}_4$ is $p \times (n - p)$ and $\mathbf{e}_4$ is $p \times 1$. The free variables in λ_3 form the column vector λ_{ld} which must be set to zero. The column vector of unknowns λ_3 can be written as

$$\lambda_3 = \begin{bmatrix} \lambda_4 \\ 0 \end{bmatrix} \tag{4.93}$$

where λ_4 is $p \times 1$ and can be obtained using back-substitution from the following upper-triangular system of linear equations

$$\mathbf{R}_4 \, \lambda_4 = \mathbf{e}_4 \tag{4.94}$$

The column vector λ can be obtained as follows

$$\lambda = \mathbf{P}_2 \begin{bmatrix} \lambda_4 \\ 0 \end{bmatrix} \tag{4.95}$$

Finally, the column vector $\Delta\mathbf{q}$ can be obtained using back-substitution from the first equation in (4.90), which is an upper-triangular system of linear equations

$$\mathbf{R}_1 \Delta\mathbf{q} = \mathbf{e}_1 - \mathbf{F}_1 \lambda \tag{4.96}$$

One advantage of the two-step QR method is that it can be checked easily from the QR factorisation of **E** that the kinematic problem is not under-guided. If $\mathbf{R}_1$ is rank deficient, it means that some DoFs are not effectively guided and the problem is under-guided. If $\mathbf{R}_1$ has full rank, the kinematic problem can be exactly-guided or over-guided (section 4.2.1).

4.5.6.3 Nullspace method

The nullspace method requires knowledge of a basis of the nullspace of $\mathbf{A}^k$ and it exploits the block structure of **C** to decouple (4.47) into two smaller systems. A nullspace method conveniently modified to take into account the linearly dependent constraints is presented in this section.

Any solution $\Delta\mathbf{q}$ of (4.47) can be written as the sum of two components, a particular solution $\mathbf{Y}\mathbf{b}^k$ and a displacement on the nullspace of $\mathbf{A}^k$, as follows

$$\Delta\mathbf{q} = \mathbf{Y}\,\mathbf{b}^k + \mathbf{Z}\,\Delta\mathbf{q}_z \tag{4.97}$$

where $\Delta\mathbf{q}_z$ is a column vector with the $(n-p)$ free variables in $\Delta\mathbf{q}$, **Y** is $n \times p$, **Z** is $n \times (n-p)$ and the matrix **[Y Z]** is nonsingular. Furthermore, $\mathbf{A}^k\,\mathbf{Z} = 0$ and $\mathbf{A}^k\,\mathbf{Y} = \mathbf{I}$. **Y** is a right inverse of $\mathbf{A}^k$ and $\mathbf{Y}\mathbf{b}^k$ is a particular solution of the second equation in (4.47). **Z** is a basis for the nullspace of $\mathbf{A}^k$ and has full column rank.

Substituting (4.97) into the first equation in (4.47) and multiplying by $\mathbf{Z}^T$, we obtain

$$\mathbf{Z}^T\mathbf{H}\,\mathbf{Z}\,\Delta\mathbf{q}_z = -(\mathbf{Z}^T\mathbf{g}^k + \mathbf{Z}^T\mathbf{H}\,\mathbf{Y}\,\mathbf{b}^k) \tag{4.98}$$

This system of equations is compatible determined because the reduced-Hessian matrix $\mathbf{Z}^T\mathbf{H}\mathbf{Z}$ is positive definite at any iteration point $\mathbf{q}^k$ (section 4.5.4.1). Then, $\Delta\mathbf{q}_z$ can be obtained from the solution of (4.98), for example by means of a Cholesky factorisation, and finally $\Delta\mathbf{q}$ is obtained by substituting $\Delta\mathbf{q}_z$ into (4.97).

Matrices **Y** and **Z** remain to be calculated. Various different nullspace methods exist, according to the different ways of choosing **Y** and **Z**. For problems in which $\mathbf{A}^k$ is sparse, a sparse Gaussian elimination is recommended for estimating **Y** and **Z** (Nocedal and Wright, 1999). Unfortunately, due to the bad conditioning of $\mathbf{A}^k$ a sparse Gaussian elimination is not appropriate.

Estimating $\mathbf{Y}$ and $\mathbf{Z}$ using a QR factorisation is a good option due to the numerical stability of this factorisation but the drawback is the computation cost of the QR factorisation.

A QR factorisation of $\mathbf{A}^k$ has the following form

$$\mathbf{A}^k\mathbf{P} = \mathbf{QR} = \begin{bmatrix}\mathbf{Q}_1 & \mathbf{Q}_2\end{bmatrix}\begin{bmatrix}\mathbf{R}_1 & \mathbf{D}_1 \\ 0 & 0\end{bmatrix} = \mathbf{Q}_1\begin{bmatrix}\mathbf{R}_1 & \mathbf{D}_1\end{bmatrix} \tag{4.99}$$

where $\mathbf{P}$ is an $n \times n$ permutation matrix, $\mathbf{Q}_1$ is $n \times p$ with orthonormal columns, $\mathbf{Q}_2$ is $n \times (n-p)$ with orthonormal columns, $\mathbf{R}_1$ is $p \times p$ and upper triangular with full rank and $\mathbf{D}_1$ is $p \times (n-p)$ and its columns are linear combinations of the columns of $\mathbf{R}_1$. Consequently, $\mathbf{Q}_1\mathbf{R}_1$ are the first p columns of $\mathbf{A}^k\mathbf{P}$, which are linearly independent and $\mathbf{Q}_1\mathbf{D}_1$ are the last $(n-p)$ columns of $\mathbf{A}^k\mathbf{P}$, which are linearly dependent of the first p columns.

The following choice of matrices $\mathbf{Y}$ and $\mathbf{Z}$, based on the QR decomposition of $\mathbf{A}^k$, satisfy the required properties for $\mathbf{Y}$ and $\mathbf{Z}$

$$\mathbf{Y} = \mathbf{Q}_1\mathbf{R}_1^{-\mathrm{T}}\mathbf{P}_1^{\mathrm{T}}, \quad \mathbf{Z} = \mathbf{Q}_2 \tag{4.100}$$

where $\mathbf{P}_1^{\mathrm{T}}$ is $p \times n$ and is a submatrix of $\mathbf{P}^{\mathrm{T}}$ composed of its first p rows. In the following paragraphs, it will be demonstrated that for this choice of $\mathbf{Y}$ the particular solution $\mathbf{Y}\mathbf{b}^k$ of the second equation in (4.47) is the minimum-norm solution. From (4.99) and since $\mathbf{A}^k$ is symmetric, the transpose of $\mathbf{A}^k\mathbf{P}$ can be written as

$$(\mathbf{A}^k\mathbf{P})^{\mathrm{T}} = \mathbf{P}^{\mathrm{T}}\mathbf{A}^k = \begin{bmatrix}(\mathbf{Q}_1\mathbf{R}_1)^{\mathrm{T}} \\ (\mathbf{Q}_1\mathbf{D}_1)^{\mathrm{T}}\end{bmatrix} \tag{4.101}$$

Note that the permutation matrix $\mathbf{P}^{\mathrm{T}}$ swaps the p linearly independent rows of $\mathbf{A}^k$ to the first p row positions. The following system of equations is equivalent to the second equation in (4.47) because only rows exchanges are performed

$$\mathbf{P}^{\mathrm{T}}\mathbf{A}^k\Delta\mathbf{q} = \mathbf{P}^{\mathrm{T}}\mathbf{b}^k \tag{4.102}$$

Substituting (4.101) into (4.102) and eliminating the $(n-p)$ dependent rows of $\mathbf{A}^k$ and the associated independent terms in $\mathbf{P}^{\mathrm{T}}\mathbf{b}^k$ the following equivalent system is obtained

$$(\mathbf{R}_1\mathbf{Q}_1)^{\mathrm{T}}\Delta\mathbf{q} = \mathbf{P}_1^{\mathrm{T}}\mathbf{b}^k \tag{4.103}$$

where the coefficient matrix $(\mathbf{R}_1\mathbf{Q}_1)^T$ is $p \times n$ and has full row rank and the column vector of independent terms $\mathbf{P}_1^T\mathbf{b}^k$ is $p \times 1$. The minimum-norm solution (Flaquer et al., 2004) of (4.103) is given by

$$\Delta\mathbf{q} = (\mathbf{R}_1\mathbf{Q}_1)\left[(\mathbf{R}_1\mathbf{Q}_1)^T(\mathbf{R}_1\mathbf{Q}_1)\right]^{-1}\mathbf{P}_1^T\mathbf{b}^k \tag{4.104}$$

Since the columns of $\mathbf{Q}_1$ are orthonormal and $\mathbf{R}_1$ is $p \times p$ with full rank, the equation (4.104) can be written as

$$\Delta\mathbf{q} = \mathbf{Q}_1\mathbf{R}_1^{-T}\mathbf{P}_1^T\mathbf{b}^k \tag{4.105}$$

Comparing the definition of $\mathbf{Y}$ in (4.100) and the relationship in (4.105) it can be concluded that the particular solution $\mathbf{Y}\mathbf{b}^k$ of the second equation in (4.47) is the minimum-norm solution.

Note that the Q-less QR factorisation implemented in Matlab®, which requires less computational cost than a QR factorisation, cannot be used because $\mathbf{Q}$ is required to form $\mathbf{Y}$ and $\mathbf{Z}$. Therefore, this method is expected to be less efficient than the two previous ones.

4.5.6.4 Two-step LU method

The two-step LU method is based on the LU decomposition or sparse Gaussian factorisation. This method solves the QP subproblem (4.25) instead of the QP subproblem (4.31). The linear system of equations in (4.25) may contain linearly dependent equations. In order to detect and remove them, a sparse LU decomposition of $\Phi_{\mathbf{q}}^k$ is computed

$$\Phi_{\mathbf{q}}^k = \mathbf{L}\mathbf{U} \tag{4.106}$$

The rows in $\mathbf{U}$ without pivots are linearly dependent and the corresponding rows in $\Phi_{\mathbf{q}}^k$ and the associated elements in Φ^k are eliminated. The new coefficient matrix and the new vector of independent terms are denoted as ${}^{li}\Phi_{\mathbf{q}}^k$ and ${}^{li}\Phi^k$ respectively. The QP subproblem can be rewritten as

$$\begin{aligned} \underset{\Delta\mathbf{q} \in \Re^n}{\text{minimize}} \quad & h(\Delta\mathbf{q}) = \frac{1}{2}\Delta\mathbf{q}^T\mathbf{H}\Delta\mathbf{q} + \mathbf{g}^{kT}\Delta\mathbf{q} + f^k \\ \text{subject to} \quad & {}^{li}\Phi_{\mathbf{q}}^k\,\Delta\mathbf{q} = -\,{}^{li}\Phi^k \end{aligned} \tag{4.107}$$

If the Lagrange's theorem is applied to the QP subproblem (4.107) as in section 4.5.3, the following linear system of equations is obtained

$$\begin{bmatrix} \mathbf{H} & {}^{li}\boldsymbol{\Phi}_{\mathbf{q}}^{k\,\mathrm{T}} \\ {}^{li}\boldsymbol{\Phi}_{\mathbf{q}}^{k} & 0 \end{bmatrix} \begin{bmatrix} \Delta\mathbf{q} \\ -\lambda_{li} \end{bmatrix} = \begin{bmatrix} -\mathbf{g}^{k} \\ -{}^{li}\boldsymbol{\Phi}^{k} \end{bmatrix} \tag{4.108}$$

The linear system of equations (4.108) is solved using a sparse Gaussian factorisation of the coefficient matrix, which is faster than the sparse QR decomposition used in the three previous methods. However, the Gaussian elimination is known to be less stable than the QR decomposition.

The two-step LU method described in this section may fail to find a solution due to the incompatibility issue described in section 4.5.2.

4.5.6.5 Reordering methods

Reordering the columns of a matrix can often make its LU or QR decompositions sparser. Therefore, computing a matrix factorisation of the reordered matrix may take less time and storage than computing the matrix factorisation of the original matrix.

Three reordering methods available in Matlab® have been tested for the direct QR, nullspace and two-step LU numerical methods. The reordering methods are *colperm*, which reorders the matrix according to increasing count of nonzero entries in each column; *symrcm*, which is the reverse Cuthill-McKee ordering; and *symamd*, which is the approximate minimum degree permutation.

For the nullspace and two-step LU numerical methods, none of the reordering methods tested gave an overall better performance than the original matrix. The reasons are one or both of the following:

1. The matrix factorisation of the reordered matrix and original matrix require approximately the same time.
2. Convergence to the solution with the desired tolerance is not achieved using the reordered matrix. However, it is achieved with the original matrix. Probably, the lack of convergence is due to the fact that the reordering methods influence the stability of the matrix factorisation algorithms.

For the direct QR method, the reverse Cuthill-McKee ordering reduces significantly the time per iteration while the other two reordering methods require approximately the same time. Therefore, only the reverse Cuthill-McKee ordering is used in combination with the direct QR method.

4.5.7 LOCAL AND GLOBAL CONVERGENCE

OTM is based on a sequence of QP subproblems which are expected to converge to the solution of OTP. In section 4.5.4, it was demonstrated that each iteration point $\mathbf{q}^k$ is a global isolated minimum of the QP subproblem (4.31). However, it has not been demonstrated that the sequence of iteration points converges to a local minimiser of (4.17).

The convergence of an algorithm can be studied from two points of view, local convergence and global convergence (Boggs and Tolle, 1995). *Local convergence* studies the behaviour of an algorithm when the iteration points are close to a solution. *Global convergence* studies the convergence of an algorithm when the first iteration point is far from the solution. Notice that the term global convergence does not mean that a global minimiser of OTP is calculated. An algorithm is said to be globally convergent if, under suitable conditions, it will converge to some local minimiser from any remote starting point. To ensure global convergence OTM is equipped with two global convergence strategies: merit function and maxmin.

The *merit function strategy* employs a merit function, which is a measure of progress towards a local minimiser, for achieving global convergence. The solution of the QP subproblem $\Delta\mathbf{q}$ is used to generate a new iteration point $\mathbf{q}^{k+1}$ by taking a step from $\mathbf{q}^k$ in the direction of $\Delta\mathbf{q}$. Instead of taking the full step, a shorter step can be considered, and the new iteration point can be written as

$$\mathbf{q}^{k+1} = \mathbf{q}^k + \alpha \Delta\mathbf{q}^k \tag{4.109}$$

where α is the step-length parameter, which can take any value between 0 and 1. The merit function φ used with OTM is defined as

$$\varphi(\mathbf{q}^k + \alpha\Delta\mathbf{q}, \mu) = f(\mathbf{q}^k + \alpha\Delta\mathbf{q}) + \frac{1}{\mu}\left\|\Phi(\mathbf{q}^k + \alpha\Delta\mathbf{q})\right\| \tag{4.110}$$

A simple line search method is used to select a value for α such that the value of the merit function φ is minimised. The value of μ varies at each iteration step and is selected such that it scales the 2-norm of Φ to the objective function f. For an iteration point $\mathbf{q}^k$, the value of μ is defined as

$$\mu = \frac{\left\|\Phi(\mathbf{q}^k + \Delta\mathbf{q})\right\|}{f(\mathbf{q}^k + \Delta\mathbf{q})} \tag{4.111}$$

The *maxmin strategy* does not require the definition of a merit function. It calculates the two different values of α that minimise the objective function and the 2-norm of Φ. From the two values of α, the one associated with the maximum of the two minima is selected as the step-length parameter α.

The global convergence strategy can be activated for all the recorded frames or only at selected frames. Two step-control modes, which define the activation/deactivation pattern of the global convergence strategy, are proposed.

The first step-control mode, called *optimal step-length*, maintains activated the same global convergence strategy for all the frames. The value of the step-length parameter α is defined by one of the two global convergence strategies selected by the user.

The second step-control mode, called *full step-length*, activates and deactivates the global convergence strategies according to the following rules:

1. The global convergence strategy is activated for the first frame and the step-length parameter α is defined by the global convergence strategy selected by the user.
2. The global convergence strategy is deactivated when convergence to the desired tolerance is reached. After convergence is reached, a full step-length ($\alpha = 1$) is taken for the following frames.
3. The global convergence strategy is reactivated when convergence to the desired tolerance is not reached after the maximum number of iterations defined by the user. The default maximum number of iterations is set to 25.

The convergence properties of OTM have been studied by means of numerical experiments provided in Chapter 6 that show that OTM is globally convergent.

4.6 WEIGHTED OTM

All driving constraints in the objective function of OTP so far have the same relative weight. However, OTM can be enhanced by allowing different weighting factors for each driving constraint. In this way the driving constraints considered more reliable can be assigned a higher weighting factor than other less reliable.

The driving constraints can be used to prescribe the motion of any dependent coordinate of the model. Therefore, the motion of any joint angle,

point coordinate or vector coordinate of the multibody model can be prescribed using driving constraints. If each driving constraint is multiplied by a weighting factor, the influence of the associated driven coordinate in the solution is proportional to the corresponding weighting factor.

For an optoelectronic motion capture system this means that different weighting factors can be assigned to each marker or even to each marker coordinate. If the skin movement artifact affecting a marker is known to be higher than others, then the marker can be assigned a smaller weighting factor. In this way the influence of this marker on the solution of the problem is reduced. Different weighting schemes can be used and OTM allows setting a different weighting factor for each driven coordinate at each frame.

For this purpose, a weighting matrix $\mathbf{W}$ is included in the objective function, and OTP is reformulated as follows

$$\begin{aligned} \underset{\mathbf{q}\in\Re^n}{\text{minimize}} \quad & f(\mathbf{q}) = \frac{1}{2}\,\Psi^{\mathrm{T}}(\mathbf{q},t)\;\mathbf{W}(t)\;\Psi(\mathbf{q},t) \\ \text{subject to:} \quad & \Phi(\mathbf{q}) = 0 \end{aligned} \tag{4.112}$$

where $\mathbf{W}$ is a weighting diagonal matrix of size $r \times r$ with positive or zero weighting factors in the main diagonal, which can be different for each driven coordinate at each frame. The NLP (4.112) defines the weighted OTP.

A weighted Hessian matrix $\mathbf{H}_{\mathrm{w}}$ and a weighted gradient vector $\mathbf{g}_w^k$ can be defined as

$$\mathbf{g}_w^k = \mathbf{S}^{\mathrm{T}}\mathbf{W}(\mathbf{S}\mathbf{q}^k - \mathbf{d}) = \mathbf{S}^{\mathrm{T}}\mathbf{W}\,\Psi^k \tag{4.113}$$

$$\mathbf{H}_w = \mathbf{S}^{\mathrm{T}}\mathbf{W}\,\mathbf{S} \tag{4.114}$$

The weighted Hessian matrix $\mathbf{H}_{\mathrm{w}}$ is a diagonal matrix with 0's in the main diagonal except in the positions corresponding to driven coordinates in which the positive or zero weighting factors associated with each coordinate are located. Therefore, $\mathbf{H}_{\mathrm{w}}$ is an $n \times n$ positive semidefinite matrix.

The weighted gradient vector $\mathbf{g}_w^k$ is similar to the unweighted gradient vector $\mathbf{g}^k$ but each element is multiplied by the weighting factor associated with each driving constraint.

In the weighted OTP (4.112), the QP subproblem that has to be solved at each iteration step is

$$\begin{aligned} \underset{\Delta\mathbf{q}\in\Re^n}{\text{minimize}} \quad & h(\Delta\mathbf{q}) = \frac{1}{2}\Delta\mathbf{q}^{\mathrm{T}}\mathbf{H}_w\,\Delta\mathbf{q} + \mathbf{g}_w^{k\,\mathrm{T}}\Delta\mathbf{q} + f^k \\ \text{subject to} \quad & \mathbf{A}^k\Delta\mathbf{q} = \mathbf{b}^k \end{aligned} \tag{4.115}$$

The weighted Hessian matrix and the weighted gradient vector are similar to their unweighted counterparts and the reasoning presented in section 4.5 for the QP subproblem (4.31) is still valid for the weighted QP subproblem (4.115).

4.6.1 EXACTLY SATISFIED DRIVING CONSTRAINTS

In the weighted OTP (4.112) the sum of the squared errors of all the driving constraints is minimised. In general, none of the driving constraints are satisfied because the error is distributed over all of them.

There are situations where some of the driving constraints are required to be satisfied exactly. For example, suppose that in a certain motion the sole of a shoe must remain exactly parallel to the ground at every time. This implies that the motion of a foot vector perpendicular to the sole has to be forced to remain parallel to the ground at every time. If this constraint is included together with all the driving constraints in the objective function of the weighted OTP, it will not be satisfied exactly. A possible solution is to include this type of driving constraints together with the kinematic constraints, making them to be satisfied exactly.

To consider this requirement the driving constraints are divided into two groups: driving constraint included in the objective function Ψ_m, whose errors are minimised and driving constraints included in the equality constraints of the optimisation problem Ψ_s, which are satisfied exactly. Then, the weighted OTP (4.112) can be rewritten as

$$\begin{aligned} \underset{\mathbf{q}\in\Re^n}{\text{minimize}} \quad & f(\mathbf{q}) = \frac{1}{2}\,\Psi_m{}^{\mathrm{T}}(\mathbf{q},t)\;\mathbf{W}_m(t)\;\Psi_m(\mathbf{q},t) \\ \text{subject to:} \quad & \begin{bmatrix} \Phi(\mathbf{q}) \\ \mathbf{W}_s(t)\,\Psi_s(\mathbf{q},t) \end{bmatrix} = 0 \end{aligned} \tag{4.116}$$

where $\mathbf{W}_m$ and $\mathbf{W}_s$ are weighting diagonal matrices associated with Ψ_m and Ψ_s respectively. $\mathbf{W}_m$ is similar to the weighting matrix presented previously. However, the weighting factors of $\mathbf{W}_s$ can be only 0's or 1's. When a weighting

factor is 0, the associated driving constraint is inactive or eliminated from the problem. When a weighting factor is 1, the associated driving constraint is active and it is considered in the solution of the problem. Both weighting matrices $\mathbf{W}_m$ and $\mathbf{W}_s$ can be different at each frame.

Mathematically a zero weighting factor in $\mathbf{W}_s$ implies that a zero equation is added to the nonlinear equality constraints and a linearly dependent equation is induced in the linearised constraints. Fortunately, as explained in section 4.5.3, OTM is designed to handle efficiently linearly dependent equations.

4.6.2 APPLICATIONS OF DRIVING CONSTRAINTS

Driving constraints in Ψ_m or Ψ_s can be used for several purposes. The three following applications have been studied in the frame of this thesis:

1. Motion reconstruction problem.
2. Generation of computer-simulated motions.
3. Convergence to the desired solution.

The motion reconstruction problem consists in estimating the joint angles of a multibody model from measured marker trajectories. The driving constraints are used in this case to prescribe the motion of the marker coordinates of the multibody model using the measured marker coordinates. These driving constraints are included in Ψ_m and the sum of their squared errors is minimised. Some additional driving constraints can be added in Ψ_m or Ψ_s, depending on the requirements, for two possible purposes:

1. Additional driving constraints can be added in Ψ_m or Ψ_s in order to include some known constraints for reducing the influence of possible errors of the measured marker coordinates. For example, suppose that the subject's left hand is grasping a fixed element during a time period of the whole motion and the position of the fixed element is exactly known. Then, a point of the hand can be constrained to remain connected to a point of the fixed element and the associated driving constraint can be included in Ψ_s. The weighting factor associated with this driving constraint must be set to zero while the hand is not in contact with the object and set to 1 while it is in contact. In this case the additional driving constraints are used to reinforce the data obtained from the motion capture system.

2. Additional driving constraints can be added in Ψ_m or Ψ_s to define the position of some body segments of the multibody model whose position is not completely defined by the markers. In this case the additional driving constraints are used to complement the data obtained from the motion capture system. The driving constraints can be used to prescribe the absolute or relative motion of the body segments:

    a. The *relative preservation posture condition* consists in imposing the condition that the relative motion between the bodies whose motion is not completely defined must follow as closely as possible a given reference posture. The reference posture is represented by a set of joint angles which define the relative position between the bodies. This concept is considered in OTM by adding in $\mathbf{q}$ the angles of the joints connecting the bodies and in $\Phi(\mathbf{q})$ the associated kinematic constraints. The motion of the joint angles is prescribed with additional driving constraints included in Ψ_m or Ψ_s depending on the requirements of the user. Then, the values of the joint angles can be set to the desired reference posture. If the driving constraints are included in Ψ_m, the weighting factors can be used to adjust the influence of the relative preservation posture condition in the reconstructed posture. Furthermore, using different weighting factors, a different "flexibility" can be assigned to each joint. In general the weighting factors associated to the relative preservation posture condition are smaller than those associated to markers because markers provide the true position of the model.

    b. The *absolute preservation posture condition* is used to prescribe the absolute motion of the bodies using points and vectors already available in the model. For example, suppose that a subject is sitting with his feet on the ground but there are not enough markers to define the position of the feet. In this situation the condition that the sole of both shoes must remain exactly parallel to the ground at every time can be used to define the position of the feet.

Both preservation posture conditions have been applied to the motions investigated in the projects REALMAN and MoDyCo and they are presented in detail in Chapter 5.

The generation of computer-simulated motions consists in estimating the motion of a whole multibody model from limited data (a few points of the model and/or a few joint angles) provided for example by a computer animator or a motion capture system and additional driving constraints. For example, suppose that a human driver turns right and left the steering wheel while holding it at the ten-to-two position. The motion of a multibody model of the human driver can be obtained from the following conditions:

- One point on each hand is fixed to a corresponding point on the steering wheel. The coordinates of the two points on the steering wheel can be expressed as a function of the steering wheel angle.
- One vector on each hand is parallel to a corresponding vector of the steering wheel. The two vectors on the steering wheel are tangent to the steering wheel and the vector on each hand is contained in the palm hand and it is perpendicular to the fingers in the anatomical position. The coordinates of the two vectors in the steering wheel can be expressed as a function of the steering wheel angle.
- The human driver adopts a ten-to-two relaxed driving position considered as the reference posture. Then, the values of the joint angles of the model can be prescribed to maintain the reference posture as close as possible.

The motion of a multibody model of a human driver can be obtained from the previous conditions where the only input variable is the steering wheel angle. This human driver motion has been used in the MoDyCo project to generate computer-simulated motions and is described in detail in section 5.2.1.

The third application of the driving constraints is the convergence to the desired solution. In section 4.5.7, the global convergence of OTM has been discussed. OTM is equipped with a global convergence strategy, which guarantees convergence to a local minimiser from any remote starting point. Unfortunately, when the initial approximation for the first frame is far from the desired solution, OTM converges to a local minimiser but it may not be the appropriate one. In this situation additional driving constraints can be included in Ψ_m during some initial frames to induce convergence to the desired solution. This approach has been applied to one REALMAN experiment which had a bad initial approximation for the first frame (section 5.4.3.7).

4.6.3 THE MISSING MARKER PROBLEM

In an optoelectronic motion capture system a marker must be visible from at least two cameras to reconstruct its position in the global coordinate system. However, sometimes it is visible to less than two cameras and its position cannot be reconstructed. This is called the *missing marker problem* and represents a major difficulty for this technique.

The missing marker problem can be alleviated by increasing the number of cameras, using special assisting devices like wands or carefully selecting the marker locations on the human body. Another alternative is to use motion capture systems which do not suffer from the missing marker problem like for example electromagnetic systems. However, the missing marker problem cannot be eliminated completely for optoelectronic motion capture systems because the markers can be occluded by different devices located in the motion capture area or by body segments, independently of the number of cameras used or the marker location in the human body.

The missing marker problem is usually handled by estimating the position of the marker during the frames in which it is missing. A common approach is to interpolate the coordinates of a marker during the frames in which it is not visible. The interpolation can be performed using for example cubic splines or other methods (Muijtjens et al., 1997). Missing markers can also be recovered by using the position of the neighbouring markers and assuming a known distance between them (Desjardins et al., 2002). Another method for minimising the missing marker problem consists in using a simplified human model during the estimation of the marker trajectories from 2D camera data (Herda et al., 2001). When a minimum of three non-missing markers on a body segment are present, the position of the missing marker can be estimated using a rigid body assumption (Söderkvist and Wedin, 1993; Wang et al., 2005). However, the methods published so far do not solve completely the missing marker problem when a marker is missing during a large number of consecutive frames.

In this thesis, the missing marker problem is considered from a different point of view, which is complementary to the methods presented above. The strategy used to deal with the missing marker problem is based on three cornerstones:

1. Joint constraints are considered in the human skeletal model and more markers than the minimum strictly necessary to define the posture of the model are used. The joint constraints can be included explicitly (e.g. natural coordinates) or implicitly (e.g. relative coordinates). When some markers are missing, this does not

represent a problem provided that the visible markers are enough to define the posture of the model.

2. The markers with a large number of consecutive missing frames, which cannot be satisfactorily estimated with other methods, are used in the motion reconstruction during the frames they are visible. This is done by exploiting the information provided by a marker when it is visible and ignoring it when is missing.
3. When a marker that is critical for defining the position of a body segment is missing, the body segment position is defined using additional information. In this way, OTM is always able to find a unique solution of the NLP problem (4.116). The implementation of this idea in the frame of OTM is explained in the next section.

The first issue can be illustrated with a simple example. Suppose a double pendulum with a spherical joint (3 DoFs) between the ground and bar 1 and a revolute joint (1 DoF) between bar 1 and bar 2 (Figure 4.7). Bar 1 has three markers (M1, M2 and M3) and bar 2 has also three markers (M4, M5 and M6). The system has four DoFs and different combinations of markers can define its position; for example, markers M1, M2 and M6 or markers M1, M4, M5 and M6 or markers M1, M5 and M6 are three possible combinations. These combinations of visible markers can change between two consecutive frames but the position of the double pendulum is always perfectly defined.

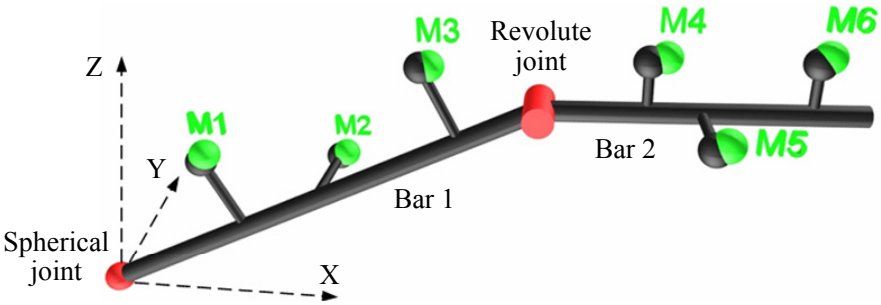

Figure 4.7: Double pendulum. Black balls are model-determined markers, which are rigidly connected to the body, and green balls are markers measured with the motion capture system. M1, M2 and M3 belong to bar 1 and M4, M5 and M6 to bar 2.

The question is how to handle mathematically the second cornerstone of the strategy for missing markers in the frame of OTM. The approach followed consists in setting the three weighting factors (one for each coordinate) associated with a marker to zero when it is missing. This is equivalent to removing the three driving constraints from the problem, which does not cause any numerical problem to the algorithm. The OTM implementation automatically detects the missing markers on each frame and sets their

associated weighting factors to zero. A weighting strategy is proposed in the next section for including and excluding markers in the motion reconstruction problem in order to avoid discontinuities on the reconstructed motions.

4.6.4 WEIGHTING STRATEGIES

In this section two new weighting strategies related to the missing marker problem are proposed. They are denominated progressive weighting and conditional weighting.

The *progressive weighting* strategy consists in progressively decreasing the weighting factor associated with a marker before it is missing, in setting it to zero during the time that marker is not visible, and increasing it progressively after it is visible again. The weighting factor decreases or increases between zero and a maximum weighting factor (w_{max}) in a predefined number of frames (N_f). The selection of both parameters w_{max} and N_f, is not automatic and must be defined by the user.

This strategy is useful for incorporating progressively into the objective function of OTP the markers that were missing a few frames before and are visible at the current frame. It also excludes progressively from the objective function those markers that were visible a few frames before and are missing at the current frame.

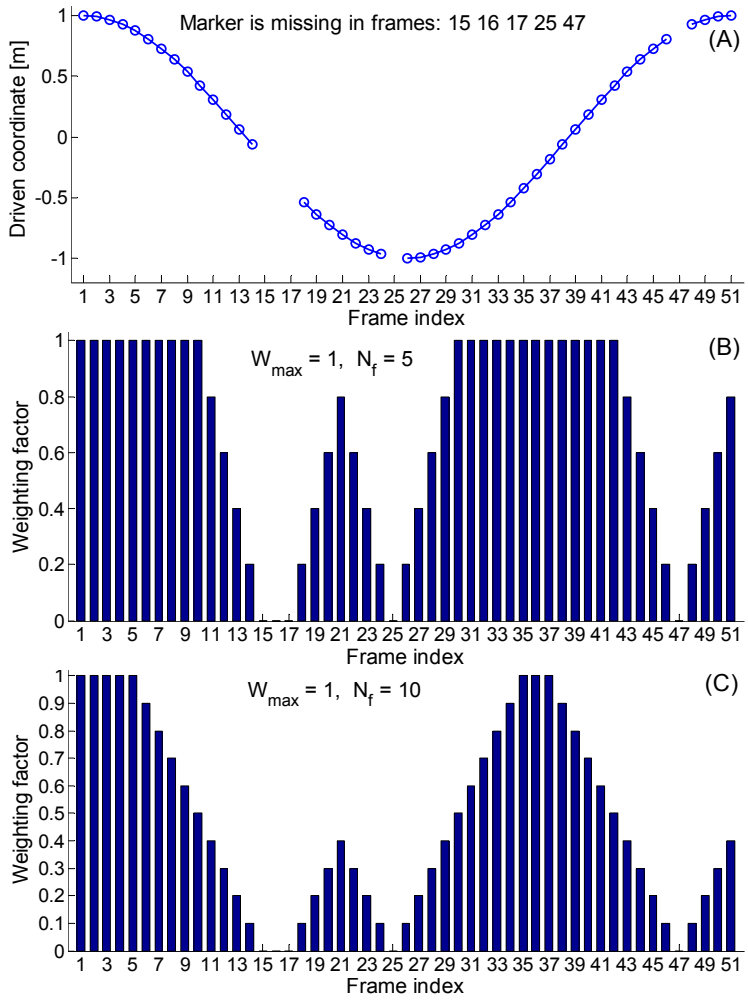

Figure 4.8: Progressive weighting strategy. (A) Generic marker coordinate (x, y or z) recorded during 51 frames. (B) Weighting factors for $N_f = 5$, $w_{max} = 1$ (C) Weighting factors for $N_f = 10$, $w_{max} = 1$.

A weighting strategy in which the weighting factor decreases suddenly from a maximum weighting factor in one frame to zero when the marker is missing in the next frame can produce discontinuities in the joint angles. The progressive weighting strategy eliminates or at least alleviates this problem by including and excluding the missing markers progressively in the objective function.

A simple example is presented in Figure 4.8 to illustrate the progressive weighting strategy. The value of a generic marker coordinate (x, y or z)

recorded during 51 frames is shown in Figure 4.8(A). The marker is missing in frames 15, 16, 17, 25 and 47, so its position at these frames is unknown. Figure 4.8(B) and Figure 4.8(C) show, for $N_f = 5 - w_{max} = 1$ and $N_f = 10 - w_{max} = 1$ respectively, how the weighting factor decreases before the marker is missing, is zero while the marker is missing, and increases after it is visible again. In this example, the small gaps in the data are used for illustrating the progressive weighting strategy. However, in practical applications small gaps (< 10 frames) in the motion capture data are not frequently encountered because they are usually interpolated by the motion capture software.

The value of w_{max} in the progressive weighting strategy can be selected for example, using the method presented by Lu and O'Connor (1999). They proposed an automatic method for selecting the weighting factor associated with each marker. For each body segment they estimated the residual error e_i from equation (4.18), where e_i is the minimum value of the function f. The body segment residual error is a measure of the markers deformation, which is mainly due to skin movement artifact. The weighting factor for all the markers located on body segment i was defined as

$$w_i = \frac{1}{e_i} \tag{4.117}$$

The *conditional weighting* strategy is used to define the position of a body segment when a marker or markers that are critical for defining its position are missing. It consists in activating one or more additional driving constraints while the critical marker is missing and deactivating them when the marker becomes visible. These additional driving constraints are used to define the position of the body segment.

Suppose a human skeletal model where the left hand, which is connected by a spherical joint to the forearm, has two markers and one of them is frequently missing. When the marker is not visible the position of the hand is not completely defined and OTP does not have a unique solution, i.e. the kinematic problem is under-guided and cannot be solved with OTM. One option to transform the problem into over-guided in order to solve it with OTM is to apply the conditional weighting strategy.

The conditional weighting strategy is used to define the relative motion between the body segment whose position cannot be determined and its adjacent body segment, which is assumed to have enough markers for determining its position. The relative angles of the joint connecting the bodies are included in $\mathbf{q}$ and the appropriate kinematic constraints in $\Phi(\mathbf{q})$. The value of one or more joint angles, depending on the joint type and the missing

markers, are prescribed with additional driving constraints included in Ψ_m. In the hand example, the three angles of the spherical joint must be included in the model. If only one marker is missing for some consecutive frames, it is enough to prescribe the value of one joint angle, for example the angle about the longitudinal axis of the hand.

The additional driving constraints associated to joint angles are deactivated, i.e. their associated weighting factors are set to zero, when the critical markers are visible and are activated when they are missing. When the markers are missing the value of the joint angles are set to their values when the markers were visible for the last time.

4.7 RELATIONSHIP BETWEEN OTM AND SQP

OTM can also be considered as a modification or a variant of the Sequential Quadratic Programming method. In this section, the relationship between OTM and the Sequential Quadratic Programming (SQP) method is shown.

The Lagrange's theorem for the OTP (4.17) can be formulated as follows. Suppose that the objective function $f(\mathbf{q})$ and the m nonlinear constraints $\Phi(\mathbf{q})$ are once continuously differentiable and assume that $\mathbf{q}^*$ is a solution of OTP. Then, provided that the Jacobian matrix $\Phi_\mathbf{q}$ of the equality constraints has full row rank, there exists a column vector of Lagrange multipliers λ^* such that

$$\mathbf{g}(\mathbf{q}^*) - \Phi_\mathbf{q}^{\mathrm{T}}(\mathbf{q}^*) \cdot \lambda^* = 0 \tag{4.118}$$

$$\Phi(\mathbf{q}^*) = 0 \tag{4.119}$$

The nonlinear equations (4.118) and (4.119) are only necessary conditions for a solution of OTP. The SQP method can be explained as the Newton-Raphson method applied to find a solution of the system of nonlinear equations given by equations (4.118) and (4.119), which has $n + m$ nonlinear equations and $n + m$ unknowns $\mathbf{q}$ and λ. The Newton-Raphson iteration is given by

$$\begin{bmatrix} \mathbf{W}^k & \Phi_\mathbf{q}^{k\,\mathrm{T}} \\ \Phi_\mathbf{q}^k & 0 \end{bmatrix} \begin{bmatrix} \Delta\mathbf{q} \\ -\Delta\lambda \end{bmatrix} = -\begin{bmatrix} \mathbf{g}^k - \Phi_\mathbf{q}^{k\,\mathrm{T}}\lambda^k \\ \Phi^k \end{bmatrix} \tag{4.120}$$

$$\mathbf{q}^{k+1} = \mathbf{q}^k + \Delta\mathbf{q}$$

$$\lambda^{k+1} = \lambda^k + \Delta\lambda$$

where $\mathbf{W}^k$ is the matrix of partial derivatives of equation (4.118) with respect to the column vector **q**, which can be written as

$$\mathbf{W}^k = \mathbf{H} - \sum_{i=1}^{m} \lambda_i^k \nabla^2 \phi_i^k \tag{4.121}$$

where $\nabla^2 \phi_i^k$ is the Hessian matrix of the *i*-th kinematic constraint. An equivalent system to (4.120) can be obtained if $\boldsymbol{\Phi}_{\mathbf{q}}^{k\,\mathrm{T}} \boldsymbol{\lambda}^k$ is subtracted from both sides of the first equation in (4.120), obtaining

$$\begin{bmatrix} \mathbf{W}^k & \boldsymbol{\Phi}_{\mathbf{q}}^{k\,\mathrm{T}} \\ \boldsymbol{\Phi}_{\mathbf{q}}^k & 0 \end{bmatrix} \begin{bmatrix} \Delta\mathbf{q} \\ -\boldsymbol{\lambda}^{k+1} \end{bmatrix} = -\begin{bmatrix} \mathbf{g}^k \\ \boldsymbol{\Phi}^k \end{bmatrix} \tag{4.122}$$

$$\mathbf{q}^{k+1} = \mathbf{q}^k + \Delta\mathbf{q}$$

But the iteration (4.122) can be viewed in an alternative way: it can be obtained by applying the Lagrange theorem to the following QP subproblem

$$\begin{aligned} \underset{\Delta\mathbf{q} \in \Re^n}{\text{minimize}} \quad & \frac{1}{2} \Delta\mathbf{q}^{\mathrm{T}} \mathbf{W}^k \Delta\mathbf{q} + \mathbf{g}^{k\,\mathrm{T}} \Delta\mathbf{q} \\ \text{subject to} \quad & \boldsymbol{\Phi}_{\mathbf{q}}^k \Delta\mathbf{q} = -\boldsymbol{\Phi}^k \end{aligned} \tag{4.123}$$

In conclusion, the SQP method can be explained as the iteration (4.122) generated by the Newton-Raphson method applied to (4.118) and (4.119) or as the sequence of QP subproblems given by (4.123).

If $\mathbf{W}^k$ is positive definite and $\boldsymbol{\Phi}_{\mathbf{q}}$ has full row rank, it can be demonstrated that the iteration (4.122) is quadratically convergent (Boggs and Tolle, 1995; Nocedal and Wright, 1999) provided that the initial approximation $\mathbf{q}^0$ is close enough to the solution $\mathbf{q}^*$. Quadratic convergence is not easy to reach in practical methods because it is often difficult to select an initial approximation close enough to the solution.

OTM has associated the QP subproblem (4.31) which resembles the QP subproblem (4.123). In consequence, OTM can be considered as a modification of the SQP method where

- $\mathbf{W}^k$ is substituted by **H** or equivalently the Hessian matrices of the kinematic constraints in (4.121) are neglected. Recall that **H** is a positive semidefinite matrix (section 4.5.1).

- The linear constraint equations of the QP subproblem (4.123) are substituted by the normal equations. The square coefficient matrix of the normal equations is in general rank deficient (section 4.5.2).

It can be concluded that OTP cannot be solved using the standard SQP method because the two assumptions required by it are not satisfied, i.e. matrix **H** is not positive definite and the coefficient matrix of the equality constraints does not have full row rank.

CHAPTER 5

METHODOLOGIES AND EXPERIMENTS

The methodologies developed in this thesis and the experiments to which these methodologies have been applied are presented in this chapter. This thesis has been partially carried out in parallel with two projects, REALMAN (section 1.1.1) and MoDyCo (section 1.1.2). The MoDyCo methodology and experiments presented in this chapter have been developed by the author in the frame of present thesis. REALMAN methodology has been designed by CEIT and other REALMAN partners. REALMAN experiments relevant to this thesis have been designed and executed by Renault, Peugeot-Citroën and INRETS.

The methodology which is typically used to study the human movement can be divided into several steps. First, a kinematic skeletal model of the human body is developed considering different assumptions depending on the level of detail required in the study. Second, the subject-specific parameters of the skeletal model are estimated and the human motion during the activity investigated is measured using a motion capture system. Third, from the skeletal model and the motion capture data, the joint angles, velocities and accelerations can be estimated using Inverse Kinematic analysis. Fourth, if the external forces acting on the human body during the activity investigated are measured and BSPs of the human skeletal model are available, then together with the joint angles, velocities and accelerations, the joint motor torques can be calculated using Inverse Dynamic analysis.

5.1 METHODOLOGY USED IN THE MODYCO PROJECT

The goal of the MoDyCo project is to estimate joint motor torques of a human driver while performing a driving manoeuvre. Two upper body models for studying steering manoeuvres have been presented in sections 3.3.1 and 3.3.2 and one lower limb model for studying braking manoeuvres in section 3.3.3. MoDyCo methodology is divided into three steps (Figure 5.1): Experimental Measurements, Inverse Kinematics and Inverse Dynamics.

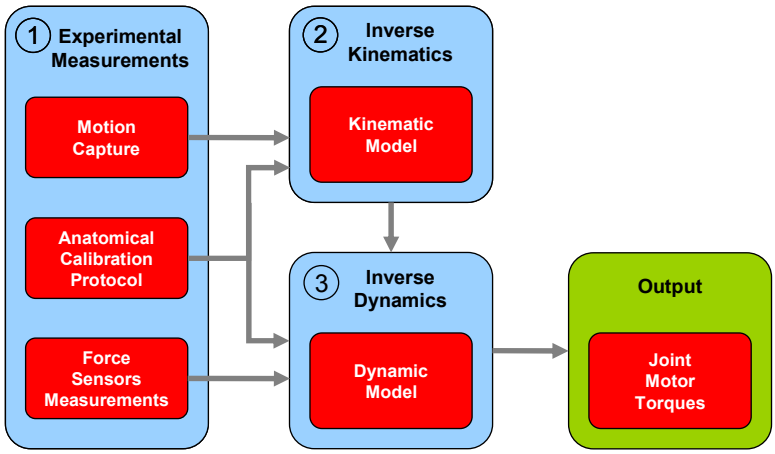

Figure 5.1: Flow chart of the MoDyCo methodology.

During the Experimental Measurements step, the human subject under investigation performs a driving manoeuvre while his motion is recorded with a motion capture system and the forces applied to the vehicle are measured with several force sensors. Furthermore, prior to the actual driving manoeuvre an Anatomical Calibration Protocol (ACP) is applied to the subject, which consists in measuring all the variables required to estimate the subject-specific parameters of a human skeletal model.

The inputs of the Inverse Kinematics step are the subject-specific parameters obtained in the ACP and the motion capture data recorded during the driving manoeuvre. The joint angles of the human skeletal model are calculated from the motion capture data using the Optimal Tracking Method (section 4.5). The joint angular velocities and accelerations are obtained by differentiation of cubic splines fitted to the joint angles.

In the Inverse Dynamics step, the joint motor torques are calculated from the joint angles, velocities and accelerations, measured external forces acting on the subject and BSPs obtained during the ACP.

5.1.1 EXPERIMENTAL MEASUREMENTS

The Experimental Measurements step is divided into three substeps: ACP, Motion Capture and Force Sensors Measurements. The ACP is performed before a driving experiment, Motion Capture and Force Sensors Measurements are performed during the experiment execution.

5.1.1.1 Anatomical calibration protocol

The goal of the Anatomical Calibration Protocol (ACP) is to measure all the variables required to estimate the subject-specific parameters of a human skeletal model of a specific subject. These subject-specific parameters are used to tailor a generic human skeletal model to the subject under investigation.

The Vicon motion capture system is used to measure all the variables of the ACP. The variables measured during ACP are the three-dimensional coordinates of markers and anatomical landmarks (ALs) in the global coordinate system (GCS) in several static predefined postures. ALs required for each human skeletal model have been presented in Chapter 3 and the markers used to measure human motion are presented in section 5.1.1.2 and section C.1 of Appendix C.

The subject-specific parameters of the human skeletal model estimated from the global coordinates of markers and ALs for each body segment are:

- Anthropometric parameters (joint parameters and BSPs) referred to the local coordinate system (LCS) of each body segment.
- Coordinates of the markers located on each body segment referred to the body segment LCS.
- Coordinates of the ALs located on each body segment referred to the body segment LCS.

ACP is divided in four different tasks (Figure 5.2). The first three tasks can be grouped into the Calibrated Anatomical Systems Technique (CAST), which is based on the experimental protocol proposed by Cappozzo et al. (1995). The fourth task consists in estimating the anthropometric parameters of the human skeletal model from the data obtained in the three previous tasks using the methods presented in Chapter 2.

5.1.1.1.1 Calibrated Anatomical Systems Technique (CAST)

CAST is based on a method with the same name proposed by Cappozzo et al. (1995). Cappozzo's CAST method was designed to estimate LCS of the body

segments of the right lower limb and the coordinates of ALs and markers in each body segment LCS. In this thesis, CAST has been applied to the right lower limb and both upper limbs, and has been extended to allow the estimation of anthropometric parameters of a human subject. CAST is composed of three different tasks (Figure 5.2): Pointer Technique, TCS Definitions and LCS Definitions.

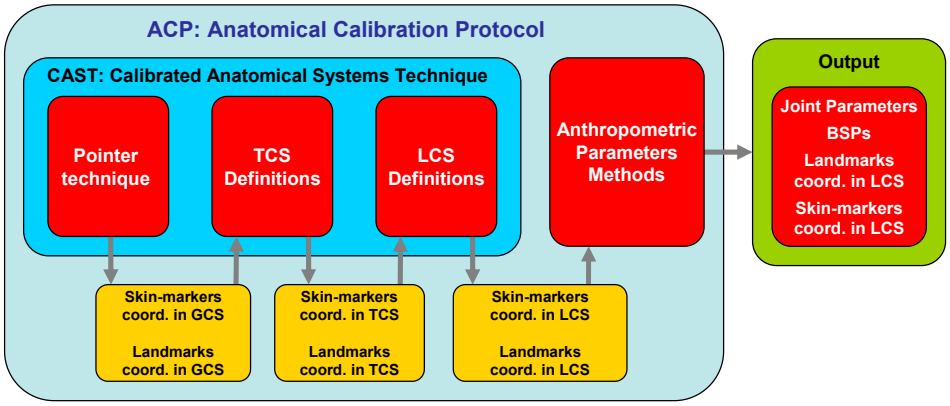

Figure 5.2: Flow chart of the Anatomical Calibration Protocol.

First task: Pointer Technique

The first task, called Pointer Technique, consists in measuring the coordinates of the ALs of each body segment referred to GCS. Two markers, which are called pointer-markers, are mounted at an adequate distance on a pointer (Figure 5.3). The pointer-markers are used to estimate the coordinates of each AL touched by the pointer. The markers located on a body segment are called skin-markers to differentiate them from the pointer-markers. CAST requires a minimum of three skin-markers per body segment as it is explained in the second task.

For each AL, the experimenter locates the tip of the pointer on it while checking that the two pointer-markers and all the skin-markers on the body segment are visible to at least two cameras. Then, one frame is recorded with the motion capture system and the process is repeated for each AL included in the human skeletal model. Each AL is associated with one frame, which is called calibration frame. The skin-markers that must be visible in each calibration frame are described in section C.2.1 of Appendix C.

In general, the relative orientation between body segments is not constrained during CAST. However, some restrictions are imposed due to the requirements of the LCS definitions and BSPs estimation methods. A detailed

description of the restrictions on the relative orientation between body segments is given in section C.2.2 of Appendix C.

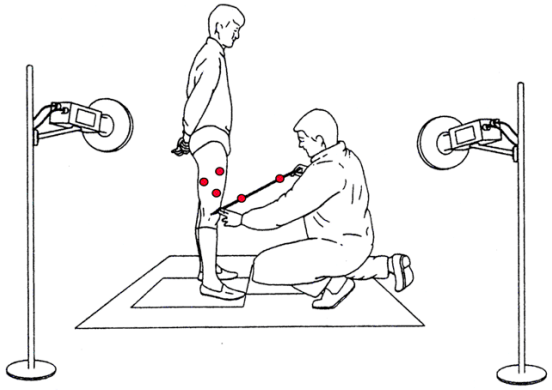

Figure 5.3: Measurement of a femur AL using a pointer with two pointer-markers. Adapted from Cappozzo et al. (1995).

The three-dimensional coordinates of each AL in GCS can be estimated from the pointer-markers as follows. The position vector of the AL j in GCS is denoted by ${}^{G}L_j$, where $j = 1,\ldots,m$ and m is the number of ALs measured on the body segment. The position vectors of the two pointer-markers in GCS, when they point to AL j, are denoted by ${}^{G}PM_1^j$ and ${}^{G}PM_2^j$. The first pointer-marker PM_1 is located far from the pointer tip and the second pointer-marker PM_2 is located close to the pointer tip (Figure 5.4). The three-dimensional coordinates of the AL j in GCS ${}^{G}L_j$ can be estimated from the two pointer-marker coordinates in GCS and the length $L_{Tip\text{-}PM1}$ between the tip of the pointer and the first pointer-marker as follows

$$ {}^{G}L_j = L_{Tip-PM_1} \cdot \frac{{}^{G}PM_2^j - {}^{G}PM_1^j}{\left\| {}^{G}PM_2^j - {}^{G}PM_1^j \right\|} \tag{5.1} $$

The position vector of skin-marker i in GCS is denoted by ${}^{G}SM_i$, where

$$ {}^{G}SM_i = \begin{bmatrix} {}^{G}sm_{ix} \\ {}^{G}sm_{iy} \\ {}^{G}sm_{iz} \end{bmatrix} \quad i = 1,\ldots,n; \quad n \geq 3 \tag{5.2} $$

and n is the number of skin-markers located on the body segment, which must be equal or greater than three.

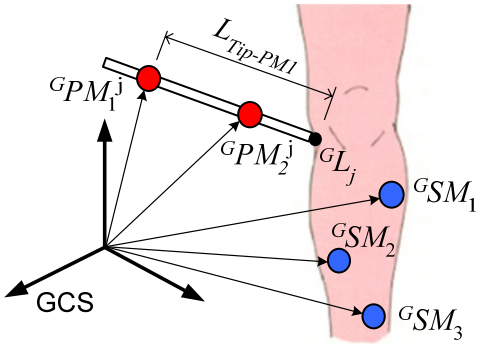

Figure 5.4: Measurement of ${}^{G}L_j$ with the help of a pointer with two pointer-markers.

Second task: TCS Definitions

The second task, called TCS Definitions, consists in estimating the coordinates of the skin-markers and ALs of each body segment in a technical coordinate system (TCS). TCSs are used to allow the positioning of skin-markers at any desired location in a body segment.

Some authors place skin-markers over ALs and define a LCS using the coordinates of ALs in GCS. ALs are usually estimated from the skin-markers located over them. This procedure requires locating skin-markers on ALs but the skin movement artifact is usually larger over ALs (Cappozzo et al., 1996). Based on Cappozzo's CAST method an intermediate TCS, between GCS and LCS, is used in this thesis to allow the positioning of skin-markers at any desired location, preferably with minimum skin movement artifact.

Cappozzo et al. (1995) did not suggest any definition for TCS. In this thesis a TCS definition, which is independent of the number of skin-markers located on the body segment, is proposed. TCS axes are defined as the principal axes of inertia of the cluster of skin-markers located on the body segment:

- TCS origin is located at the centroid of the cluster of skin-markers.
- TCS x-axis is defined as the principal axis of inertia associated with the largest moment of inertia (MoI).
- TCS y-axis is defined as the principal axis of inertia associated with the second largest MoI.
- TCS z-axis is defined as the principal axis of inertia associated with the smallest MoI.

To calculate TCS axes of a body segment, the skin-marker coordinates in GCS are transformed to another coordinate system GCS* parallel to GCS but

located at the centroid of the cluster of skin-markers (TCS origin), whose position is given by

$$ {}^{G}d_{TCS} = \sum_{i=1}^{n} \frac{{}^{G}SM_i}{n} = \frac{1}{n} \begin{bmatrix} \sum_{i=1}^{n} {}^{G}sm_{ix} \\ \sum_{i=1}^{n} {}^{G}sm_{iy} \\ \sum_{i=1}^{n} {}^{G}sm_{iz} \end{bmatrix} \tag{5.3} $$

The skin-marker coordinates of a body segment in GCS* are calculated as follows

$$ {}^{G*}SM_i = {}^{G}SM_i - {}^{G}d_{TCS} \tag{5.4} $$

The inertia tensor I for a discrete cluster of skin-markers is given by the following matrix

$$ I = \begin{bmatrix} \sum_{i=1}^{n}\left[({}^{G*}sm_{iy})^2 + ({}^{G*}sm_{iz})^2\right] & -\sum_{i=1}^{n} {}^{G*}sm_{ix} \cdot {}^{G*}sm_{iy} & -\sum_{i=1}^{n} {}^{G*}sm_{ix} \cdot {}^{G*}sm_{iz} \\ -\sum_{i=1}^{n} {}^{G*}sm_{ix} \cdot {}^{G*}sm_{iy} & \sum_{i=1}^{n}\left[({}^{G*}sm_{ix})^2 + ({}^{G*}sm_{iz})^2\right] & -\sum_{i=1}^{n} {}^{G*}sm_{iy} \cdot {}^{G*}sm_{iz} \\ -\sum_{i=1}^{n} {}^{G*}sm_{ix} \cdot {}^{G*}sm_{iz} & -\sum_{i=1}^{n} {}^{G*}sm_{iy} \cdot {}^{G*}sm_{iz} & \sum_{i=1}^{n}\left[({}^{G*}sm_{ix})^2 + ({}^{G*}sm_{iy})^2\right] \end{bmatrix} \tag{5.5} $$

The three eigenvectors E_1, E_2 and E_3 of the inertia tensor I define the three principal axes of inertia of the cluster of skin-markers. In this thesis E_1 is defined as the eigenvector associated with the largest eigenvalue, E_2 to the second largest eigenvalue and E_3 to the smallest eigenvalue. According to the TCS definition proposed previously, E_1, E_2 and E_3 are the TCS x-axis, TCS y-axis and TCS z-axis respectively referred to GCS.

During the first task, for each AL of a body segment one calibration frame is recorded with the motion capture system, i.e. each body segment has associated m calibration frames. From the calibration frame j, the coordinates in GCS of the measured AL and the skin-markers in the body segment can be obtained. Using these data, the coordinates of the skin-markers and ALs in TCS can be estimated following the three subsequent subtasks (Figure 5.5):

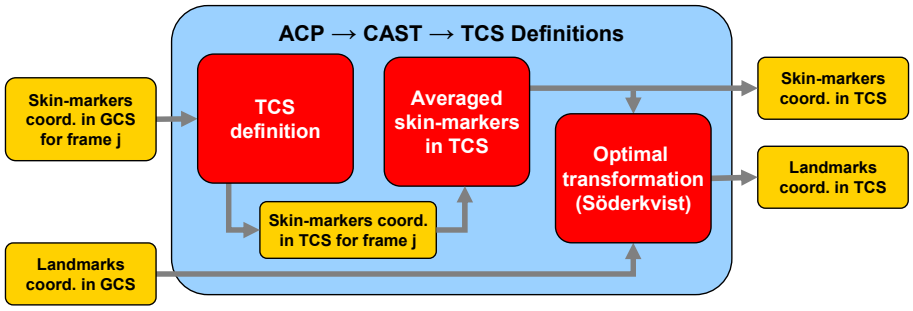

Figure 5.5: Flow chart of TCS Definitions task, 2nd task of CAST.

1. Applying the TCS definition to calibration frame *j* associated with a body segment, the following variables can be estimated (Figure 5.6):
   a. The TCS origin ${}^{G}d_{T}{}^{j}$ in calibration frame *j* referred to GCS can be estimated using equation (5.3).
   b. The rotation matrix between TCS and GCS in calibration frame *j* can be defined as follows

$$ {}^{G}R_{T}{}^{j} = \left[E_1^j \quad E_2^j \quad E_3^j \right] \tag{5.6} $$

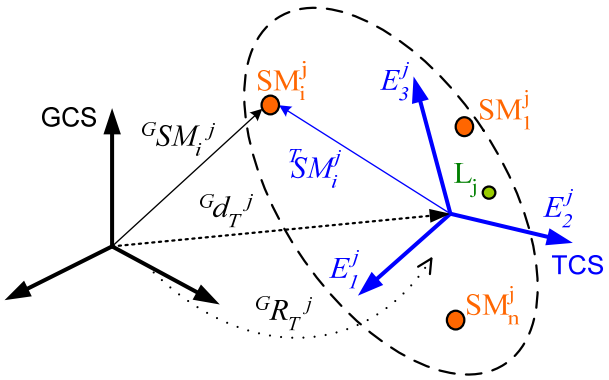

Figure 5.6: Position vector of skin-marker *i* in calibration frame *j* referred to TCS.

   c. The coordinates of the skin-markers located on a body segment referred to TCS can be estimated for each calibration frame: for skin-marker *i* in calibration frame *j* these coordinates are given by

$$ {}^{T}SM_i^j = \left[{}^{G}R_{T}{}^{j} \right]^{-1} \cdot \left[{}^{G}SM_i{}^{j} - {}^{G}d_{T}{}^{j} \right] \tag{5.7} $$

Due to experimental errors, the coordinates of skin-markers of a body segment in TCS are different for each calibration frame. In the next subtask, the averaged skin-marker coordinates in TCS are estimated in order to use single skin-marker positions in TCS.

2. The averaged coordinates of the skin-markers located on a body segment referred to TCS are calculated from the skin-marker coordinates in TCS estimated for each calibration frame in the previous subtask. The averaged coordinates of skin-marker *i* in TCS are given by

$$ {}^{T}\overline{SM}_i = \sum_{j=1}^{m} \frac{{}^{T}SM_i^j}{m} = \frac{1}{m} \begin{bmatrix} \sum_{j=1}^{m} {}^{T}sm_i^j{}_x \\ \sum_{j=1}^{m} {}^{T}sm_i^j{}_y \\ \sum_{j=1}^{m} {}^{T}sm_i^j{}_z \end{bmatrix} = \begin{bmatrix} {}^{T}\overline{sm}_{ix} \\ {}^{T}\overline{sm}_{iy} \\ {}^{T}\overline{sm}_{iz} \end{bmatrix} \tag{5.8} $$

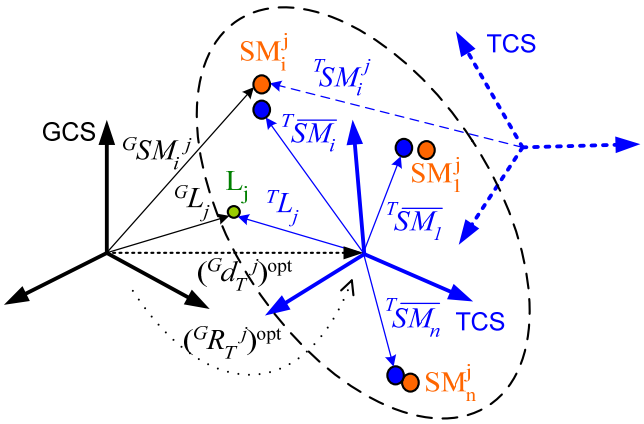

Figure 5.7: Optimal transformation between GCS and TCS using averaged skin-marker coordinates in TCS.

3. The coordinates of each AL of a body segment in TCS are estimated using ${}^{T}\overline{SM}_i$ and an optimal transformation between GCS and TCS (Figure 5.7). The rotation matrix ${}^{G}R_T{}^{j}$ and TCS origin ${}^{G}d_T{}^{j}$ estimated for each calibration frame in the first subtask are no longer valid because the averaged skin-marker coordinates in TCS are considered. For each calibration frame the optimal position

vector $({}^{G}d_{T}{}^{j})^{opt}$ and optimal rotation matrix $({}^{G}R_{T}{}^{j})^{opt}$ between GCS and TCS are estimated from ${}^{T}\overline{SM}_{i}$ and ${}^{G}SM_{i}$ of the n skin-markers using Söderkvist's method (Söderkvist and Wedin, 1993). Note that Söderkvist's method requires a minimum of three skin-markers per body segment. Then, the coordinates of the AL j of a body segment in calibration frame j are given by

$$ {}^{T}L_{j} = \left[({}^{G}R_{T}{}^{j})^{opt} \right]^{-1} \cdot \left[{}^{G}L_{j} - ({}^{G}d_{T}{}^{j})^{opt} \right] \quad j = 1, \cdots, m \tag{5.9} $$

The data obtained for each body segment in the second task are the averaged coordinates of the skin-markers in TCS and the ALs in TCS.

Third task: LCS Definitions

The third task, called LCS Definitions, consists in estimating the transformation between TCS and LCS and the coordinates of skin-makers and ALs in LCS (Figure 5.8). The position vector ${}^{T}d_{L}$ of the LCS origin referred to TCS and the rotation matrix ${}^{T}R_{L}$ between TCS and LCS can be estimated from the LCS definitions given in section 3.3 for each body segment. Then, the coordinates of skin-maker i and AL j of the body segment in LCS are given by

$$ {}^{L}\overline{SM}_{i} = \left[{}^{T}R_{L} \right]^{-1} \cdot \left[{}^{T}\overline{SM}_{i} - {}^{T}d_{L} \right] \quad i = 1, \cdots, n \tag{5.10} $$

$$ {}^{L}L_{j} = \left[{}^{T}R_{L} \right]^{-1} \cdot \left[{}^{T}L_{j} - {}^{T}d_{L} \right] \quad j = 1, \cdots, m \tag{5.11} $$

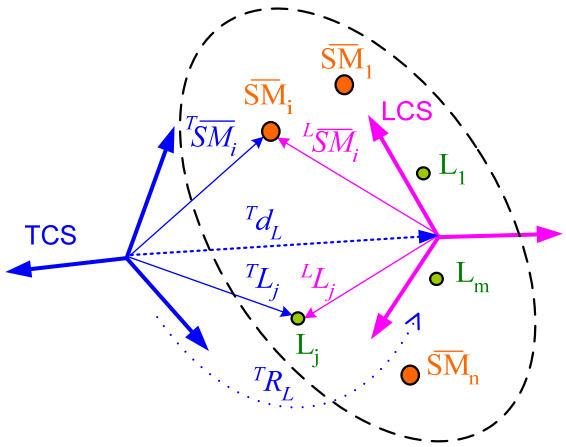

Figure 5.8: Coordinates of skin-markers and ALs in LCS.

CAST procedure assumes a minimum of three skin-markers located on each body segment in order to define a TCS. However, the scapula and clavicle in the UBMS (section 3.3.1) and ClSc in the UBM (section 3.3.2) have only one associated skin-marker. In this case the coordinates of skin-markers and ALs in LCS are estimated directly from the calibration frames associated with the corresponding body segment. The estimation of these LCSs is based on the position of their joint centres, which is presented in next section. Therefore, the explanation of the methods for estimating these three LCSs is postponed to section 5.1.1.1.3.

5.1.1.1.2 Anthropometric Parameters Methods

The fourth task of ACP is the Anthropometric Parameters Methods task (Figure 5.9). It consists in estimating the anthropometric parameters of a human skeletal model from the data obtained in the three previous tasks, using the methods presented in Chapter 2.

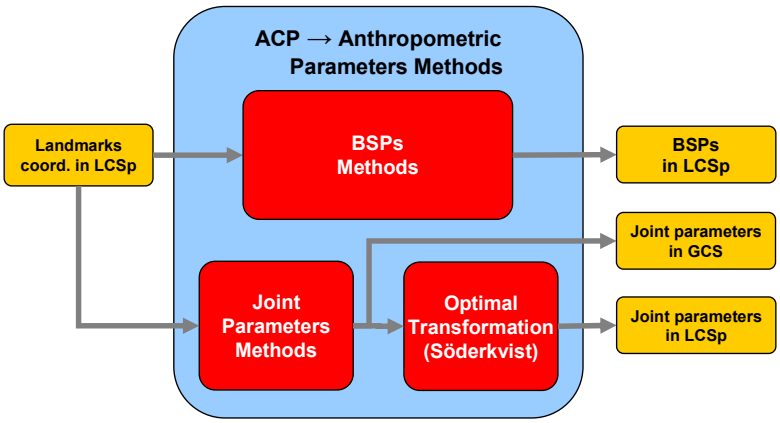

Figure 5.9: Flow chart of the Anthropometric Parameters Methods task.

CAST requires the two pointer-markers and all the skin-markers on a body segment to be visible to at least two cameras. In order to estimate joint parameters more skin-markers are required to be visible in some of the calibration frames. These calibration frames are called shared calibration frames. The skin-markers that must be visible in each shared calibration frame are described in section C.2.1 of Appendix C.

In a shared calibration frame it is required that the two pointer-markers, all skin-markers of a body segment and all skin-markers of the distal body segment connected to it are visible to at least two cameras. The AL measured in a shared calibration frame belongs to the proximal body segment. The joint parameters (joint centre position and/or joint axis vector) are estimated in LCS

of the proximal body segment (LCSp) and then, the shared calibration frame is used to estimate the joint parameters in LCS of the distal body segment (LCSd). The Anthropometric Parameters Methods task is composed of three different subtasks (Figure 5.9):

1. Joint parameters in LCSp. The ALs in LCSp are estimated in the LCS Definitions task and the joint parameters can be estimated from them by using the joint parameter methods presented in section 3.3 for each human skeletal model. These joint parameters are: joint centre coordinates in LCSp for spherical joints, joint centre and joint axis coordinates in LCSp for revolute joints, and joint centre and first joint axis coordinates in LCSp for universal joints.
2. Joint parameters in GCS. The coordinates of the element or elements shared between the proximal and distal body segments referred to the GCS are estimated from the shared calibration frame (Figure 5.10). The following data are known:
   - Joint centre ${}^{Lp}JC$ and/or joint axis ${}^{Lp}JA$ in LCSp estimated in the previous subtask.
   - Position vector ${}^{Tp}d_{Lp}$ of the LCSp origin referred to TCSp and rotation matrix ${}^{Tp}R_{Lp}$ between TCSp and LCSp estimated in CAST.
   - For the j shared calibration frame, the optimal position vector of TCSp origin $({}^{G}d_{Lp}{}^{j})^{opt}$ and the optimal rotation matrix $({}^{G}R_{Tp}{}^{j})^{opt}$ between GCS and TCSp estimated in CAST.

   The coordinates of the joint centre ${}^{G}JC$ and/or joint axis ${}^{G}JA$ in GCS are given by

$$ {}^{G}JC = ({}^{G}d_{Tp}{}^{j})^{opt} + ({}^{G}R_{Tp}{}^{j})^{opt}\left[{}^{Tp}d_{Lp} + {}^{Tp}R_{Lp}\ {}^{Lp}JC\right] \qquad (5.12) $$

$$ {}^{G}JA = ({}^{G}R_{T}{}^{j})^{opt}\ {}^{Tp}R_{Lp}\ {}^{Lp}JA \qquad (5.13) $$

   The AL measured in the shared calibration frame belongs to the proximal body segment but the distal body segment does not have any associated AL. The joint centre ${}^{G}JC$ and/or joint axis ${}^{G}JA$ in GCS estimated in this subtask can be associated with the distal body segment in the shared calibration frame. Therefore, the shared calibration frame is used twice, first with the proximal body segment and second with the distal body segment.

Then, the joint centre ${}^{Ld}JC$ and/or joint axis ${}^{Ld}JA$ in LCSd will be estimated from the shared calibration frame, together with the other calibration frames associated with the distal body segment, following the CAST procedure presented in the previous section.

3. BSPs of the proximal body segment. They can be estimated from the coordinates of the ALs in LCSp using the two methods described in section 3.3 and section B.3 of Appendix B. One method requires the distance between two ALs, which is defined as the body segment length, and the coordinates of one AL, which is used as a reference to locate the body segment CoM. The second method requires the height and weight of the subject.

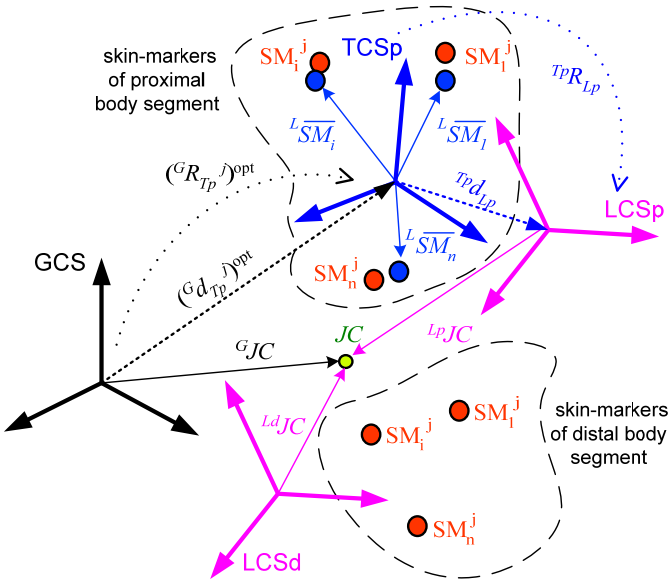

Figure 5.10: Estimation of joint centre in LCSd from shared calibration frame.

The anthropometric parameters estimated during the Anthropometric Parameters Methods task are the joint parameters in LCSp and GCS, and BSPs of the proximal body segment.

5.1.1.1.3 LCS of Clavicle, Scapula and ClSc

The body segments scapula and clavicle in the UBMS (section 3.3.1) and the ClSc in the UBM (section 3.3.2) have only one associated skin-marker. The CAST procedure presented in section 5.1.1.1.1 cannot be applied because it needs a minimum of three skin-markers located on each body segment in order to estimate each LCS.

The coordinates of the skin-marker and ALs in LCS for the clavicle, scapula and ClSc are estimated directly from the calibration frames associated with each body segment. The estimation of these LCSs is based on the position of their joint centres.

UBMS has only one skin-marker over the joint between the scapula and the clavicle. This skin-marker can be associated with both scapula and clavicle for calculation purposes in CAST. However, in the Inverse Kinematic step it is assumed to be rigidly attached only to the clavicle in the UBMS and only to ClSc in the UBM.

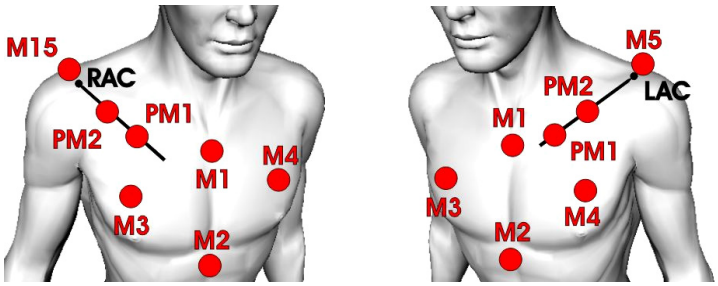

Figure 5.11: Shared calibration frame between right clavicle and right scapula (left) and left clavicle and left scapula (right).

Clavicle LCS

The clavicle has only two ALs (AC and SC) and one shared calibration frame (section C.2.1 of Appendix C). In this shared calibration frame, the skin-markers of the thorax and the skin-marker of the clavicle are visible and AC is measured with the pointer (Figure 5.11). The coordinates of the skin-marker and the ALs in clavicle-LCS are estimated as follows:

1. The coordinates of AC in GCS (^{G}AC) can be obtained directly from the calibration frame using equation (5.1).
2. The optimal transformation $(^{G}d_{ThorL})^{opt}$ and $(^{G}R_{ThorL})^{opt}$ between the four thorax skin-markers in GCS of the single calibration frame available for the clavicle and the four thorax skin-markers in thorax-LCS obtained in CAST procedure can be estimated using Söderkvist's method (Söderkvist and Wedin, 1993) (see section 4.3.3.2). The coordinates of SC in the calibration frame referred to GCS (^{G}SC) are given by

$$^{G}SC = (^{G}d_{ThorL})^{opt} + (^{G}R_{ThorL})^{opt} \cdot {}^{ThorL}SC \qquad (5.14)$$

where $^{ThorL}SC$ are the coordinates of SC landmark in thorax-LCS.

3. The position vector ${}^{G}d_{ClavL}$ of the clavicle-LCS origin, referred to GCS, and the rotation matrix ${}^{G}R_{ClavL}$ between GCS and clavicle-LCS can be estimated from the clavicle-LCS definition given in section 3.3. Then, the coordinates of the skin-marker and ALs in clavicle-LCS are given by

$$ {}^{ClavL}SM_i = \left[{}^{G}R_{ClavL}\right]^{-1}.\left[{}^{G}SM_i - {}^{G}d_{ClavL}\right] \quad i=1 \tag{5.15}$$

$$ {}^{ClavL}L_j = \left[{}^{G}R_{ClavL}\right]^{-1}.\left[{}^{G}L_j - {}^{G}d_{ClavL}\right] \quad j=1,2 \tag{5.16}$$

Scapula LCS

The scapula has five ALs (AC, TS, AI, AA and PC) and five associated calibration frames but only one skin-marker, which is the same skin-marker associated with the clavicle. While measuring the five ALs in each calibration frame, the scapula is only allowed to translate. This is required because with one skin-marker associated with the scapula only translations can be compensated. The coordinates of the skin-marker and the ALs in scapula-LCS are estimated as follows

1. One calibration frame is selected as the reference position and the remaining ALs are translated to the reference position as follows

$$ {}^{G}L_i^{\mathrm{Ref}} = {}^{G}L_i + \left({}^{G}SM^{\mathrm{Ref}} - {}^{G}SM_i\right) \quad i=1,\cdots,4 \tag{5.17}$$

   where ${}^{G}L_i^{\mathrm{Ref}}$ is the position vector of AL i in the reference position, ${}^{G}SM^{Ref}$ is the position vector of the skin-marker in the calibration frame selected as the reference and ${}^{G}SM_i$ is the position vector of the skin-marker in the calibration frame i corresponding to the AL i.

2. The position vector ${}^{G}d_{ScapL}$ of the scapula-LCS origin referred to GCS and the rotation matrix ${}^{G}R_{ScapL}$ between GCS and the scapula-LCS can be estimated from the coordinates of the ALs in the reference position by applying the scapula-LCS definition given in section 3.3. Then, the coordinates of the skin-maker and the ALs in scapula-LCS are given by

$$ {}^{ScapL}SM_i = \left[{}^{G}R_{ScapL}\right]^{-1}.\left[{}^{G}SM_i^{\mathrm{Ref}} - {}^{G}d_{ScapL}\right] \quad i=1 \tag{5.18}$$

$$ {}^{ScapL}L_j = \left[{}^{G}R_{ScapL}\right]^{-1}.\left[{}^{G}L_j^{\mathrm{Ref}} - {}^{G}d_{ScapL}\right] \quad j=1,\cdots,5 \tag{5.19}$$

3. From the coordinates of ALs in scapula-LCS, the joint centre coordinates of GHJ ($^{ScapL}GHJC$) in scapula-LCS can be estimated using Meskers' regression method (Meskers et al., 1998) (section 2.1.8 and section B.2.1 of Appendix B).

ClSc LCS

ClSc has only two ALs (SC and GHJC) and the same associated shared calibration frame like the clavicle. The coordinates of the skin-marker and the ALs in ClSc-LCS are estimated as follows

1. The coordinates of SC in GCS (^{G}SC) are estimated from the calibration frame similarly to the clavicle.
2. The coordinates of GHJC in the calibration frame referred to GCS ($^{G}GHJC$) can be estimated from $^{ScapL}GHJC$.
3. The position vector $^{G}d_{ClScL}$ of the ClSc-LCS origin referred to GCS and the rotation matrix $^{G}R_{ClScL}$ between GCS and ClSc-LCS can be estimated from the ClSc-LCS definition given in section 3.3. Then, the coordinates of the skin-maker and the ALs in ClSc-LCS can be calculated similarly to the clavicle.

5.1.1.2 Motion capture

In the MoDyCo project, the motion of a human subject performing a driving manoeuvre was recorded at 50 Hz using the Vicon motion capture system. The motion capture system was composed of 12 cameras and a large number of skin-markers that were located on the skin of each body segment. The 38 skin-markers used to measure the motion of the subject are depicted in Figure 5.12. A more detailed description of the location of the skin-markers is given in section C.1 of Appendix C. With the aim of analysing the movements in a qualitative way, the subject was filmed with one video camera while performing the prescribed driving manoeuvre. The videos recorded were used to understand possible problems occurring during the Inverse Kinematic analysis.

The motion capture system provides the three-dimensional coordinates of skin-markers in GCS at each frame. They are usually named *skin-marker trajectories*. It is assumed that the skin-markers are rigidly attached to the relevant body segment (section 3.1), i.e. the coordinates of skin-markers in each body segment LCS are constant.

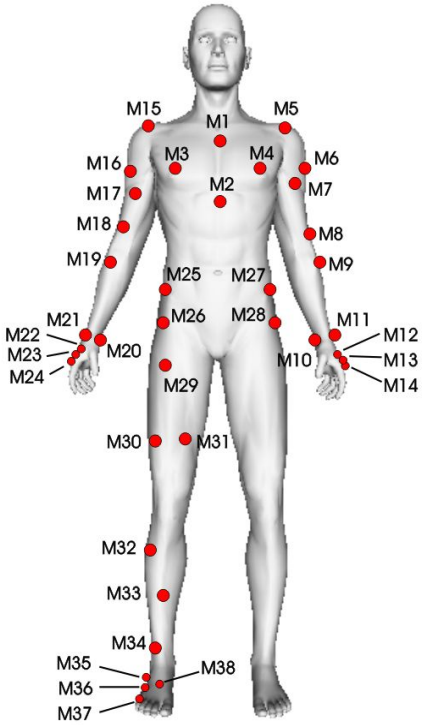

Figure 5.12: Locations of the skin-markers in the MoDyCo project.

5.1.1.3 Force Sensors Measurements

The vehicle mock-up used to investigate driving manoeuvres was equipped with force sensors at the steering wheel and brake pedal. The force sensors measured the forces applied by the driver to the vehicle during the experiment execution. These measured forces were used to estimate the external forces acting on the human subject at the contact points between the subject and the vehicle. At the time of writing this document, the vehicle mock-up was not fully operational and force measurements in real experiments have not been recorded.

5.1.2 Inverse Kinematics

The goal of the Inverse Kinematics step (Figure 5.13) is to estimate the joint angles, velocities and accelerations of a human skeletal model starting from the coordinates of skin-markers in GCS recorded with the motion capture system. The inputs to the Inverse Kinematics step, which are the outputs of the Experimental Measurements step, are the following:

- Coordinates of skin-markers in GCS measured with the motion capture system during a driving manoeuvre.
- Joint parameters referred to each body segment LCS.
- Coordinates of skin-markers in each body segment LCS.
- Coordinates of ALs in each body segment LCS.

Joint parameters and coordinates of skin-markers and ALs in each body segment LCS are used to tailor a generic human skeletal model to the subject under investigation. Two upper body models for studying steering manoeuvres and one lower limb model for studying braking manoeuvres are used in the MoDyCo project (section 3.3). The kinematic constraints of the three models are obtained with the help of the Matlab® Symbolic Toolbox.

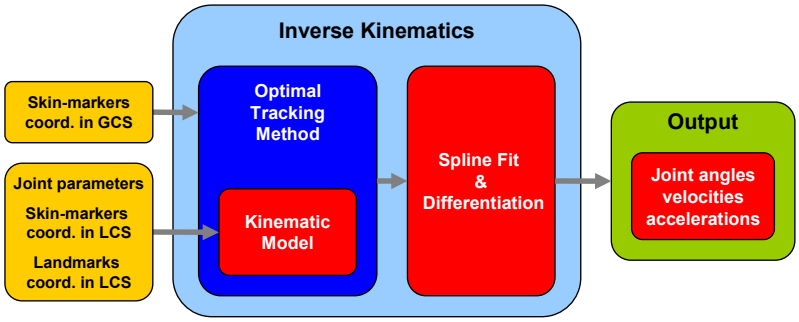

Figure 5.13: Flow chart of Inverse Kinematics in the MoDyCo project.

The joint angles of the subject-specific skeletal model can be obtained from the coordinates of skin-markers in GCS at each frame using Inverse Kinematic methods. The resultant inverse kinematic problem is over-guided (section 4.2.1) due to the number and location of the skin-markers and the topology of the kinematic models. The over-guided kinematic problems obtained for each driving experiment are solved with OTM (see Chapter 4), which gives the joint angles of a human skeletal model at each frame. OTM has been implemented in Matlab® 7.0.1. In order to obtain joint angular velocities and accelerations cubic splines are fitted to the joint angle values and then differentiated.

5.1.3 INVERSE DYNAMICS

The Inverse Dynamics step (Figure 5.14) estimates the joint motor torques of a human skeletal model. The inputs of the Inverse Dynamics step come from Experimental Measurements and Inverse Kinematics steps and are the following:

- Joint angles, velocities and accelerations of the model.
- Joint parameters referred to each body segment LCS.
- Coordinates of ALs in each body segment LCS.
- BSPs of each body segment.
- External forces acting on the subject.

Joint parameters, BSPs and ALs coordinates in each body segment LCS are used to tailor a generic human skeletal model to the subject under investigation. The kinematic and dynamic models are the same, except for BSPs which are required for the Inverse Dynamic analysis. The dynamic models have been implemented with the Matlab® SimMechanics Toolbox.

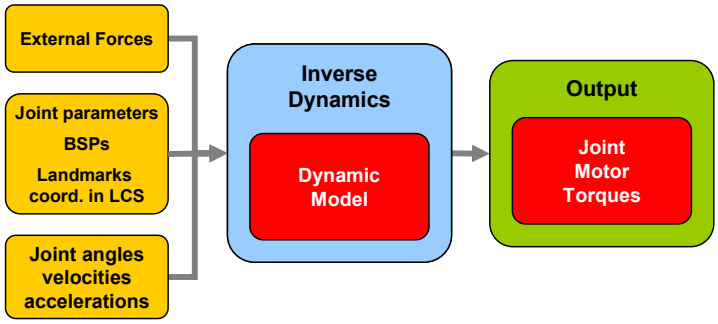

Figure 5.14: Flow chart of Inverse Dynamics in the MoDyCo project.

5.2 MODYCO EXPERIMENTS

The MoDyCo methodology developed in the frame of this thesis has been used to analyse steering and braking manoeuvres of a human driver. At the time of writing this document, real experiments have not been recorded, so only the ACP and the Inverse Kinematics step have been tested using data from the literature and computer-simulated trials of one steering manoeuvre.

5.2.1 STEERING MANOEUVRE

The computer-simulated steering manoeuvre used to test the Inverse Kinematics step consists in turning the steering wheel right and left by a human driver. The driver holds the steering wheel at the ten-to-two position during the whole motion. The motion of the steering wheel angle θ_{sw} is defined as

$$\theta_{sw} = A_{sw} \sin(\omega_{sw} t) \tag{5.20}$$

where A_{sw} is the amplitude of the steering wheel angle, ω_{sw} is the frequency, and t the simulation time.

The steering manoeuvre defined above has been simulated with the weighted OTM proposed in section 4.6. Note that the weighted OTM is used here to generate a computer-simulated motion instead of solving the motion reconstruction problem. The motion of the multibody system is defined with the following driving constraints:

1. Two points Q^h and P^h on each hand are considered to be fixed to two corresponding points Q^{sw} and P^{sw} located on the steering wheel (Figure 5.15). The Cartesian coordinates of Q^{sw} and P^{sw} can be expressed as a function of the steering wheel angle defined in (5.20).

$$P^{sw} = \begin{bmatrix} p_x^{sw}(\theta_{sw}) \\ p_y^{sw}(\theta_{sw}) \\ p_z^{sw}(\theta_{sw}) \end{bmatrix}, \quad Q^{sw} = \begin{bmatrix} q_x^{sw}(\theta_{sw}) \\ q_y^{sw}(\theta_{sw}) \\ q_z^{sw}(\theta_{sw}) \end{bmatrix} \tag{5.21}$$

   The motion of Q^h and P^h can be prescribed with six driving constraints using the coordinates of Q^{sw} and P^{sw} respectively. These driving constraints are included in Ψ_s, so that they are exactly satisfied. The six driving constraints can be written as follows

$$\Psi_s = \begin{bmatrix} p_x^h - p_x^{sw}(\theta_{sw}) \\ p_y^h - p_y^{sw}(\theta_{sw}) \\ p_z^h - p_z^{sw}(\theta_{sw}) \\ q_x^h - q_x^{sw}(\theta_{sw}) \\ q_y^h - q_y^{sw}(\theta_{sw}) \\ q_z^h - q_z^{sw}(\theta_{sw}) \end{bmatrix} \tag{5.22}$$

2. Two vectors U^h and V^h on each hand are considered to be parallel to two corresponding vectors U^{sw} and V^{sw} located on the steering wheel (Figure 5.15). Vectors U^{sw} and V^{sw} are tangent to the steering wheel and vectors U^h and V^h are contained in the palm hand and are perpendicular to the fingers, as shown in Figure 5.15. Similarly to the points in the previous section, the Cartesian coordinates of U^{sw} and V^{sw} can be expressed as a function of the steering wheel angle. Then, the motion of U^h and V^h can be prescribed with six driving constraints using the coordinates of U^{sw} and V^{sw} respectively. These

driving constraints are exactly satisfied because they are included in Ψ_s.

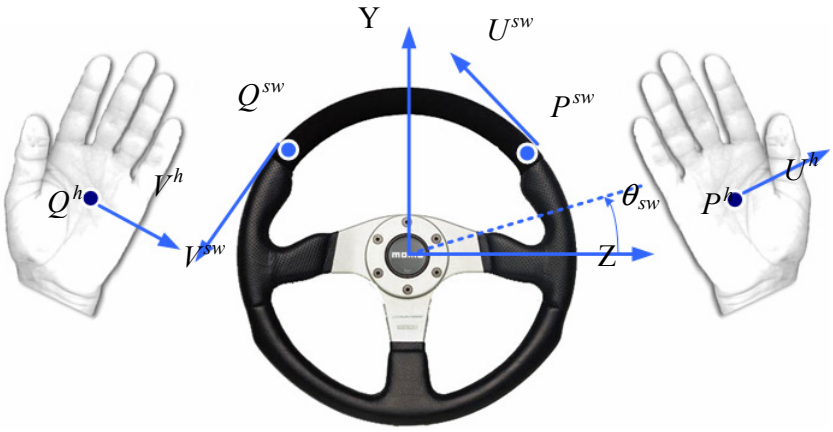

Figure 5.15: Points and vectors on the steering wheel and both hands used to define driving constraints of the model.

3. The four previous conditions (12 constraint equations in Ψ_s) are not enough to define all DoFs of the human skeletal model. A relative preservation posture condition (sections 4.2.2.3 and 4.6.2) is included in Ψ_m to prescribe the relative motion of the body segments during the whole motion. The relative preservation posture condition adds relative coordinates (joint angles) to the model. In the reference posture the joint angles are selected so that the driver adopts a ten-to-two relaxed driving position and the pelvis position is defined by the H-point[3] of each vehicle. The value of each joint angle has associated a different weighting factor in order to obtain a realistic steering manoeuvre.

Two different upper limb models are proposed to study steering manoeuvre, the UBMS (section 3.3.1) and the UBM (section 3.3.2). The two original upper limb models are modified in order to include the additional driving constraints previously described. The models obtained are called UBMS-INV and UBM-INV. Therefore, four upper limb models are required: the two original upper limb models, which are used to reconstruct the motion from the computer-simulated marker trajectories; and UBMS-INV and UBM-INV, which are used to generate the computer-simulated motions.

[3] The H-point is a reference axis or mid-point that estimates the hip joint center of a mid-sized male occupant.

5.2.1.1 Experimental vehicle mock-up

A multi-adjustable experimental vehicle mock-up (Figure 5.16) is used to investigate steering and braking manoeuvres. It is composed of one seat, three pedals and a steering wheel. Four different configurations of the steering wheel, corresponding to four real vehicles (Table 5.1), are considered during the steering experiments.

The vehicle mock-up is equipped with force sensors on the steering wheel and the braking pedal in order to measure the forces applied by the driver on the vehicle. Furthermore, a screen located in front of the subject is used to give a visual input to the driver. At the time of writing this document, the vehicle mock-up was not fully operational and real experiments have not been recorded. Instead, computer-simulated motions have been generated for testing the MoDyCo methodology.

Figure 5.16: Vehicle mock-up used for the MoDyCo experiments.

Configuration	H-point [mm]			Steering wheel centre [mm]			Angle between vertical & steering wheel plane [deg]
	x	y	z	x	y	z	
PF1	1277.8	-335	345	915	-335	715	65.5
PF2	1281.5	-345	350	921	-345	700	65.5
PF3	1342.7	-380	265	987	-380	637	66.0
PF4	1156.7	-375	596	783.8	-375	954	59.8

Table 5.1: Configurations of the steering wheel investigated in the steering experiments.

5.2.1.2 Anatomical calibration protocol

The Anatomical Calibration Protocol (ACP) used in the MoDyCo experiments has been presented in section 5.1.1.1. The input data for the ACP of each subject are generated by combining ALs from two sources and estimating

approximately the skin-marker coordinates on each body segment. The coordinates of the ALs for the upper body have been estimated from VRML graphic objects of the Maurel upper limb model (Maurel, 1999) (section 3.2.1.6). The coordinates of the ALs for the right leg have been obtained from the database of Kepple et al. (1998).

The ACP has not been validated thoroughly due to the lack of real experimental data. In the literature, the data about the accuracy and precision of this type of methods are scarce. Erdemir and Piazza (1999) evaluated the accuracy of a linear pointer similar to the one presented in section 5.1.1.1 on a steel plate using a Vicon motion capture system. The averaged error of the pointer tip calculated in 35 experimental trials was 3.15 mm (SD 0.74).

Meskers et al. (1998) reported an *in vitro* intra-observer accuracy of AL measurements of 0.96, 1.02 and 1.0 mm for the x-, y- and z-coordinates respectively. The inter-observer accuracy was 1.73, 1.90 and 1.57 mm. Note that accuracy is given *in vitro*, i.e. the ALs were measured on defleshed bones and not *in vivo* when the skin thickness is relevant.

Della Croce et al. (1999) studied AL identification errors for 21 ALs in the pelvis and lower limb in two different subjects. They used a stick with two pointer-markers according to the CAST protocol proposed by Cappozzo et al. (1995). The intra- and inter-experimenter precisions (standard deviation of the distance from the mean position) were in the range 4.8-21 mm and 11.5-24.8 mm, respectively. Rabuffetti et al. (2002) estimated the variability in identifying the position of 21 ALs distributed over the whole body using the same methodology as Della Croce et al. (1999). The inter-experimenter precision was in the range 4.1-19.2 mm and the intra-subject precision (the subject under examination identified ALs on his/her own body) was in the range 4.1-11.3 mm. The intra-subject precision was investigated because the experimental protocol was designed for motion analysis applications in space.

As real experimental data were not available at the moment of writing this thesis, the ACP has been evaluated using computer-simulated ALs coordinates. In section 6.5 the errors in the subject-specific parameters associated with the measurement errors of ALs during the ACP are analysed.

5.2.1.3 Motion capture

As no real experiments have been conducted, computer-simulated motion data have been generated for the steering manoeuvre described above, for four different vehicle configurations (Table 5.1) at a 50 Hz frequency. The skin-marker coordinates obtained from the computer-simulated experiment are

considered the true values, i.e. they are free from errors. Then, artificial noise is added to these true data in order to generate the data that would be really captured in the experiment.

There are two sources of errors, instrumental errors due to the motion capture system, and skin movement artifact due to the relative movement between skin-markers and the underlying bone caused by passive and active soft tissues (section 3.1.2). It is assumed that instrumental errors are removed using smoothing techniques and, consequently, this source of error is not added to the computer-simulated motion data. Skin movement artifact is simulated by a continuous noise model (Chèze et al., 1995; Lu and O'Connor, 1999; Roux et al., 2002) of the form $A_{sma}\ \sin(\omega_{sma}\ t+\varphi_{sma})$, where A_{sma} is the amplitude of the noise, ω_{sma} is the frequency, t the simulation time and φ_{sma} the phase angle.

Cappozzo et al. (1996) provided quantitative information regarding skin movement artifact in the lower limb. Skin-marker displacement with respect to the underlying bone during voluntary movements ranged from a few millimetres up to 40 mm. They found that skin movement artifact was greater near the proximal end of the lower limb segments. Roux et al. (2002) assumed that the experimental observations of Cappozzo et al. for the lower limb were also valid for the upper arm and forearm. They considered that A_{sma} could vary between 0 and 20 mm for skin-markers located on the proximal end of a segment, and between 0 and 10 mm for skin-markers located on the distal end of a segment.

For a steering manoeuvre each skin-marker on each body segment is assigned a different value of A_{sma}. The lower and upper limits selected for A_{sma} in the steering manoeuvre are summarised in Table 5.2. These values are based on Cappozzo et al. (1996) and Roux et al. (2002) but they have been adapted to the steering manoeuvre. Skin movement artifact usually contains the same frequencies as those of the movement studied. Then, ω_{sma} is varied between zero and three times the frequency (ω_{sw}) of the computer-simulated experiments (Chèze et al., 1995; Lu and O'Connor, 1999; Roux et al., 2002). The value of φ_{sma} is varied between 0 and 2π (Chèze et al., 1995; Lu and O'Connor, 1999; Roux et al., 2002).

The computer-simulated trials of the steering manoeuvre are generated with the upper limb models UBMS-INV and UBM-INV. These two models are obtained by adding the additional driving constraints presented in the beginning of section 5.2.1, to the upper limb models UBMS (section 3.3.1) and UBM (section 3.3.2) respectively. Four computer-simulated trials of the steering manoeuvre are generated for each upper limb model, one for each

vehicle configuration (Table 5.1). Then, three different random patterns of simulated skin-movement artifact are added to each of the eight computer-simulated motions obtaining a total of 24 trials of the steering manoeuvre, 12 for each upper limb model.

For each steering manoeuvre, the parameters of the noise model, A_{sma}, ω_{sma} and φ_{sma}, are selected randomly for each skin-marker coordinate to lie between the lower and upper limits defined in Table 5.2. The parameters for the motion of the steering wheel angle are the same for all the trials of the steering manoeuvre, A_{sw} = 60 deg and ω_{sw} = 40 deg/s.

Body segment	A_{sma} [mm]		ω_{sma}	φ_{sma} [rad]
	Proximal area	Distal area		
Pelvis (fixed)	0	0	0 - 3ω_{sw}	0 - 2π
Thorax	0 – 2.5	0 - 5	0 - 3ω_{sw}	0 - 2π
ClSc or Clavicle	-	0 - 10	0 - 3ω_{sw}	0 - 2π
Upper arm	0 - 20	0 - 10	0 - 3ω_{sw}	0 - 2π
Forearm	0 - 20	0 - 10	0 - 3ω_{sw}	0 – 2π
Hand	0 - 5	0 - 5	0 - 3ω_{sw}	0 - 2π

Table 5.2: Parameters of the noise model for the skin movement artifact. Noise amplitude (A_{sma}) is different for skin-markers on the proximal or distal end of a body segment.

5.3 REALMAN METHODOLOGY

As it is explained in section 1.1.1, the REALMAN methodology is divided in two basic levels: Simulation level and Experimental level (Dufour et al., 2003; Suescun and Pargada, 2003). Two different types of experiments are considered in the Experimental level: motion experiments and joint torque experiments. Motion experiments are designed to study the human motion during different vehicle-related activities. For example, door handling, safety belt handling or ingress-egress motions. Joint torque experiments are designed to measure the maximal and intermediate torques at each joint for several postures. During both types of experiments discomfort questionnaires are filled by the subject in order to gather discomfort data.

Only motion experiments without considering the discomfort questionnaires are relevant to the objectives of this thesis. Accordingly only these motion experiments are described in detail. The main goal of the motion experiments is to estimate the joint angles of the RAMSIS whole body model adjusted to a specific subject from the skin-marker trajectories. A motion experiment of the REALMAN Experimental level is divided into four steps (Figure 5.17):

1. Anatomical Calibration Protocol (ACP) estimates the parameters of the RAMSIS whole body model for the specific subject under investigation.
2. A Vicon motion capture system measures the three-dimensional coordinates of skin-markers in GCS at 50 Hz while the subject is performing a predefined motion.
3. Inverse Kinematics analysis is performed with the Compamm multibody software. Thereby the reconstructed human motion is obtained.
4. Ergonomic analysis of the reconstructed human motion is made by using the ergonomic design software RAMSIS and the motion data is included in the motion database.

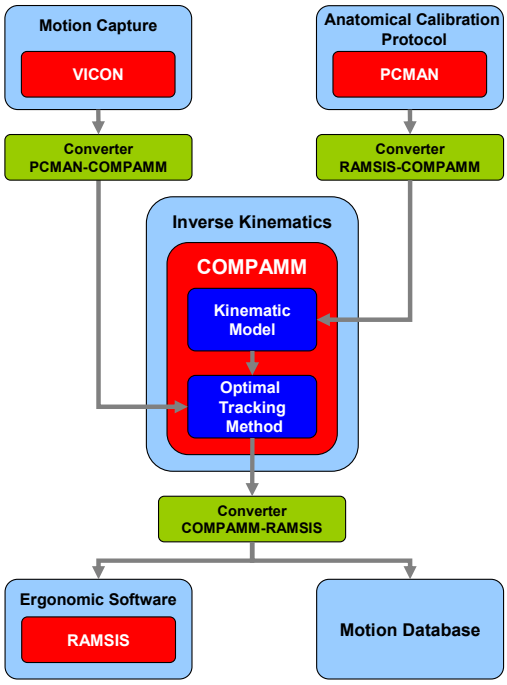

Figure 5.17: Flow chart of the REALMAN Experimental level.

5.3.1 ANATOMICAL CALIBRATION PROTOCOL

The software PCMAN (Seitz and Bubb, 1999; Seitz et al., 2000; Seitz and Bubb, 2001) is used to adjust semi-automatically the RAMSIS model to a specific subject. The main software features have been described in section 2.1.15.2. The RAMSIS parameters estimated by PCMAN in a static posture are:

- Coordinates of RAMSIS skeleton points in GCS. Most skeleton points coincide with joint rotation centres.
- Unit vectors of each body segment LCS in X, Y and Z directions referred to GCS.
- Unit vectors of each joint coordinate system (JCS) in X, Y and Z directions referred to GCS.
- Coordinates of the skin-markers located on the subject in GCS.
- External body surface of the RAMSIS model.

The unit vectors of each JCS are estimated because in the RAMSIS model, the joint rotations between two adjacent body segments are defined between JCS of the proximal body segment and LCS of the distal body segment.

PCMAN provides the position of the skin-markers in a static posture referred to CGS but this option is not used due to the following problems found by Renault and Peugeot-Citroën in a preliminary study:

- Some skin-markers appear at the same location in all the photographs and with only four photographs it is difficult or sometimes impossible to identify them.
- The accuracy of the skin-markers location given by PCMAN is low compared to Vicon. The error distances with PCMAN range from 2 to 15 mm with an average of 5 mm while Vicon accuracy is better than 1 mm.

The positions of the skin-markers in the same static posture used for PCMAN are recorded with Vicon in order to estimate skin-marker coordinates in GCS. The same GCS is used for both PCMAN and Vicon or an appropriate transformation is applied. The skin-marker coordinates in each body segment LCS can be obtained easily from the following data:

- The unit vectors of each body segment LCS in X, Y and Z directions referred to GCS estimated by PCMAN in a static posture.
- The skin-marker coordinates in GCS in the same static posture recorded simultaneously with Vicon.

All REALMAN experiments share the same basic Anatomical Calibration Procedure but there are slight differences between the experiments. Therefore, a detailed description of the Anatomical Calibration Procedure is presented in the section "Anatomical Calibration Procedure" of each experiment.

5.3.2 MOTION CAPTURE

The motion of the human subject, while performing a predefined movement, is recorded in the REALMAN project using the Vicon motion capture system at 50 Hz. The configuration and the number of skin-markers and cameras used to measure the human motion are different depending on the experiment and are defined for each experiment in the corresponding section.

It is assumed that the skin-markers are rigidly attached to the relevant body segment (section 3.1), i.e. the coordinates of skin-markers in each body segment LCS are constant.

The motion of the subject is filmed with one or more video cameras, depending on the experiment, while performing the predefined motion. These videos are used to understand possible problems occurring during the Inverse Kinematic analysis and to help the subjects to fill the discomfort questionnaires.

5.3.3 INVERSE KINEMATICS

The Inverse Kinematic Analysis has been performed with two different implementations of the Optimal Tracking Method presented in Chapter 4. One implementation in Compamm was used during the REALMAN project and an improved implementation in Matlab® was used to test some new features of OTM after the conclusion of REALMAN.

5.3.3.1 OTM implementation in Compamm

During the REALMAN project, the Inverse Kinematic Analysis was performed with the MBS software Compamm developed at CEIT. Compamm is a general purpose software tool for the kinematic and dynamic simulation of planar and three-dimensional mechanisms with open- and closed-loops. It is based on the natural coordinates concept (García de Jalón et al., 1986; García de Jalón et al., 1987; García de Jalón and Bayo, 1994), which describes the position and orientation of bodies through the Cartesian components of points and vectors located at the mechanism joints.

A model of a mechanical system is defined by using a proprietary modelling language, which consists of a series of statements, each defining a particular physical component of the mechanism. In the frame of the REALMAN project the RAMSIS model has been described with the Compamm modelling language (Suescun and Pargada, 2003).

In the Inverse Kinematics analysis, the joint angles of the RAMSIS model are estimated from the recorded global coordinates of the skin-markers.

The resultant Inverse Kinematic problem is over-guided or it can be converted to an over-guided one by using one or more of the following strategies, which modify the RAMSIS model:

1. Add a relative preservation posture condition (section 4.2.2.3) to the RAMSIS model.
2. Substitute one or more joints of the RAMSIS model in order to reduce the number of DoFs.

For each experiment, the original RAMSIS model described in section 3.4 requires different modifications. These modifications are described in the section "RAMSIS model and driving constraints" of each experiment.

During the REALMAN project, Compamm has been extended with the capability of solving over-guided kinematic problems using OTM. In the REALMAN project, an earlier implementation of OTM has been used, which includes the following features:

- From the four numerical methods presented in section 4.5.6.4, only the two-step LU method is available.
- A global convergence strategy is not included (section 4.5.7) and convergence from any remote starting point cannot be guaranteed. Therefore, a good initial approximation for the first frame is required.
- The weighted OTP (4.112) is used. Therefore, all the driving constraints are in the objective function and some of them cannot be exactly satisfied as explained in section 4.6.1.
- From the applications of the driving constraints presented in section 4.6.2, only the relative and absolute preservation posture conditions were available.
- The two weighting strategies proposed in section 4.6.4 were not implemented and the trajectories of the missing markers were interpolated by the REALMAN partners.

OTM implementation in Compamm is efficient in terms of CPU time, although not completely stable due to numerical problems caused by the sparse Gaussian elimination and the incompatibility issue described in section 4.5.2. In the REALMAN project, priority was given to efficiency over stability due to the large number of trials (>6000) that had to be analysed. The effect of the stability problem was that the early implementation of OTM used in Compamm could not solve a small percentage of the trials (section 6.3.1).

The kinematic constraints of the RAMSIS model are generated by Compamm from the description of the RAMSIS model in the Compamm modelling language.

5.3.3.2 OTM implementation in Matlab®

After the conclusion of the REALMAN project, an improved OTM implementation has been developed in Matlab® 7.0.1. This new implementation includes all the OTM features and numerical methods presented in Chapter 4. It is more stable at the price of a lower efficiency in terms of CPU time. The OTM implementation in Matlab® has also been used both in the MoDyCo and REALMAN projects.

In order to test the performance of the OTM implementation in Matlab®, 10 trials of the vehicle accessibility experiment, 4 trials of the door handling experiment and 10 trials of the generic arm reaching experiment have been solved and the results are presented in Chapter 6. The Inverse Kinematic problem obtained from each trial is over-guided or it can be converted to an over-guided one. The strategies used to convert under-guided problems in over-guided are described in the section "RAMSIS model and driving constraints" of each experiment.

In the OTM implementation in Matlab® the kinematic constraints of the RAMSIS model are obtained with the help of the Matlab® Symbolic Toolbox.

5.3.4 ERGONOMIC ANALYSIS

The motion data obtained from the motion and joint torque experiments and the discomfort questionnaires filled by each subject during both experiments are used by the ergonomics experts to build discomfort assessments models and predictive motion modelling methods. This ergonomic issue is not relevant in the context of the present thesis and it is not discussed.

5.4 REALMAN EXPERIMENTS

The methodology of REALMAN has been used to analyse several vehicle-related human motions. The motion experiments considered are safety belt handling, vehicle accessibility, door handling, maximal joint angles and generic arm reaching. For each experiment a large number of trials (Table 5.3) have been recorded using several subjects and different configurations of the parameters of the experiment. REALMAN experiments relevant to this thesis have been designed and executed by Renault, PSA Peugeot-Citroën and INRETS.

Motion experiment	Partner	Number of subjects	Trials per subject	Total number of trials
Door handling	Renault-PSA-INRETS	15	18	270
Vehicle accessibility	Renault-PSA	20	12	240
Maximal joint angles	INRETS	40	47	1880
Generic arm reaching	INRETS	40	94	3760
Safety belt handling	INRETS-Renault-PSA	24	29	696

Table 5.3: Total number of trials for each experiment of the REALMAN project.

5.4.1 DOOR HANDLING

Open and close motions of the car door were investigated in this experiment. The experiment was designed and executed by Renault, Peugeot-Citroën and INRETS. A preliminary study was performed on 20 car drivers while they were getting into their car, closed and opened the door while sitting in the seat, and got out of their car. It showed that people used the door handle while getting in and out of the car. Very few of them first opened the door and then, got out or got into the car.

Based on this preliminary study, a protocol for a laboratory investigation on the use of the door handles was defined. Two different tasks were defined, a close door task and an open door task. In the close door task, the start posture was sitting with the left arm straight but relaxed, the left hand on the handle and the door opened. Then, when asked, the subject had to close the door and go to a driving posture. In the open door task, the starting posture was a driving one, and then, the subject was asked to get out of the car. The purpose of the study was to investigate the use of the door handles but as people use them mostly in order to get out they were asked to do so. However, the Inverse Kinematic analysis is limited to upper limb movements.

5.4.1.1 Experimental vehicle mock-up

The same multi-adjustable experimental vehicle mock-up used for the vehicle accessibility experiment described in section 5.4.2.1 was used to investigate the door handling. A large number of design parameters can be adjusted on this vehicle mock-up but only three design parameters of the vehicle door were chosen as independent variables in this experiment. The vehicle mock-up parameters were adjusted to the Peugeot 307 values. The seat height was fixed at 300 mm representing an average seat height position.

5.4.1.2 Subjects

Fifteen volunteer subjects took part in the experiment (Table 5.4): five short females, five average-height males and five tall males. The subjects were chosen according to their stature: 5th percentile female, 50th percentile male and 95th percentile male of the population of French car drivers. All subjects were experienced drivers with 1-year minimum driving experience.

Group	Number	Stature percentile	Driving experience
Short females	5	5%	> 1 year
Average height males	5	50%	> 1 year
Tall males	5	95%	> 1 year

Table 5.4: Main characteristics of the subjects for the door handling experiment.

5.4.1.3 Motion capture

Door handling motions were recorded at 50 Hz with the Vicon motion capture system. Nine cameras were used and their location around the experimental vehicle mock-up is shown in Figure 5.18 and Figure 5.20. Thirty-six skin-markers, placed mainly on the upper limbs, were used to measure the motion of the subject. The locations of the skin-markers are described in section D.1.3 of Appendix D. Three markers were placed on the seat, four markers on the roof, one on the steering wheel, three on the door and four on other locations of the vehicle mock-up. All these markers were used to define the same global coordinate system for every subject and as a calibration corpus for PCMAN.

One video camera installed in front of the subject filmed the motion during the door handling experiment. These videos were used to understand possible problems occurring during the Inverse Kinematic analysis and to help the subjects to fill the discomfort questionnaires.

5.4.1.4 Anatomical calibration protocol

The software PCMAN was used to adjust the RAMSIS whole body model to each subject. In this experiment, four photos (Figure 5.18) at different angles of a single seated posture were taken in order to be closer to the experimental conditions. The positions of the skin-markers in GCS in the seated posture were recorded with Vicon instead of PCMAN due to the reasons presented in section 5.3.1. The same GCS was used for PCMAN and Vicon.

Figure 5.18: Four photos of the seated posture used for anatomical calibration with PCMAN in the door handling experiment. Reproduced from (Dufour et al., 2003).

5.4.1.5 RAMSIS model and driving constraints

Two complementary strategies were applied in the OTM implementation in Compamm when some DoFs of the model were not defined by the skin-markers available in the experiment. Firstly, some joints were substituted for other joints with fewer DoFs. Secondly, preservation posture conditions (sections 4.2.2.3 and 4.6.2) were included in the definition of the model.

In the door handling experiment, the hindfoot, toes and spine had no associated skin-marker and the shank had only one. Therefore, several DoFs of the RAMSIS model were not defined and the kinematic problem was under-guided. The following modifications were included in order to transform the under-guided kinematic problem into over-guided:

- The knee joints of the original RAMSIS model were substituted by revolute joints and the original ankle joints and hindfoot-toes joints

by weld joints. A weld joint allows no relative motion and the bodies linked by it move as a single body.

- The positions of the six body segments of the spine were defined with a relative preservation posture condition. The reference posture selected was the initial position of the spine given by PCMAN. The driving constraints associated with the relative preservation posture condition were included in Ψ_m and therefore the sum of their squared errors was minimised.

The OTM implementation in Matlab® can handle the shortage of skin-markers in several ways without modifying the multibody model structure or at least keeping the modifications to a minimum. Only four trials out of 270 of the door handling experiment were used to test the OTM features proposed in Chapter 4. The original RAMSIS model was used and the only modified joints were the two hindfoot-toes joints which were substituted by weld joints. The following additional driving constraints were included to prescribe the motion of the DoFs not defined by the available skin-markers:

- The longitudinal axis of the hindfoot was constrained to be perpendicular to the ground and its medio-lateral axis was constrained to be parallel to the ground. These two conditions were included in Ψ_s and therefore they were exactly satisfied. This is an absolute preservation posture condition.

- The positions of the six body segments of the spine were defined with a relative preservation posture condition as explained above.

- The joint angles of the wrist joints were included in the model and constrained to be zero. This condition is equivalent to minimise the squared sum of the wrist joint angles. As the wrist joint is a universal joint and the hand has only one associated skin-marker, two local minimisers exist. The condition on the wrist joint angles induces convergence to the appropriate solution. The driving constraints were included in Ψ_m and were multiplied by a weighting factor smaller than the one corresponding to the skin-marker of the hand.

- In the four trials used to test the OTM implementation in Matlab®, the skin-markers RHND and LANK (section D.1.3 of Appendix D) were frequently missing. Both skin-markers are critical because when RHND is missing the position of the right hand is undefined and when LANK is missing the position of the left shank, left foot and left toes are undefined, and therefore the kinematic problem is

under-guided. In this situation, the conditional weighting strategy presented in section 4.6.4 was used to transform the under-guided kinematic problem into over-guided. The joint angles of the left knee joint were included in the model. Then, LANK and the left knee joint angles, and RHND and the right wrist joint angles were associated by a conditional weighting strategy. The auxiliary driving constraints originating from the conditional weighting strategy were included in Ψ_m.

5.4.1.6 Experimental design

Three design parameters related to the car design were chosen as independent variables: horizontal distance between the door handle and the H-point, vertical distance between the door handle and the H-point and horizontal distance between the median plane of the car seat and the external side of the rocker panel.

Each subject performed 18 door handling trials and the total number of trials for the 15 subjects that participated in the experiment was 270. The whole procedure of the experiment did not exceed 3.5 hours per subject.

5.4.2 VEHICLE ACCESSIBILITY

Ingress-egress motions were investigated in this experiment. The experiment was designed and executed by Renault and Peugeot-Citroën. During the ingress-egress motion the subject executed the following steps:

1. Stand at a specific location with hands opened, walk to the vehicle mock-up and reach the door handle.
2. Open the door.
3. Ingress in the vehicle mock-up.
4. Put both hands on the steering wheel and the legs on the pedals.
5. Egress out of the vehicle mock-up.
6. Walk to the initial position and stand there with the hands opened.

A preliminary experimental campaign was performed on 23 car drivers using four real vehicles. For bulk and manoeuvrability reasons, the front and back parts of the vehicles were removed (Figure 5.19). The vehicles used in this preliminary study were Citroën Saxo 5 doors, Renault Megane 5 doors, Renault Kangoo and Peugeot 806. This study allowed to define the geometrical parameters of the vehicle, which influence the movements of the driver.

Figure 5.19: Renault Megane. Exterior and interior of the modified vehicle. Reproduced from (Dufour et al., 2003).

5.4.2.1 Experimental vehicle mock-up

A multi-adjustable experimental vehicle mock-up (Figure 5.20) was used to investigate vehicle accessibility. Seventeen design parameters can be adjusted on this vehicle mock-up (Table 5.5 and Figure 5.21).

N	Axis	Description	Minimum	Maximum
1*	Z	H point – Ground	400 mm	800 mm
2*	Z	Floor – H point	230 mm	460 mm
3	X	Steering wheel centre – H point	300 mm	450 mm
4*	Z	Steering wheel centre – H point	300 mm	450 mm
5	-	Slope of steering column – H point	20º	30º
6*	-	Width rocker panel – H point	300 mm	600 mm
7*	Z	Rocker panel – H point	100 mm	400 mm
8*	-	Cant rail – H point	100 mm	400 mm
9*	Z	Cant rail – H point	600 mm	900 mm
10	X	Low of lower front pillar – H point	400 mm	900 mm
11	X	High of lower from pillar – H point	400 mm	1000 mm
12	Z	High of lower from pillar – H point	300 mm	900 mm
13	-	Slope of front pillar – H point	20º	35º
14	X	Low of centre pillar – H point	0 mm	400 mm
15	X	Centre pillar – H point	0 mm	500 mm
16	X	Low of centre pillar – H point	0 mm	500 mm
17	Z	Centre pillar – H point	300 mm	900 mm

Table 5.5: Maximum and minimum values of the adjustable parameters of the vehicle mock-up. *Design parameters modified in the vehicle accessibility experiment.

5.4.2.2 Subjects

Twenty volunteer subjects took part in the experiment (Table 5.6). This population was distributed in 3 groups according to their stature percentile of the population of French car drivers. The three groups were: short females (5th

percentile female), average height males (50th percentile male) and tall males (95th percentile male). All subjects were experienced drivers with minimum 1-year driving experience.

Group	Number	Height
Short female	6	1.51 m – 1.62 m
Average height male	8	1.62 m -1.75 m
Tall male	6	1.75 m – 1.89 m

Table 5.6: Population characteristics for the vehicle accessibility experiment.

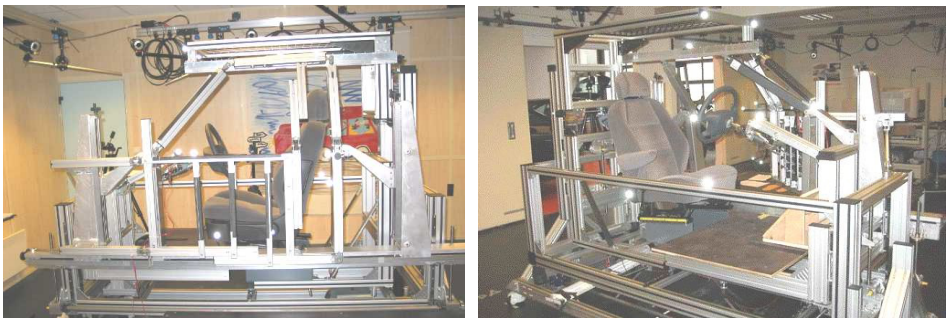

Figure 5.20: Vehicle mock-up for vehicle accessibility experiment (Dufour et al., 2003).

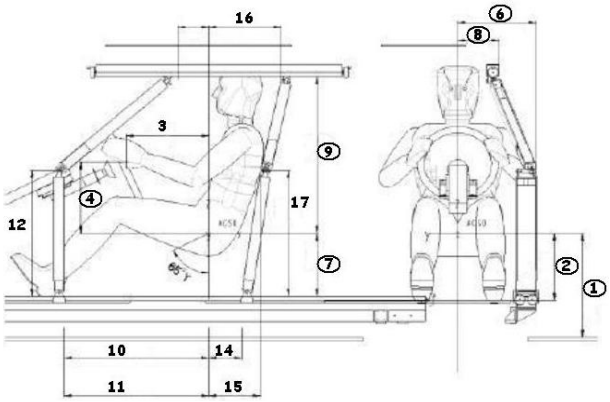

Figure 5.21: Adjustable parameters in the vehicle mock-up for vehicle accessibility. Design parameters modified in the experiment are encircled (Dufour et al., 2003).

5.4.2.3 Anatomical calibration protocol

The software PCMAN was used to adjust the RAMSIS whole body model to each subject. In this experiment, four simultaneous digital photos (Figure 5.22) of three different postures were taken. The three postures considered were a standing posture (Figure 2.7), a "pharaoh" posture (Figure 2.7) and a "Christ"

posture. The digital photos were taken simultaneously with four digital cameras located at fixed positions. This allowed to perform a single calibration for a group of subjects. A 3D structure with 10 fixed markers was used as a calibration corpus for PCMAN.

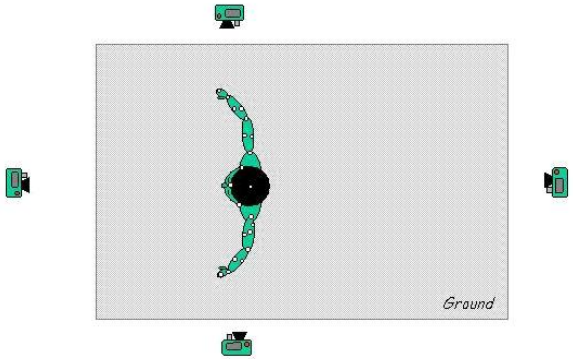

Figure 5.22: Disposition of the four digital cameras for the Anatomical Calibration Protocol in the vehicle accessibility experiment. Reproduced from (Dufour et al., 2003).

The positions of the skin-markers in GCS were not calculated with PCMAN due to the reasons presented in section 5.3.1. Instead, the positions of the skin-markers in GCS were recorded with Vicon in the "Christ" posture.

5.4.2.4 Motion capture

Ingress-egress motions were recorded at 50 Hz with the Vicon motion capture system. Twelve cameras were used and their location around the experimental vehicle mock-up is shown in Figure 5.23.

Cameras 1 to 5, 10 and 11 recorded the motion of the subject when he was inside the vehicle mock-up. Cameras 1, 10 and 11 overhung the measure space while cameras 2 to 5 were at the subject level. Additionally, cameras 10 and 11 were used to detect the skin-markers when the subject was leaving or entering to the vehicle mock-up. Cameras 6 to 9 and 12 recorded the motion of the subject when he was outside the vehicle mock-up. Forty-nine skin-markers were used to measure the motion of the subject, whose locations are described in section D.1.2 of Appendix D. Four additional markers were located on the door of the vehicle mock-up to record its motion.

Four synchronised video cameras filmed the whole movement of the subject from four different angles. These videos were used to understand possible problems occurring during the Inverse Kinematic analysis and to help the subjects to fill the discomfort questionnaires.

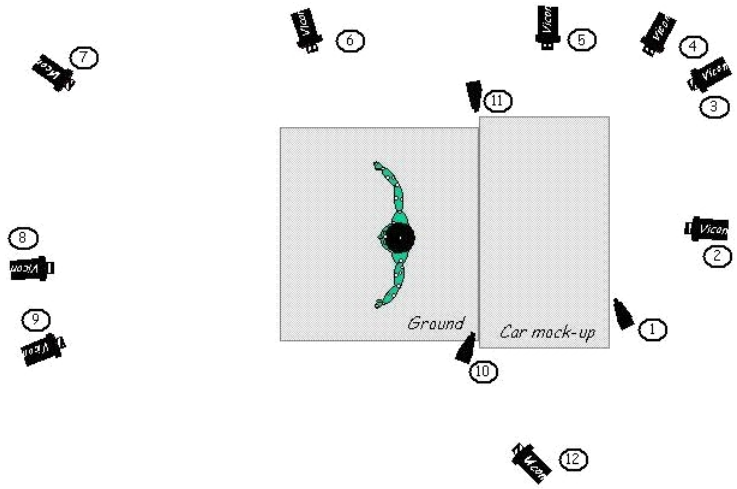

Figure 5.23: Distribution of Vicon cameras for the vehicle accessibility experiment. Reproduced from (Dufour et al., 2003).

5.4.2.5 RAMSIS model and driving constraints

The same strategies as in the door handling experiment (section 5.4.1.5) were applied in the OTM implementation in Compamm when some DoFs of the model were not defined by the skin-markers available in the experiment.

In the vehicle accessibility experiment, the spine had not any associated skin-marker. Therefore, the positions of the six body segments of the spine were not defined and the kinematic problem was under-guided. The under-guided kinematic problem was transformed into over-guided by adding a relative preservation posture condition for the spine. The reference posture selected was the initial position of the spine given by PCMAN. The driving constraints associated with the relative preservation posture condition were included in Ψ_m and therefore the sum of their squared errors was minimised.

Ten trials of the vehicle accessibility experiment out of 240 were used to test the OTM implementation in Matlab®. The following additional driving constraints were included to prescribe the motion of the DoFs not defined by the available skin-markers:

- The positions of the six body segments of the spine were defined with a relative preservation posture condition as explained above.
- The joint angles of the wrist joints were included in the model and constrained to be zero. These conditions on the wrist joint angles induce convergence to the appropriate solution (see section 5.4.1.5 for further details).

5.4.2.6 Experimental design

Among the 17 adjustable parameters of the vehicle mock-up, seven independent variables were chosen by Peugeot-Citroën and Renault. The remaining 10 adjustable parameters of the vehicle mock-up were fixed. Twelve different configurations were defined in order to study the influence of the each of the 7 parameters on the vehicle accessibility. These configurations are described in Table 5.7. For each configuration, the twenty subjects performed an ingress-egress motion, giving a total of 240 ingress-egress trials. The whole procedure of the experiment did not exceed 4.5 hours per subject.

5.4.3 MAXIMAL JOINT ANGLES AND GENERIC ARM REACHING

Maximal joint angles and generic arm reaching experiments were designed and executed by INRETS (Chevalot and Wang, 2004). Only those experiments relevant to this work are presented in this section.

5.4.3.1 Maximal joint angles

Each subject performed 47 maximal voluntary joint motions in a seated position. The joint maximum range of motion was defined as the maximum range that a joint can move actively without being forced. Joints maximum ranges of motion were measured in the classical anatomic directions (abduction-adduction, flexion-extension and lateral-medial) as well as in circumduction motions, which involve simultaneous motions in two axes. The total number of trials for the 40 subjects who participated in the experiment was 1880 (40 subjects × 47 motions per subject).

Configuration	Adjustable parameter number (see Table 5.5)						
	1	2	4	6	7	8	9
C01	464	230	333	381	111	156	727
C02	578	230	385	481	111	226	727
C03	464	310	385	381	111	226	783
C04	578	310	333	481	111	156	783
C05	464	310	385	481	191	156	727
C06	578	310	333	381	191	226	727
C07	464	230	333	481	191	226	783
C08	578	230	385	381	191	156	783
M09	521	270	359	431	151	191	755
P10	557	345	359	436	192	178	738
P11	488	236	353	470	109	168	757
P12	793	349	350	475	345	286	761

Table 5.7: Configurations of the vehicle mock-up investigated in the vehicle accessibility experiments. All values in mm.

The subjects were asked to seat on a flat stool without seat back and to perform the joint motions with maximum amplitude. The stool height was adjusted so that the knees were flexed around 90 degrees. In order to restrict the pelvis movement relative to the seat, the subjects were belted on the stool using a strap. As this pelvis restriction may affect the trunk movements especially in lateral flexion, the subjects were also asked to repeat all trunk movements without the pelvis being attached.

The joints considered in this study were the wrist, elbow, shoulder complex, sternoclavicular, combined motion of the joints of the dorso-lumbar column and combined motion of the joints of the cervical column.

5.4.3.2 Generic arm reaching

The subjects were asked to seat on a flat stool without seat back and the stool height was adjusted so that the knees were flexed around 90 degrees. The subjects were belted on the stool using a strap in order to restrain movements of the pelvis relative to the stool. Five different experiments were designed:

- Maximum reaching in a seated position.
- Pointing to a non-directional control.
- Influence of the orientation constraints on reaching motions.
- Influence of tasks on reaching motions.
- Combined motions.

Only the first two experiments are relevant to this work and are explained in this section.

5.4.3.2.1 Maximum reaching in a seated position

The objective of this type of motion was to measure maximum reach positions with and without trunk participation for each subject. The data were used to define the location of targets to be reached in the remaining experiments.

5.4.3.2.2 Pointing to a non-directional control

In this experiment, the right index finger had to reach and push a toggle switch without imposing a pushing direction. The targets were located in several positions as follows:

- The subject was located in 5 different orientations (Figure 5.24) with regard to the vertical plane of an experimental apparatus designed to hold the toggle switch (Figure 5.26). The sagittal plane of the subject

or orientation plane was located at 0° (P000), -45° (N045), 45° (P045), 90° (P090) and 135° (P135) with respect to the vertical plane of the apparatus.

- The targets were located at 5 different heights (Figure 5.24): height of the stool (H1), half height between the stool and the shoulder (H2), height of the shoulder (H3), height of the eyes (H4), and the height corresponding to the elevation of 135° from the arm natural rest position (H5). The 5 heights remained fixed for the 5 orientation planes. However, they were dependent on the subject size.

- The targets were located at 4 different distances (Figure 5.24). Maximum reach (MR) and arm reach (AR) are the maximum reachable distances with and without torso displacement respectively. Intermediate reach (IR) is the half of the distance between AR and MR. Proximal reach (PR) is a distance that only exists for height H2 and H3 and it corresponds to the distance AR minus the hand length. The distances were determined for each plane, i.e. the distances of the targets are subject and plane dependent.

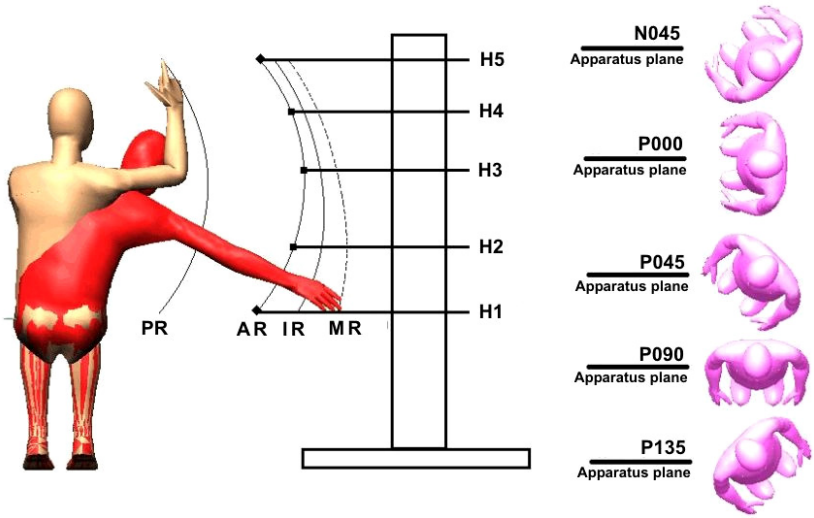

Figure 5.24: Location of targets for the generic arm reaching experiment. Reproduced from (Dufour et al., 2003).

For each orientation plane, 17 positions of the target were defined (Figure 5.25). Target location 6 corresponding to height H2 and distance IR was repeated twice (R2, R3) for testing repeatability. Then, for each orientation plane, 19 trials were recorded. Target location 1 (H1, AR) corresponding to the

orientation plane N045 was not used in the experiment due to the interferences between the target and the subject left knee. The total number of trials per subject was 94 (19 positions × 5 orientation planes – 1 location (H1, AR, N045)) and the total number of trials for the 40 subjects who participated in the experiment was 3760.

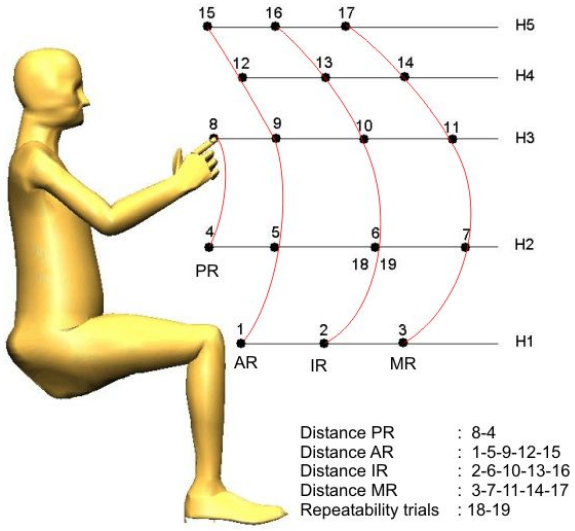

Figure 5.25: Locations of the target for a given orientation of the subject with regard to the vertical plane of the experimental apparatus. Reproduced from (Dufour et al., 2003).

5.4.3.3 Subjects

Twenty young and twenty aged subjects participated in the experiment (Table 5.8). They were divided into four groups: 10 young men (25-35 years old), 10 young women (25-35 years old), 10 aged men (65-80 years old) and 10 aged women (65-80 years old). Prior to the experiment, a medical check-up was performed by a medical doctor in order to assure that the subjects had neither musculoskeletal abnormalities nor any history of trauma.

Group	N	Age (Years)	Stature (mm)	Weight (kg)	Torso height (mm)	Arm length (mm)
Young men	10	27±3	1826±84	74±7	953±36	839±44
Young women	10	27±4	1648±40	59±6	871±28	765±34
Aged men	10	71±4	1694±54	76±14	895±29	801±27
Aged women	10	70±4	1611±64	67±10	851±36	787±42
All subjects	40	48±2	1695±102	69±11	892±50	798±45

Table 5.8: Main characteristics of the subjects for the maximal joint angles and generic arm reaching experiments (mean ± SD).

5.4.3.4 Experimental apparatus

A multi-adjustable experimental apparatus was used to investigate generic arm reaching and prehension movements (Figure 5.26). It is composed of one stool, one big pillar, one small pillar and 5 cantilever horizontal bars. The stool is equipped with a strap in order to restrain movements of the pelvis relative to the stool. An index attached to the stool allows setting accurate and repeatable angular positions of the stool with respect to the apparatus plane. The small pillar allows adjustments of the 5 bars in height. Once the heights are fixed, the bars can slide and be fixed into their housings. This allows adjustments of the distance from targets to subject at each height. Graduations were written on the bars in order to facilitate the reproduction of a measured distance. A toggle switch was optionally placed at the end of each of the 5 bars.

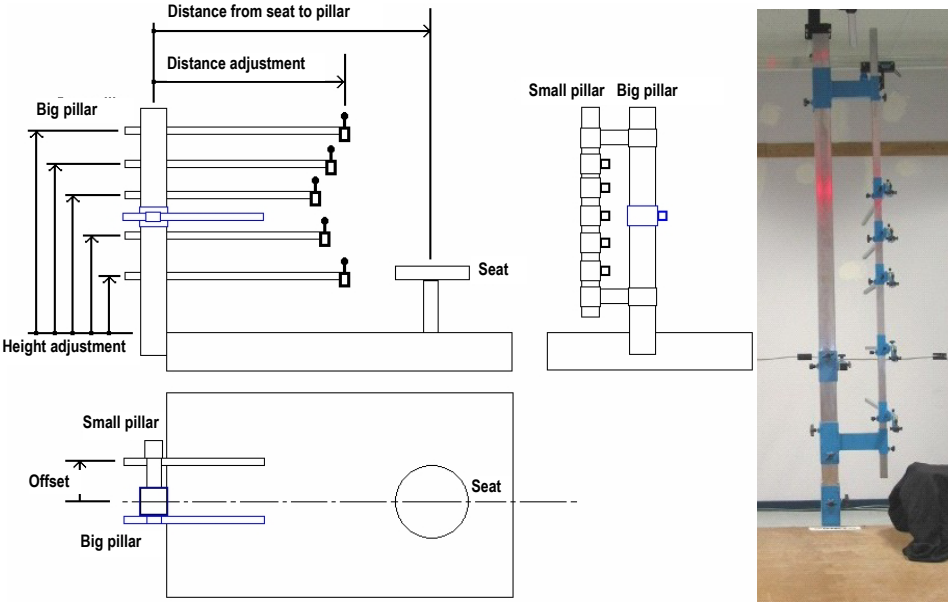

Figure 5.26: Experimental apparatus used for generic arm reaching experiment (left) and picture of the actual apparatus (right). Reproduced from (Dufour et al., 2003).

5.4.3.5 Anatomical Calibration Protocol

The software PCMAN was used to adjust the RAMSIS whole body model to each subject. A minimum of three photos from different views were taken simultaneously in three predefined postures. The positions of the skin-markers in GCS were recorded with Vicon instead of PCMAN due to the reasons presented in section 5.3.1.

5.4.3.6 Motion capture

Maximal joint angles and generic arm reaching motions were recorded at 50 Hz with the Vicon motion capture system, using ten cameras. Thirty-eight skin-markers were used and their locations are described in section D.1.3 of Appendix D. Three additional markers were placed on the stool and were used to define the same GCS for every subject.

With the aim of analysing the movements in a qualitative way, one video camera filmed the whole movement of the subject. As in the previous experiments, these videos were used to understand possible problems occurring during the Inverse Kinematic analysis and to help the subjects to fill the discomfort questionnaires.

5.4.3.7 RAMSIS model and driving constraints

The same strategies as in the door handling experiment (section 5.4.1.5) were applied in the OTM implementation in Compamm when some DoFs of the model were not defined by the skin-markers available in the experiment.

In the generic arm reaching experiment the left hand, feet and both toes had no associated skin-marker, the shanks had one associated skin-marker each, and the spine had five associated skin-markers. Therefore, several DoFs of the RAMSIS model were not defined and the kinematic problem was under-guided. The following modifications were included in order to transform the under-guided kinematic problem into over-guided:

- The knee joints of the original RAMSIS model were substituted by revolute joints and the original ankle joints, hindfoot-toes joints and left wrist joint by weld joints.
- The spine was modelled with six body segments and had five associated skin-markers. Therefore, the available skin-markers were not enough to define the position of the six body segments and some DoFs were not guided. A relative preservation posture condition was used to define the position of the spine. The reference posture selected was the initial position of the spine given by PCMAN. The driving constraints associated with the relative preservation posture condition were included in Ψ_m. The weighting factors associated with the five skin-markers were bigger than those associated with the joint angles included by the relative preservation posture condition.

Ten trials of the generic arm reaching experiment out of 3760 were used to test the OTM implementation in Matlab®. The original RAMSIS model was used and the only modified joints were the hindfoot-toes joints and the left wrist joint, which were substituted by weld joints. The following additional driving constraints were included in order to prescribe the motion of the DoFs not defined by the available skin-markers:

- The longitudinal axis of the hindfoot was constrained to be perpendicular to the ground and its medio-lateral axis was constrained to be parallel to the ground. These two conditions were included in Ψ_s. This is an absolute preservation posture condition.
- The positions of the six body segments of the spine were defined with a relative preservation posture condition as explained above.

Note that unlike the vehicle accessibility and door handling experiments, the joint angles of the right wrist joint were not constrained to be zero because in this experiment the right hand had two skin-markers associated.

In all the ten trials of the generic arm reaching experiment, the initial approximation for the first frame provided by PCMAN was far from the true initial solution. For some trials, OTM converged with the help of the global convergence strategy to a local minimiser but this was not the appropriate minimiser (see section 6.4.4 for an example). The solution adopted to force convergence towards the appropriate solution was to include additional driving constraints in Ψ_m during some initial frames. After a few frames these additional driving constraints were deactivated, i.e. their associated weighting factors were set to zero. In the generic arm reaching experiment, six vectors of the multibody model were guided during the first frames with suitable values, using additional driving constraints.

5.4.4 SAFETY BELT HANDLING

Safety belt buckling-unbuckling motions were investigated in this experiment designed and executed by Renault, Peugeot-Citroën and INRETS (Monnier et al., 2002; Monnier et al., 2003). A preliminary study was performed on 27 car drivers while they buckled the safety belt in their own cars. Three different strategies to reach the safety belt were identified (Figure 5.27):

- Most of the car drivers reach the safety belt with the right hand (Right hand strategy).
- The second most frequent strategy consists in using the left hand above the left elbow (Left hand up strategy).

- Least of the car drivers reach the safety belt with the left hand under the left elbow (Left hand down strategy).

Figure 5.27: Strategies of reaching the safety belt: Right hand strategy (left), Left hand up strategy (centre) and Left hand down strategy (right). From (Dufour et al., 2003).

5.4.4.1 Experimental vehicle mock-up

A multi-adjustable experimental vehicle mock-up (Figure 5.28) was used to investigate the safety belt handling. It is composed of one seat, two pedals, a steering wheel, a door (in a mesh form), and a central pillar on which the upper anchorage point and a rail allowing for the modification of the position of the lower anchorage point are fixed. The seat height, defined as the H-point height, was fixed at 300 mm, representing an average seat height position. The distance between the central plane of the seat and the anchorage points of the safety belt was also fixed, following the average value of today's cars.

Figure 5.28: Vehicle mock-up used during the safety belt handling experiment. Reproduced from (Dufour et al., 2003).

5.4.4.2 Subjects

Twenty-four volunteer subjects took part in the experiment: six short females, six average height males, six tall males and six aged average height males (above 59 years old). The subjects on each of the four groups were chosen according to their stature: 5th percentile female (short females), 50th percentile male (average height males) and 95th percentile male (tall males) of the population of French car drivers. All subjects were experienced drivers with 1-year minimum driving experience. The main characteristics of the four groups are summarised in Table 5.9.

	Short women (n=6)	**Average Men (n=6)**	**Tall men (n=6)**	**Aged average men (n=6)**	**All subjects (n=24)**
Stature	1552 ± 35	1730 ± 21	1910 ± 52	1735 ± 38	1732 ± 134
Sitting height	830 ± 30	913 ± 24	958 ± 32	912 ± 18	903 ± 53
Waist circumference	733 ± 77	862 ± 85	918 ± 70	930 ± 101	861 ± 112
Upper arm length	315 ± 33	337 ± 20	373 ± 20	330 ± 23	339 ± 32
Forearm-hand length	413 ± 16	478 ± 12	523 ± 24	478 ± 24	473 ± 44
Weight (kg)	56 ± 10	72 ± 10	93 ± 11	79 ± 11	75 ± 17
Age (year)	39 ± 7	38 ± 15	25 ± 2	61 ± 2	41 ± 16

Table 5.9: Main characteristics of the subjects (mean ± SD). All distances in mm.

Figure 5.29: Layout of the nine cameras of the motion capture system used in the safety belt handling experiment. Reproduced from (Dufour et al., 2003).

5.4.4.3 Motion capture

Safety belt buckling-unblucking motions were recorded at 50 Hz with the Vicon motion capture system, using nine cameras whose location around the

experimental vehicle mock-up is shown in Figure 5.29. Thirty-eight skin-markers, mainly placed on the upper limbs, were used to measure the motion of the subject. The locations of the skin-markers are described in section D.1.1 of Appendix D. Four additional markers were placed on the seat and remained fixed during all the trials. They were used to define the same global coordinate system for every subject.

With the aim of analysing the movements in a qualitative way, one video camera was installed in front of the subject. These videos were used to understand possible problems occurring during the Inverse Kinematic analysis and to help the subjects to fill the discomfort questionnaires.

5.4.4.4 Anatomical calibration protocol

The software PCMAN was used to adjust the RAMSIS whole body model to each subject. The standard PCMAN procedure is to take two orthogonal pictures of two different standing postures. In this experiment, four photos (Figure 5.30) at different angles of a single seated posture were taken, in order to be closer to the experimental conditions.

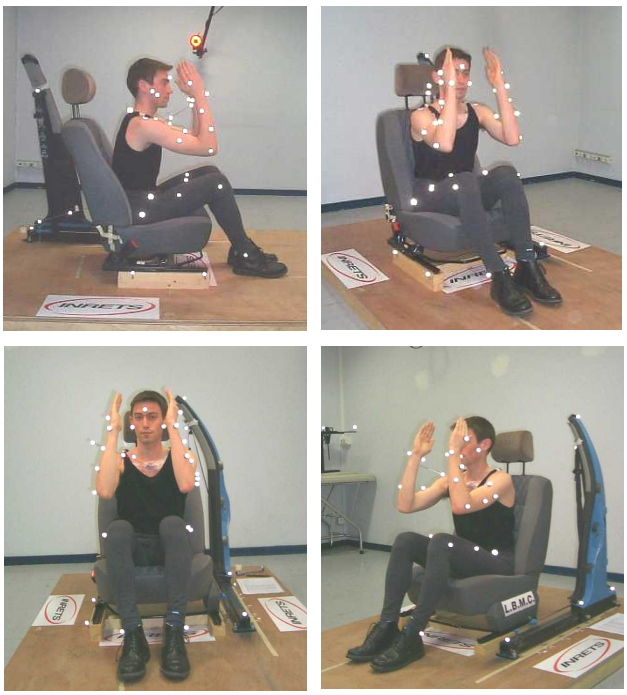

Figure 5.30: Four photos at different angles of the seated posture used for anatomical calibration with PCMAN in the safety belt handling experiment. From (Dufour et al., 2003).

The positions of the skin-markers in GCS were not measured with PCMAN due to the reasons presented in section 5.3.1. Instead the positions of the skin-markers in GCS were recorded with Vicon. The same GCS was used for PCMAN and Vicon.

5.4.4.5 RAMSIS model and driving constraints

The same strategies as in the door handling experiment (section 5.4.1.5) were applied in the OTM implementation in Compamm when some DoFs of the model were not defined by the skin-markers available in the experiment. In the safety belt handling experiment, the hindfoot, toes and spine had not any associated skin-marker and the shank had only one. Therefore, several DoFs of the RAMSIS model were not defined and the kinematic problem was under-guided. The following modifications were included to transform the under-guided kinematic problem into over-guided:

- The knee joints of the original RAMSIS model were substituted by revolute joints and the original ankle joints and hindfoot-toes joints by weld joints.
- The positions of the six body segments of the spine were defined with a relative preservation posture condition. The reference posture selected was the initial position of the spine given by PCMAN. The driving constraints associated with the relative preservation posture condition were included in Ψ_m and therefore the sum of their squared errors was minimised.

Unlike the previous experiments the safety belt handling experiment was not used to test the OTM implementation in Matlab® because trials of this experiment were not available.

5.4.4.6 Experimental design

Four independent variables were studied in this experiment. Three of them are related to the car design: the longitudinal position of the upper anchorage point (X), the height of the tongue (Z) and the way in which the lower point (LP) of the safety belt is fixed (Figure 5.31). This lower point of the safety belt can be either fixed to the centre pillar, to the seat or it may slide along a rail. As it is difficult to compare the movements and the feeling of discomfort when different reaching strategies are used, the reaching strategy was chosen as the fourth independent variable. A total of 696 safety belt handling trials were recorded. The whole procedure of the experiment did not exceed 3.5 hours per subject.

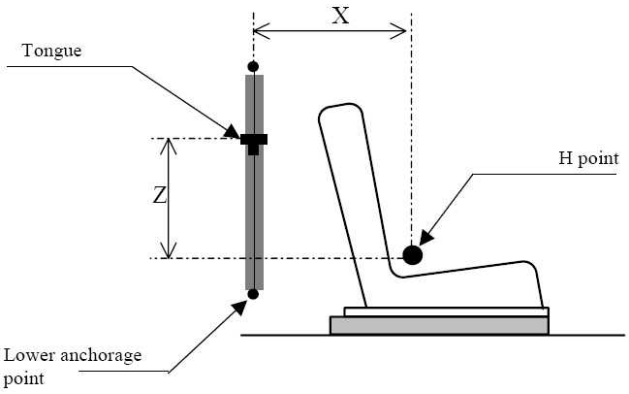

Figure 5.31: Variables studied in the experimental vehicle mock-up: Upper anchorage point location (X), tongue height (Z) and the three ways the lower anchorage point can be fixed (fixed to the centre pillar, fixed to the seat or it may slide along a rail (Dufour et al., 2003).

CHAPTER 6

RESULTS AND DISCUSSION

This chapter evaluates and discusses the performance of the methods, strategies and protocols developed in this thesis for the motion reconstruction problem.

Section 6.1 presents the OTM solvers specifically developed for solving the Optimal Tracking Problem and the strategies of motion reconstruction analysed in this chapter. The main characteristics of the human skeletal models and experiments used to test OTM performance and to evaluate the strategies of motion reconstruction are summarised in section 6.2. Section 6.3 presents the parameters used to measure performance and the results of the OTM performance while the results of the evaluation of the strategies for motion reconstruction are presented in section 6.4.

In the frame of the MoDyCo project, an Anatomical Calibration Protocol for estimating subject-specific parameters of a human skeletal model is proposed in Chapter 5. In section 6.5 the errors in the subject-specific parameters associated with the measurement errors of anatomical landmarks in the Anatomical Calibration Protocol are analysed.

6.1 OTM SOLVERS AND STRATEGIES OF MOTION RECONSTRUCTION

6.1.1 OTM SOLVERS

OTM is a new optimisation method specifically designed for solving the Optimal Tracking Problem (OTP) defined in section 4.5 and which can be

used both for solving the motion reconstruction problem and for generating computer-simulated motions. OTM is a collection of four numerical methods (direct QR, two-step QR, nullspace and two-step LU), two strategies for achieving global convergence to a local minimum (merit function and maxmin strategies), two step-control modes (optimal step-length and full step-length), and one reordering method (reverse Cuthill-McKee) of the coefficient matrix **C**. The reordering method was used only in combination with the direct QR method.

Solver code	Numerical method	Step-control mode	Global convergence strategy
A1f	Direct QR	optimal step-length	merit function
A2f	Direct QR	full step-length	merit function
Ar1f	Direct QR / reordering	optimal step-length	merit function
Ar2f	Direct QR / reordering	full step-length	merit function
B1f	Two-step QR	optimal step-length	merit function
B2f	Two-step QR	full step-length	merit function
C1f	Nullspace	optimal step-length	merit function
C2f	Nullspace	full step-length	merit function
D1f	Two-step LU	optimal step-length	merit function
D2f	Two-step LU	full step-length	merit function
A1x	Direct QR	optimal step-length	maxmin
A2x	Direct QR	full step-length	maxmin
Ar1x	Direct QR/reordering	optimal step-length	maxmin
Ar2x	Direct QR/reordering	full step-length	maxmin
B1x	Two-step QR	optimal step-length	maxmin
B2x	Two-step QR	full step-length	maxmin
C1x	Nullspace	optimal step-length	maxmin
C2x	Nullspace	full step-length	maxmin
D1x	Two-step LU	optimal step-length	maxmin
D2x	Two-step LU	full step-length	maxmin

Table 6.1: OTM solvers used for the motion reconstruction problem and for generating computer-simulated motions. Numerical methods: direct QR (A), two-step QR (B), nullspace (C), two-step LU (D). Global convergence strategy: merit function strategy (f), maxmin strategy (x). Step-control mode: optimal step-length (1), full step-length (2). Reordering: reverse Cuthill-McKee.

In this thesis a particular solver is defined as a combination of a numerical method, a global convergence strategy, a step-control mode and a reordering method. The different solvers investigated are summarised in Table 6.1. Recall that there are two implementations of OTM, one in Matlab® and

another in Compamm. All the solvers defined in Table 6.1 were tested in the Matlab® implementation. However, as explained in section 5.3.3.1, only the two-step LU method, without global convergence strategy and with full step-length (α=1) for all frames was used in the Compamm implementation.

6.1.2 MOTION RECONSTRUCTION STRATEGIES

In this chapter, the following strategies presented in Chapter 4 for the missing marker problem and other issues related to motion reconstruction are evaluated:

- Progressive weighting strategy (section 4.6.4).
- Conditional weighting strategy (section 4.6.4).
- Relative preservation posture condition (section 4.6.2).
- Absolute preservation posture condition (section 4.6.2).
- Convergence to the desired solution (section 4.6.2).

The five strategies have been developed and tested in the frame of OTM and all of them take advantage of the structure of the weighted OTP presented in section 4.6.1. However, they are general strategies and can be used with other optimisation methods.

All strategies have not been applied to each experiment. Table 6.2 summarises the motion reconstruction strategies used in each experiment. The main characteristics of each experiment used to test the strategies are described in the next section.

Motion reconstruction strategy	Experiment
Progressive weighting strategy	Generic arm reaching Door handling
Conditional weighting strategy	Door handling
Relative preservation posture condition	Generic arm reaching Door handling Vehicle accessibility Steering manoeuvre for UBM-INV Steering manoeuvre for UBMS-INV
Absolute preservation posture condition	Generic arm reaching Door handling Steering manoeuvre for UBM-INV Steering manoeuvre for UBMS-INV
Convergence to the desired solution	Generic arm reaching

Table 6.2: Summary of the motion reconstruction strategies used in each experiment.

6.2 MOTION RECONSTRUCTION PROBLEMS AND COMPUTER-SIMULATED MOTIONS

The performance of the OTM implementation in Matlab® was tested on five motion reconstruction problems and two computer-simulated motion problems. A motion reconstruction problem is defined by a human skeletal model and a human motion recorded with a motion capture system (Table 6.3).

Experiment	Human skeletal model	Number of trials	Project
Vehicle accessibility	RAMSIS whole body model	10	REALMAN
Door handling	RAMSIS whole body model	4	REALMAN
Generic arm reaching	RAMSIS whole body model	10	REALMAN
Steering manoeuvre	UBM	12	MoDyCo
Steering manoeuvre	UBMS	12	MoDyCo

Table 6.3: Motion reconstruction problems solved with OTM.

A computer-simulated motion problem is defined by a human skeletal model and a computer-simulated motion (Table 6.4). The kinematic constraints of all the human skeletal models were obtained with the help of the Matlab® Symbolic Toolbox. The main characteristics of the experiments and human skeletal models are presented in the next four subsections.

Computer-simulated motion	Human skeletal model	Number of trials	Project
Steering manoeuvre	UBM-INV	4	MoDyCo
Steering manoeuvre	UBMS-INV	4	MoDyCo

Table 6.4: Computer-simulated motion problems solved with OTM.

6.2.1 VEHICLE ACCESSIBILITY

Ten out of 240 trials of the vehicle accessibility experiment were used to test the OTM implementation in Matlab® (Table 6.5). The initial approximation for the first frame was very close to the true initial solution for the ten trials. Renault and Peugeot-Citroën smoothed the recorded marker coordinates and interpolated all the missing markers (Dufour et al., 2003). Therefore, all markers were visible on every frame and the weighting strategies presented in section 4.6.4 were not necessary for these trials.

The original RAMSIS model was modified in order to prescribe the motion of the DoFs not defined by the available markers (section 5.4.2.5). The motion reconstruction strategies used to prescribe their motion with additional driving constraints are summarised in Table 6.6.

Trial code	Subject	Vehicle setup	Frames	Time	Noise level	Missing markers	Initial approx.
VA01	S01	C01	1388	27.76 s	smoothed	none	good
VA02	S01	C02	1105	22.10 s	smoothed	none	good
VA03	S01	C03	1145	22.90 s	smoothed	none	good
VA04	S01	C04	1109	22.18 s	smoothed	none	good
VA05	S01	C05	1228	24.56 s	smoothed	none	good
VA06	S02	C03	1051	21.02 s	smoothed	none	good
VA07	S02	P11	1262	25.24 s	smoothed	none	good
VA08	S03	C03	968	19.36 s	smoothed	none	good
VA09	S05	M09	1242	24.84 s	smoothed	none	good
VA10	S05	P12	1218	24.36 s	smoothed	none	good

Table 6.5: Trials of the vehicle accessibility experiment used to test OTM performance. The vehicle setup code is presented in Table 5.7. Noise level: indicates if the marker coordinates are the original raw data or they have been smoothed. Initial approx.: quality of the initial approximation for the first frame.

Generalised coordinates added to the model	Strategy	Constraint type[1]	Purpose
Joint angles of the right wrist (UNIV joint)	Rel. preservation posture condition	Ψ_m	Induce convergence to the right solution
Joint angles of the left wrist (UNIV joint)	Rel. preservation posture condition	Ψ_m	Induce convergence to the right solution
Joint angles of the spine (1 UNIV joint, 5 SPH joints)	Rel. preservation posture condition	Ψ_m	Prescribe the motion of the spine bodies.

Table 6.6: Modifications of the original RAMSIS model for the vehicle accessibility experiment. [1]The additional driving constraints associated with the new generalised coordinates can be included in Ψ_m or in Ψ_s (section 4.6.1).

Variable	Vehicle accessibility	Door handling	Generic arm reaching
Generalised coordinates (q)	684	654	660
Natural coordinates	663	633	645
Relative coordinates	21	21	15
Driven coordinates (z)	156	126	150
Kinematic constraints (Φ)	647	635	642
Independent constraints	626	614	627
Redundant constraints	21	21	15
Driving constraints (Ψ)	156	126	150
Matrices:			
Φ_q	647 × 684	635 × 654	642 × 660
H, A	684 × 684	654 × 654	660 × 660
C	1368 × 1368	1308 × 1308	1320 × 1320

Table 6.7: Size of the RAMSIS model for the vehicle accessibility, door handling and generic arm reaching experiments.

Table 6.7 summarises the sizes of the variables of the RAMSIS model used in the motion reconstruction of the vehicle accessibility, door handling and generic arm reaching experiments. Note that the number of generalised coordinates plus the number of kinematic constraints is greater than 1200 for the three experiments.

The motion reconstruction is formulated as a nonlinear constrained optimisation problem, called OTP (section 4.5). According to Benson et al. (2003), an optimisation problem can be classified as large-scale if the number of variables (generalised coordinates) plus the number of constraints (kinematic constraints) is at least 1000. Therefore, OTP for the vehicle accessibility, door handling and generic arm reaching experiments is a large-scale optimisation problem.

6.2.2 DOOR HANDLING

Four trials out of 270 of the door handling experiment were used to test the OTM implementation in Matlab® (Table 6.8).

Trial code	Subject	Vehicle setup	Frames	Time	Noise level	Missing markers	Initial approx
DH01	01YM	C01	176	3.52 s	raw data	Table 6.9	good
DH02	01YM	C07	185	3.70 s	raw data	Table 6.9	good
DH03	04FL	C02	177	3.54 s	raw data	Table 6.9	good
DH04	12SP	C02	171	3.42 s	raw data	Table 6.9	good

Table 6.8: Trials of the door handling experiment used to test OTM performance. The vehicle setup code is presented in Table 5.7. Noise level: indicates if the marker coordinates are the original raw data or they have been smoothed. Initial approx.: quality of the initial approximation for the first frame.

The initial approximation for the first frame was very close to the true initial solution for all the trials. The original marker coordinates measured by Vicon were used, i.e. the motion data had missing markers (Table 6.9) and were not smoothed. Therefore, the progressive weighting and conditional weighting strategies were applied to these trials.

The progressive weighting strategy was applied to all the missing markers (Table 6.9), while the conditional weighting strategy was applied to markers RHND and LANK (section 5.4.1.5). Both markers are critical to define the position of the right hand and left leg respectively. When RHND is missing, the position of the right hand is undefined, and when LANK is missing, the positions of the left shank, left hindfoot and left toes are undefined. The other missing markers are not critical because there are sufficient visible markers to

define the position of all the body segments of the RAMSIS model at every frame (Table 6.9).

Marker name	Door handling trial							
	01YM_C01		01YM_C07		04FL_C02		12SP_C02	
	Frame index	%	Frame index	%	Frame index	%	Frame index	%
Head								
LHED			23-65	23.2	1-7	4.0	1-26	15.2
RHED					1-4	2.3		
FHED							1-5	2.9
Spine								
VRC7	130-176	26.7	1-85,99-169	84.3	75-115	23.2	104-151	28.1
Pelvis								
RASI					1-66	37.3		
Left arm								
LACC					1,119-136	10.7		
LUAT	1-5	2.8			1-5	2.8		
LUAI					1-9	5.1	1-5	2.9
LFAE							84-99	9.4
LFAI	149-166	10.2						
LWRB	1-30, 38-58	29.0	1-50, 57-76	37.8			1-46, 59-129	68.4
Left leg								
LTHI			1	0.5	1-9	5.1		
LKNE					95-177	46.9	1-74	43.3
LANK	63-99	21.0	83-108	14.1	1-55, 62-177	96.6	1-51, 69-171	90.1
Right arm								
RFAE	1-5	2.8						
RFAI	1-10	5.7						
RWRA	1-55	31.3						
RWRB			1-2	1.1	1-8	4.5		
RHND					1-10	5.6		
Right leg								
RKNE	1-10	5.7	1-63	34.1				

Table 6.9: Summary of the missing markers in the four door handling trials. Frame index: Index of the frames in which the marker is missing. %: Percentage of the frames in which the marker is missing.

The modifications of the original RAMSIS model were the same as for the vehicle accessibility experiment plus some additional modifications for the feet (section 5.4.1.5). In the door handling experiment, markers were not located on the feet and therefore their motion was not defined. The feet were constrained to remain parallel to the ground using an absolute preservation

posture condition. The modifications included in the model are summarised in Table 6.10. The sizes of the variables of the RAMSIS model used in the motion reconstruction of the door handling experiment are summarised in Table 6.7.

Body	Generalised coordinates added to model	Strategy	Constraint type[1]	Purpose
Right hindfoot	-	Abs. preservation posture condition	Ψ_s	Prescribe the motion of right foot
Left hindfoot	-	Abs. preservation posture condition	Ψ_s	Prescribe the motion of left foot
Right hand	Joint angles of the right wrist (UNIV joint)	Rel. preservation posture condition	Ψ_m	Induce convergence to the right solution
Left hand	Joint angles of the left wrist (UNIV joint)	Rel. preservation posture condition	Ψ_m	Induce convergence to the right solution
Bodies of the spine	Spine joint angles (1 UNIV joint, 5 SPH joints)	Rel. preservation posture condition	Ψ_m	Prescribe the motion of the spine bodies

Table 6.10: Modifications of the original RAMSIS model for the door handling experiment.
[1]Additional driving constraints can be included in Ψ_m or Ψ_s (section 4.6.1).

6.2.3 GENERIC ARM REACHING

Ten out of 3760 trials of the generic arm reaching experiment were used to test the OTM implementation in Matlab® (Table 6.11). The initial approximation for the first frame was far from the true initial solution. OTM converged with the help of a global convergence strategy to a local minimiser, but this was not always the appropriate minimiser. In order to force convergence towards the appropriate solution, additional driving constraints, which were activated only during the first three frames, were included in Ψ_m (see section 5.4.3.7 for details).

The original marker trajectories measured by Vicon were used to perform the motion reconstruction. Although the motion data were not smoothed, their quality was very good and there were very few missing markers (Table 6.13). The progressive weighting strategy was used for the few markers that were missing for some frames. The conditional weighting strategy was not necessary as no critical markers were missing.

While markers were not located on the feet, the spine had five associated skin-makers, which were not sufficient to define the position of the six body segments of the spine (section 5.4.3.7). The feet were constrained to remain

parallel to the ground using an absolute preservation posture condition and the position of the spine was defined with a relative preservation posture condition. The modifications included in the model are summarised in Table 6.12. The sizes of the variables of the RAMSIS model used in the motion reconstruction of the generic arm reaching experiment are summarised in Table 6.7.

Trial code	Subject	Target location	Frames	Time	Noise level	Missing markers	I. A.
GR01	04_SD	P000-H3-MR	155	3.10 s	raw data	none	bad
GR02	04_SD	P090-H1-MR	180	3.60 s	raw data	none	bad
GR03	04_SD	P135-H5-MR	191	3.82 s	raw data	none	bad
GR04	05_MF	P045-H4-IR	222	4.44 s	raw data	Table 6.13	bad
GR05	06_FC	N045-H2-PR	123	2.46 s	raw data	none	bad
GR06	07_DP	P135-H2-AR	235	4.70 s	raw data	Table 6.13	bad
GR07	08_BS	P000-H2-PR	187	3.74 s	raw data	none	bad
GR08	09_SF	P090-H1-AR	167	3.34 s	raw data	none	bad
GR09	09_SF	P090-H2-MR	181	3.62 s	raw data	none	bad
GR10	13_PT	N045-H2-R3	191	3.82 s	raw data	Table 6.13	bad

Table 6.11: Generic arm reaching trials used to test OTM performance. The target location code is explained in section 5.4.3.2. I.A.: quality of the initial approximation for the first frame.

Body	Generalised coordinates added to model	Strategy	Constraint type[1]	Purpose
Right hindfoot	-	Abs. preservation posture condition	Ψ_s	Prescribe motion of right foot
Left hindfoot	-	Abs. preservation posture condition	Ψ_s	Prescribe motion of left foot
Bodies of the spine	Spine joint angles (5 SPH joints)	Rel. preservation posture condition	Ψ_m	Prescribe motion of the spine bodies

Table 6.12: Modifications of the original RAMSIS model for the door handling experiment. [1]Additional driving constraints can be included in Ψ_m or Ψ_s (section 4.6.1).

Trial code	Marker names			
	crest_l (pelvis)		mhe_r (right upper arm)	
	Frame index	%	Frame index	%
GR04	1-3	1.4		
GR06			96-147	22.1
GR10	1-33	17.3		

Table 6.13: Summary of the missing markers in the ten generic arm reaching trials. Frame index: Index of the frames in which the marker is missing. %: Percentage of the frames in which the marker is missing.

6.2.4 STEERING MANOEUVRE

At the time of writing this document, real experiments have not been recorded in the frame of the MoDyCo project. Therefore, computer-simulated trials of one steering manoeuvre have been generated to test the skeletal models and the OTM implementation in Matlab®. The same steering manoeuvre has been simulated with two upper limb models called UBMS-INV and UBM-INV (section 5.2.1). Four computer-simulated trials been generated for each upper limb model (Table 6.14 and Table 6.15), one for each of the four vehicle configurations.

Trial code	Subject	Vehicle setup	Frames	Time
PF1w	S01	PF1	151	3.02 s
PF2w	S01	PF2	151	3.02 s
PF3w	S01	PF3	151	3.02 s
PF4w	S01	PF4	151	3.02 s

Table 6.14: Computer-simulated trials generated with UBMS-INV.

Trial code	Subject	Vehicle setup	Frames	Time
PF1wo	S01	PF1	151	3.02 s
PF2wo	S01	PF2	151	3.02 s
PF3wo	S01	PF3	151	3.02 s
PF4wo	S01	PF4	151	3.02 s

Table 6.15: Computer-simulated trials generated with UBM-INV.

The marker coordinates obtained from the computer-simulated motions are considered the true values, i.e. they are free from errors. Then, artificial noise is added to these true data in order to generate realistic motion data. Twenty four trials, twelve for each upper limb model, were generated by adding three different random patterns of simulated skin-movement artifact to each of the eight computer-simulated motions (section 5.2.1.3).

The twelve trials for UBMS and the twelve trials for UBM have the same main characteristics (Table 6.16). However, they have different patterns of simulated skin-movement artifact and are generated with different upper limb models. Note that a single subject was used to generate all the motions. Due to the lack of real data, the coordinates of the anatomical landmarks of this subject were obtained from two sources in the literature (section 5.2.1.2).

In the MoDyCo project, most of the body segments have a minimum of three markers, hence the method of Söderkvist (1993) (see section 4.3.3.2) can be used to estimate a good initial approximation for the first frame. For body segments with less than three markers, a good initial approximation can also be

obtained from the markers on those body segments and the data obtained from the adjacent bodies. The missing marker problem was not simulated. Therefore, all markers were visible on every frame and the weighting strategies presented in section 4.6.4 were not necessary for these trials.

Trial code UBMS	Trial code UBM	Vehicle setup	Frames	Time	Noise level	Missing markers	Initial approx.
S01w	S01wo	PF1	151	3.02 s	s.s.m.a	none	good
S02w	S02wo	PF1	151	3.02 s	s.s.m.a	none	good
S03w	S03wo	PF1	151	3.02 s	s.s.m.a	none	good
S04w	S04wo	PF2	151	3.02 s	s.s.m.a	none	good
S05w	S05wo	PF2	151	3.02 s	s.s.m.a	none	good
S06w	S06wo	PF2	151	3.02 s	s.s.m.a	none	good
S07w	S07wo	PF3	151	3.02 s	s.s.m.a	none	good
S08w	S08wo	PF3	151	3.02 s	s.s.m.a	none	good
S09w	S09wo	PF3	151	3.02 s	s.s.m.a	none	good
S10w	S10wo	PF4	151	3.02 s	s.s.m.a	none	good
S11w	S11wo	PF4	151	3.02 s	s.s.m.a	none	good
S12w	S12wo	PF4	151	3.02 s	s.s.m.a	none	good

Table 6.16: Trials of the steering manoeuvre experiment used to test OTM performance. Noise level - s.s.m.a.: simulated skin movement artifact (section 5.2.1.3). Initial approx.: quality of the initial approximation for the first frame.

Table 6.17 summarises the size of the variables of the four upper limb models used. Recall that UBMS-INV and UBM-INV are used to generate the computer-simulated motions while UBMS and UBM are used to reconstruct the motion from the computer-simulated marker trajectories.

Variable	UBMS	UBMS-INV	UBM	UBM-INV
Generalised coordinates (q)	354	371	300	317
Natural coordinates	339	339	291	291
Relative coordinates	15	32	9	26
Driven coordinates (z)	96	33	90	27
Kinematic constraints (Φ)	340	386	282	328
Independent constraints	325	354	273	302
Redundant constraints	15	32	9	26
Degrees of freedom	29	17	27	15
Driving constraints (Ψ)	96	33	90	27
Matrices:				
Φ_q	340 × 354	386 × 371	282 × 300	328 × 317
H, A	354 × 354	371 × 371	300 × 300	317 × 317
C	708 × 708	742 × 742	600 × 600	634 × 634

Table 6.17: Size of the human skeletal models of the MoDyCo project.

6.3 OTM PERFORMANCE

The performance of OTM for solving the motion reconstruction problem and for generating computer-simulated motions is evaluated in this section. The two implementations of OTM, one in Matlab® and another in Compamm, have been evaluated differently.

The performance of the Compamm implementation for reconstructing all the REALMAN experiments (>6000 trials) was studied only qualitatively by some of the REALMAN partners. The results provided by them are presented in section 6.3.1. In section 6.3.2 the performance of the Matlab® implementation is studied quantitatively using a subset of 24 trials of the REALMAN experiments and the 32 computer-simulated trials of the MoDyCo project. Finally, in section 6.3.3 Compamm and Matlab® implementations are compared using 10 trials of the vehicle accessibility experiment.

6.3.1 OTM IMPLEMENTATION IN COMPAMM

6.3.1.1 Safety belt handling and generic arm reaching

INRETS reported results for the safety belt handling and generic arm reaching experiments (Renard et al., 2004; Wang et al., 2005). The reconstructed motions were evaluated in two steps. First, the model-determined marker coordinates calculated with Compamm were compared with the measured marker coordinates. Second, the reconstructed motions were assessed visually. The visual inspection was necessary because a reconstructed motion may appear unnatural even when model-determined marker trajectories are close to the measured ones.

For the safety belt handling experiment, 24 subjects performed 696 trials. Due to the missing marker problem (progressive weighting and conditional weighting strategies were not available during the REALMAN project), 662 trials were usable for motion reconstruction and 93% of them were visually validated.

Motion	Successfully captured motions	Visually validated motions	% of visually accepted motions
Safety belt handling*	662	619	93%
Generic arm reaching	1880	1711	91%

Table 6.18: Summary of the evaluation of safety belt handling and generic arm reaching motions. *Only the safety belt reaching phase was considered.

For the generic arm reaching experiment 20 subjects performed 1880 trials in the whole arm reachable space from a seated position. The reconstructed motions looked smooth, very realistic and "human-like" in most of the cases (68%). In other cases (23%), the reconstructed motions were realistic but not smooth, troubles like trembling of some body segments during a short period and/or small discontinuities were detected. These troubles may be due to an inappropriate data smoothing, a too high tolerance for accepting a solution or the lack of convergence to the desired tolerance. An appropriate post-processing was applied to correct these defaults. If these small imperfections are accepted, the number of visually acceptable movements was 1711, representing 91% of the motions. The results of motion evaluation of both experiments are summarised in Table 6.18.

It has to be noted that visual inspection is subjective and person-dependent. Rejection was mainly based on motion discontinuity. Movements with small trembling or very short discontinuities were accepted because these defaults can be corrected by an appropriate post-processing. To illustrate the quantitative difference between reconstructed and recorded motions, two examples are presented (Table 6.19 and Table 6.20), one for each experiment.

Body segment	Marker name	Subject 1		Subject 2	
		Mean (mm)	Std (mm)	Mean (mm)	Std (mm)
Hand	smc_r	11.8	13.7	12.1	13.9
	vmc_r	13.4	14.2	13.5	13.4
	ls_r	15.6	12.1	15.9	10.9
	ms_r	11.2	12.3	12.2	12.2
Forearm	forearm1	10.9	9.1	11.4	8.1
	forearm2	10	10.8	10.8	10.5
	forearm3	11.8	10	10.7	8.4
	lhe_r	13.2	10.8	10.6	7.7
	mhe_r	13.5	13.8	7.5	7.3
Upper arm	arm1	10.4	9.1	7.6	6.2
	arm2	10.8	9.3	9.6	7.2
	arm3	13.2	9.8	11.4	7.3
Torso	Head_r	4	3.6	3.7	3.0
	Head_l	6	5.4	4.3	3.5
	Head_f	4.5	4.2	4.0	3.4
Pelvis	psis_r	3.2	2.3	3.0	2.2
	psis_l	2.7	2.4	2.1	1.6
	crest_r	3.9	2.7	2.6	1.7
	crest_l	7.6	4.9	2.7	2.0

Table 6.19: Average distance between model-determined and measured marker trajectories from two participants of the generic arm reaching experiment. Marker locations are described in section D.1.3 of Appendix D.

Table 6.19 shows the average distance between model-determined and measured marker trajectories from two participants of the generic arm reaching experiment. An error of less than 20 mm in average for all markers was obtained. Higher error was found for the markers situated in the distal body segments. This is probably due to the fact that the markers' accelerations on the distal body segments are higher and the relative motion between the markers and the underlying bone is bigger. However, other variables like the measurement errors in the Anatomical Calibration Protocol, the weighting factors associated to each marker or the measurement errors of the nearby markers have also a decisive influence in the mean distance error.

Table 6.20 shows the average distance between model-determined and measured marker trajectories from 9 safety belt handling trials of one subject. The mean and standard deviation of these distances for 8 representative markers are presented. The markers located on the arms were well followed as their mean distance was lower than 13 mm. On the other hand, markers located on segments near the spine were less well followed as their mean distance was greater than 20 mm (RACC, STRN and FHED). This might be due to excessively large values of the weights associated to the joint angles of the spine used to define the relative preservation posture condition. For large weight values, the posture of the spine is very close to the reference posture defined by the relative preservation posture condition. However, the higher the weights associated to the joint angles of the spine, the larger the distance errors of the markers on segments near the spine (see section 6.4.3 for details).

Body segment	Approximated location	Marker	Mean (mm)	Std (mm)
Head	Front head	FHED	29.4	2.5
Torso	Sternum (below)	STRN	24.5	3.4
Left clavicle	Left acromion	LACC	15.2	2.9
Left arm	Left elbow	LELB	3.7	0.7
	Left wrist (thumb side)	LWRA	12.5	0.5
Right clavicle	Right acromion	RACC	27.2	3.8
Right arm	Right elbow	RELB	9.4	1.3
	Right wrist (thumb side)	RWRA	3.7	1.5

Table 6.20: Mean and standard deviation of the distance between measured and model-determined markers. Marker locations are described in section D.1.1 of Appendix D.

6.3.1.2 Door handling

Renault and Peugeot-Citroën reported results for the door handling experiment (Renard et al., 2003; Renard et al., 2004). The quality of the reconstructed

motions was assessed visually by comparing the reconstructed motions and the videos recorded during the experimental procedure. An example is presented in Figure 6.1 and Figure 6.2 showing the comparison between snapshots of the real video and the reconstructed motion at the same selected frames.

Figure 6.1: Snapshots of a video recorded during a door handling trial.

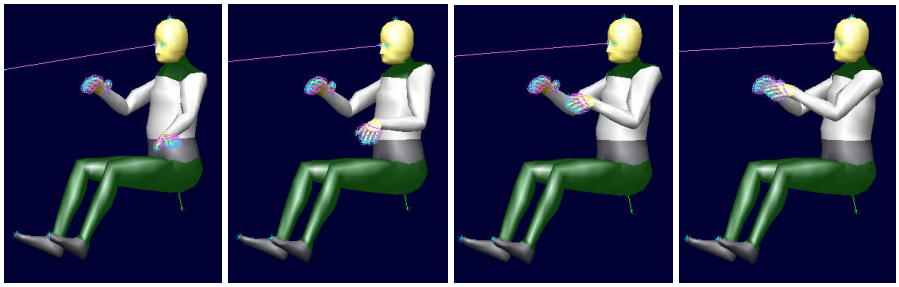

Figure 6.2: Snapshots of the reconstructed motion at the same frames that in Figure 6.1.

According to the visual evaluation, the reconstructed motions were classified into 3 categories, based on the quality of the reconstructed motion: "good quality", "medium quality" and "bad quality". A precise description of each category was not reported by Renault and Peugeot-Citroën.

Motions	Number	% of recorded	% of reconstructed
Recorded	270	100%	
Reconstructed	171	63%	100%
Good quality	77	29%	45%
Medium quality	67	25%	39%
Bad quality	27	10%	16%

Table 6.21: Summary of the evaluation of reconstructed motions for the door handling.

For the door handling experiment, 270 trials were recorded. However, only 171 motions were successfully reconstructed (Table 6.21). The rest of the motions were not reconstructed either due to the missing marker problem, or due to unexpected errors in one of the tools used in the REALMAN methodology (PCMAN, Compamm or converters between data formats).

6.3.1.3 Vehicle accessibility

Renault and Peugeot-Citroën reported results for the vehicle accessibility experiment (Renard et al., 2004). The quality of the reconstructed motions was assessed visually, similarly to the door handling experiment. 80% of the motions reconstructed by Compamm were classified as good quality motions, while 20% of them were rejected due to their bad quality.

6.3.2 OTM IMPLEMENTATION IN MATLAB®

The performance of each OTM solver of the Matlab® implementation was quantified with four performance parameters, which are defined in the next section. The values of the performance parameters are discussed for five motion reconstruction problems (sections 6.3.2.2 to 6.3.2.6) and two computer-simulated motion problems (sections 6.3.2.7 and 6.3.2.8). All the problems were solved using a Pentium IV 3.00 GHz.

6.3.2.1 Performance parameters

In order to quantify and compare the efficiency of each OTM solver, four performance parameters are defined as follows:

1. The *convergence profile* (*CP*) is a bar plot that depicts the quality of the solution found by a solver. The *convergence rate* (*CR*) is defined as the percentage of frames that converged to the solution for a given tolerance value, usually 10^{-3}, 10^{-4}, 10^{-5}, 10^{-6} and 10^{-7}. The *CP* shows the *CR* for one solver and several tolerance values (e.g. Figure 6.7 shows the CPs of several solvers). OTM accepts an iteration point as the solution when the 2-norm of $\mathbf{\Phi(q)}$ is less than a predefined tolerance. Unfortunately, sometimes the maximum number of iterations (*nMaxIter*) defined by the user is reached but the 2-norm of $\mathbf{\Phi}$ is greater than the predefined tolerance. The default value of *nMaxIter* for a solver was 25.

2. The *total time* (*T-t*) is the total elapsed time required to reconstruct the motion of all the trials considered in one experiment. It is a global measure of the performance of a solver because it includes the influence of all the parameters that affect it: numerical method, step-control mode, global convergence strategy, size of the skeletal model and measurement errors.

3. The *relative convergence rate* (RCR_i) measures the difference between the mean convergence rate MCR_i of solver i and the best mean convergence rate MCR_b.

$$RCR_i = MCR_i - MCR_b \tag{6.1}$$

where MCR_i is defined as the mean CR_i of solver i for all the studied tolerances, and MCR_b is defined as the maximum MCR_i for all the studied solvers. For example, suppose that CR_i is 99%, 95% and 91% for tolerances 10^{-5}, 10^{-6} and 10^{-7} respectively. Then, MCR_i is 95%. If MCR_b is 98%, then, RCR_i is 3%.

4. The *relative speed rate* (RSR_i) measures the relative speed between solver i and the fastest solver:

$$RSR_i = 100 \cdot \left(\frac{SR_i - SR_b}{SR_b} \right) \tag{6.2}$$

where the speed rate SR_i of solver i is defined as the mean T-t for all the studied tolerances, and the best speed rate SR_b is defined as the minimum SR_i. For example, suppose that T-t is 100 s, 120 s and 140 s for tolerances 10^{-5}, 10^{-6} and 10^{-7} respectively. Then, SR_i is 120 s. If SR_b is 80 s, then, RSR_i is 50%. This means that solver i is 50% slower than the fastest solver.

RCR and *RSR* are relative measures of a solver performance with regard to the best solver for a given experiment. Therefore, they are performance parameters valid for each experiment but cannot be compared across different experiments. The *CR* for a given tolerance does not always achieve 100%. The percentage of frames that do not achieve the desired tolerance coincides approximately with the number of frames that reach *nMaxIter*. There are at least three effects that prevent *CR* from reaching 100%:

1. If the initial approximation for the first frame is not sufficiently close to the true initial solution, the *nMaxIter* defined by the user can be reached before achieving the desired tolerance. This may happen during a few initial frames if the initial approximation is very far from the true initial solution. In this thesis, this phenomenon is called the *initial approximation effect*. This effect is illustrated with the first two frames of the GR04 trial reconstructed with the solver A1f for a tolerance of 10^{-7}. (Figure 6.3 and Figure 6.4). Although the value of the objective function and the 2-norm of Φ decrease in the first frame, a solution with the desired tolerance cannot be reached

after 25 iterations. In the second frame, using as initial approximation the last iteration point of the first frame, the solution is reached after 10 frames. If *nMaxIter* had been set to 40, the solver would have converged to the solution in the first frame.

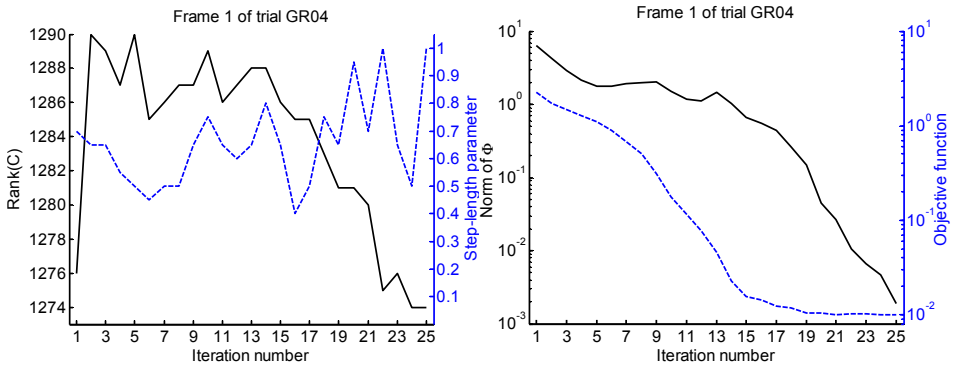

Figure 6.3: Initial approximation effect in the 1st frame of GR04 trial.

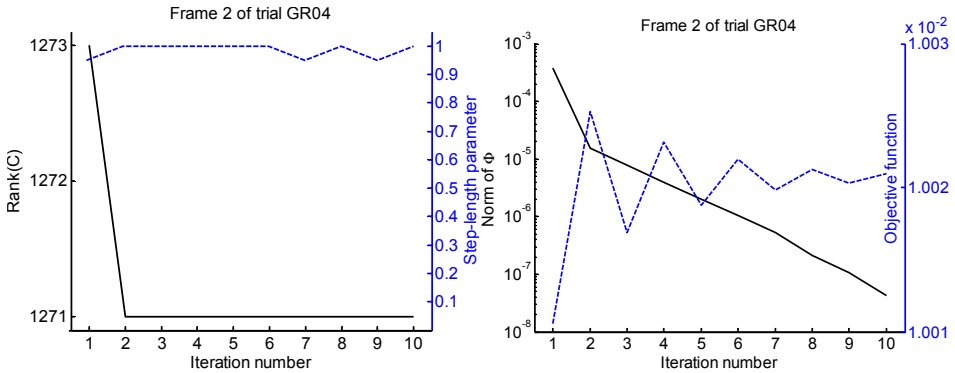

Figure 6.4: Initial approximation effect in the 2nd frame of GR04 trial.

2. The global convergence strategy selects the value of the step-length α such that acceptable progress towards the solution is made. However, this is not always true and the global convergence strategy can select an excessively short step-length. If this behaviour appears during too many iterations, the *nMaxIter* can be reached before achieving the desired tolerance. In this thesis, such behaviour is called the *strand effect*. This effect is illustrated using the same frame reconstructed with the solvers A1f (Figure 6.5) and A1x (Figure 6.6) for a tolerance of 10^{-7}. Using A1f the iteration point is close to the solution ($\|\Phi\| \approx 2 \times 10^{-5}$) but the global convergence strategy selects a small step-length parameter and after 25 iterations the desired tolerance is not reached. However, A1x, which only differs from

A1f in the global convergence strategy, does not suffer the strand effect and reaches the solution in 6 iterations.

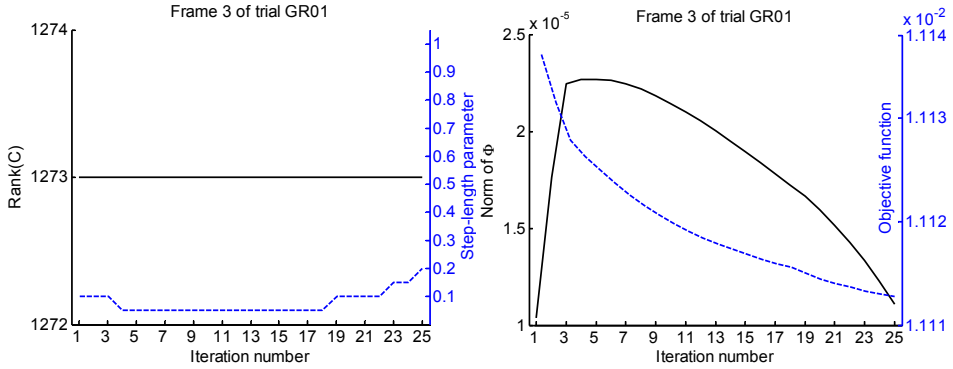

Figure 6.5: Strand effect in the 3rd frame of GR01 trial reconstructed with A1f.

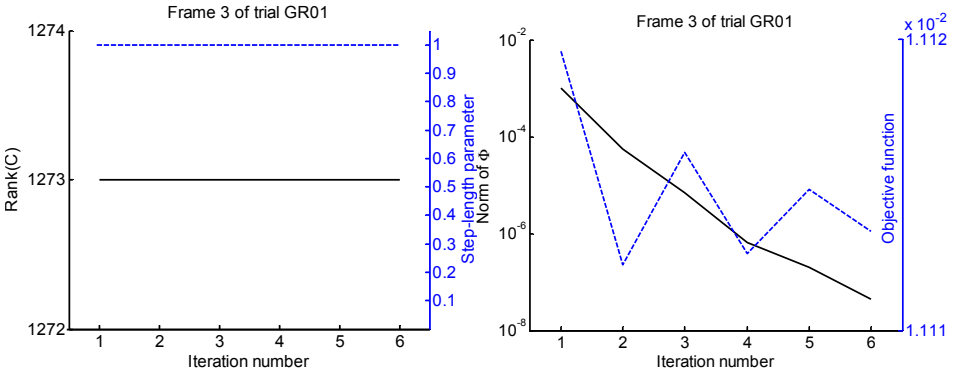

Figure 6.6: No strand effect in the 3rd frame of GR01 trial reconstructed with A1x.

3. Recall that the coefficient matrix **C** is singular and its condition number is infinite (section 4.5.6). This means that stable numerical methods for matrix factorisation must be used. Sometimes the matrix factorisation algorithm may have stability problems and the desired tolerance may not be reached within the ***nMaxIter*** selected by the user. In this thesis, the stability problems of the matrix factorisation algorithm are referred to as the *instability effect*.

Apart from the numerical methods, step-control modes and the global convergence strategies presented in the previous section, the performance parameters of a solver depend at least on the following additional parameters:

1. The size of the skeletal model, i.e. the number of generalised coordinates, the number of kinematic constraints and the number of redundant constraints. In general, a large skeletal model requires

more iterations per frame and a larger *T-t* than a small skeletal model.

2. Tolerance for accepting a solution. The smaller the tolerance, the larger is the number of iterations per frame and *T-t* for reaching a solution. Furthermore, for a fixed *nMaxIter* the *CP* is worse for smaller tolerances, i.e. the percentage of frames that achieve the desired tolerance decreases.

3. Measurement errors, i.e. errors in the Anatomical Calibration Protocol and errors in the recorded marker trajectories. If the measurement errors are large, the distance between the solutions of two consecutive frames is larger. Thus, the initial approximation for the current frame, which is the solution of the previous frame, is farther. Therefore, the number of iterations per frame and *T-t* required to achieve the desired tolerance are bigger for large measurement errors than for small ones.

The different experiments are not directly comparable because the size of the skeletal models, measurement errors, additional driving constraints and weighting strategies are different. Trials of the same experiment, although they have different number of frames, are comparable. Therefore, the performance of the solvers is evaluated independently for each experiment.

6.3.2.2 Generic arm reaching

The convergence profiles (CPs) of the solvers using the maxmin strategy (code x, see Table 6.1) for global convergence are shown in Figure 6.7 and in Figure 6.8 for the merit function strategy (code f).

Figure 6.7 shows that the step-control mode does not affect significantly the CPs of the solvers using the maxmin strategy. Both step-control modes, optimal step-length (code 1) and full step-length (code 2), give similar CPs for solvers using the same numerical method. For example, B1x and B2x, which only differ in the step-control mode, have very similar CPs.

On the other hand, the step-control mode affects significantly the CPs of the solvers using the merit function strategy (Figure 6.8). The step-control mode 2 gives better CPs than the step-control mode 1 for solvers with the same numerical method. The reason for this behaviour is that the maxmin strategy is less sensitive to the strand effect than the merit function strategy.

The CPs of the solvers A1x, A2x, Ar1x, Ar2x, B1x, B2x, A2f, Ar2f, B2f and C2f are comparable and the quality of the solutions are similar. The rest of the solvers give worse CPs when compared with the previous ones.

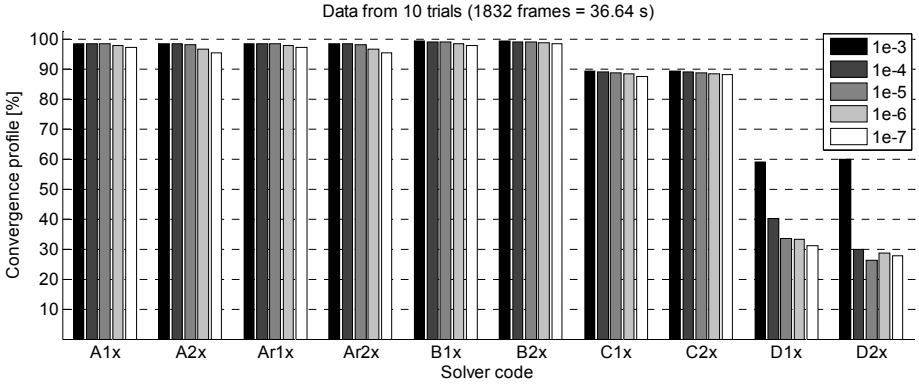

Figure 6.7: CPs using the maxmin strategy (x) for the generic arm reaching trials.

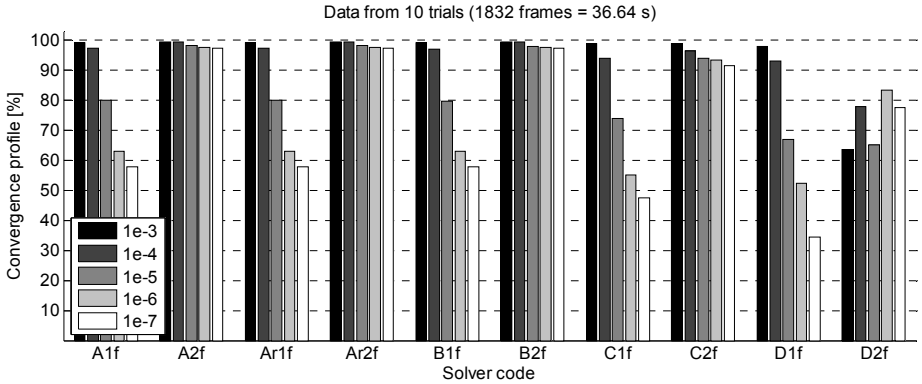

Figure 6.8: CPs using the merit function strategy (f) for the generic arm reaching trials.

The solver D2f has an unusual behaviour because the percentage of frames that achieve the desired tolerance increases when the tolerance is increased. This unusual behaviour of D2f is caused by the strand effect, which depends on the iteration point. For each different value of the tolerance, the solutions obtained for each frame are slightly different. Then, it may happen that for a higher value of the tolerance, the achieved solution does not suffer the strand effect, while for a lower tolerance it does, and the opposite is also true. Furthermore, the two-step LU numerical method (code D) is based on the LU decomposition and therefore the solvers D1x, D1f, D2x and D2f are affected by the instability effect more than the rest of the solvers, which are based on the QR decomposition. It is well known that the LU decomposition is less stable than the QR decomposition.

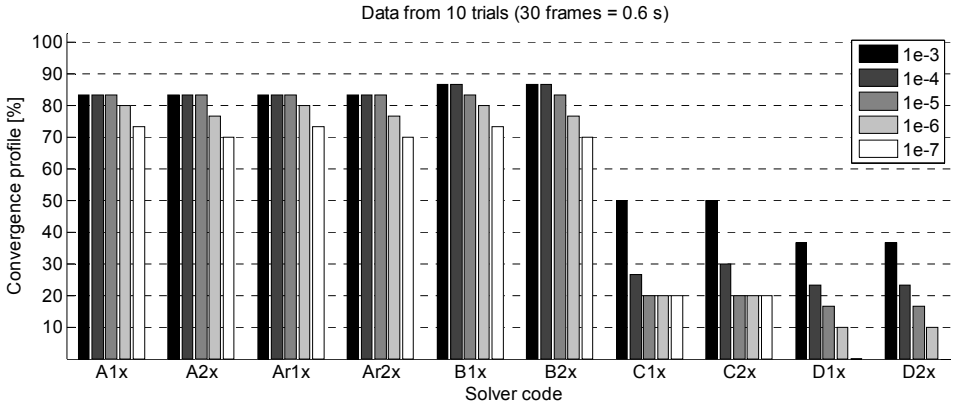

Figure 6.9: CPs using the maxmin strategy (x) for the first 3 frames of the 10 generic arm reaching trials.

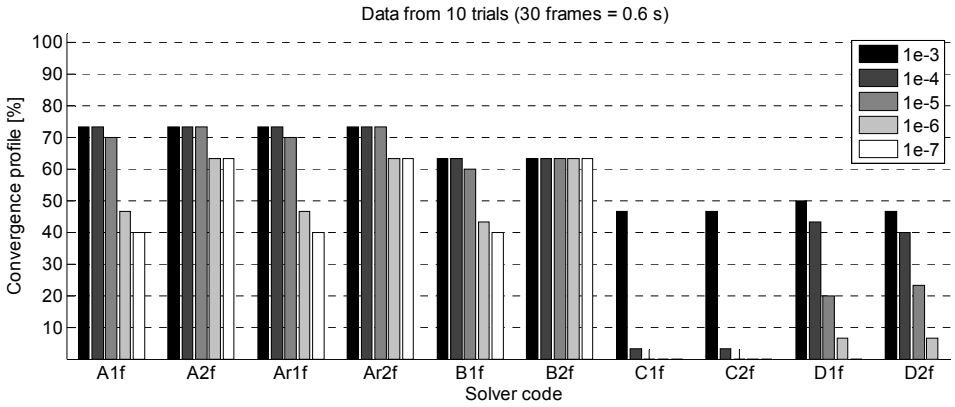

Figure 6.10: CPs using the merit function strategy (f) for the first 3 frames of the 10 generic arm reaching trials.

The initial approximation for the first frame was far from the true initial solution for the 10 trials. Additional driving constraints included in Ψ_m were activated only during the first three frames in order to force convergence towards the appropriate solution. Therefore, the first frames of each trial may not reach the desired tolerance within the *nMaxIter*, as they are affected by the initial approximation effect. The CPs for the first 3 frames of each trial are shown in Figure 6.9 and Figure 6.10. A bad initial approximation affects the performance of the solvers, especially those based on the nullspace (C) and two-step LU (D) methods. For example, the solvers D1x, D2x, C1f, C2f, D1f and D2f do not reach a tolerance of 10^{-7} for none of the first 3 frames of each trial.

The total time (*T-t*) of the solvers using the maxmin strategy for global convergence are shown in Figure 6.11 and in Figure 6.12 for the merit function strategy. Two different scales are used in Figure 6.12 in order to show appropriately the *T-t* of each solver.

Similarly to what happens with the CP, the step-control mode does not affect the *T-t* using the maxmin strategy (Figure 6.11). On the other hand, the step-control mode significantly affects the *T-t* using the merit function strategy (Figure 6.12). The step-control mode 2 gives smaller *T-t* than the step-control mode 1 for solvers using the same numerical method. This is due to the fact that the solvers with the step-control mode 1 reach more times the *nMaxIter*.

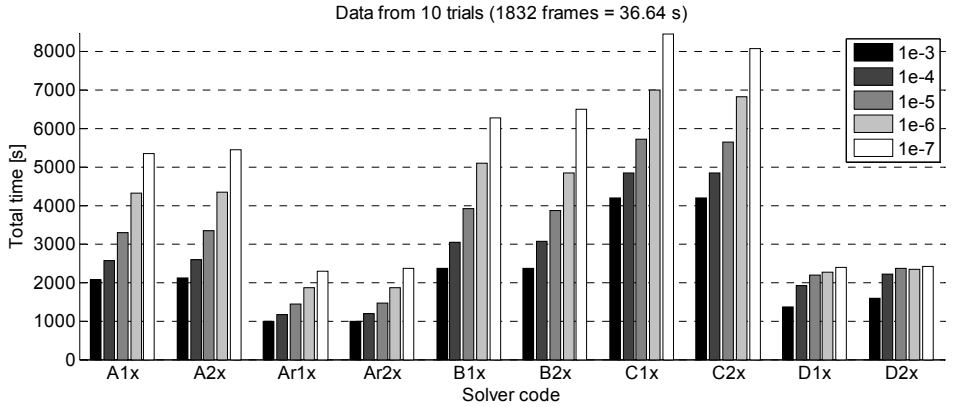

Figure 6.11: *T-t* using the maxmin strategy (x) for the generic arm reaching trials.

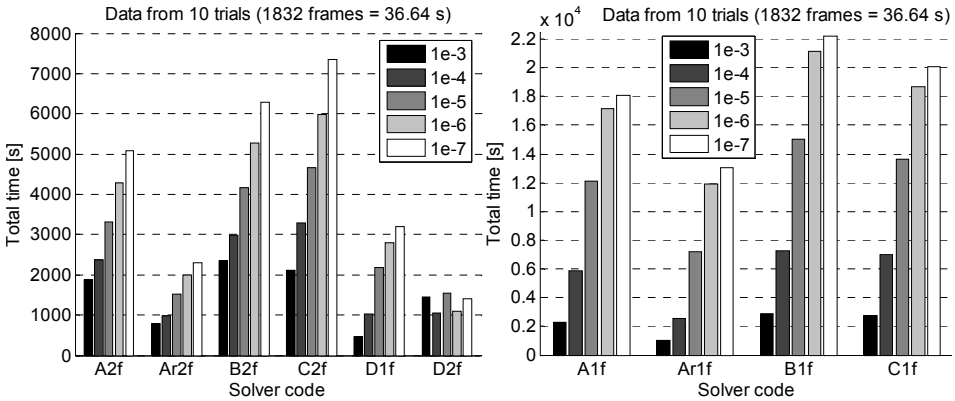

Figure 6.12: *T-t* using the merit function strategy (f) for the generic arm reaching trials.

The overall performance of the solvers is compared in Table 6.22 using the relative convergence (*RCR*) and the relative speed (*RSR*) rates. The fastest solver is D2f but its CP is 25.5% worse than the best CP. The solver B2x has

the best CP but it is 216.9% slower than the fastest solver. The fastest solvers after D2f are Ar2f, Ar1x and Ar2x. Furthermore, their CPs are only 0.6%, 0.8% and 1.4% respectively worse than the best CP. Therefore, these three solvers have a better overall performance for this experiment.

Solver code	*RCR*	*RSR*	Solver code	*RCR*	*RSR*
A1x	**-0.8%**	170.0%	A1f	-19.5%	751.2%
A2x	**-1.5%**	173.9%	A2f	**-0.6%**	159.5%
*Ar1x	**-0.8%**	**19.2%**	Ar1f	-19.4%	447.7%
*Ar2x	**-1.4%**	**21.0%**	*Ar2f	**-0.6%**	**15.7%**
B1x	**-0.1%**	217.8%	B1f	-19.6%	949.8%
B2x	**Best**	216.9%	B2f	**-0.6%**	222.5%
C1x	-10.3%	363.5%	C1f	-25.1%	852.1%
C2x	-10.1%	354.1%	C2f	-4.1%	258.4%
D1x	-59.5%	55.8%	D1f	-30.1%	48.3%
D2x	-64.5%	67.5%	D2f	-25.5%	**Fastest**

Table 6.22: *RCR* and *RSR* for the generic arm reaching trials. The best *RCR* and *RSR* are highlighted in bold. *Best solvers.

6.3.2.3 Door handling

The CPs using the maxmin strategy (x) are shown in Figure 6.13 and the CPs using the merit function strategy (f) in Figure 6.14. The trials were not affected by the initial approximation effect as the initial approximation was good.

Note that the CPs of the solvers D1x, D2x, D1f and D2f are very poor because none of the 709 frames converged to the desired tolerance for the five tolerances investigated. These solvers reached the *nMaxIter* for all the frames. These bad results were independent of the used step-control mode and global convergence strategy.

Similarly to the previous experiment, the step-control mode does not affect the CPs using the maxmin strategy (Figure 6.13). However, it affects significantly all the CPs with the merit function strategy (Figure 6.14). The step-control mode 2 gives better CPs than the step-control mode 1 for solvers with the same numerical method.

The CPs of the solvers A1x, A2x, Ar1x, Ar2x, B1x, B2x, C2x, A2f, Ar2f and B2f are similar. They achieve the desired tolerance for almost 100% of the frames, for each of the studied tolerances. The remaining solvers give worse CPs compared with the previous ones.

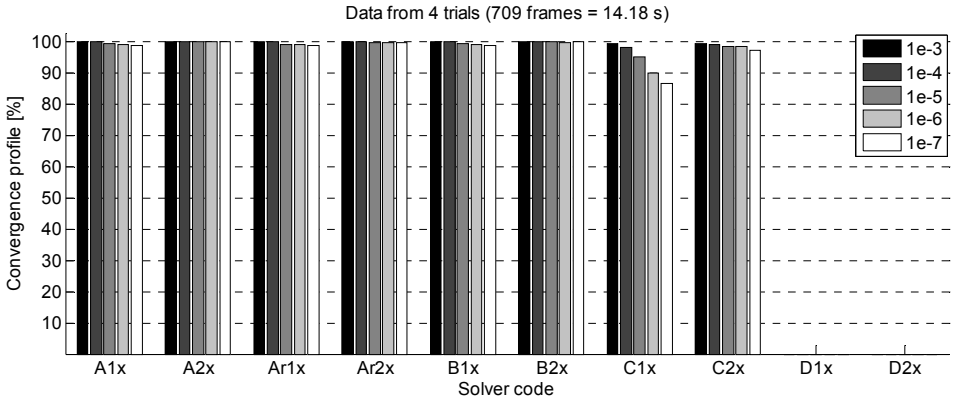

Figure 6.13: CPs using the maxmin strategy for the door handling trials.

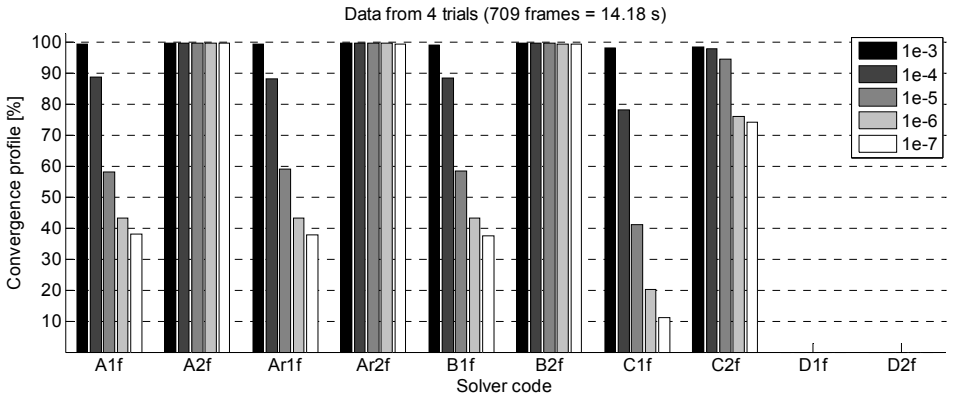

Figure 6.14: CPs using the merit function strategy for the door handling trials.

The *T-t* using the maxmin strategy is shown in Figure 6.15 and in Figure 6.16 for the merit function strategy. The step-control mode 2 gives smaller *T-t* for all the solvers except for D1x and D2x, which require exactly the same *T-t* (Figure 6.15). The solvers D1x and D2x do not achieve the desired tolerance for none of the frames, i.e. the *nMaxIter* is reached for all the frames. Furthermore, in this situation both step-control modes are equivalent because the global convergence strategy is always activated (see section 4.5.7). This explains why both solvers require the same *T-t*.

The step-control mode 2 gives significantly smaller *T-t* using the merit function strategy except for D1f and D2f, which require the same *T-t* (Figure 6.16) due to the same reasons explained in the previous paragraph. However, D1x and D2x are faster than D1f and D2f. This difference is due to the different computation time required by the two global convergence strategies.

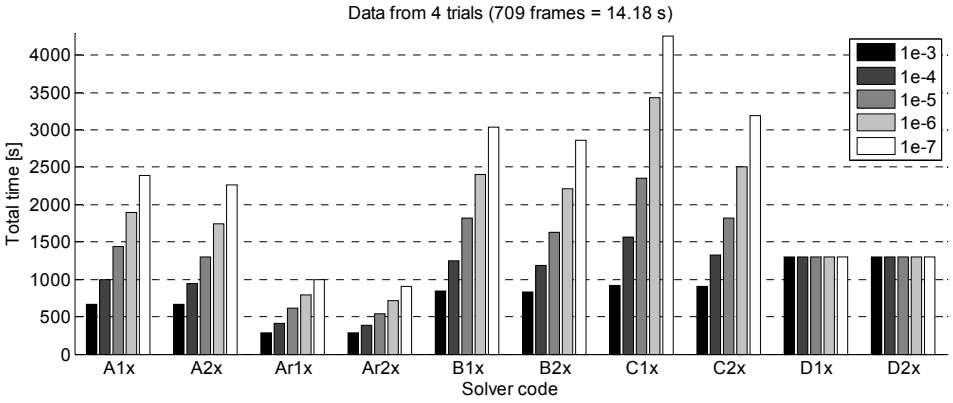

Figure 6.15: *T-t* using the maxmin strategy for the door handling trials.

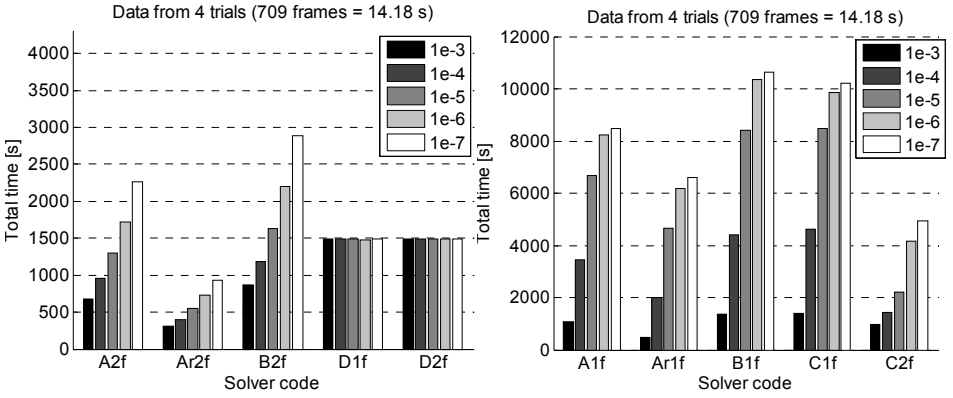

Figure 6.16: *T-t* using the merit function strategy for the door handling trials.

Solver code	*RCR*	*RSR*	Solver code	*RCR*	*RSR*
A1x	**-0.5%**	161.4%	A1f	-34.4%	886.7%
A2x	**Best**	144.7%	A2f	**-0.3%**	144.7%
*Ar1x	**-0.5%**	**10.0%**	Ar1f	-34.4%	603.5%
*Ar2x	**-0.1%**	**Fastest**	*Ar2f	**-0.3%**	**3.5%**
B1x	**-0.5%**	230.2%	B1f	-34.6%	1142.5%
B2x	**-0.1%**	208.8%	B2f	**-0.2%**	210.4%
C1x	-6.0%	342.8%	C1f	-50.0%	1122.2%
C2x	-1.4%	244.5%	C2f	-11.6%	384.3%
D1x	-100.0%	130.1%	D1f	-100.0%	163.0%
D2x	-100.0%	129.8%	D2f	-100.0%	163.2%

Table 6.23: *RCR* and *RSR* for the door handling trials. The best *RCR* and *RSR* are highlighted in bold. *Best solvers.

The overall performance of the solvers is compared in Table 6.23. The solver A2x has the best CP but is 144.7% slower than the fastest solver. The

fastest solver is Ar2x and its CP is only 0.1% worse than the best CP. The fastest solvers after Ar2x are Ar2f and Ar1x. Furthermore, their CPs are only 0.3% and 0.5% respectively worse than the best CP. Therefore, solvers Ar2x, Ar2f and Ar1x have a better overall performance for this experiment.

6.3.2.4 Vehicle accessibility

The trials of the vehicle accessibility were solved only with the twelve solvers shown in Figure 6.17 and Figure 6.18. The solvers B1x, B2x, C1x, C2x, B1f, B2f, C1f and C2f were not used because in a preliminary test they were found to be significantly slower than the other solvers and their CPs were similar or worse.

The CPs of the solvers using the maxmin strategy (x) are shown in Figure 6.17 and in Figure 6.18 for the merit function strategy (f). These trials were not affected by the initial approximation effect because the initial approximation for the first frame was good.

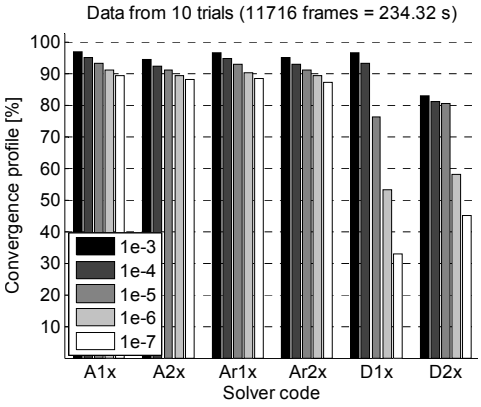

Figure 6.17: CPs using the maxmin strategy for the vehicle accessibility trials.

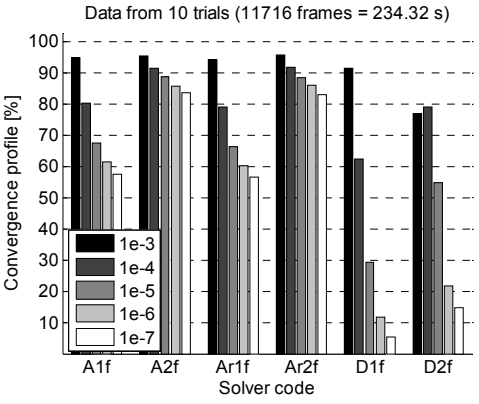

Figure 6.18: CPs using the merit function strategy for the vehicle accessibility trials.

The CPs of A1x, A2x, Ar1x, Ar2x, A2f and Ar2f are similar. The remaining solvers give worse CPs. The step-control mode affects significantly the CPs of the solvers using the merit function strategy (Figure 6.18), with the step-control mode 2 being the best option.

The maxmin strategy (Figure 6.19) gives smaller *T-t* than the merit function strategy (Figure 6.20) in all the cases. The step-control mode does not affect significantly the *T-t* needed by the solvers that use the maxmin strategy. However, it affects the *T-t* of the solvers with the merit function strategy, being the step-control mode 2 the one which gives smaller *T-t*.

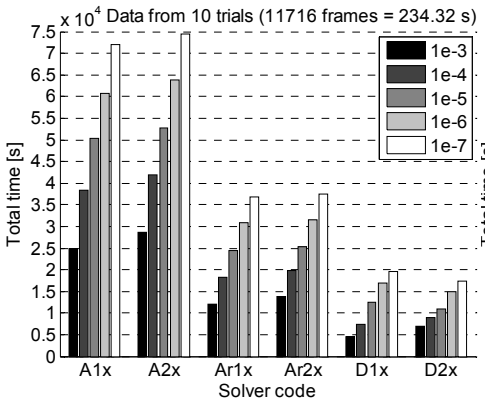

Figure 6.19: *T-t* using the maxmin strategy for the vehicle accessibility trials.

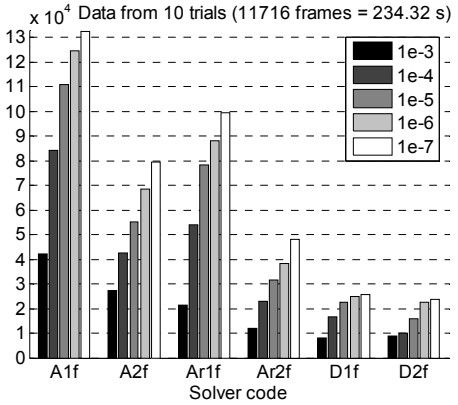

Figure 6.20: *T-t* using the merit function strategy for the vehicle accessibility trials.

The overall performance of the solvers is compared in Table 6.24. The solver A1x has the best CP but it is 317.8% slower than the fastest solver. The fastest solver is D2x but its CP is 23.6% worse than the best CP. There is no solver with a CP close to the best and a speed close to the fastest. The solvers with the best overall performance, although considerably slower than the fastest solver, are Ar1x, Ar2x and Ar2f.

Solver code	*RCR*	*RSR*	Solver code	*RCR*	*RSR*
A1x	**Best**	317.8%	A1f	-20.8%	738.3%
A2x	**-2.1%**	343.8%	A2f	**-4.1%**	362.8%
*Ar1x	**-0.47%**	107.8%	Ar1f	-21.8%	477.8%
*Ar2x	**-1.9%**	117.4%	*Ar2f	**-4.1%**	159.6%
D1x	-22.7%	**3.3%**	D1f	-53.1%	**65.5%**
D2x	-23.6%	**Fastest**	D2f	-43.7%	**36.7%**

Table 6.24: *RCR* and *RSR* for the vehicle accessibility trials. The best *RCR* and *RSR* are highlighted in bold. *Best solvers.

The CPs of the best solvers are quite disappointing when compared with the two previous experiments. The best solvers in the two previous experiments achieve a tolerance of 10^{-7} for almost 100% of the frames, while in the vehicle accessibility it is below 90%. Additionally, the speed of the solvers with the best overall performance is more than 100% slower than the fastest solvers. One reason for these results is that the measurement errors are considerably bigger in the vehicle accessibility trials compared to the other two experiments (see section 6.3.2.9 for details). Furthermore, two questions can be studied in order to gain a better understanding of the performance of the solvers:

- *nMaxIter* was set to 25 for all experiments in order to make a fair comparison between the experiments. However, this value can be modified for improving the CP, though at the price of a bigger *T-t*.
- The tolerance reached by those frames which did not achieve the desired tolerance is also relevant. Suppose that the tolerance is set to 10^{-7} and the percentage of frames that achieve this tolerance is 90%. Assuming that 10^{-4} is a reasonable value for accepting a solution, then a solver is suitable for the problem if the tolerance achieved in the remaining frames is less than 10^{-4}.

These two issues have been investigated for a tolerance of 10^{-7} using the two solvers with the best overall performance (Ar1x and Ar2x) and the two fastest solvers (D1x and D2x). Figure 6.21 shows the tolerance achieved in each frame using five tolerance intervals and *nMaxIter* = 25. If tolerances up to 10^{-4} are considered suitable, the percentage of frames that achieve the desired tolerance are 94.7%, 93.7%, 90.9% and 92.2% for Ar1x, Ar2x, D1x and D2x respectively. Figure 6.22 is similar to Figure 6.21 but with *nMaxIter* = 50. If tolerances up to 10^{-4} are considered suitable, the percentage of frames that achieve the desired tolerance are 96.7%, 95.4%, 96.6% and 96.3% for Ar1x, Ar2x, D1x and D2x respectively. As expected, increasing *nMaxIter* increases both the percentage of frames that achieve the desired tolerance (10^{-7}), and the percentage of frames that achieve a tolerance less than 10^{-4}. This improvement is obtained at the price of a bigger *T-t* (Figure 6.23).

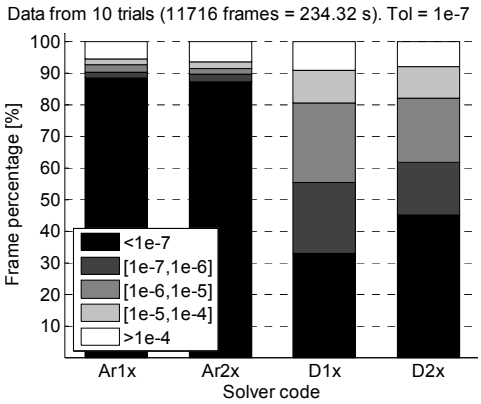

Figure 6.21: Percentage of frames that converged to tol = 10^{-7} and tolerance intervals of the remaining frames for Ar1x, Ar2x, D1x and D2x. *nMaxIter* = 25.

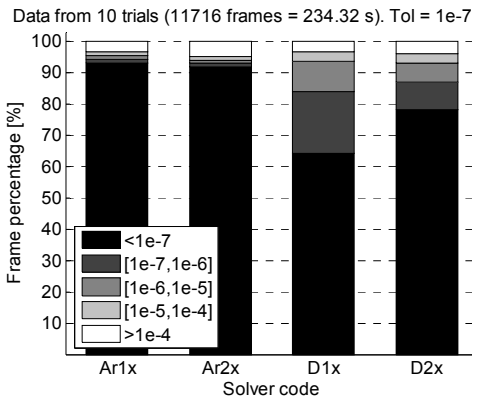

Figure 6.22: Percentage of frames that converged to tol = 10^{-7} and tolerance intervals of the remaining frames for Ar1x, Ar2x, D1x and D2x. *nMaxIter* = 50.

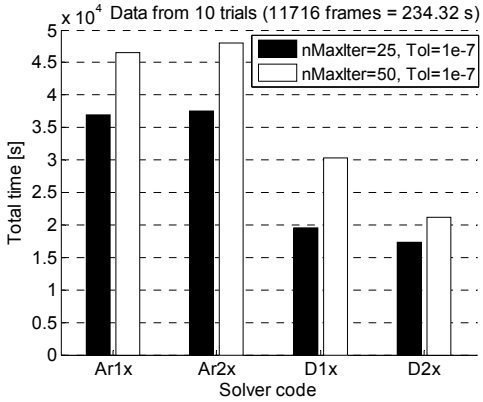

Figure 6.23: *T-t* for solvers Ar1x, Ar2x D1x and D2x using two values of *nMaxIter*.

If *nMaxIter* is set to 50, the tolerance is set to 10^{-7} and solutions with a tolerance less than 10^{-4} are accepted, then D1x and D2x are the best solvers. They are faster than Ar1x and Ar2x and the percentage of frames that achieve the desired tolerance are similar.

6.3.2.5 Steering manoeuvre for UBM

Six solvers using the maxmin strategy (A1x, A2x, B1x, B2x C1x and C2x) achieve the desired tolerance for the 100% of the frames (Figure 6.24). The step-control mode only affects the CPs of Ar1x, Ar2x, D1x and D2x, the step-control mode 1 being the best option.

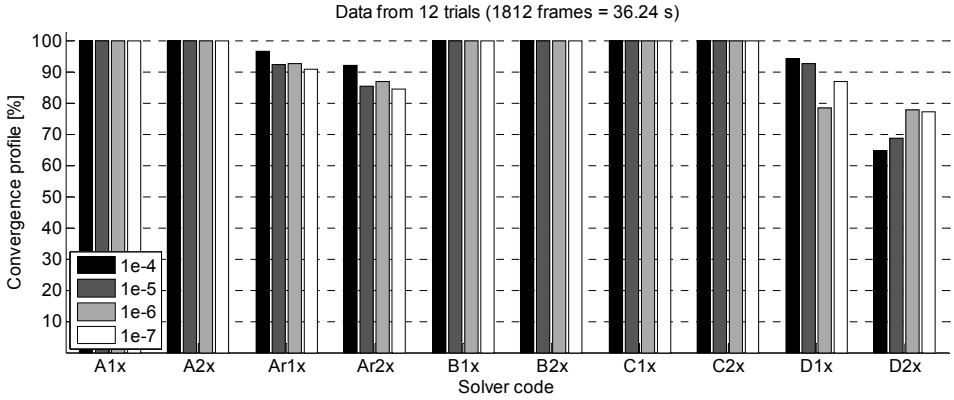

Figure 6.24: CPs using the maxmin strategy for the steering manoeuvre with UBM.

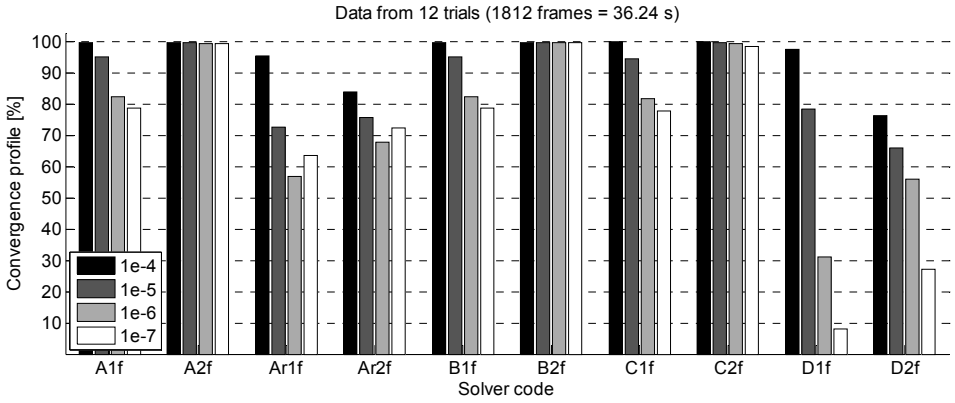

Figure 6.25: CPs using the merit function strategy with UBM.

The CPs of the solvers using the merit function strategy do not show a clear trend with regard to the used step-control mode or numerical method (Figure 6.25). The step-control mode 2 gives better CP for the direct QR (A), two-step QR (B) and nullspace (C) numerical methods. The solvers based on the direct QR method with reordering (Ar1f and Ar2f) give bad CPs compared to those based on the direct QR (A1f and A2f). The only difference between these last four solvers is the reordering method. Therefore, it can be concluded that the reordering method affects the stability of the direct QR method and consequently the CPs. The CPs for all the solvers based on the two-step LU (D) numerical method are poor. As explained in section 6.3.2.2, the LU decomposition is especially affected by the instability effect.

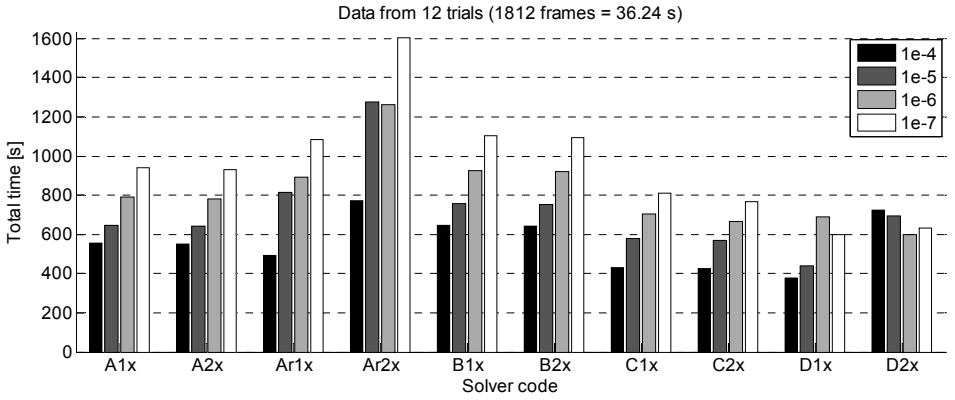

Figure 6.26: *T-t* using the maxmin strategy for the steering manoeuvre with UBM.

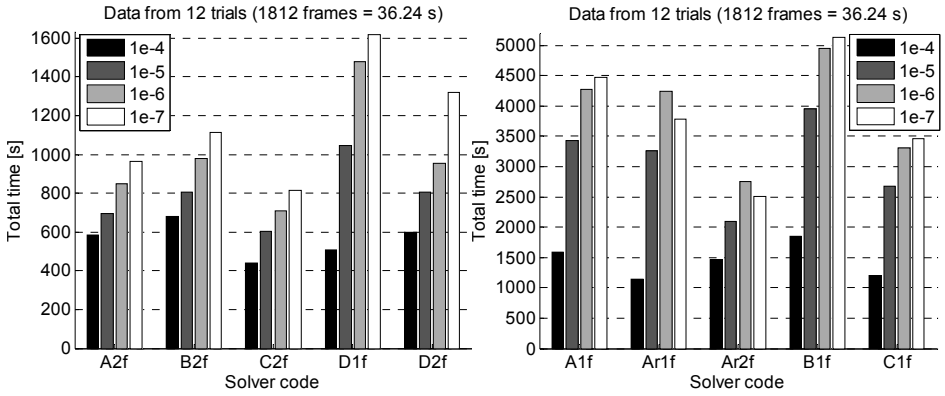

Figure 6.27: *T-t* using merit function strategy for the steering manoeuvre with UBM.

The maxmin strategy (x) gives smaller *T-t* (Figure 6.26) than the merit function strategy (f) (Figure 6.27). The step-control mode does not affect significantly the *T-t* of the solvers using the maxmin strategy, except for Ar1x-Ar2x and D1x-D2x (Figure 6.26). For these four solvers the step-control mode 1 gives smaller *T-t* than the step-control mode 2. The step-control mode 2 gives smaller *T-t* for all the solvers with the merit function strategy (Figure 6.27).

The overall performance of the solvers is compared in Table 6.25. There are six solvers, A1x, A2x, B1x B2x, C1x and C2x, which achieve the desired tolerance for the 100% of the frames and for all the studied tolerances. Additionally, the solvers A2f and C2f give good CPs, which are only 0.3% and 0.5% inferior to the best CP.

Solver code	*RCR*	*RSR*	Solver code	*RCR*	*RSR*
A1x	**Best**	**39.2%**	A1f	-10.9%	554.1%
A2x	**Best**	**38.1%**	A2f	**-0.3%**	46.9%
Ar1x	-6.8%	55.8%	Ar1f	-27.8%	490.0%
Ar2x	-12.6%	133.1%	Ar2f	-25.0%	318.1%
B1x	**Best**	63.1%	B1f	-10.9%	654.3%
B2x	**Best**	61.8%	B2f	-0.3%	69.5%
*C1x	**Best**	**19.7%**	C1f	-11.4%	404.4%
*C2x	**Best**	**15.3%**	*C2f	**-0.5%**	**21.9%**
D1x	-11.8%	**Fastest**	D1f	-46.1%	120.8%
D2x	-27.8%	25.9%	D2f	-43.5%	74.6%

Table 6.25: *RCR* and *RSR* for the steering manoeuvre with UBM. The best *RCR* and *RSR* are highlighted in bold. *Best solvers.

The fastest solver is D1x but its CP is 11.8% worse than the best CP. The eight solvers with good CPs, classified from the fastest to the slowest, are: C2x, C1x, C2f, A2x, A1x, A2f, B2x and B1x. The three solvers with the best

overall performance are C2x, C1x and C2f. However, the other five solvers have very good CPs and their *T-t* can be considered competitive when compared with the three previous solvers.

6.3.2.6 Steering manoeuvre for UBMS

The solvers Ar2x, C1x, C2x, D1x, D2x, Ar2f, C1f, C2f, D1f and D2f do not achieve the desired tolerance for none of the 1812 frames. All these solvers are affected by the instability effect. Therefore, the CPs and *T-t* of these solvers are not shown in the figures. The CPs of the solvers using the maxmin strategy (x) are shown in Figure 6.28 and with the merit function strategy (f) in Figure 6.29. The CPs of the solvers A1x, A2x, B1x, B2x, A2f and B2f achieve the desired tolerance for almost 100% of the frames, for each of the studied tolerances.

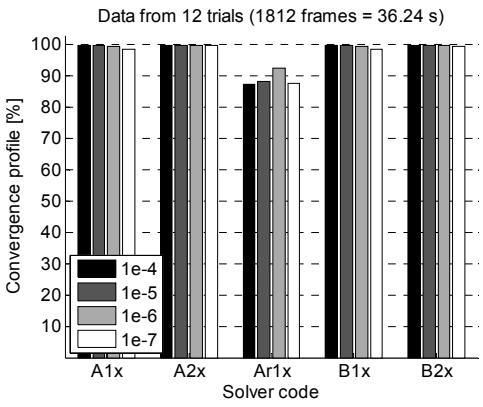

Figure 6.28: CPs using the maxmin strategy for the steering trials with UBMS.

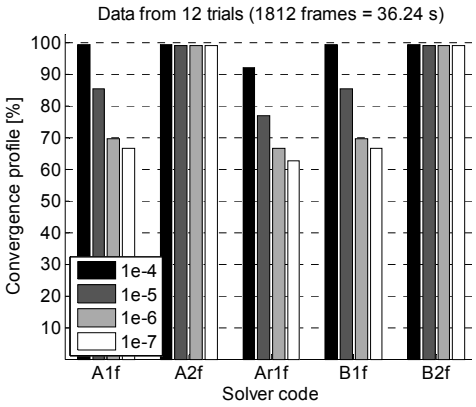

Figure 6.29: CPs using the merit function strategy for the steering trials with UBMS.

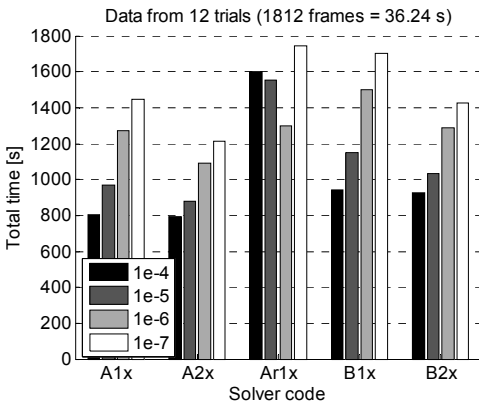

Figure 6.30: *T-t* using the maxmin strategy for the steering manoeuvre with UBMS.

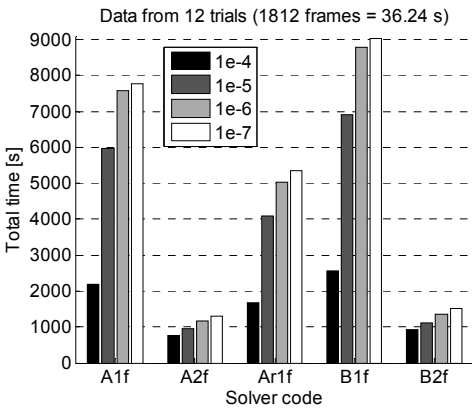

Figure 6.31: Right: *T-t* using the merit function strategy for UBMS.

The maxmin strategy (x) gives a smaller *T-t* than the merit function strategy (f) for all the solvers (Figure 6.30 and Figure 6.31). However, the solvers A2f and B2f give *T-t* only slightly worse than their counterparts A2x and B2x. Note that the step-control mode 2 gives a smaller *T-t* than the step-control mode 1 for all the solvers.

The performance of each solver is compared in Table 6.26. The solver A2x achieves the desired tolerance for the 100% of the frames and is also the fastest solver. There are other five solvers, A1x, B1x B2x, A2f and B2f, which have good CPs. All of them have competitive *T-t*, B1x being the slowest with *RSR* equal to 33.1%. The three solvers with the best overall performance are A2x, B2x and A2f. However, the solvers A1x, B1x and B2f have very good CPs and their *T-t* can be considered competitive when compared with the three previous solvers.

Solver code	*RCR*	*RSR*	Solver code	*RCR*	*RSR*
A1x	**-0.3%**	**13.1%**	A1f	-19.3%	491.5%
*A2x	**Best**	**Fastest**	*A2f	**-0.3%**	**5.2%**
Ar1x	-10.8%	55.8%	Ar1f	-25.0%	306.7%
B1x	**-0.3%**	33.1%	B1f	-19.4%	586.1%
*B2x	**Best**	**17.6%**	B2f	**-0.4%**	23.7%

Table 6.26: *RCR* and *RSR* for the steering manoeuvre with UBMS. The best *RCR* and *RSR* are highlighted in bold. *Best solvers.

6.3.2.7 Steering manoeuvre for UBM-INV

The UBM-INV skeletal model has more kinematic constraints than generalised coordinates (Table 6.17). This is due to the fact that many joint angles with their associated redundant constraints have been included into the model (section 5.2.1). The joint angles are used to define a relative preservation posture condition for the human driver. Furthermore, the additional constraints included in Ψ_s for defining the steering manoeuvre form a closed-loop between the arms and the steering wheel.

If the number of kinematic constraints is bigger than the number of generalised coordinates, the nullspace (C) and two-step LU (D) numerical methods cannot be used. The nullspace method may fail to find a basis for the nullspace of $\mathbf{A}^k$. The two-step LU method may have difficulties for identifying the linearly dependent constraints in $\Phi_{\mathbf{q}}{}^k$. Furthermore, it may fail to find a solution due to incompatibility issue described in section 4.5.2. This means that if the number of redundant constraints is greater than the number of DoFs of

the multibody system, then the linearised constraint equations are incompatible for any column vector **q** that does not satisfy the kinematic constraints.

The CPs of the solvers using the maxmin strategy (x) are shown in Figure 6.32 and with the merit function strategy (f) in Figure 6.33. All the solvers achieve the desired tolerance for the 100% of the frames, for each of the four studied tolerances.

The *T-t* of the solvers using the maxmin strategy is shown in Figure 6.34 and with the merit function strategy in Figure 6.35. All the solvers have very similar *T-t*, although B1x, B2x, B1f and B2f are slightly slower than the other solvers.

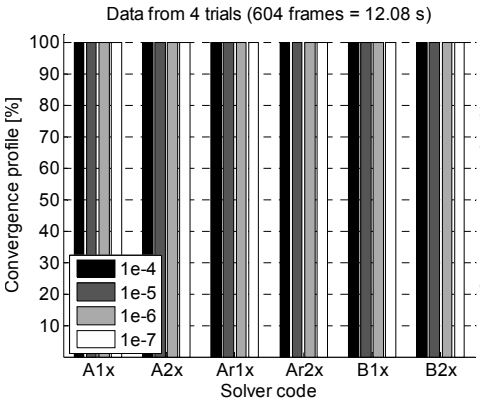

Figure 6.32: CPs using the maxmin strategy for the 4 trials with UBM-INV.

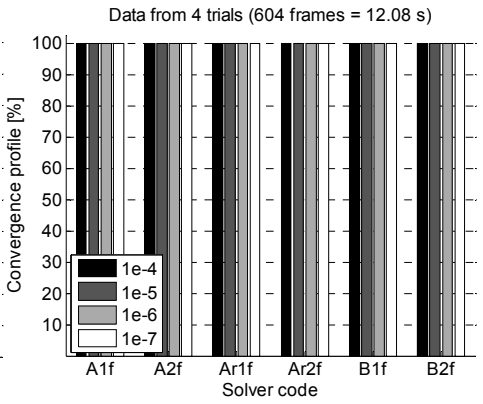

Figure 6.33: CPs using the merit function strategy for the 4 trials with UBM-INV.

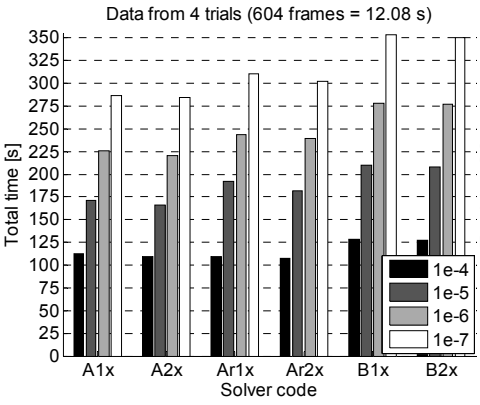

Figure 6.34: *T-t* using the maxmin strategy for the 4 trials with UBM-INV.

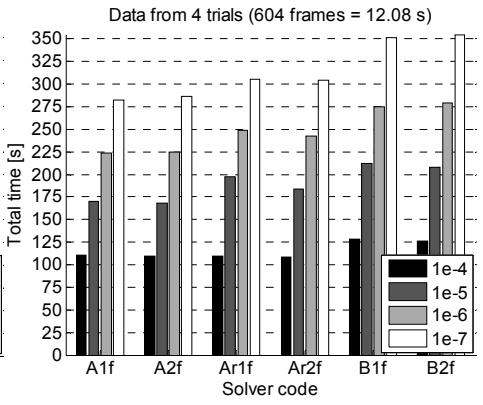

Figure 6.35: *T-t* using the merit function strategy for the 4 trials with UBM-INV.

The three solvers with the best overall performance are A2x, A1f and A2f (Table 6.27). However, the solvers A1x, Ar2x, Ar2f, Ar1x and Ar1f are only 2.1%, 6.5%, 7.5%, 9.6% and 10.4% slower than the fastest solver. Even the other four remaining solvers, B1x, B2x, B1f and B2f are less than 25% slower than the fastest solver.

Solver code	*RCR*	*RSR*	Solver code	*RCR*	*RSR*
A1x	**Best**	**2.1%**	*A1f	**Best**	**0.8%**
*A2x	**Best**	**Fastest**	*A2f	**Best**	**1.1%**
Ar1x	**Best**	9.6%	Ar1f	**Best**	10.4%
Ar2x	**Best**	6.5%	Ar2f	**Best**	7.5%
B1x	**Best**	24.2%	B1f	**Best**	24.0%
B2x	**Best**	23.4%	B2f	**Best**	24.1%

Table 6.27: *RCR* and *RSR* for the steering manoeuvre with UBM-INV. The best *RCR* and *RSR* are highlighted in bold. *Best solvers.

6.3.2.8 Steering manoeuvre for UBMS-INV

Similarly to UBM-INV, UMBS-INV has more kinematic constraints than generalised coordinates (Table 6.17) and the nullspace (C) and two-step LU (D) numerical methods cannot be used. UBMS-INV contains three closed-loops: two for each shoulder complex and one between the arms and the steering wheel, which is defined by the additional constraints included in Ψ_s (section 5.2.1).

The CPs of all the solvers achieve the desired tolerance for the 100% of the frames, for each of the four studied tolerances. The *T-t* of the solvers using the maxmin strategy is shown in Figure 6.36 and with the merit function strategy in Figure 6.37. The step-control mode and the global convergence strategy do not influence significantly the *T-t* of each solver. Only the numerical method affects *T-t*.

The overall performance of the solvers is compared in Table 6.28. All the solvers achieve the desired tolerance for 100% of the frames, for each of the four studied tolerances. The four solvers with the best overall performance are Ar1f, Ar1x, Ar2f and Ar2x.

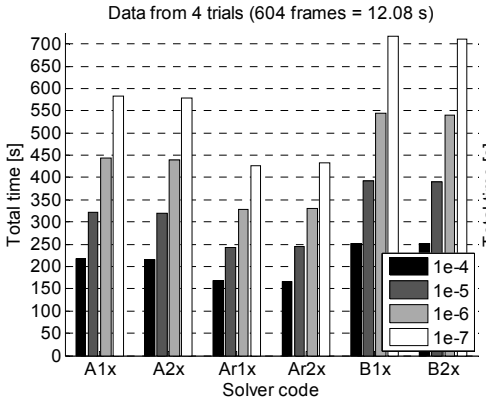

Figure 6.36: *T-t* using the maxmin strategy for the 4 steering trials with UBMS-INV.

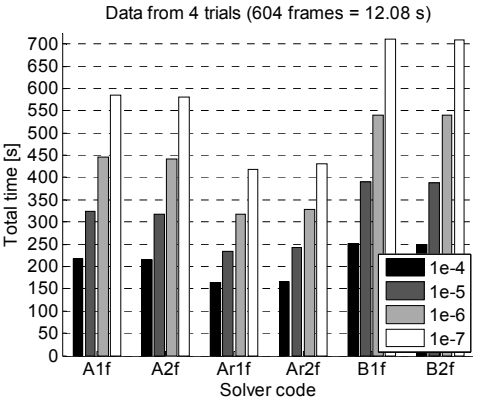

Figure 6.37: *T-t* using the merit function strategy with UBMS-INV.

Solver code	*RCR*	*RSR*	Solver code	*RCR*	*RSR*
A1x	**Best**	38.0%	A1f	**Best**	38.5%
A2x	**Best**	37.0%	A2f	**Best**	37.1%
*Ar1x	**Best**	**2.6%**	*Ar1f	**Best**	**Fastest**
*Ar2x	**Best**	**3.5%**	*Ar2f	**Best**	**2.9%**
B1x	**Best**	68.0%	B1f	**Best**	67.2%
B2x	**Best**	66.7%	B2f	**Best**	66.3%

Table 6.28: *RCR* and *RSR* for the steering manoeuvre with UBMS-INV. The best *RCR* and *RSR* are highlighted in bold. *Best solvers.

6.3.2.9 Discussion of the performance parameters

The performance of the twenty solvers tested on five motion reconstruction problems and two computer-simulated motion problems is summarised in Table 6.29. The solvers Ar1x, Ar2x and Ar2f give the best overall performance for the three motion reconstruction problems of the REALMAN project: generic arm reaching, door handling and vehicle accessibility. These three problems are characterised by:

- A whole body model without closed-loops, defined with more than 650 generalised coordinates.
- A large-scale NLP problem which has associated a coefficient matrix **C** of size bigger than 1300×1300.

The solvers Ar1x, Ar2x and Ar2f are also competitive for the computer-simulated motions generated with UBM-INV and UBMS-INV in the MoDyCo project, although they are not always the best. The main features of these two computer-simulated motion problems are:

- Upper body models with closed-loops: UBM-INV contains one closed-loop between the arms and the steering wheel (section 5.2.1) and UBMS-INV contains the same closed-loop plus an additional one in each shoulder complex between thorax, clavicle and scapula (section 3.3.1). Both models require more than 300 generalised coordinates for their definition.

- A NLP problem which has associated a coefficient matrix **C** of size about 600 × 600. Moreover, as the number of kinematic constraints is greater than the number of generalised coordinates, the nullspace (C) and two-step LU (D) numerical methods cannot be used.

Solver code	PROBLEM						
	Generic reaching	Door handling	Vehicle accessibility	UBM	UBMS	UBM-INV	UBMS-INV
A1x				2	2	2	
A2x				2	**1**	**1**	
Ar1x	**1**	**1**	**1**			2	**1**
Ar2x	**1**	**1**	**1**		NC	2	**1**
B1x				2	2		
B2x				2	1		
C1x				**1**	NC	X	X
C2x				**1**	NC	X	X
D1x		NC			NC	X	X
D2x		NC			NC	X	X
A1f						1	
A2f				2	1	1	
Ar1f						2	**1**
Ar2f	**1**	**1**	**1**		NC	2	**1**
B1f							
B2f					2		
C1f					NC	X	X
C2f				**1**	NC	X	X
D1f		NC			NC	X	X
D2f		NC			NC	X	X

Table 6.29: Comparison of the OTM solvers. 1: best solver; 2: solvers with CP similar to the best solver, although slower but with a competitive speed; NC: none of the frames converged to the desired tolerance; X: solver that cannot be used for the problem.

However, solvers Ar1x, Ar2x and Ar2f have a poor performance for the two problems that use the models UBMS and UBM. The main features of these two motion reconstruction problems are:

- Upper body models defined with more than 350 generalised coordinates. UBMS has two closed-loops, one on each shoulder

complex between thorax, clavicle and scapula. UBM has no closed-loops.

- A NLP problem which has associated a coefficient matrix **C** of size bigger than 700×700.

Solvers C1x, C2x and C2f have the best overall performance for UBM. However, they have a poor performance for the other six problems. Even these three solvers cannot be used for UBM-INV and UBMS-INV because they have more kinematic constraints than generalised coordinates (see section 6.3.2.7). Solvers A1x, A2x and A2f have a good performance for UBMS and UBM, although they are not always the best.

In summary, solvers Ar1x, Ar2x and Ar2f give a good performance for the two computer-simulated motion problems and three out of five motion reconstruction problems. The other two motion reconstruction problems can be solved with a good performance using these solvers but without the reordering method, i.e. A1x, A2x and A2f.

The seven problems studied (five motion reconstruction and two computer-simulated motion problems) are not directly comparable among them because the size of the models, measurement errors and motion reconstruction strategies are different. However, the mean time per frame (*MTF*) required by a solver to find the solution of the problem is used in an attempt to compare them. *MTF* is calculated for the best solver of each problem with $nMaxIter = 25$ (Table 6.30).

UBM	UBM-INV	UBMS	UBMS-INV	Door handling	Generic arm reaching	Vehicle accessibility
C2x	A2x	A2x	Ar1f	Ar2f	Ar2f	Ar1x

Table 6.30: Best solver with *nMaxIter* = 25 for each motion reconstruction problem or computer-simulated motion problem.

Figure 6.38 shows the *MTF* for each problem and for several tolerance values. As expected, for smaller tolerances *MTF* is bigger as the number of iterations needed to achieve the desired tolerance increases. The size of the model, defined as the number of generalised coordinates plus the number of nonlinear equality constraints of the NLP problem (4.116), has a big influence in *MTF*. Obviously, the bigger the problem size the bigger is *MTF*.

However, it is surprising that *MTF* of the vehicle accessibility is more than twice of *MTF* of the door handling or generic arm reaching, as they have comparable sizes. The influence of the motion reconstruction strategies cannot explain this large difference in *MTF* as they only add a few driving constraints

in the objective function and/or in the equality constraints and modify the weighting factors. These changes in the NLP problem (4.116) can only affect *MTF* slightly. The measurement errors are supposed to be one of the main causes for such a big difference in *MTF* and they are studied next.

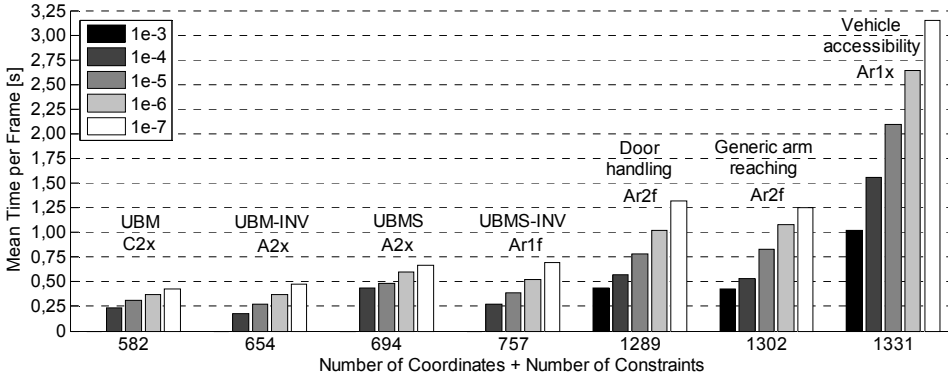

Figure 6.38: MTF required by the best solver for each problem.

The measurement errors of one representative trial of door handling, generic arm reaching and vehicle accessibility problems are shown in Figure 6.39, Figure 6.40 and Figure 6.41 respectively, using the distance errors of the markers. The *distance error of a marker* is defined as the distance between the measured and model-determined marker for a given frame. Although the distance errors of the markers of all trials are not shown, they are quite similar for all trials within an experiment. The distribution of the distance errors is not symmetric so a bloxplot is used to represent their distribution as it is more appropriate for skewed distributions. The distance error is calculated after the motion is reconstructed and depends on the reconstruction method and the tolerance for accepting the solution. The distance errors are calculated for a tolerance of 10^{-7} and with the best OTM solver for each motion reconstruction problem (Table 6.30).

The medians of the distance errors of the markers are similar in the three trials (Figure 6.39, Figure 6.40 and Figure 6.41) and most of them are between 5 and 25 mm. However, the ranges between the maximum and minimum distance error are considerably bigger for the vehicle accessibility trial (Figure 6.42). This means that the dispersion of distance errors in the vehicle accessibility trials is bigger, and thus affects directly the performance of the solvers.

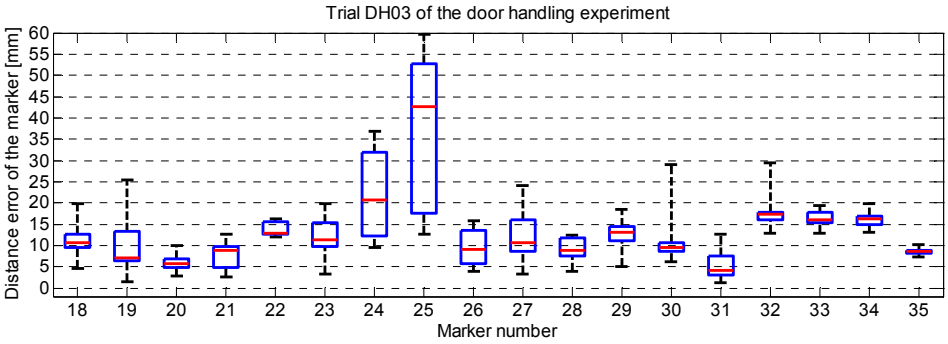

Figure 6.39: Distance errors of representative markers of the door handling trials. Marker locations are described in section D.1.3-Appendix D.

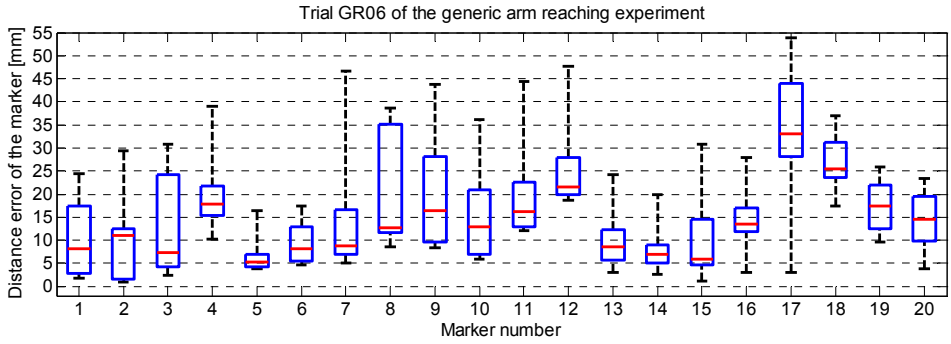

Figure 6.40: Distance errors of representative markers of the generic arm reaching trials. Marker locations are described in section D.1.4-Appendix D.

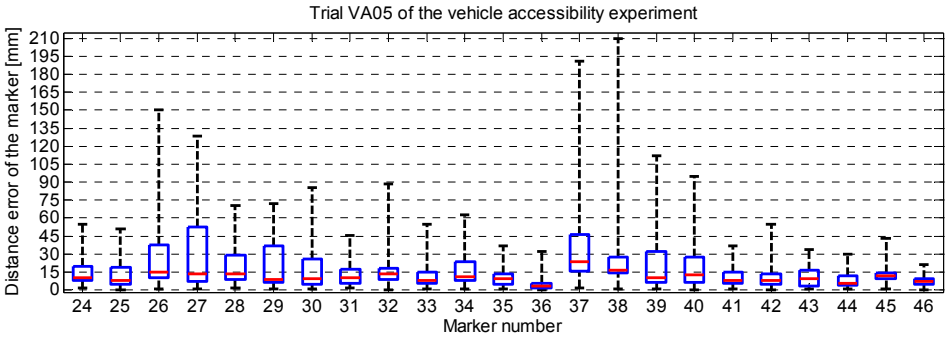

Figure 6.41: Distance errors of representative markers of the vehicle accessibility trials. Marker locations are described in section D.1.2-Appendix D.

These large ranges between the maximum and minimum distance errors can account for the big *MTF* in Figure 6.38. It can also explain the poor CPs (only about 90% of the frames converged to the desired tolerance) of the vehicle accessibility trials compared to the CPs (almost 100% of the frames

converged to the desired tolerance) of the door handling and generic arm reaching trials. Suppose that the solution of the NLP problem (4.116) for a given frame is known, i.e. the posture of the skeletal model that minimises the driving constraints and satisfies the kinematic constraints is known. This skeletal model posture is used as the initial approximation for the next frame. If the solution in the next frame is far from the initial approximation because some markers suffer a big change in position, the solver requires more iterations to achieve the desired tolerance. In the worst case, the solver may fail to reach the desired tolerance within the *nMaxIter* defined by the user. Obviously, more iterations per frame produce and increase in *MTF*.

An additional cause for the large values of *MTF* for the vehicle accessibility trials compared to the door handling or generic arm reaching trials is the different type of motions. While in the vehicle accessibility trials all body segments of the skeletal model have large displacements and rotations, in the door handling or generic arm reaching trials the subject is sitting and only the upper body moves. Therefore, the distance between the solution in the previous frame and the current frame is bigger in the vehicle accessibility and the solver requires more iterations to achieve the desired tolerance.

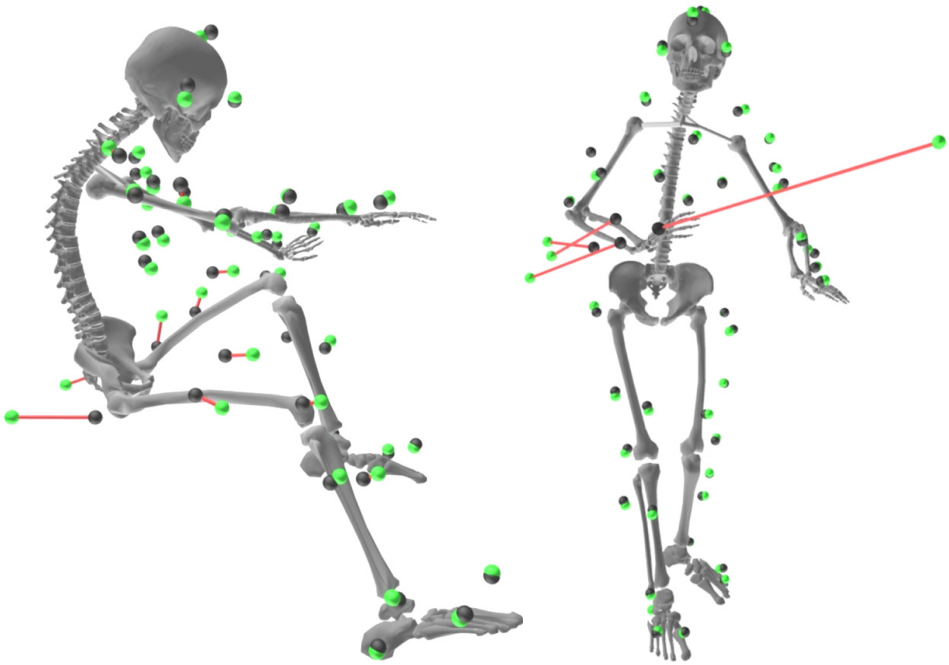

Figure 6.42: Frames of the trials VA02 (left) and VA07 (right) showing large distance errors for some markers. Black and green balls are model-determined and measured markers respectively.

The *MTF* of the vehicle accessibility can be reduced under some assumptions already presented in section 6.3.2.4. If *nMaxIter* is set to 50, the tolerance is set to 10^{-7} and solutions with a tolerance less than 10^{-4} are accepted, then D2x can be considered the best solver as it is faster than Ar1x and the percentage of frames that achieve the desired tolerance are similar (Table 6.31). For these conditions, *MTF* of the vehicle accessibility is significantly reduced, although it is still about 45% slower than *MTF* for the door handling or generic arm reaching.

nMaxIter	Tol	Ar1x		D2x	
		% of frames tol < 10^{-4}	*MTF*	% of frames tol < 10^{-4}	*MTF*
25	10^{-7}	94.7%	3.15 s	92.2%	1.47 s
50	10^{-7}	96.7%	3.97 s	96.3%	1.81 s

Table 6.31: Performance of solvers Ar1x and D2x for a tolerance of 10^{-7} and two values of *nMaxIter* (25 and 50).

6.3.3 COMPARISON OF COMPAMM AND MATLAB® IMPLEMENTATIONS

In this section the performance of the two OTM implementations is compared using the 10 trials of the vehicle accessibility experiment presented in section 6.2.1. From the 10 trials, 5 were classified as good quality trials by Renault and Peugeot-Citroën during the REALMAN project and 5 as bad quality trials. Only the solvers Ar1x, Ar2x, D1x and D2x of Matlab® implementation are considered in the comparison: Ar1x and Ar2x are the two best solvers with *nMaxIter* = 25 for the vehicle accessibility trials and D1x and D2x are based on the two-step LU method also used in Compamm. The motion of all the trials was reconstructed using a Pentium IV 3.00 GHz for both implementations.

Table 6.32 shows the total elapsed time needed by Compamm to reconstruct the motion of each vehicle accessibility trial and the percentage of frames that achieved a tolerance of 10^{-7}. Compamm could not reconstruct the complete motion of three trials because the solver diverged at a given frame and could not converge during the remaining frames. This was due to the fact that the solver implemented in Compamm was not equipped with a global convergence strategy. The percentage of frames that achieved the desired tolerance is quite low compared to solvers Ar1x, Ar2x, D1x and D2x.

Trial code	Frames	Total elapsed time	Percentage of frames that achieved a tolerance of 10^{-7}
VA01	1388	6 min 15 s (375 s)	30.9%
VA02	1105	8 min 44 s (524 s)	11.7%
VA03	1145	10 min 9 s (609 s)	8.6%
VA04	1109	5 min 16 s (316 s)	29.9%
VA05	1228	Divergence at frame 498	-
VA06	1051	5 min 28 s (328 s)	28.2%
VA07	1262	5 min 51 s (351 s)	38.5%
VA08	968	5 min 35 s (335 s)	21.7%
VA09	1242	Divergence at frame 373	-
VA10	1218	Divergence at frame 324	-

Table 6.32: Trials of the vehicle accessibility simulated in Compamm.

Figure 6.43 shows the percentage of frames that achieved the desired tolerance summing up the seven trials that converged. Furthermore, the tolerance reached by those frames that could not achieve the desired tolerance (10^{-7}) within *nMaxIter* (25) is also shown. The percentage of frames that reached a tolerance less than 10^{-4} using the Compamm solver was quite low compared to D1x and D2x. As the Compamm solver and D1x and D2x only differ in the global convergence strategy, it can be concluded that the use of a global convergence strategy improves the percentage of frames that achieve a given tolerance at least for the 10 vehicle accessibility trials studied.

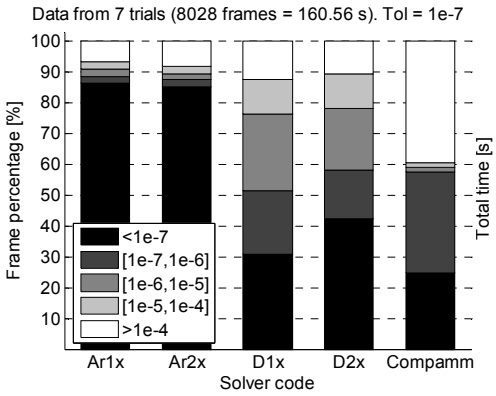

Figure 6.43: Percentage of frames that achieved tol = 10^{-7} and tolerance intervals for the remaining frames.

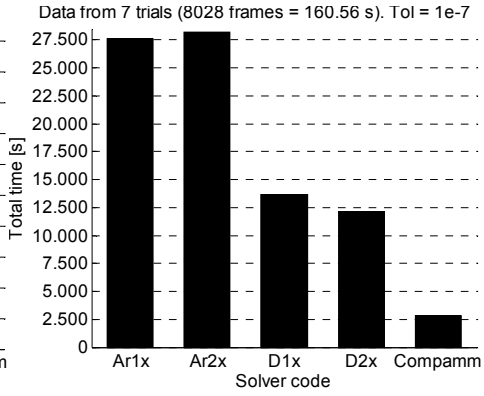

Figure 6.44: *T-t* for the 7 trials of the vehicle accessibility experiment that converged.

The *T-t* needed by Compamm to reconstruct the motion of the seven trials is more than four times quicker that the *T-t* required by D1x and D2x. The global convergence strategy requires only a very small percentage (<4%)

of the *T-t* and it cannot account for this huge difference. The main reason could be that Compamm is very efficient in terms of computational time in comparison with Matlab®.

6.3.4 EFFICIENCY OF OTM AND OTHER METHODS

OTM has been classified in section 4.3.3.3 as a global optimisation method (GOM) in the sense that it minimises the global measurement error introduced by the skin movement artifact. The reduction of the errors and the variability in the estimation of position and orientation of each body segment due to skin movement artifact is similar for all GOMs as the assumptions are comparable. The main differences between GOMs are in the type of skeletal models they can solve (e.g. with or without closed-loops) and the efficiency in terms of CPU time.

Studies on the assessment of the performance of GOMs have not been found in the literature. Only Bodenheimer et al. (1997) presented efficiency results of their GOM. Their model of the whole body was defined with relative coordinates and had 44 DoFs and 18 body segments. The motion reconstruction problem was formulated as a nonlinear unconstrained optimisation problem and was solved using a quasi-Newton BFGS optimisation method. The motion reconstruction of a walk motion of 6.7 s recorded at 30 Hz required 306 seconds on a Pentium 133 MHz and 4389 iterations. This gives a mean number of iterations per frame of 21.8 and MTF of 1.53 s. These results are difficult to compare with the motions reconstructed in this thesis due to the different human skeletal models and CPU used.

6.4 EVALUATION OF STRATEGIES FOR MOTION RECONSTRUCTION

6.4.1 PROGRESSIVE WEIGHTING STRATEGY

The progressive weighting strategy has been evaluated in four door handling trials and ten generic arm reaching trials. Recall that the progressive weighting strategy consists in decreasing progressively the weighting factor associated with a marker before it is missing, in setting it to zero during the time the marker is missing, and increasing it progressively after it is visible again (section 4.6.4). The weighting factor decreases or increases between zero and a maximum weighting factor (w_{max}) in a predefined number of frames (N_f). The selection of both parameters w_{max} and N_f is not automatic and must be defined by the user.

As the purpose of this section is to demonstrate the suitability of the progressive weighting strategy for motion reconstruction, the results presented were obtained with the original raw data provided by the motion capture system: marker trajectories were not smoothed and missing markers were not interpolated even for small gaps in the data.

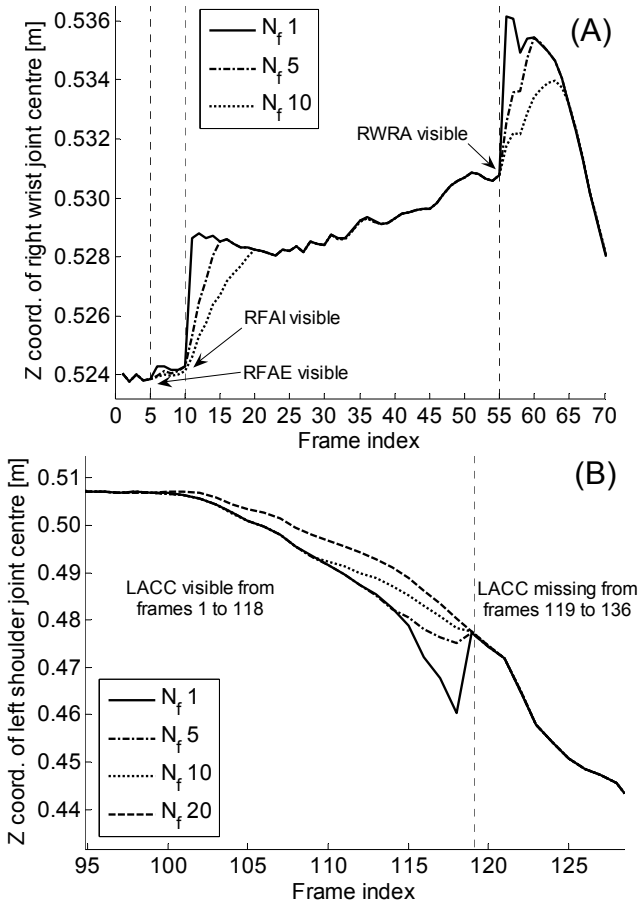

Figure 6.45: Progressive weighting strategy. (A) *Z*-coordinate of the wrist joint centre for N_f = 1, 5 and 10. The markers RFAE, RFAI and RWRA on the forearm are missing during the first frames. They become visible at frames 5, 10 and 55 respectively. (B) *Z*-coordinate of the left shoulder joint centre for N_f = 1, 5, 10 and 20. The marker LACC on the left clavicle over the acromion is missing between frames 119 to 136.

The effect of the progressive weighting strategy on the coordinates of two joint centres, for the trial DH03 of the door handling experiment and for different values of N_f is illustrated in Figure 6.45. The right forearm had four markers (Figure 6.46): RWRB was always visible but RFAE, RFAI and RWRA

were missing for frames 1-5, 1-10 and 1-55, respectively (Table 6.9). These missing markers are not a problem as one marker is sufficient to define the position of the forearm. This is because the elbow was modelled with one universal joint in the RAMSIS whole body model. Each time a new marker becomes visible, the position and orientation of the forearm is affected, because the new visible marker is included in the objective function of the NLP problem (4.116), especially if the distance error between the measured and model-determined marker is big.

In Figure 6.45(A), each time that a marker becomes visible (at frames 5, 10 and 55) the z-coordinate of the right wrist joint centre changes its value. When N_f is 1, the z-coordinate changes suddenly because the marker is included in the objective function with the same weighting factor as the other markers. For bigger values of N_f, the influence of the new visible marker in the posture of the model is incorporated progressively and the change in the joint centre is not so abrupt.

The marker LACC is located on the left clavicle over the acromion. For the door handling trial depicted in Figure 6.45(B) it was missing from frames 119 to 136 (Table 6.9). For $N_f = 1$, the z-coordinate of the shoulder joint centre changes suddenly when the marker is missing at frame 119. For $N_f = 20$, the weighting factor associated to LACC starts decreasing 20 frames before the marker is missing. In this way the influence of LACC in the posture of the model is removed progressively and the sudden change in the coordinate is eliminated.

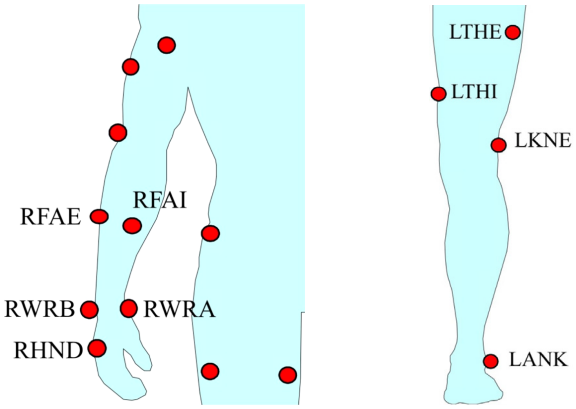

Figure 6.46: Markers in the right arm (left) and left leg (right) for the door handling trials.

The progressive weighting strategy proposed for the missing marker problem does not require any method to estimate or interpolate the position of a marker when is missing. However, these methods (Muijtjens et al., 1997; Herda et al., 2001; Desjardins et al., 2002) are not incompatible with the

progressive weighting strategy and can be used to improve the quality of the motion reconstruction. The progressive weighting strategy uses all the markers that are visible at each frame for determining the posture of the human skeletal model and the missing markers are automatically removed from the problem. Therefore, missing markers are not a problem provided that there are sufficient markers for defining the posture of all body segments of the model.

A limitation of the progressive weighting strategy is that the parameters w_{max} and N_f are not selected automatically and must be defined by the user by trial and error. The optimal value of N_f is difficult to obtain because it depends on many factors and probably it will be different for each coordinate and for each gap on the data. Currently, the same value of w_{max} is used for all the markers, although a different value could be defined for each marker depending on its noise level.

6.4.2 CONDITIONAL WEIGHTING STRATEGY

When a marker that is critical for defining the position of a body segment is missing, a conditional weighting strategy is used. It consists in activating one or more additional driving constraints, while the critical marker is missing, and deactivating them when it becomes visible. These additional driving constraints are used to define the position of the body segment (section 4.6.4).

The conditional weighting strategy was applied only to the four door handling trials because no critical markers were missing in the other investigated trials. In particular, it was applied to the right hand, left shank and left foot. The left foot had no markers and the marker LANK on the left shank (Figure 6.46) was missing from frames 63 to 99 (Table 6.9). Therefore, as the ankle and knee joints have both 2 degrees of freedom, the foot and shank motion was not defined during these frames.

In order to define the motion of the left shank and foot, which was composed of hindfoot and toes body segments, the following conditions were included in the model (see section 6.2.2 for details):

- A conditional weighting strategy, which was only active while LANK was missing, was used to set the value of the two knee joint angles to their values when LANK was visible for the last time.
- The hindfoot was constrained to remain parallel to the ground using the absolute preservation posture condition. This condition was included in Ψ_s and therefore it was exactly satisfied.
- The toes and hindfoot were connected by a weld joint, which allows no relative motion between the body segments.

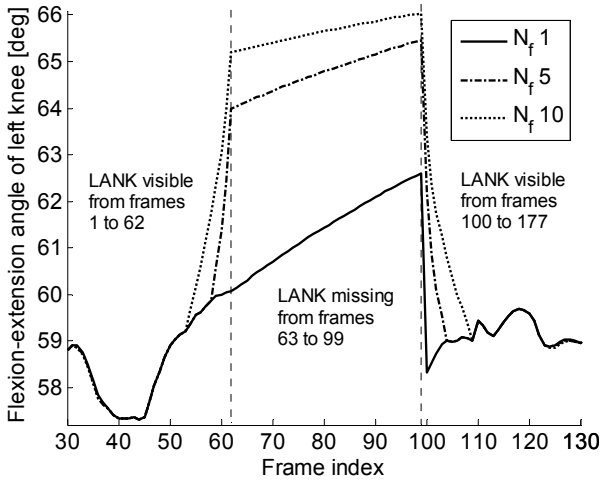

Figure 6.47: Influence of the conditional weighting strategy, progressive weighting strategy and the absolute preservation posture condition in the flexion-extension angle of the left knee. The three strategies have influence on the flexion-extension angle.

Recall that the driving constraints of the conditional weighting strategy are included in Ψ_m and their errors are minimised but they are not exactly satisfied. Therefore, the motion of the two knee joint angles depends on the absolute preservation posture condition for the hindfoot, on the value of N_f selected for the progressive weighting strategy and on the conditional weighting strategy (Figure 6.47). For example, for $N_f = 5$, the weighting factor associated to LANK starts decreasing five frames before the marker disappears at frame 63. The value of the flexion-extension angle at frame 63 is different for each value of N_f because for each different weighting factor the minimum of the NLP problem (4.116) is different. From frames 63 to 99, the flexion-extension angle is set to its value at frame 63 using additional driving constraints, which are included in Ψ_m. Therefore, the value of the angle between frames 63 to 99 is not exactly its value at frame 63. It actually depends on all the strategies used to define the motion of shank and hindfoot.

The conditional weighting strategy is only activated when the marker or markers associated to this strategy are missing. Therefore, it can be applied to any marker considered *a priori* as a critical marker for defining the motion of a body segment. If the marker is never missing during the recorded movement, the conditional weighting strategy is not activated and the solution is not influenced by it.

The conditional weighting strategy may not give a realistic motion if the markers are missing during a large number of frames, but it has two advantages. First, OTM is always able to find a unique solution of the NLP

problem (4.116). Only the body segments affected by the missing markers may not have an appropriate motion. Second, those parts of the reconstructed motion, where the critical markers are visible, are considered valid and can be used for further analysis. Even those body segments not affected significantly by the missing critical markers can be considered valid results. Otherwise, recorded motions with critical missing markers cannot be analysed unless other techniques are used.

6.4.3 RELATIVE AND ABSOLUTE PRESERVATION POSTURE CONDITION

Another problem with motion capture systems is the impossibility of measuring completely the motion of some bones (e.g. vertebrae or scapula) using external markers fixed on the skin, because of the relative skin/bone movement and insufficient number of markers. The relative and absolute preservation posture conditions can be used to solve this problem (see section 4.6.2 for details).

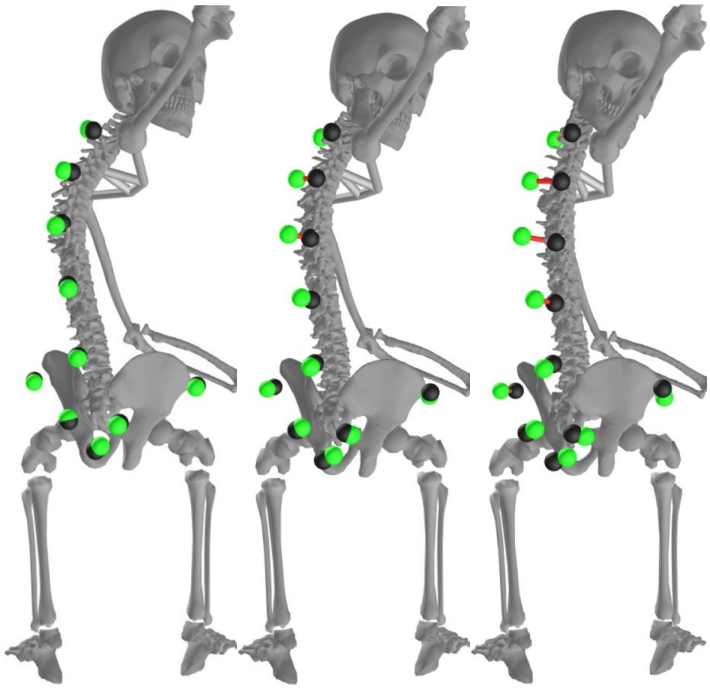

Figure 6.48: Generic reach movement showing the relative preservation posture condition for the spine and the absolute preservation posture condition for the feet, at the same time instant. Black and green balls are model-determined and measured markers respectively. Only the markers on the pelvis and spine are shown for clarity. The weighting factors of the spine angles used for the relative preservation posture condition are 0.001, 0.1 and 1 for the left, centre and right images.

In the three motion reconstruction problems of the REALMAN project, there were not sufficient markers located on the spine for determining the position of the 6 body segments modelling it. In the vehicle accessibility movements there were no markers on the spine. In the door closing movements, one marker was located on the neck over the 7th cervical vertebra. In the generic reach movements, five markers were located along the spine at different locations (two of them on the same body segment). These markers were not enough to define completely the position of the 6 spine bodies.

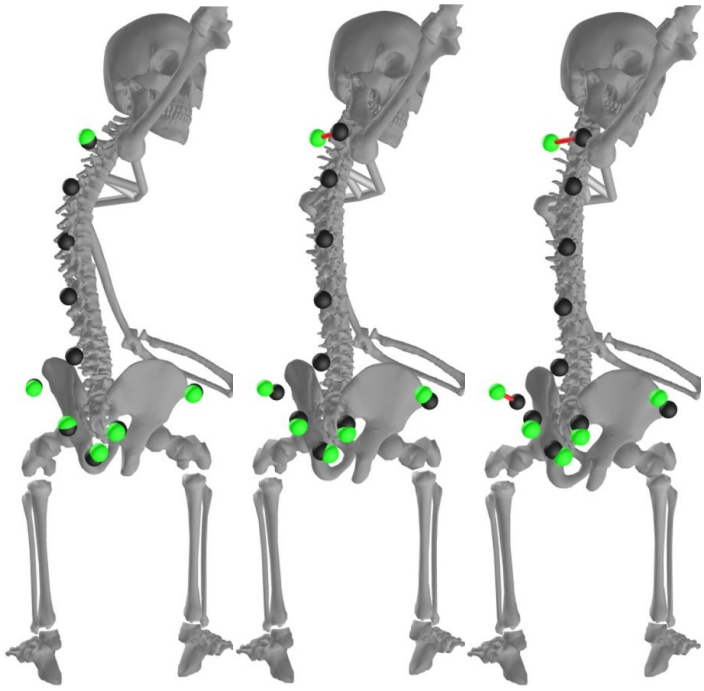

Figure 6.49: Generic reach movement showing the relative preservation posture condition for the spine and the absolute preservation posture condition for the feet, at the same time instant. Only one marker was used for the spine. Black and green balls are model-determined and measured markers respectively. Only the markers on the pelvis and spine are shown for clarity. The weighting factors of the spine angles are 0.001, 0.1 and 1 for the left, centre and right images.

The relative preservation posture condition is illustrated only qualitatively. The position adopted by the 6 body segments modelling the spine for three different weighting factor schemes is depicted in Figure 6.48 at the same time instant. In this generic reach movement, the subject was sitting on a stool and pushed a toggle switch situated in an elevated position at his right. The reference posture for the spine used by the relative preservation posture condition was provided by the PCMAN software, based on the pictures used

for fitting a digital human to the subject under study. In those pictures, the subject adopted a normal sitting position with his arms along the trunk (see section 5.4.3.5).

In Figure 6.48 the weighting factors used for all the joint angles of the spine are 0.001, 0.1 and 1 for the left, centre and right images respectively while the weighting factor for all markers was 1. It can be seen that for small spine weighting factors (Figure 6.48-left), the spine is more flexible and the markers on the spine are well followed. For high weighting factors (Figure 6.48-right), the spine remains closer to the reference posture and the markers on the spine are less well followed. The value of the weighting factors of the spine also affects the posture adopted by other body segments, especially those connected directly to the spine, as it can be seen clearly for the head. It can also be seen in Figure 6.48 how both feet remain parallel to the ground due to the absolute preservation posture condition.

Figure 6.49 shows three images of the same generic reach movement at the same time instant and with the same weighting factors as in Figure 6.48. The only difference is that in Figure 6.49 only one marker on the spine is used to reconstruct the motion. These images show more clearly the effect of the relative preservation posture condition in the posture of the spine. It can be seen that the spine postures obtained using five markers or only one are quite similar. A limitation of the relative preservation posture condition is that the reference posture is the same for the whole reconstruction motion, which may limit a realistic motion reconstruction when the range of motion is large. Furthermore, the weighting factors associated to the joint angles of the spine had all the same value for the whole motion. This can be improved by using different weighting factors for each joint angle based on biomechanical criteria.

6.4.4 CONVERGENCE TO THE DESIRED SOLUTION

OTM is equipped with two different strategies for global convergence, which guarantee convergence to a local minimiser from any remote starting point. Unfortunately, when the initial approximation of the first frame is far from the desired solution like in Figure 6.50, OTM converges to a local minimiser, which might be however not the right one. For example, in Figure 6.51 the left clavicle is rotated approximately 180º about its longitudinal axis with respect to the correct position and the right femur and tibia-fibula are rotated roughly 90º about their longitudinal axes.

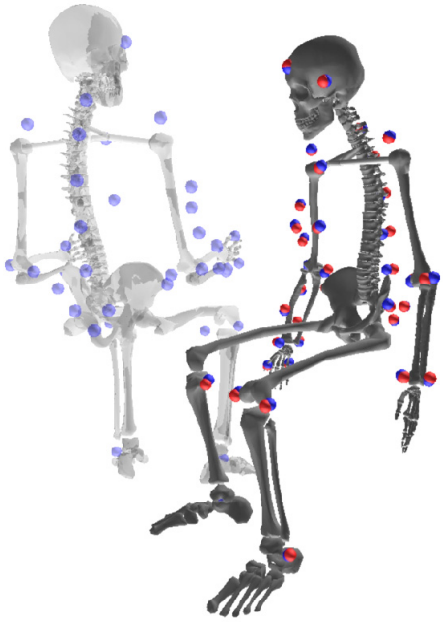

Figure 6.50: Initial approximation for the first frame of a generic reaching trial. Red and blue balls correspond to the measured and model-determined markers respectively. The light-grey skeleton is the initial approximation and the dark-grey the solution for the first frame.

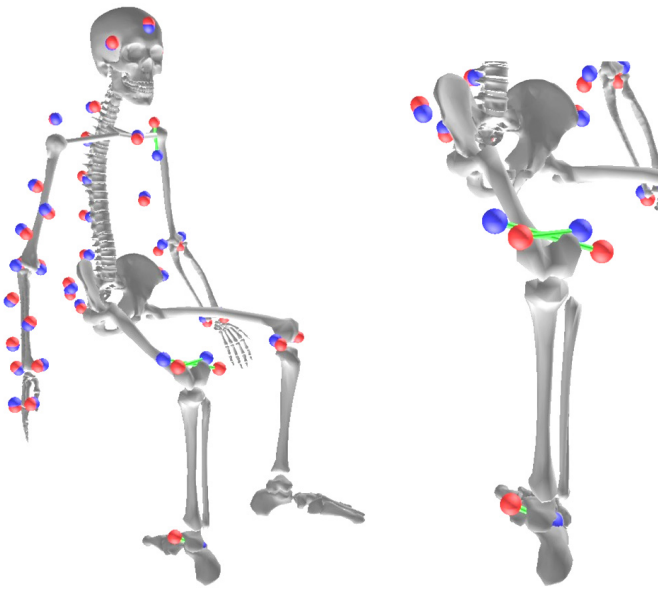

Figure 6.51: Convergence to an inappropriate local minimiser. Red and blue balls correspond to the measured and model-determined markers respectively. Green lines join measured and model-determined markers. Left: General view of the solution found by OTM. Right: Detail of the right leg.

The strategy of *convergence to the desired solution* consists in adding additional driving constraints to Ψ_m, which are only activated during the first initial frames in order to force convergence to the appropriate solution. This problem was found only in some of the ten generic arm reaching movements because the initial approximation for the first frame was far from the true initial solution. Table 6.33 summarises the different situations. In these ten trials, six vectors of the RAMSIS model were guided during the first three frames with suitable values, using additional driving constraints included in Ψ_m. After the three initial frames the ten trials converged to the appropriate solution.

Trial code	Solution given by OTM without applying the strategy of convergence to the desired solution	Solution given by OTM applying the strategy of convergence to the desired solution
GR01	inappropriate local minimiser (right clavicle rotated 180º)	appropriate local minimiser
GR02	inappropriate local minimiser (left clavicle rotated 180º and right femur and tibia-fibula rotated 90º)	appropriate local minimiser
GR03	appropriate local minimiser	appropriate local minimiser
GR04	inappropriate local minimiser (right clavicle rotated 180º and both femurs and tibia-fibulas rotated 90º)	appropriate local minimiser
GR05	appropriate local minimiser	appropriate local minimiser
GR06	appropriate local minimiser	appropriate local minimiser
GR07	inappropriate local minimiser (left clavicle rotated 180º)	appropriate local minimiser
GR08	appropriate local minimiser	appropriate local minimiser
GR09	appropriate local minimiser	appropriate local minimiser
GR10	inappropriate local minimiser (right femur and tibia-fibula rotated 90º)	appropriate local minimiser

Table 6.33: Solutions obtained by OTM for the ten generic arm reaching trials with and without applying the strategy of convergence to the desired solution. All rotations are about the longitudinal axes of each body segments. The rotation angles are approximated.

6.5 ANATOMICAL CALIBRATION PROTOCOL

In the frame of the MoDyCo project, an Anatomical Calibration Protocol (ACP) for estimating the subject-specific parameters of a human skeletal model tailored to a specific subject was presented in section 5.1.1.1. The inputs of ACP are the three-dimensional coordinates of several anatomical landmarks (ALs) of the subject. These ALs are measured with a Vicon motion capture system using a pointer technique. Three possible sources of errors in the estimation of the ALs are the following:

1. Errors in the estimation of the markers located on the pointer due to the motion capture system.
2. Errors in the estimation of the pointer tip due to the design of the pointer (Erdemir and Piazza, 1999).
3. Incorrect position measurement of ALs due to a wrong identification by the experimenter. ALs are not points but surfaces, sometimes large and irregular and their identification by palpation is subject to both intra- and inter-experimenter variability. Furthermore, ALs are covered by soft tissue of variable thickness.

In this section the errors in the anthropometric parameters due to the AL estimation errors are studied. The anthropometric parameters investigated are:

- Centre of mass (CoM) position referred to the local coordinate system (LCS) of each body segment.
- Moments of inertia at the CoM referred to the body segment LCS.
- Joint centres and joint axes referred to the global coordinate system.
- ALs coordinates in each body segment LCS.

As real experimental data were not available at the moment of writing this thesis, the ACP has been evaluated using computer-simulated ALs coordinates. ALs of one subject were obtained by combining ALs from two sources: Maurel upper limb model (Maurel, 1999) for the upper body and Kepple et al. (1998) database for the lower limbs. These ALs are considered the true ALs positions and the anthropometric parameters estimated from them, the true anthropometric parameters. The terms "true ALs positions" and "true anthropometric parameters" do not mean that they are calculated with high accuracy but that they are selected as a reference. Recall that BSPs are estimated using two methods proposed by Zatsiorsky and co-workers (section 2.2) and joint parameters using several methods based on regression equations and other techniques (section 2.1).

Measurements errors were added to the true ALs positions in order to generate fifty computer-simulated calibration trials. The magnitude of the measurement errors were taken from the literature. Della Croce et al. (1999) studied AL identification errors for 21 ALs in the pelvis and lower limb in two different subjects using a pointer with two pointer-markers. The intra- and inter-experimenter precisions (standard deviation of the distance from the mean position) were in the range 4.8-21 mm and 11.5-24.8 mm, respectively. Rabuffetti et al. (2002) estimated the variability in identifying the position of 21 ALs distributed over the whole body using the same methodology as Della

Croce et al. (1999). The inter-experimenter precision was in the range 4.1-19.2 mm and the intra-subject precision (the subject under examination identified ALs on his/her own body) was in the range 4.1-11.3 mm.

Number	Description	3D SD	Coord. SD
L1	7th cervical vertebra	16.8[R]	9.7
L2	8th thoracic vertebra	16.8[A]	9.7
L3	Incisura jugularis (suprasternal notch)	6.5[R]	3.7
L4	Processus xiphoideus	10.9[R]	6.3
L6/L5	Right and left sternoclavicular joint	6.5[A]	3.7
L20/L7	Right and left acromioclavicular joint	17.9[A]	10.3
L21/L8	Right and left trigonum spinae scapulae	13.2[A]	7.6
L22/L9	Right and left angulus inferior	13.2[A]	7.6
L23/L10	Right and left angulus acromialis or acromion	17.9[R]	10.3
L24/L11	Right and left processus coracoideus	13.2[A]	7.6
L26/L13	Right and left lateral epicondyle of humerus	10.8[R]	6.2
L27/L14	Right and left medial epicondyle of humerus	10.8[A]	6.2
L29/L16	Right and left radial styloid	8.7[A]	5.0
L30/L17	Right and left ulnar styloid	8.7[R]	5.0
L32/L19	Right and left 3rd dactylion	6.5[A]	3.7
L34/L33	Right and left posterior superior iliac spine	14.9[R]	8.6
L36/L35	Right and left anterior superior iliac spine	13.2[R]	7.6
L37	Pubic symphysis	14.9[A]	8.6
L39	Right lateral epicondyle of the femur	14.6[R]	8.4
L40	Right medial epicondyle of the femur	14.9[D]	8.6
L42	Right lateral condyle of tibia	13.8[D]	8.0
L43	Right medial condyle of tibia	19.7[D]	11.4
L44	Right lateral malleolus	8.6[R]	5.0
L45	Right medial malleolus	15.3[D]	8.8
L47	Right pterion or pternion. Posterior point of the heel	16.2[D]	9.3
L48	Right acropodion. The tip of the second metatarsal	13.9[D]	8.0
L49	Omphalion or navel	7.3[R]	4.2
L50	3rd lumbar vertebra	16.8[A]	9.7
L51	Vertex. The most cranial point of the head	17.9[A]	10.3

Table 6.34: Standard deviations (SDs) in mm of the normally distributed noise (mean = 0) added to the true ALs positions. [D]SD taken form Della Croce et al. (1999). [R]SD taken from Rabuffetti et al. (2002). [A]SD estimated from SDs of other ALs with similar features.

Based on the AL identification errors presented by Della Croce et al. (1999) and Rabuffetti et al. (2002), the computer-simulated measurement errors added to the true ALs positions were modelled as a random noise with a normal distribution of zero mean value and a different standard deviation (SD) for each AL. The SD of each AL was taken, if available, from the inter-experimenter SD provided by Rabuffetti et al. (2002) or otherwise from Della Croce et al. (1999). The SDs of ALs not included in the two studies were

estimated from the SDs of ALs with similar characteristics. Table 6.34 summarises SDs selected for each AL.

The same SD was used for each coordinate of an AL. For example, Della Croce et al. (1999) estimated an inter-experimenter precision (SD of the distance from the mean position) of 14.9 mm for the medial epicondyle of the femur. Therefore, a SD of 8.6 mm ($=14.9/\sqrt{3}$) was used for each coordinate. This distribution ensured a maximum position measurement error of 22.15 mm (99% confidence) for each direction and consequently a maximum error of 38.36 mm for the distance between the true and computer-simulated AL position.

Table 6.35 shows the influence of the ALs measurement errors in the estimation of the CoM position referred to each body segment LCS. The two following definitions are used to quantify the measurement errors:

- The distance error is defined as the distance between the true CoM position and the CoM position calculated in a computer-simulated calibration trial.
- The percentage distance error is defined as the distance error divided by the corresponding body segment length.

Body name	Mean distance error (mm)	SD (mm)	Mean percentage distance error (%)	SD (%)
Thorax	4.8	2.6	1.3	0.7
Upper arm	6.1	4.4	2.2	1.5
Forearm	3.1	2.3	1.2	0.9
Hand	4.4	2.0	2.4	1.1
Pelvis	7.4	3.6	3.3	1.6
Thigh	5.4	3.7	1.3	0.9
Shank	34.2	25.2	8.2	6.0
Foot	11.0	5.5	5.6	2.8

Table 6.35: Influence of the AL measurement errors in the CoM position.

The accuracy of the CoM position is quantified using the mean distance error and mean percentage distance error of the CoM, calculated from the fifty computer-simulated calibration trials. The precision of the CoM position is quantified using the SD of the distance error and the SD of the percentage distance error. The CoM mean distance error and CoM mean percentage error are in the range 3.1–11.0 mm and 1.2–5.6% respectively, except for the shank. The SDs of CoM distance error and CoM percentage error are in the range 1.8–5.5 mm and 0.7–2.8% respectively, except for the shank.

The precision and accuracy of the CoM position of the shank are significantly worse than of the other body segments. The CoM of the shank is assumed to be located along the line connecting the knee and ankle joint centres. However, the longitudinal axis of the shank LCS follows the ISB recommendations (Wu et al., 2002), which is based on the position of landmarks RLC(L42), RMC(L43), RLM(L44) and RMM (L45). Landmarks RLM (L44) and RMM (L45) are very close to each other and small errors produce large variations in the shank longitudinal and mediolateral axes. If the precision and accuracy of the shank CoM position are calculated in the global coordinate system instead of the shank LCS, the CoM mean distance error is 5.8 mm (SD 2.47 mm) and the CoM mean percentage distance error is 1.39% (SD 0.59%). Therefore, the ISB recommendation on the shank LCS definition is very sensitive to ALs measurement errors.

The influence of the ALs measurement errors in the estimation of the moments of inertia about the local x-, y- and z-axis of each body segment are shown in Table 6.36, Table 6.37 and Table 6.38 respectively. Similarly to the CoM, the following two definitions are used to quantify measurement errors:

- The moment of inertia (MoI) error is defined as the difference between the true MoI and the MoI calculated in a computer-simulated calibration trial.
- The percentage MoI error is defined as the MoI error divided by the true MoI.

The accuracy of each MoI is quantified using the mean MoI error and mean percentage MoI error. The precision of each MoI is quantified using the SD of the MoI error and SD of the percentage MoI error. The mean MoI error and mean percentage MoI error about the three axes are in the range 6.38×10^{-2} – 2.58×10^{-5} kgm^2 and 2.3 – 8.2% respectively. The SDs of MoI error and percentage MoI error are in the range 2.2×10^{-2} – 1.36×10^{-5} kgm^2 and 2.0 – 6.4% respectively. The single exception is the percentage MoI error about the local y-axis (approximately longitudinal) of the shank, which is 19.4% (SD 20.1%). However, the mean percentage MoI error of the shank about an axis passing through the knee and ankle joint centres is 3.22% (SD 2.49%). Similarly to the CoM this large error and variability of the shank MoI about the y-axis is due to high sensitivity of the shank LCS definition to the ALs measurement errors.

Body name	True MoI	Mean MoI error (kgm^2)	SD (kgm^2)	Mean percentage MoI error (%)	SD (%)
Thorax	9.31×10^{-1}	2.81×10^{-2}	1.96×10^{-2}	3.0	2.1
Upper arm	1.17×10^{-2}	7.58×10^{-4}	6.27×10^{-4}	6.4	5.3
Forearm	6.56×10^{-3}	2.85×10^{-4}	2.14×10^{-4}	4.3	3.2
Hand	8.65×10^{-4}	3.55×10^{-5}	2.21×10^{-5}	4.1	2.6
Pelvis	1.93×10^{-1}	1.18×10^{-2}	8.91×10^{-3}	6.1	4.6
Thigh	2.06×10^{-1}	1.28×10^{-2}	8.85×10^{-3}	6.2	4.3
Shank	3.58×10^{-2}	9.58×10^{-4}	7.95×10^{-4}	2.7	2.2
Foot	9.59×10^{-4}	7.82×10^{-5}	6.15×10^{-5}	8.2	6.4

Table 6.36: Influence of the AL measurement errors in the MoI about the local x-axis.

Body name	True MoI	Mean MoI error (kgm^2)	SD (kgm^2)	Mean percentage MoI error (%)	SD (%)
Thorax	2.71×10^{-1}	6.38×10^{-3}	5.34×10^{-3}	2.3	2.0
Upper arm	4.05×10^{-3}	2.61×10^{-4}	2.16×10^{-4}	6.5	5.3
Forearm	1.26×10^{-3}	5.47×10^{-5}	4.10×10^{-5}	4.3	3.2
Hand	5.30×10^{-4}	2.17×10^{-5}	1.36×10^{-5}	4.1	2.6
Pelvis	1.76×10^{-1}	1.08×10^{-2}	8.13×10^{-3}	6.1	4.6
Thigh	4.22×10^{-2}	2.63×10^{-3}	1.81×10^{-3}	6.2	4.3
Shank	6.81×10^{-3}	1.32×10^{-3}	1.37×10^{-3}	19.4	20.1
Foot	3.74×10^{-3}	3.05×10^{-4}	2.40×10^{-4}	8.2	6.4

Table 6.37: Influence of the AL measurement errors in the MoI about the local y-axis.

Body name	True MoI	Mean MoI error (kgm^2)	SD (kgm^2)	Mean percentage MoI error (%)	SD (%)
Thorax	1.07	3.09×10^{-2}	2.2×10^{-2}	2.9	2.1
Upper arm	1.32×10^{-2}	8.50×10^{-4}	7.04×10^{-4}	6.5	5.3
Forearm	6.05×10^{-3}	2.62×10^{-4}	1.97×10^{-4}	4.3	3.2
Hand	1.30×10^{-3}	5.33×10^{-5}	3.32×10^{-5}	4.1	2.6
Pelvis	1.55×10^{-1}	9.53×10^{-3}	7.14×10^{-3}	6.2	4.6
Thigh	2.06×10^{-1}	1.28×10^{-2}	8.85×10^{-3}	6.2	4.3
Shank	3.34×10^{-2}	1.76×10^{-3}	1.56×10^{-3}	5.3	4.7
Foot	4.12×10^{-3}	3.36×10^{-4}	2.64×10^{-4}	8.2	6.4

Table 6.38: Influence of the AL measurement errors in the MoI about the local z-axis.

The mean distance error between the true joint centre and the joint centre calculated from each computer-simulated calibration trial is shown in Table 6.39. These distance errors have been calculated in the global coordinate system so that the influence of the LCS definition is not included.

Furthermore, most of the joint centres are defined as the LCS origins and the influence of the ALs measurement errors cannot be quantified from their local coordinates. The mean distance errors are in the range 5.6 – 19.7 mm and the SDs in the range 1.9 – 7.7 mm.

Joint centre	Mean distance error (mm)	SD (mm)
Sternoclavicular	6.1	2.1
3rd lumbar vertebra	16.3	6.4
Acromioclavicular	6.1	2.6
Glenohumeral	13.8	5.2
Elbow	10.0	4.1
Wrist	6.0	2.4
Hip	19.7	7.7
Knee	8.8	4.1
Ankle	6.1	4.1

Table 6.39: Distance error of the joint centre position.

Table 6.40 shows the mean angle error (MAE) of the three revolute joint axes. Acoording to Stokdijk (1999) the MAE is defined as

$$MAE = \frac{1}{N}\sum_{i=1}^{N} \text{acos}(U_{true} \cdot U_i) \tag{6.3}$$

where U_{true} is the true unit vector in the joint axis direction, U_i is the calculated unit vector for trial i and N is the number of computer-simulated trials.

Joint axis	Mean angle error (deg)	SD (deg)
Elbow	6.8	4.1
Knee	9.2	4.9

Table 6.40: Mean angle error of the joint axis of the revolute joints.

The accuracy and precision of the local coordinates of the ALs are quantified using the mean error and SD of each coordinate and also the 3D mean error and SD (Table 6.41). The ALs defined as the origins of each LCS are not shown as their mean errors and SDs in each direction are always zero. Excluding the ALs of the shank, the maximum mean errors and SDs are below 5.2 mm and 20 mm for each direction and the 3D mean errors and SDs are below 5.2 mm and 30.4 mm.

Three landmarks of the shank (L41, L42 and L43) have significantly bigger 3D mean errors and SDs than the other ALs. The cause for this poor accuracy and precision is the same as explained for the CoM and MoI: the high sensitivity of the shank LCS definition to ALs measurement errors, especially

errors on RLM (L44) and RMM (L45). The landmarks L41, L42 and L43 are far from the origin and small variations in the shank z-axis (defined by the line connecting L44 and L45) produce large variations in z-coordinates of these landmarks.

Body segment	Landmark	X (mm)		Y (mm)		Z (mm)		3D (mm)	
		ME	SD	ME	SD	ME	SD	ME	SD
Thorax	L1	0	0	-1.6	13.9	0.6	8.5	1.7	16.3
	L2	0.3	9.3	-3.5	11.9	0.8	7.5	3.6	16.9
	L4	-0.3	9.3	-1.0	7.4	-0.2	6.4	1.1	13.5
	L5	0.2	4.6	-1.4	5.0	-0.8	5.6	1.6	8.8
	L6	-0.8	4.9	-0.4	6.0	1.8	5.1	2.0	9.3
	L49	-2.3	17.6	1.0	5.8	-1.6	18.4	3.0	26.1
	L50	-1.2	19.8	-2.7	11.9	-2.5	19.8	3.9	30.4
Clavicle	L20	0.6	4.8	0	0	0	0	0.6	4.8
Scapula	L20	-2.0	16.4	2.0	14.6	1.0	14.1	3	26.1
	L21	-2.4	14.0	0	0	0	0	2.4	14.0
	L22	3.4	18.4	-0.1	10.8	0	0	3.4	21.3
	L24	-2.1	17.2	1.8	11.8	0.5	9.3	2.8	22.8
	L25	-0.1	12.3	0	12.0	0.2	12.3	0.2	21.1
Upper arm	L26	0.7	4.7	3.1	11.9	0	0	3.2	12.8
	L27	-0.7	4.7	4.3	10.8	0	0	4.4	11.8
	L28	0.7	4.7	3.1	11.8	0	0	3.2	12.7
Forearm	L28	0	0	1.0	7.2	0	0	1.0	7.2
	L29	0	3.5	0.6	3.5	0	0	0.6	4.9
	L30	0	3.5	-0.6	3.5	0	0	0.6	4.9
Pelvis	L33	1.4	8.0	1.3	6.3	0	11.8	1.9	1.6
	L34	0.5	9.5	-1.3	6.3	1.0	10.8	1.7	5.7
	L35	0	0	0	0	-0.3	4.3	0.3	4.3
	L36	0	0	0	0	0.3	4.3	0.3	4.3
	L37	-0.6	12.2	-0.4	12.2	-2.6	11.7	2.7	19.7
	L38	-0.2	16.7	2.1	16.7	0.2	3.1	2.1	21.6
Thigh	L39	0	0	-5.2	15.7	-0.4	6.0	5.2	1.8
	L40	0	0	-1.2	17.4	0.4	6.0	1.3	18.4
	L41	0	0	-3.2	17.7	0	0	3.2	15.7
Foot	L47	0.5	10.6	-0.3	8.6	1.5	11.3	1.6	17.7
	L48	0.7	9.6	0.2	9.7	0	0	0.7	13.6
Shank	L41	1.7	8.3	-7.0	15.9	3.0	73.7	7.8	75.8
	L42	1.5	10.4	-7.0	13.7	2.5	69.1	7.6	71.2
	L43	-1.5	10.4	-5.4	23.2	5.8	67.7	8.1	72.3
	L44	0	0	0	0	1.2	2.1	1.2	2.1
	L45	0	0	0	0	-1.2	2.1	1.2	2.1
Hand	L32	0	8.5	0.7	4.5	2.1	9.2	2.2	13.3

Table 6.41: Mean error (ME) and standard deviation (SD) of each landmark in the relevant local coordinate system.

CHAPTER 7

CONCLUSIONS AND FUTURE WORK

The research presented in this thesis has been focused on the improvement of the 3D analysis of human movement. The main issues addressed have been:

- The problem of motion reconstruction of human movements using large and medium-size skeletal models with open- and closed-loops.
- Two problems inherent to optoelectronic motion capture systems: the missing marker problem and the impossibility of measuring completely the motion of some bones under the skin.
- The estimation of subject-specific parameters of a human skeletal model using a motion capture system and some additional inexpensive instrumentation.
- The development of several human skeletal models suitable for analysing different human movements.

7.1 CONCLUSIONS

As a result of the investigations carried out, several conclusions have been obtained and are presented next. They are organised according to the four issues mentioned above and presented by order of relevance.

7.1.1 MOTION RECONSTRUCTION

Among the three types of motion reconstruction methods (direct, segmental optimisation and global optimisation methods), the global optimisation

methods (GOMs) have been considered the most suitable for the problems faced in this thesis. GOMs published so far in the literature are designed for open-loop models described with relative coordinates and are usually formulated as nonlinear unconstrained optimisation problems. They are not valid for human skeletal models with closed-loops defined with relative coordinates and neither for models defined with natural coordinates.

A new motion reconstruction method, which can be classified as a GOM, valid for large-size human skeletal models with open- and closed-loops has been developed. The human skeletal models used for motion reconstruction have been defined with natural coordinates because of the potential advantages of these coordinates. The use of natural coordinates for the motion reconstruction method leads to a nonlinear constrained optimisation problem with only equality constraints:

- The objective function is quadratic and is defined as the sum of the squared distances between the measured and model-determined markers.
- The nonlinear equality constraints are the kinematic constraints that define the human skeletal model. The kinematic constraints usually include redundant equations in the practical cases.

This optimisation problem that originates from the motion reconstruction method is called in this thesis Optimal Tracking Problem (OTP). Its structure has been specially designed to handle the new strategies proposed for dealing with the two common problems of optoelectronic motion capture systems mentioned previously.

When OTP has redundant equality constraints, it cannot be solved by most of the optimisation methods published so far. In this thesis a new optimisation method called Optimal Tracking Method (OTM) has been developed specifically for such an optimisation problem. The main features of OTM are:

- It can solve OTP with and without redundant equality constraints.
- It can solve OTP for large-size human skeletal models defined using natural coordinates with a reasonable efficiency in terms of CPU time.
- It is equipped with four different numerical methods for solving OTP, which have been tested on computer-simulated and experimental data.
- It is globally convergent, i.e. it can converge to a local minimiser from any remote starting point. Two strategies for global

convergence and two step-control modes, which control the activation/deactivation pattern of the global convergence strategy, have been proposed and tested. However, the convergence to the desired minimiser cannot always be guaranteed. This drawback has been solved by using a new strategy, which consists in including additional driving constraints only during the first initial frames in order to induce convergence to the desired solution.

Due to the lack of experimental data for validating the human skeletal models of the MoDyCo project, computer-simulated motions for steering manoeuvres have been generated using the new motion reconstruction method itself. This has been possible due to the particular structure of OTP and the full exploitation of the motion reconstruction strategies proposed in this thesis.

Two different implementations of OTM have been used, one in Matlab® and another in Compamm. The Matlab® implementation includes all the OTM features and motion reconstruction strategies proposed in this thesis. The Compamm implementation includes only one numerical method based on Gaussian factorisation for solving OTP and the relative preservation posture condition.

The OTM implementation in Compamm has been used in the REALMAN project to reconstruct the motion of more than 6000 trials using the RAMSIS whole body model. Some deficiencies were detected in this implementation, which have been completely solved in the Matlab® implementation by improving OTM and developing new motion reconstruction strategies.

The performance of OTM implementation in Matlab® has been tested on five motion reconstruction problems, which included 48 motions, and two computer-simulated motion problems, which included 8 motions. The OTM performance has been quantified using four performance parameters. From all the possible combinations of the four numerical methods for solving OTP, two global convergence strategies and two step-control modes tested, those combinations that use the direct QR numerical method have shown the best average performance for the studied problems. However, no combination has been found that gives the best performance for all the problems.

An efficiency comparison between the Matlab® and Compamm implementations of OTM showed that Compamm is four times faster than Matlab® for the vehicle accessibility trials. Therefore, an improvement in the OTM efficiency compared to Matlab® is expected if OTM and all the new motion reconstruction strategies are fully implemented in Compamm.

7.1.2 PROBLEMS OF OPTOELECTRONIC MOTION CAPTURE SYSTEMS

The missing marker problem is usually handled by estimating its position during the frames in which it is missing. However, the methods published so far do not solve completely this problem when the marker is missing during a large number of consecutive frames. In this thesis, the missing marker problem has been considered from a different point of view, which is compatible and complementary with the existing methods. The new strategy proposed for dealing with the missing marker problem is based on three cornerstones:

1. Joint constraints are considered in the multibody model of the human skeletal system and more markers than the minimum strictly necessary to define the posture of the model are used. When some markers are missing, this does not represent a problem provided that the visible markers are enough to define the posture of the model.
2. The markers with a large number of consecutive missing frames, which cannot be satisfactorily estimated with the available methods, are used for the motion reconstruction only when they are visible and are neglected when they are missing. This idea is the basis of the progressive weighting strategy proposed in this thesis, which minimises the possible discontinuities in the reconstructed motion.
3. When a marker that is critical for defining the position of a body segment is missing, the body segment position is defined using a new strategy called conditional weighting. This strategy has three advantages. First, OTM is always able to find a unique solution of OTP. Second, the motion of those body segments not affected by the critical marker can be considered valid and can be used for further analysis. Third, it can be applied to any marker considered *a priori* as a critical marker for defining the motion of a body segment. If the marker is never missing during the recorded movement, the conditional weighting strategy is not activated and the solution is not influenced by it. The drawback of this strategy is that it might not give realistic motions if the markers are missing during a large number of consecutive frames.

The progressive weighting and the conditional weighting strategies have been tested on several motion experiments with satisfactory results.

The motion of some bones cannot be measured using external markers fixed on the skin because of the relative skin/bone movement and the impossibility of estimating the bone motion with the markers that can be located on the body segment. In this thesis, the motion of these bones has

been estimated using a new method called relative preservation posture condition. This condition consists in imposing the relative motion between the body segments whose motion is not completely defined. Their relative motion must follow as closely as possible a given reference posture. Weighting factors are used to adjust the influence of the relative preservation posture condition in the reconstructed motion.

The relative preservation posture condition has been applied to the motion of the spine, which has been modelled with six body segments. Three cases have been investigated, depending on the number of markers located on the spine: with no markers on the spine for the vehicle accessibility trials, with one marker for the door handling trials and with five markers for the generic arm reaching trials. Satisfactory results have been obtained in the three cases.

There are situations in which markers have not been placed on some body segments but their motion can be estimated from additional conditions from the environment. In these cases the absolute preservation posture condition can be applied in order to prescribe the absolute motion of the bodies using points and vectors already available in the model. This method has been applied to the feet, which have been constrained to remain parallel to the ground, with satisfactory results.

7.1.3 SUBJECT-SPECIFIC PARAMETERS

The methods used for estimating the subject-specific parameters have been limited by the available measurement equipment and the total time required by each method. As a large number of subjects had to be studied, the total measuring time was an important issue. The methods based on anatomical landmarks have been selected since they satisfy the two previous requirements. Furthermore, ISB and van der Helm recommendations on definitions of local coordinate systems have been used. These recommendations define each local coordinate system as a function of several anatomical landmarks. For this reason, some anatomical landmarks have already been measured, thus representing an advantage for methods based on anatomical landmarks. The methods used for each type of subject-specific parameter are:

- Joint parameters have been estimated using regression methods whenever these methods exist for a joint. When regression methods, which are based on anatomical landmarks, are not available, other methods based on anatomical landmarks are used.
- Inertia parameters have been estimated using Zatsiorsky's proportion method and Zatsiorsky's linear regression method based on total body height and weight. The first method is used when the

subject studied has characteristics similar to Zatsiorsky's subject database and the second when the subject is outside the database range.

- The position of anatomical landmarks and markers on each body segment has been estimated with a new Anatomical Calibration Protocol proposed in this thesis, which is partially based on Cappozzo's CAST method.

The precision of the subject-specific parameters depends mainly on the measurement errors of the anatomical landmarks. The precision has been evaluated using computer-simulated data and generally the precision of the subject-specific parameters of each body segment is similar to the measurement precision of the anatomical landmarks. The shank is the exception, due to its local coordinate system definition, which is very sensitive to measurement errors on the anatomical landmarks.

A new detailed measurement protocol has been proposed for measuring 42 anatomical landmarks that are required for estimating all the subject-specific parameters. Additionally, a methodology has been developed for estimating all the subject-specific parameters from the positions of 42 anatomical landmarks. The anatomical landmarks have been measured using an optoelectronic motion capture system and a stick with two markers mounted on it at an adequate distance.

7.1.4 HUMAN SKELETAL MODELS

Three new partial models of the human skeleton have been developed: two upper body models with different level of complexity for studying steering manoeuvres and one right lower limb model for studying braking manoeuvres. The two upper limb models differ in the model of the shoulder complex. One model has a simplified shoulder complex without scapula in which the clavicle is connected directly to the humerus. The other model includes the clavicle, scapula and humerus, with the scapula connected to the thorax through the scapulothoracic joint forming a closed-loop mechanism. The complete definition of the three models depends exclusively on a set of anatomical landmarks. The local coordinate systems of the body segments follow the 2002 ISB recommendations and van der Helm's 1997 recommendations. The most recent ISB recommendations (2005) have not been followed because they were published after the realisation of this thesis. However, the anatomical landmarks used by the 2005 ISB recommendations are the same as the ones used in this thesis, and therefore it is straightforward to apply them.

Besides, a human skeletal model of the whole body based on the RAMSIS model has been used for studying several types of vehicle-related motions.

7.1.5 SOFTWARE IMPLEMENTATION

A toolbox, which includes all the developments carried out in this thesis, has been implemented in Matlab®. This toolbox allows performing all the motion reconstruction process, except for the experimental phase. It allows creating symbolic multibody models of the human skeleton using natural coordinates, estimating subject-specific parameters from the anatomical landmarks measured during the Anatomical Calibration Protocol, reconstructing the motion of a subject from motion capture data using OTM and including the new motion reconstruction strategies.

7.2 FUTURE WORK

After the conclusions obtained in this thesis some recommendations for future research work are proposed.

- The performance of OTM could be improved by:
    1. Developing more efficient methods for solving the sparse linear system of equations arising in OTM.
    2. Handling more efficiently the redundant equations of the kinematic constraints.
    3. Improving the global convergence strategies and the step-control modes.
    4. Defining an adaptive value for the maximum number of iterations. Currently the maximum number of iterations for each frame is set by the user and has a fixed value during the whole reconstruction process. An adaptive value could be defined such that if the strand effect is detected, the iteration is stopped or if acceptable progress towards the solution is being made, the iteration continues. This enhancement could solve the initial approximation effect.
- The motion reconstruction method can be enhanced by including inequality constraints in OTP. This would require improving OTM in order to handle this type of constraints. Inequality constraints can be used to include for example joint limits or additional constraints from the environment (e.g. collision avoidance).

- The efficiency in terms of CPU time of the OTM implementation in Matlab® seems reasonable but it could be improved. The efficiency comparison between Matlab® and Compamm implementations showed that Compamm is four times faster than Matlab® for the vehicle accessibility trials. Therefore, if all OTM features and motion reconstruction strategies are fully implemented in Compamm, an improvement in the OTM efficiency is foreseen.

- The progressive weighting strategy for the missing marker problem depends on two parameters that are defined by trial and error. An automatic method for estimating the optimal value for these parameters could be designed.

- Currently, the same value of the weighting factors is used for all the markers independently of their noise level. A weighting scheme based on a double motion reconstruction could be suggested. First, a motion reconstruction with the same weighting factor for all markers would be executed. From this reconstructed motion the distance errors between the measured and model-determined markers could be calculated and weighting factors proportional to these distance errors could be derived. Second, a new motion reconstruction with new values would be performed.

- The reference posture used for the relative preservation posture condition is the same during the whole reconstruction and this may not provide a realistic motion when the range of motion is large. Furthermore, the weighting factors associated to the joint angles of the spine have all the same value during the whole motion. These two issues could be improved: firstly, by using several reference postures which could depend on several parameters; secondly, by using different weighting factors for each joint angle based on biomechanical criteria.

- The estimation of the subject-specific parameters was limited by the measurement equipment available and by the total time required by each method. The quality of the subject-specific parameters could be enhanced by using better measurement equipments like 3D whole body scanners or medical diagnostic technologies. Such techniques require expensive instrumentation, may involve high radiation levels and require large post-processing times. However, their usage for estimating subject-specific parameters could be further investigated.

- A comparative study between state-of-the-art motion reconstruction methods using natural coordinates and relative coordinates is suggested as a topic for further research. A fair comparison should include human skeletal models with open- and closed-loops and different levels of measurement errors.

APPENDIX A

KINEMATIC PROBLEMS EXAMPLES

A.1 EXACTLY-GUIDED KINEMATIC PROBLEM WITH ONE REDUNDANT CONSTRAINT

The goal of this example is to show the difficulties that can be encountered in an exactly-guided kinematic problem with redundant constraints when the Newton-Raphson method is used to solve it. A simple 2D pendulum of length L is analysed in this example (Figure A.1). The pendulum is defined by two points A and B. Point A is fixed and the pendulum turns around it. The system has one DoF and three dependent coordinates (B_x, B_y and α).

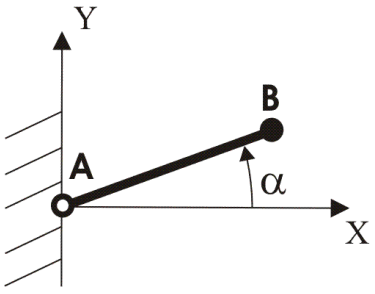

Figure A.1: Simple pendulum with one relative angle.

Therefore, there must be two kinematic constraints, which define the multibody system:

- One rigid body constraint, which imposes a constant length between points A and B

$$B_x{}^2 + B_y{}^2 - L^2 = 0 \tag{A.1}$$

- One relative coordinate constraint corresponding to angle α

$$B_x - L\cos\alpha = 0 \tag{A.2}$$

Note that there are two possible angle constraints, one using $\sin\alpha$ and another using $\cos\alpha$. When α is close to 0º or 180º, the constraint (A.2) is not valid and when α is close to +90º or -90º the constraint (A.3) is not valid (see section 2.1.3 in García de Jalón and Bayo (1994) for details).

$$B_y - L\sin\alpha = 0 \tag{A.3}$$

If the motion of the multibody is prescribed with one driving constraint, the kinematic problem is exactly-guided according to the definition in section 4.2.1. If the coordinate B_x is chosen as the driven coordinate and $g(t)$ is a given function of time, the driving constraint can be formulated as follows:

$$B_x - g(t) = 0 \tag{A.4}$$

There are two options: switching between constraints (A.2) and (A.3) depending on the value of α, or including always both equations and leaving the equation solver the responsibility of disregarding the less appropriate equation at each position. If both relative angle constraints are included due to convenience of implementation, the vector of kinematic constraints is:

$$\mathbf{\Phi(q)} = \begin{bmatrix} B_x - L\cos\alpha \\ B_y - L\sin\alpha \\ B_x{}^2 + B_y{}^2 - L^2 \end{bmatrix} = 0 \tag{A.5}$$

where $\mathbf{q}$ is the column vector of dependent coordinates

$$\mathbf{q} = \begin{bmatrix} B_x \\ B_y \\ \alpha \end{bmatrix} \tag{A.6}$$

The vector of driving constraints is

$$\Psi(\mathbf{q}) = [B_x - g(t)] = 0 \tag{A.7}$$

This exactly-guided kinematic problem can be solved using the Newton-Raphson method (see section 4.2.2.1). The linear approximation of the constraint equations is

$$\begin{bmatrix} \Phi_{\mathbf{q}} \\ \Psi_{\mathbf{q}} \end{bmatrix} \Delta\mathbf{q} = -\begin{bmatrix} \Phi \\ \Psi \end{bmatrix} \tag{A.8}$$

where the Jacobian matrix of the constraints is

$$\begin{bmatrix} \Phi_{\mathbf{q}} \\ \Psi_{\mathbf{q}} \end{bmatrix} = \begin{bmatrix} 1 & 0 & L\sin\alpha \\ 0 & 1 & -L\cos\alpha \\ 2B_x & 2B_y & 0 \\ 1 & 0 & 0 \end{bmatrix} \tag{A.9}$$

Applying Gaussian elimination to the linear system of equations (A.8)

$$\begin{bmatrix} 1 & 0 & L\sin\alpha \\ 0 & 1 & -L\cos\alpha \\ 0 & 0 & -2B_xL\sin\alpha + 2B_yL\cos\alpha \\ 0 & 0 & 0 \end{bmatrix} \cdot \begin{bmatrix} \Delta B_x \\ \Delta B_y \\ \Delta\alpha \end{bmatrix} = \begin{bmatrix} \Phi(1) \\ \Phi(2) \\ \Phi(3) - 2B_x\Phi(1) - 2B_y\Phi(2) \\ \Psi(1) - \Phi(1) + \dfrac{\sin\alpha}{2(B_y\cos\alpha - B_x\sin\alpha)}\left(\Phi(3) - 2B_x\Phi(1) - 2B_y\Phi(2)\right) \end{bmatrix} \tag{A.10}$$

It can be seen that the fourth term of the right hand side vector (vector of inhomogeneous terms) is zero when all the constraints are satisfied. But in general, it is different from zero and the linear system of equations is incompatible. Hence, the Newton-Raphson method fails to solve this exactly-guided kinematic problem when redundant constraints are used.

A.2 OVER-GUIDED KINEMATIC PROBLEM WITH ONE REDUNDANT CONSTRAINT

The purpose of this example is to illustrate the difficulties that can be found in the first-order Taylor approximation of the kinematic constraints in the QP subproblem (4.25) when there are redundant constraints in an over-guided kinematic problem (see section 4.5.2).

The simple pendulum of the previous example is used. The three kinematic constraints (A.5) are used to describe this multibody system, where one of them is redundant. If the motion of the multibody is prescribed with two driving constraints, the kinematic problem is over-guided (there is only one DoF) according to the definition in section 4.2.1. In the previous example the coordinate Bx is the only driven coordinate. If B_y is also chosen as a driven coordinate, and $h(t)$ is a given function of time, a new driving constraint can be added

$$B_y - h(t) = 0 \tag{A.11}$$

Then, the vector of driving constraints is

$$\Psi(\mathbf{q}) = \begin{bmatrix} B_x - g(t) \\ B_y - h(t) \end{bmatrix} = 0 \tag{A.12}$$

This problem can be formulated as the NLP problem (4.17). The equality constraints are (A.5) and the objective function originates from the squared sum of the driving constraints (A.4) and (A.11). This problem can be solved with the method presented in section 4.5.1. Consider the QP subproblem (4.25) for a given instant of time. In this example the linear approximation of the nonlinear constraints (A.5) is

$$\Phi_{\mathbf{q}} \Delta\mathbf{q} = -\Phi \tag{A.13}$$

Applying Gaussian elimination to the linear system of equations (A.13)

$$\begin{bmatrix} 1 & 0 & L\sin\alpha \\ 0 & 1 & -L\cos\alpha \\ 0 & 0 & -2B_x L\sin\alpha + 2B_y L\cos\alpha \end{bmatrix} \cdot \begin{bmatrix} \Delta B_x \\ \Delta B_y \\ \Delta\alpha \end{bmatrix} = \\ = -\begin{bmatrix} B_x - L\cos\alpha \\ B_y - L\sin\alpha \\ 2L(B_x\cos\alpha + B_y\sin\alpha) - (B_x^2 + B_y^2 + L^2) \end{bmatrix} \tag{A.14}$$

From the analysis of (A.14), the potential problems with the linearised constraints in the QP subproblem can be identified. Three possible situations can arise:

- If all the constraints are satisfied (Figure A.2), the linear system of equations (A.14) becomes

$$\begin{bmatrix} 1 & 0 & L\sin\alpha \\ 0 & 1 & -L\cos\alpha \\ 0 & 0 & 0 \end{bmatrix} \begin{bmatrix} \Delta B_x \\ \Delta B_y \\ \Delta\alpha \end{bmatrix} = \begin{bmatrix} 0 \\ 0 \\ 0 \end{bmatrix} \tag{A.15}$$

There are two linearly independent constraints, i.e. the rank of $\Phi_{\mathbf{q}}$ is two. There is one free variable and the QP subproblem (4.25) can be solved.

- If the constraints are not satisfied (Figure A.3), the terms $\Phi_{\mathbf{q}}(3,3)$ and $\Phi(3)$ are distinct from zero and there are three linearly independent constraints, i.e. the rank of $\Phi_{\mathbf{q}}$ is three. The linear system of equations (A.14) is compatible determined. Therefore, the feasible region of the QP subproblem (4.25) is a single point, which is obtained from the solution of the compatible determined linear system of equations (A.14).

- If the constraints are not satisfied (Figure A.4), but the following condition is fulfilled

$$\frac{B_y}{B_x} = \tan\alpha \tag{A.16}$$

then, the term $\Phi_{\mathbf{q}}(3,3)$ is zero and $\Phi(3)$ is distinct from zero. This means that the linear system of equations (A.14) is incompatible. The QP subproblem (4.25) does not have a solution because a feasible region does not exist.

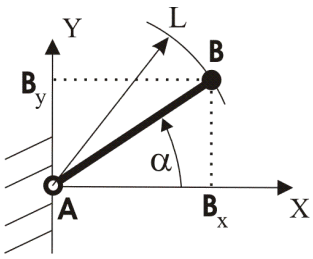

Figure A.2: **q** when all the constraints are satisfied.

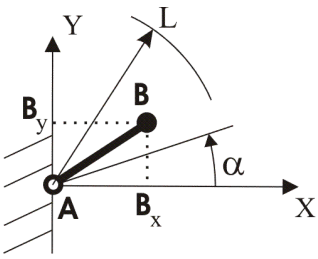

Figure A.3: **q** when the constraints are not satisfied.

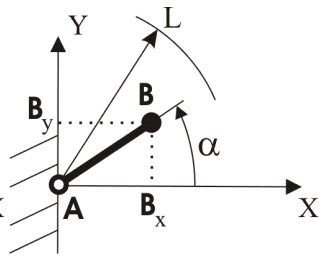

Figure A.4: **q** when condition (A.16) is fulfilled.

A.3 OVER-GUIDED KINEMATIC PROBLEM WITH TWO REDUNDANT CONSTRAINTS

From the previous example it can be thought that the linearised constraint equations may become incompatible only rarely. In the example presented in this section (Figure A.5), it is shown that this is not so. If the number of redundant constraints is greater than the number of DoFs of the multibody system, then the linearised constraint equations are incompatible for any column vector **q** that does not satisfy the kinematic constraints.

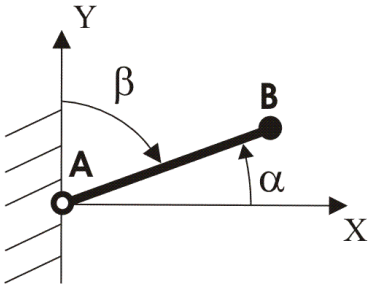

Figure A.5: Simple pendulum with two relative angles.

This example is similar to the previous one but for the introduction of two redundant constraints. An additional relative angle coordinate β is considered and one new redundant constraints originating from this relative angle is included in $\Phi(\mathbf{q})$

$$\Phi(\mathbf{q}) = \begin{bmatrix} B_x - L\sin\beta \\ B_y - L\cos\beta \\ B_x - L\cos\alpha \\ B_y - L\sin\alpha \\ {B_x}^2 + {B_y}^2 - L^2 \end{bmatrix} = 0 \tag{A.17}$$

The simple pendulum has one DoF and there are two redundant constraints in (A.17). The new relative angle β must be added to the column vector **q** of dependent coordinates:

$$\mathbf{q} = \begin{bmatrix} B_x \\ B_y \\ \alpha \\ \beta \end{bmatrix} \tag{A.18}$$

As in the previous example, the linear approximation of the constraint equations is given by equation (A.13). The Jacobian matrix $\Phi_{\mathbf{q}}$ of the constraints is now:

$$\Phi_{\mathbf{q}}(\mathbf{q}) = \begin{bmatrix} 1 & 0 & 0 & -L\cos\beta \\ 0 & 1 & 0 & L\sin\beta \\ 1 & 0 & L\sin\alpha & 0 \\ 0 & 1 & -L\cos\alpha & 0 \\ 2B_x & 2B_y & 0 & 0 \end{bmatrix} \tag{A.19}$$

The linear system of equations (A.13) for this example is overconstrained because there are five linear constraint equations and only four variables. $\Phi_{\mathbf{q}}$ is a 5 × 4 matrix and therefore its maximum row rank is four. This example is more difficult to analyse analytically and some of its characteristics are shown using three numerical examples:

- Consider the following vector of dependent coordinates

$$\mathbf{q} = \begin{bmatrix} \sqrt{2}L/2 \\ \sqrt{2}L/2 \\ 45\dfrac{\pi}{180} \\ 45\dfrac{\pi}{180} \end{bmatrix} \tag{A.20}$$

Substituting this vector $\mathbf{q}$ in the linear system of equations (A.13) and applying Gaussian elimination gives

$$\begin{bmatrix} 1 & 0 & 0 & -\sqrt{2}L/2 \\ 0 & 1 & 0 & \sqrt{2}L/2 \\ 0 & 0 & 1 & 1 \\ 0 & 0 & 0 & 0 \\ 0 & 0 & 0 & 0 \end{bmatrix} \cdot \begin{bmatrix} \Delta B_x \\ \Delta B_y \\ \Delta\alpha \\ \Delta\beta \end{bmatrix} = \begin{bmatrix} 0 \\ 0 \\ 0 \\ 0 \\ 0 \end{bmatrix} \tag{A.21}$$

This value of vector $\mathbf{q}$ satisfies all the constraints. There are tree linearly independent constraints, i.e. the rank of $\Phi_{\mathbf{q}}$ is three and therefore the linear system of equations (A.21) is underdetermined. Then, the QP subproblem (4.25) can be solved because there is one free variable.

- Consider now the following value of the vector of dependent coordinates

$$\mathbf{q} = \begin{bmatrix} \sqrt{2}L/4 \\ \sqrt{2}L/4 \\ 45\dfrac{\pi}{180} \\ 45\dfrac{\pi}{180} \end{bmatrix} \tag{A.22}$$

Substituting this vector **q** in equation (A.13) and applying Gaussian elimination gives

$$\begin{bmatrix} 1 & 0 & 0 & -\sqrt{2}L/2 \\ 0 & 1 & 0 & \sqrt{2}L/2 \\ 0 & 0 & 1 & 1 \\ 0 & 0 & 0 & 0 \\ 0 & 0 & 0 & 0 \end{bmatrix} \cdot \begin{bmatrix} \Delta B_x \\ \Delta B_y \\ \Delta\alpha \\ \Delta\beta \end{bmatrix} = \begin{bmatrix} -\sqrt{2}L/4 \\ -\sqrt{2}L/4 \\ 0 \\ -L^2/4 \\ 0 \end{bmatrix} \tag{A.23}$$

This value of vector **q** does not satisfy all the constraints. The rank of $\Phi_{\mathbf{q}}$ is three and the term $\Phi(4)$ is distinct from zero. Therefore, the linear system of equations (A.23) is incompatible. Then, the QP subproblem (4.25) does not have a feasible region.

- Finally, consider the following value of the vector of dependent coordinates

$$\mathbf{q} = \begin{bmatrix} L \\ L \\ 45\dfrac{\pi}{180} \\ 30\dfrac{\pi}{180} \end{bmatrix} \tag{A.24}$$

Substituting this column vector **q** in the linear system of equations (A.13) and applying Gaussian elimination gives

$$\begin{bmatrix} 1 & 0 & 0 & -\sqrt{3}L/2 \\ 0 & 1 & 0 & L/2 \\ 0 & 0 & 1 & \sqrt{3}/\sqrt{2} \\ 0 & 0 & 0 & 1 \\ 0 & 0 & 0 & 0 \end{bmatrix} \cdot \begin{bmatrix} \Delta B_x \\ \Delta B_y \\ \Delta\alpha \\ \Delta\beta \end{bmatrix} = \begin{bmatrix} L/2 \\ L-\sqrt{3}L/2 \\ \left(1-\sqrt{2}\right)/\sqrt{2} \\ \left(\sqrt{3}+1-2\sqrt{2}\right)/\left(\sqrt{3}-1\right) \\ \left(2\sqrt{2}-3\right)L^2 \end{bmatrix} \tag{A.25}$$

This value of vector **q** does not satisfy any of the constraints. The rank of $\Phi_{\mathbf{q}}$ is four and the term $\Phi(5)$ is distinct from zero, therefore the linear system of equations (A.25) is incompatible. Then, the QP subproblem (4.25) does not have a feasible region.

APPENDIX B

ANTHROPOMETRIC PARAMETERS

B.1 ANATOMICAL LANDMARKS DESCRIPTION

The three human skeletal models of the MoDyCo project presented in Chapter 3 are based on the use of anatomical landmarks (Figure B.1) for estimating joint parameters and BSPs, and for defining the local coordinate system (LCS) of each body segment. The following table describes each anatomical landmark.

Number	Landmark	Description
L1	C7	7th Cervical vertebra. Processus spinosus of 7th cervical vertebra.
L2	T8	8th Thoracic vertebra. Processus spinosus of 8th thoracic vertebra.
L3	IJ	Incisura Jugularis. Deepest point of incisura jugularis (suprasternal notch).
L4	PX	Processus Xiphoideus. Most caudal point on sternum.
L6/L5	RSC/LSC	Right and Left Sternoclavicular joint.
L20/L7	RAC/LAC	Right and Left Acromioclavicular joint. The most dorsal point of the acromioclavicular joint.
L21/L8	RTS/LTS	Right and Left Trigonum Spinae scapulae. Mid point of triangular surface on medial border of the scapula in line with the scapula spine.
L22 L9	RAI/LAI	Right and Left Angulus Inferior. Most caudal point of scapula.
L23 L10	RAA/LAA	Right and Left Angulus Acromialis or acromion. Most latero-dorsal point of scapula.
L24/L11	RPC/LPC	Right and Left Processus Coracoideus. Most ventral point of processus coracoideus.

Number	Landmark	Description
L25*/L12*	RGHJC/LGHJC	Right and Left Glenohumeral Joint Centre.
L26/L13	RLEH/LLEH	Right and Left Lateral Epicondyle of Humerus. Most caudal point on lateral epicondyle of the humerus.
L27/L14	RMEH/LMEH	Right and Left Medial Epicondyle of Humerus. Most caudal point on the medial epicondyle of the humerus.
L28*/L15*	REJC/LEJC	Right and Left Elbow Joint Centre.
L29/L16	RRS/LRS	Right and Left Radial Styloid. Most caudo-dorsal point on radial styloid.
L30/L17	RUS/LUS	Right and Left Ulnar Styloid. Most caudo-lateral point on ulnar styloid.
L31*/L18*	RWJC/LWJC	Right and Left Wrist Joint Centre.
L32/L19	RDAC3/LDAC3	Right and Left 3rd Dactylion. The tip of the 3rd digit of the hand.
L34/L33	RPSIS/LPSIS	Right and Left Posterior Superior Iliac Spine.
L36/L35	RASIS/LASIS	Right and Left Anterior Superior Iliac Spine.
L37	PS	Pubic Symphysis.
L38*	RHJC	Right Hip Joint Centre.
L39	RLEF	Right Lateral Epicondyle of the Femur
L40	RMEF	Right Medial Epicondyle of the Femur
L41*	RKJC	Right and Left Knee Joint Centre.
L42	RLC	Right Lateral Condyle of tibia. The most lateral point on the border of the lateral tibial condyle.
L43	RMC	Right Medial condyle of tibia. The most medial point on the border of the medial tibial condyle
L44	RLM	Right Lateral malleolus. Tip of the lateral malleolus
L45	RMM	Right Medial malleolus. Tip of the medial malleolus
L46*	RAJC	Right and Left Ankle Joint Centre.
L47	RHEEL	Right Pterion or pternion. Posterior point of the heel.
L48	RTTIP	Right Acropodion. The tip of the second metatarsal.
L49	OMPH	Omphalion or navel.
L50	LV3	3rd Lumbar Vertebra. Processus spinosus of 3rd Lumbar Vertebra.
L51	VERT	Vertex. The most cranial point of the head, when the head is oriented in the Frankfort or Anatomical plane.

Table B.1: Acronym and description of anatomical landmarks used in the three human skeletal models of the MoDyCo project. * Joint rotation centres estimated from anatomical landmarks. They cannot be found by palpation.

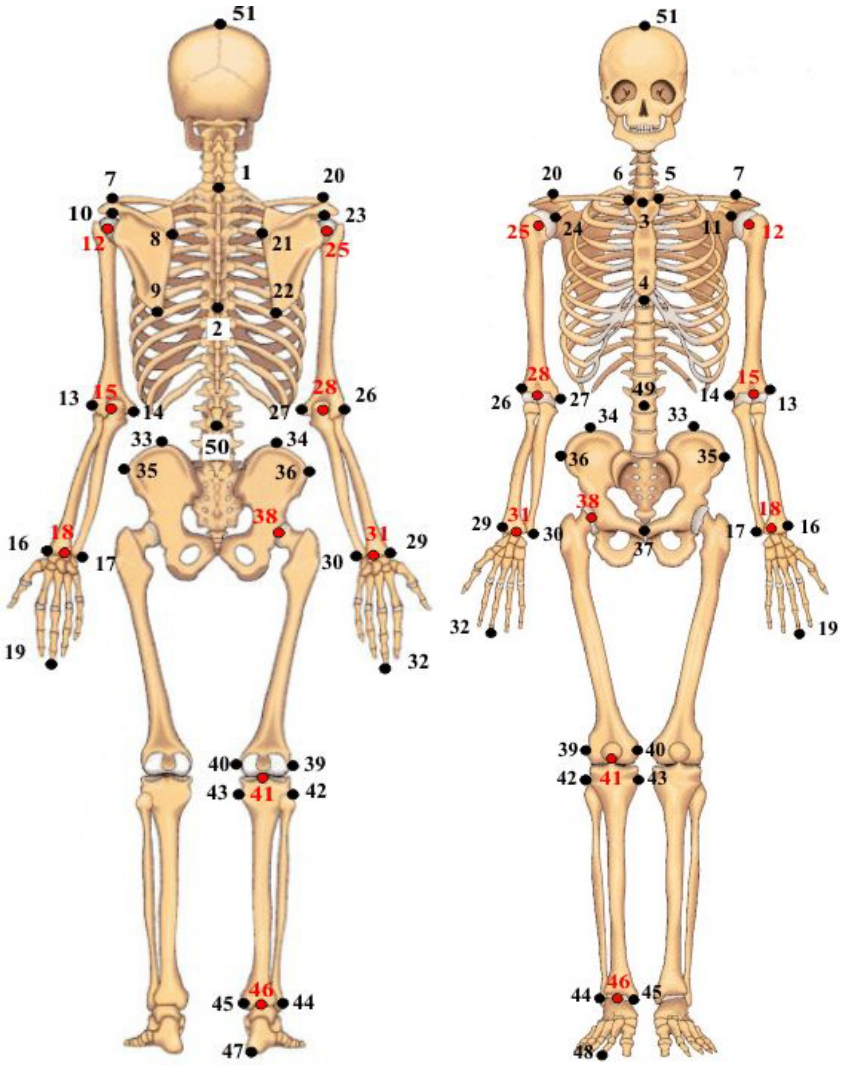

Figure B.1: Anatomical landmarks of the MoDyCo project (black dots) and joint centres estimated from anatomical landmarks (red dots).

B.2 JOINT PARAMETERS

Joint parameter methods for the MoDyCo project have been selected in Chapter 3. In this section, the methods for estimating the joint parameters of the glenohumeral joint, elbow joint, thorax-pelvis joint and hip joint are described in detail.

B.2.1 GLENOHUMERAL JOINT CENTRE: MESKERS ET AL. (1998)

Meskers et al. (1998) developed a linear regression method (Table B.4) for estimating the glenohumeral joint centre *in vivo*. Five scapula anatomical landmarks, which are defined in Table B.2, were used to estimate the joint centre coordinates in the scapula LCS (Table B.3). Thirty-six defleshed scapulae were used in their study. The glenohumeral joint centre prediction from scapula geometry parameters by linear regression resulted in a RMSE between measured and predicted glenohumeral joint centre of 2.32 mm for the x-coordinate, 2.69 mm for the y-coordinate and 3.04 mm for the z-coordinate.

Acronym	Definition
AC	The most dorsal point of the acromioclavicular joint.
TS	Trigonum spinae. At the medial scapular border in line with the spina scapulae.
AI	Angulus inferior. The most caudal point of the scapula.
AA	Angulus Acromialis. At the dorsolateral curvature of the scapular spine.
PC	The most ventral point of the processus coracoideus

Table B.2: Anatomical landmark definitions used by Meskers et al. (1998).

Element	Definition
Origin	AC.
X-axis	$AC - TS / \|AC - TS\|$
Z-axis	Perpendicular to the plane through AC, TS and AI, pointing backwards.
Y-axis	Perpendicular to X and Z pointing upwards.

Table B.3: Definition of scapula LCS used by Meskers et al. (1998).

X-Coordinate		Y-Coordinate		Z-Coordinate	
Regressor	Coefficient	Regressor	Coefficient	Regressor	Coefficient
Offset	18.9743	Offset	-3.8791	Offset	9.2629
PC_X	0.2434	L_{AC-AA}	-0.3940	PC_Z	1.0255
AI_X	0.2341	PC_Y	0.1732	PC_Y	-0.2403
L_{AI-AA}	0.1590	AI_X	0.1205	L_{TS-PC}	0.1720
PC_Y	0.0558	L_{AC-PC}	-0.1002		
SD fitting error (first data set, n=18)			2.81 mm (x)	3.39 mm (y)	3.45 mm (z)
SD validation error (second data set, n=18)			2.32 mm (x)	2.68 mm (y)	3.04 mm (z)

Table B.4: Regression linear equations and their *in vitro* fitting and validation error.

B.2.2 ELBOW JOINT CENTRE AND AXES: STOKDIJK ET AL. (1999)

Stokdijk et al. (1999) proposed a method to determine the position and orientation of the mean optimal flexion-extension axis of the elbow *in vivo*. Ten healthy subjects participated in the study. The mean dispersion, calculated as the standard deviation of all positions and directions of the instantaneous

helical axes, was 2.37, 1.36 and 1.19 cm for the position and 1.43, 4.87 and 4.41° for the orientation in the LCS of the humerus (Table B.5). The position and orientation of the mean optimal flexion-extension axis was considerably deviated from the line through MEH and LEH.

Element	Definition
Origin	GHJC estimated according to Meskers et al. (1998).
Y-axis	$\left[{}^{G}GHJC-\left({}^{G}MEH+{}^{G}LEH\right)/2\right] \Big/ \left\|{}^{G}GHJC-\left({}^{G}MEH+{}^{G}LEH\right)/2\right\|$
Z-axis	Perpendicular to Y-axis and line $({}^{G}LEH-{}^{G}MEH)$. Pointing backwards
X-axis	Perpendicular to Y-axis and Z-axis.

Table B.5: Definition of humerus LCS used by Stokdijk et al. (1999).

Subj.	S_{optx}	S_{opty}	S_{optz}	e (cm)
1	−1.70	0.83	−1.72	1.14
2	−2.66	1.01	−0.85	1.08
3	−4.50	1.02	−2.68	1.26
4	−1.75	0.10	−1.56	0.66
5	0.38	1.04	−1.61	1.26
6	−1.07	−0.67	−0.90	1.42
7	−2.05	1.54	−2.87	0.72
8	−0.35	0.61	−2.55	2.04
9	−1.36	1.23	−1.47	0.76
10	−0.80	1.40	−2.36	1.21
Mean *(sd)*	−1.59 *(1.34)*	0.81 *(0.66)*	−1.86 *(0.72)*	1.15 *(0.40)*
GH *(sd)*	−3.54 *(0.40)*	28.19 *(1.83)*	0.00 *(0.00)*	
EL *(sd)*	0.00 *(0.00)*	0.00 *(0.00)*	0.00 *(0.00)*	
EM *(sd)*	−7.07 *(0.81)*	−0.54 *(0.63)*	0.00 *(0.00)*	
PU 90° *(sd)*	1.67 *(6.22)*	−0.28 *(0.28)*	−25.96 *(2.39)*	

Table B.6: Position vector of the optimal pivot point (S_{optx}, S_{opty}, S_{optz}) of the flexion-extension axis referred to the humerus LCS with its origin shifted to the lateral epicondyle of the humerus (LEH). GH: glenohumeral joint centre (GHJC); EL: lateral epicondyle of the humerus (LEH); EM: medial epicondyle of the humerus (MEH); PU: Ulnar Styloid (US); e: estimated error.

The positions and orientations of the mean optimal flexion-extension axes and their estimation errors for the 10 subjects that participated in the study are presented in Table B.6 and Table B.7. The angles between the mean flexion-extension axis and the respective humeral axes are 15.3, 82.3 and 77.7°. The low inter-subject variability means that by healthy people, the flexion-extension axis of the elbow does not show a great dispersion.

Subj.	N_{optx}	N_{opty}	N_{optz}	e (deg)
1	0.9029	0.1498	0.4084	3.79
2	0.9820	0.1580	0.1368	4.06
3	0.9911	0.1101	0.1224	4.18
4	0.9558	0.1915	0.2331	4.03
5	0.9035	0.1189	0.4228	4.24
6	0.9795	0.1572	0.1480	4.15
7	0.9840	0.1471	0.1510	4.91
8	0.9949	0.0905	0.0818	3.14
9	0.9632	0.1074	0.2551	3.28
10	0.9888	0.1075	0.1651	5.41
Mean *(sd)*	0.9646 *(0.0345)*	0.1338 *(0.0315)*	0.2124 *(0.1183)*	4.12 *(0.67)*

Table B.7: Optimal flexion-extension elbow axis (N_{optx}, N_{opty}, N_{optz}) referred to humerus LCS with its origin shifted to LEH; e: estimated error.

B.2.3 THORAX-PELVIS JOINT: SNYDER ET AL. (1972)

The thorax-pelvis joint is a fictitious joint between the thorax and pelvis and is modelled as a spherical joint. The joint centre is assumed to lie between the 2nd and 3rd lumbar vertebra following the approach of Anderson and Pandy (1999) and it is estimated according to Snyder et al. (1972).

Snyder et al. (1972) presented a prediction method for estimating the location of seven joint centres (between two successive vertebrae) of the spine. The location of the joints was referred to the most superior dorsal palpable points on the spinous process of each vertebra (Table B.8). The data of Snyder et al. (1972) are reproduced from Chaffin et al. (1999, p. 68).

Joint to Body Surface Point	Distance Mean (cm)	Vector mean angle from 12:00 (vertical) with + clockwise[a]
L5/S1 disc to L5 spine surface point	9.04	-84°
L2/L3 disc to L2 spine surface point	8.79	-92°
T12/L2 disc to T12 spine surface point	7.77	-102°
T8/T9 disc to T8 spine surface point	8.03	-104°
C7/T1 disc to C7 spine surface point	7.47	-65°
C5/C6 disc to C5 spine surface point	7.59	-77°
C2/C3 disc to C2 spine surface point	8.03	-90°

Table B.8: Location of spine joints referred to most superior dorsal palpable points on the spinous process of each vertebra. From Chaffin et al. (1999, p. 68). [a]Angles were measured with subjects in erect seated postures.

B.2.4 HIP JOIN CENTRE: SEIDEL ET AL. (1995)

Seidel et al. (1995) presented a regression method for estimating HJC location from anatomical landmarks based on direct measurements performed on

defleshed pelves of sixty five cadavers (35 female and 30 male; 75.1 yr SD 12.6). HJC location as a function of anatomical landmarks was similar for both genders. The pelvis LCS is defined in Table B.9.

Element	Definition
Frontal plane	Plane passing through both ASISs and the pubic symphysis.
Origin	At the respective ASIS side being measured.
X-axis	Anteroposterior (positive posterior)
Y-axis	Mediolateral (positive medial-defined by ASISs).
Z-axis	Superior-inferior (positive inferior)

Table B.9: Definition of the pelvis LCS used by Seidel et al. (1995).

Pelvic width is defined as the distance between the left and right ASIS, pelvic depth is the distance between the ASISs and PSISs midpoints and pelvic height is the perpendicular distance from the pubic symphysis to a line passing through the left and right ASIS. HJC location in pelvis LCS is 14% of pelvic width along the medio-lateral axis (SD 3%, r=0.85, mean error 0.58 cm), 34% of pelvic depth along the anteroposterior axis (SD 2%, r=0.54, mean error 0.30 cm) and 79% of pelvic height along the superior-inferior axis (SD 5%, r=0.81, mean error 0.35 cm).

B.3 BODY SEGMENT PARAMETERS

Methods for estimating BSPs must be applied to subjects with the same anthropometric features as the subjects database used to generate the BSPs methods. For this reason, two different methods are used:

- Zatsiorsky's proportion method (Zatsiorsky et al., 1990a) adjusted by De Leva (1996a) to additional anatomical landmarks and joint centres is used for subjects with features similar to the database.
- Zatsiorsky's linear regression method based on total body height and weight (Zatsiorsky and Seluyanov, 1983) is used for subjects outside the database range.

B.3.1 ZATSIORSKY'S PROPORTION METHOD

Zatsiorsky's proportion method gives the mass of each body segment as a percentage of the whole body mass and the centre of mass (CoM) location and radii of gyration about the anatomical axes at the CoM as a percentage of the body segment length (Table B.10 and Table B.11). The length of each body segment is defined between two anatomical landmarks and/or joint centres of the body segment (Table B.10 and Table B.12). The CoM location is supposed to lie in the body segment longitudinal axis and it is referred to an anatomical

landmark or a joint centre. The anatomical landmarks or joint centres used as reference to define the CoM location are listed in the column "origin" in Table B.10.

Body Segment	Segment length		Mass (%)		Longitudinal CoM location (%)	
	Origin	Endpoint	F	M	F	M
Head	VERT	C7	6.68	6.94	48.41	50.02
Upper Trunk	IJ	PX	15.45	15.96	50.50	50.66
Middle Trunk	PX	OMPH	14.65	16.33	45.12	45.02
Lower Trunk	OMPH	HJC(1)	12.47	11.17	49.20	61.15
Upper arm	GHJC	EJC	2.55	2.71	57.54	57.72
Forearm	EJC	WJC	1.38	1.62	45.59	45.74
Hand	WJC	DAC3	0.56	0.61	34.27	36.24
Thigh	HJC	KJC	14.74	14.16	36.12	40.95
Shank	KJC	AJC	4.81	4.33	43.52	43.95
Foot	HEEL	TTIP	1.29	1.37	40.14	44.15

Table B.10: Zatsiorsky's proportion parameters adjusted by De Leva (1996a) for females (F) and males (M). Body segment masses are relative to total body mass. Body segment CoM locations are referenced to points listed in the column "Origin" and are relative to body segment length. (1) Body segment length is defined in the longitudinal direction. In the lower trunk this means that the segment length is only the longitudinal component of the distance vector between OMPH and HJC.

Body Segment	Sagittal r (%)		Transverse or frontal r (%)		Longitudinal r (%)	
	F	M	F	M	F	M
Head	27.1	30.3	29.5	31.5	26.1	26.1
Upper Trunk	46.6	50.5	31.4	32.0	44.9	46.5
Middle Trunk	43.3	48.2	35.4	38.3	41.5	46.8
Lower Trunk	43.3	61.5	40.2	55.1	44.4	58.7
Upper arm	27.8	28.5	26.0	26.9	14.8	15.8
Forearm	26.1	27.6	25.7	26.5	9.4	12.1
Hand	24.4	28.8	20.8	23.5	15.4	18.4
Thigh	36.9	32.9	36.4	32.9	16.2	14.9
Shank	26.7	25.1	26.3	24.6	9.2	10.2
Foot	29.9	25.7	27.9	24.5	13.9	12.4

Table B.11: Zatsiorsky's proportion parameters adjusted by De Leva (1996a) for females (F) and males (M). Radii of gyration (r) are relative to body segment length.

In section 3.3, the LCS of each body segment was defined. Zatsiorsky's method provides the radii of gyration of each body segment with regard to the sagittal, longitudinal and frontal (or transverse) axes (Figure B.2). The equivalence between the LCSs defined in this thesis and Zatsiorsky's LCSs is presented in Table B.12.

Body Segment	Segment length		X-axis	Y-axis	Z-axis
	Origin	Endpoint			
Head	VERT (L51)	C7 (L1)	Frontal	Longitudinal	Sagittal
Thorax	IJ (L3)	OMPH (L49)	Frontal	Longitudinal	Sagittal
L. Upper arm	LGHJC(L12)	LEJC (L15)	Frontal	Longitudinal	Sagittal
L. Forearm	LEJC (L15)	LWJC (L18)	Sagittal	Longitudinal	Frontal
L. Hand	LWJC (L18)	LDAC3 (L19)	Frontal	Longitudinal	Sagittal
R. Upper arm	RGHJC (L25)	REJC (L28)	Frontal	Longitudinal	Sagittal
R. Forearm	REJC (L28)	RWJC (L31)	Sagittal	Longitudinal	Frontal
R. Hand	RWJC (L31)	RDAC3 (L32)	Frontal	Longitudinal	Sagittal
Pelvis	OMPH (L49)	RHJC(1) (L38)	Sagittal	Longitudinal	Frontal
R. Thigh	RHJC (L38)	RKJC (L41)	Sagittal	Longitudinal	Frontal
R. Shank	RKJC (L41)	RAJC (L46)	Sagittal	Longitudinal	Frontal
R. Foot	RHEEL (L47)	RTTIP (L48)	Longitu.	Frontal	Sagittal

Table B.12: Definition of body segment lengths and equivalence between Zatsiorsky's LCSs and LCSs used in this project. (1) Body segment length is defined in the longitudinal direction. In the lower trunk this means that the segment length is only the longitudinal component of the distance vector between OMPH and RHJC.

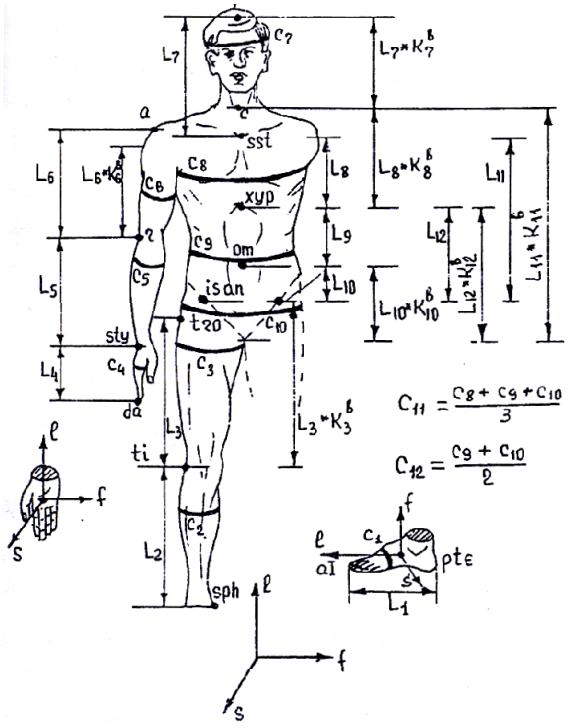

Figure B.2: LCS of each body segment used by Zatsiorsky. Axes are named longitudinal (ℓ), sagittal (s) and transverse or frontal (f).

B.3.2 ZATSIORSKY'S LINEAR REGRESSION METHOD

Zatsiorsky's linear regression method based on total body height and weight gives BSPs as linear regression equations using as predictors in each equation only the total body height and weight of the subject under investigation. The linear regression equations are in the form:

$$y = B_0 + B_1 W + B_2 H$$

where B_0, B_1 and B_2 are the coefficients of the regression equations, W is the total body weight in kg, H is the body height in cm, and y is the predicted BSP. The coefficients of the regression equations for the mass, CoM location and three moments of inertia are given in Table B.13, Table B.14, Table B.15, Table B.16 and Table B.17 respectively. The units of each BSP are indicated in each corresponding table.

Segment	B_0	B_1	B_2	R	SD
Foot	−0.829	0.0077	0.0073	0.702	0.101
Shank	−1.592	0.0362	0.0121	0.872	0.219
Hip	−2.649	0.1463	0.0137	0.891	0.721
Hand	−0.1165	0.0036	0.00175	0.516	0.063
Forearm	0.3185	0.01445	−0.00114	0.786	0.101
Upper arm	0.250	0.03012	−0.0027	0.837	0.178
Head	1.296	0.0171	0.0143	0.591	0.322
Upper part of the torso	8.2144	0.1862	−0.0584	0.798	1.142
Middle part of the torso	7.181	0.2234	−0.0663	0.828	1.238
Lower part of the torso	−7.498	0.0976	0.04896	0.743	1.020

Table B.13: Coefficients for estimating the mass (kg) of each body segment.

Segment	B_0	B_1	B_2	R	SD
Foot	3.767	0.065	0.033	0.530	1.1
Shank	−6.05	−0.039	0.142	0.510	1.25
Hip	−2.42	0.038	0.135	0.600	1.31
Hand	4.11	0.026	0.033	0.383	1.12
Forearm	0.192	−0.028	0.093	0.371	1.14
Upper arm	1.67	0.03	0.054	0.368	1.4
Head	8.357	−0.0025	0.023	0.288	0.69
Upper part of the torso	3.32	0.0076	0.047	0.258	1.19
Middle part of the torso	1.398	0.0058	0.045	0.437	1.18
Lower part of the torso	1.182	0.0018	0.0434	0.320	1.0

Table B.14: Coefficients for estimating the CoM location (cm) along the longitudinal axis. The reference point to locate each CoM is given in Table B.10.

Segment	B_0	B_1	B_2	R	SD
Foot	−100.	0.480	0.626	0.75	6.8
Shank	−1105.	4.59	6.63	0.85	48.6
Hip	−3557.	31.7	18.61	0.84	248.
Hand	−19.5	0.17	0.116	0.50	3.7
Forearm	−64.	0.95	0.34	0.71	10.2
Upper arm	−250.7	1.56	1.512	0.62	27.6
Head	−78.	1.171	1.519	0.40	42.5
Upper part of the torso	81.2	36.73	−5.97	0.73	297.
Middle part of the torso	618.5	39.8	−12.87	0.81	237.
Lower part of the torso	−1568.	12.	7.741	0.69	156.

Table B.15: Coefficients for estimating the MoI about the anteroposterior axis (kg cm^2).

Segment	B_0	B_1	B_2	R	SD
Foot	−97.09	0.414	0.614	0.77	5.77
Shank	−1152.	4.594	6.815	0.85	49.
Hip	−3690.	32.02	19.24	0.85	244.
Hand	−13.68	0.088	0.092	0.43	2.7
Forearm	−67.9	0.855	0.376	0.71	9.6
Upper arm	−232.	1.525	1.343	0.62	26.6
Head	−112.	1.43	1.73	0.49	40.
Upper part of the torso	367.	18.3	−5.73	0.66	171.
Middle part of the torso	263.	26.7	−8.0	0.78	175.
Lower part of the torso	−934.	11.8	3.44	0.73	117.

Table B.16: Coefficients for estimating the MoI about the transverse axis (kg cm^2).

Segment	B_0	B_1	B_2	R	SD
Foot	−15.48	0.144	0.088	0.55	2.7
Shank	−70.5	1.134	0.3	0.47	22.
Hip	−13.5	11.3	−2.28	0.89	49.
Hand	−6.26	0.0762	0.0347	0.43	1.8
Forearm	5.66	0.306	−0.088	0.66	2.9
Upper arm	−16.9	0.662	0.0435	0.44	12.5
Head	61.6	1.72	0.0814	0.42	35.6
Upper part of the torso	561.	36.03	−9.98	0.81	212.
Middle part of the torso	1501.	43.14	−19.8	0.87	188.
Lower part of the torso	−775.	14.7	1.685	0.78	116.

Table B.17: Coefficients for estimating the MoI about the longitudinal axis (kg cm^2).

APPENDIX C

MODYCO - EXPERIMENTAL MEASUREMENTS

C.1 MARKERS LOCATION

The markers used to measure human motion in MoDyCo project are depicted in Figure C.1 and Figure C.2. A more precise description of the markers location is given in Table C.1.

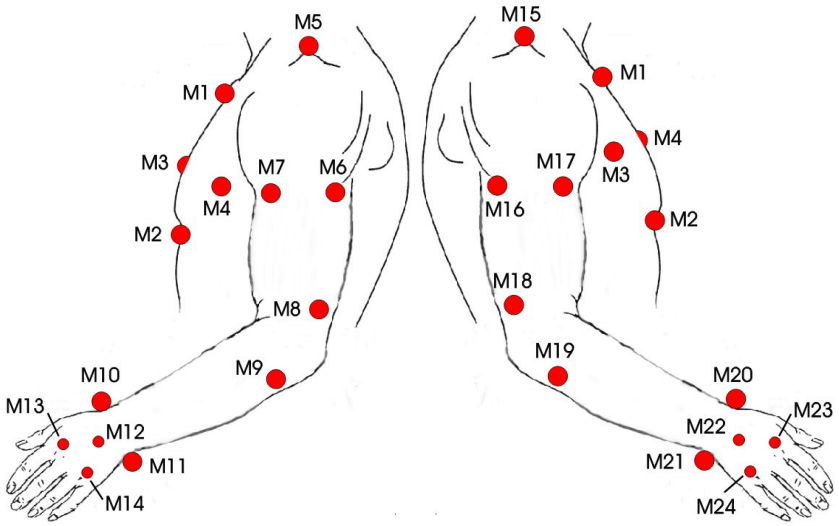

Figure C.1: Markers location for MoDyCo project in left and right arms.

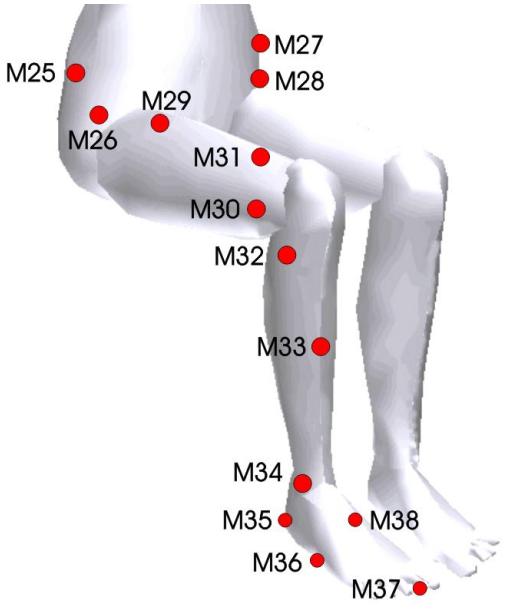

Figure C.2: Markers location for MoDyCo project in pelvis and right leg.

Number	Body segment	Location
M1	Thorax	Near the incisura jugularis (IJ)
M2	Thorax	Below the processus xiphoideus (PX), roughly 2–4 cm
M3	Thorax	Option 1: Above the right thelion and 2 – 3 cm. under a horizontal line passing through the incisura jugularis (IJ) Option 2: Below the right thelion and on the 9th right rib
M4	Thorax	Option 1: Above the left thelion and 2–3 cm under a horizontal line passing through Incisura Jugularis (IJ) Option 2: Below the left thelion and on the 9th left rib
M5	Left Clavicle Left Scapula	On the left acromion, close to the left acromioclavicular joint (LAC)
M6	Left Upper Arm	On the proximal upper arm
M7	Left Upper Arm	On the proximal upper arm
M8	Left Upper Arm	On the distal upper arm
M9	Left Forearm	On the proximal ulna at a palpable point slightly distal to the tip of the olecranon
M10	Left Forearm	Near the left radial styloid (LRS)
M11	Left Forearm	Near the left ulnar styloid (LUS)
M12	Left Hand	Distal 1 - 2 cm. to the left wrist joint centre (LWJC)
M13	Left Hand	Distal end of the II metacarpal bone
M14	Left Hand	Distal end of the IV metacarpal bone
M15	Right Clavicle Right Scapula	On the right acromion, close to the right acromioclavicular joint (RAC)
M16	Right Upper Arm	On the proximal upper arm

Number	Body segment	Location
M17	Right Upper Arm	On the proximal upper arm
M18	Right Upper Arm	On the distal upper arm
M19	Right Forearm	On the proximal ulna at a palpable point slightly distal to the tip of the olecranon
M20	Right Forearm	Near the right radial styloid (RRS)
M21	Right Forearm	Near the right ulnar styloid (RUS)
M22	Right Hand	Distal 1 - 2 cm. to the right wrist joint centre (RWJC)
M23	Right Hand	Distal end of the II metacarpal bone
M24	Right Hand	Distal end of the IV metacarpal bone
M25	Pelvis	On the crest of the ilium, 5 - 7 cm dorsal to the right anterior superior iliac spine (RASIS)
M26	Pelvis	Near the right anterior superior iliac spine (RASIS)
M27	Pelvis	On the crest of the ilium, 5 - 7 cm dorsal to the left anterior superior iliac spine (LASIS)
M28	Pelvis	Near the left anterior superior iliac spine (LASIS)
M29	Right Thigh	On the proximal thigh
M30	Right Thigh	On the distal thigh
M31	Right Thigh	On the distal thigh
M32	Right Shank	Near the head of the right fibula
M33	Right Shank	On the middle of the tibia
M34	Right Shank	Near the right lateral malleolus (RLM)
M35	Right Foot	Close to the heel but on the right lateral side of the right shoe
M36	Right Foot	On the lateral side of the right shoe sole, roughly in the middle of the sole
M37	Right Foot	On the right shoe sole, close to the right acropodion or tip of the second metatarsal (RTTIP)
M38	Right Foot	On the right shoe, roughly over the cuneiform bones

Table C.1: Description of markers locations in the MoDyCo project.

C.2 ANATOMICAL CALIBRATION PROTOCOL

C.2.1 MARKER VISIBILITY ON EACH FRAME

In CAST protocol it is only required that the two pointer-markers and all the markers on the body segment are visible to at least two cameras. In order to estimate joint parameters more markers are required to be visible in some of the calibration frames. The markers that must be visible in each calibration frame are described in Table C.2.

In one calibration frame it is required that the two pointer-markers, all markers of a body segment and all markers of the distal body segment connected to it are visible to at least two cameras. This calibration frame is

called shared calibration frame and the anatomical landmark measured belongs to the proximal body segment. Joint parameters (joint centre position vector and/or joint axis vector) are estimated in LCS of the proximal body segment and then the shared calibration frame is used to estimate the joint parameters in LCS of the distal body segment.

Frame	Landmark	Visible markers	Frame	Landmark	Visible markers
1	L1	M1 M2 M3 M4	22	L26	M16 M17 M18
2	L2	M1 M2 M3 M4	23 S	L27	M16 M17 M18 M19 M20 M21
3	L3	M1 M2 M3 M4	24	L29	M19 M20 M21
4	L4	M1 M2 M3 M4	25 S	L30	M19 M20 M21 M22 M23 M24
5	L5	M1 M2 M3 M4	26	L32	M22 M23 M24
6	L6	M1 M2 M3 M4	27	L33	M25 M26 M27 M28
7 S	L7	M1 M2 M3 M4 M5	28	L34	M25 M26 M27 M28
8	L8	M1 M2 M3 M4 M5	29	L35	M25 M26 M27 M28
9	L9	M1 M2 M3 M4 M5	30	L36	M25 M26 M27 M28
10	L10	M5	31 S	L37	M25 M26 M27 M28 M29 M30 M31
11 S	L11	M5 M6 M7 M8	32	L39	M29 M30 M31
12	L13	M6 M7 M8	33 S	L40	M29 M30 M31 M32 M33 M34
13 S	L14	M6 M7 M8 M9 M10 M11	34	L42	M32 M33 M34
14	L16	M9 M10 M11	35	L43	M32 M33 M34
15 S	L17	M9 M10 M11 M12 M13 M14	36	L44	M32 M33 M34
16	L19	M12 M13 M14	37 S	L45	M32 M33 M34 M35 M36 M37 M38
17 S	L20	M1 M2 M3 M4 M15	38	L47	M35 M36 M37 M38
18	L21	M1 M2 M3 M4 M15	39	L48	M35 M36 M37 M38
19	L22	M1 M2 M3 M4 M15	40	L49	M1 M2 M3 M4 M25 M26 M27 M28
20	L23	M15	41 S	L50	M1 M2 M3 M4 M25 M26 M27 M28
21 S	L24	M15 M16 M17 M18	42 S	L51	M1 M2 M3 M4

Table C.2: Markers visible in each calibration frame. S Shared calibration frame used to estimate joint parameters in distal body segments.

C.2.2 RESTRICTIONS DURING STATIC LANDMARK MEASUREMENTS

In general the relative orientation between body segments is not constrained during CAST. However, some restrictions on the relative orientation between body segments are imposed for the measurement of some anatomical

landmarks due to LCS definitions and the BSPs estimation method of some body segments. The conditions and restrictions required to measure each anatomical landmark is presented in the next table.

Frame	Description of conditions and restrictions
1-6	No restrictions.
7–11	The left scapula is only allowed to translate (it cannot rotate). This is required because the scapula moves under the skin and the single marker over the scapula can only capture its translations. When the landmarks of the scapula are measured the subject is allowed to perform small trunk translations but he cannot move his left arm and left clavicle or rotate the trunk.
12	No restrictions.
13	The long axis of the right upper arm and right forearm must be approximately aligned. The angle between the z-axis of the right forearm and the plane containing the right upper arm landmarks RMEH, RLEH and RGHJC must be close to zero. The right arm must be extended along the trunk with the hand extended and the palm parallel to the sagittal plane (plane of symmetry of the body).
14	No restrictions.
15-16	The long axis of the second metacarpal bone of the hand must be approximately aligned with the long axis of the forearm. Fingers must be extended and next to one another.
17-21	Same restrictions than frames 7-11
22	No restrictions.
23	Same restriction than frame 13
24	No restrictions.
25-26	Same restrictions than frames 15–16
27-36	No restrictions.
37-39	The plantar aspect of the foot must be placed on the floor and the long axis of the tibia/fibula (the line connecting the landmarks IC and IM) must be approximately perpendicular to the floor. The subject must wear shoes and the landmarks RHEEL and RTTIP must be measured with the shoes on. In this way, the relation between the foot anatomy, the shoe and the markers on the shoe can be determined. It must be remembered that the markers of the right foot are placed on the shoe not on the foot.
40	The trunk must be straight (The subject cannot bend his spine)
41	The trunk must be straight (The subject cannot bend his spine).
42	The thorax longitudinal axis and the head longitudinal axis must be aligned.

Table C.3: Conditions and restrictions for each frame during CAST protocol.

APPENDIX D

REALMAN - EXPERIMENTAL MEASUREMENTS

D.1 MARKERS LOCATION

D.1.1 SAFETY BELT HANDLING

Safety belt buckling-unblucking motions were recorded at 50 Hz with the Vicon motion capture system. Thirty-eight markers, mainly placed on the upper limbs, were used to measure the motion. The locations of the markers are described in Table D.1 and Figure D.1.

N	Acronym	Body segment	Description
1	LHED	Head	Right temple
2	RHED	Head	Left temple
3	FHED	Head	Glabella (flat bone between the eyebrows)
4	VRC7	Thorax	Between C7 and T1
-	CLAV1	Wand	On the wand pointing to the suprasternale. Near the subject.
-	CLAV2	Wand	On the wand pointing to the suprasternale. Far from the subject.
-	STR1	Wand	On the wand pointing to the substernale. Near the subject.
-	STR2	Wand	On the wand pointing to the substernale. Far from the subject.
5	CLAV	Thorax	Suprasternale. This is not a real marker. Its position is estimated from markers CLAV1 and CLAV2 which are on a wand of length L_{wand} as follows: $CLAV=CLAV2+L_{wand}\cdot\frac{(CLAV1-CLAV2)}{\|CLAV1-CLAV2\|}$

N	Acronym	Body segment	Description
6	STRN	Thorax	Substernale. This is not a real marker. Its position is estimated from markers STR1 and STR2 which are on a wand of length L_{wand} as follows: $\mathrm{STRN} = \mathrm{STR2} + L_{\mathrm{wand}} \cdot \frac{(\mathrm{STR1}-\mathrm{STR2})}{\lVert \mathrm{STR1}-\mathrm{STR2} \rVert}$
7	LASI	Pelvis	Left anterior superior iliac spine
8	RASI	Pelvis	Right anterior superior iliac spine
-	RTRC	Right thigh	Right trochanter. For dissymmetry and only used by Vicon.
9	LACC	Left clavicle	Left acromion.
10	LUAT	Left upper arm	Left upper arm top
11	LUAE	Left upper arm	Left upper arm exterior
12	LUAI	Left upper arm	Left upper arm interior
13	LELB	Left upper arm	Left elbow
14	LFAE	Left forearm	Left forearm exterior
15	LFAI	Left forearm	Left forearm interior
16	LWRA	Left forearm	Left wrist (thumb side)
17	LWRB	Left forearm	Left wrist (finger side)
18	LHND	Left hand	Left hand
19	LTHI	Left thigh	Left thigh internal
20	LTHE	Left thigh	Left thigh external
21	LKNE	Left thigh	Left knee
22	LANK	Left shank	Left ankle
23	RACC	Right clavicle	Right acromion.
24	RUAE	Right upper arm	Right upper arm exterior
25	RUAI	Right upper arm	Right upper arm interior
26	RELB	Right upper arm	Right elbow
27	RFAE	Right forearm	Right forearm exterior
28	RFAI	Right forearm	Right forearm interior
29	RWRA	Right forearm	Right wrist (thumb side)
30	RWRB	Right forearm	Right wrist (finger side)
31	RHND	Right hand	Right hand
32	RTHI	Right thigh	Right thigh internal
33	RTHE	Right thigh	Right thigh external
34	RKNE	Right thigh	Right knee
35	RANK	Right shank	Right ankle

Table D.1: Description of markers location for safety belt handling experiment.

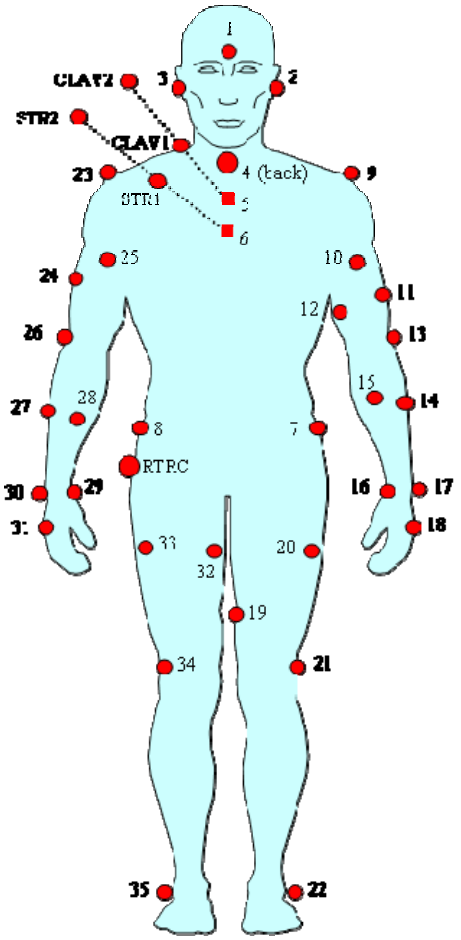

Figure D.1 Markers location for the safety belt handling experiment.

D.1.2 VEHICLE ACCESSIBILITY

Ingress-egress motions were recorded at 50 Hz with the Vicon motion capture system. Forty-nine markers were used to measure the motion. The locations of the markers are described Figure D.2 in and Table D.2. Four additional markers were located on the door of the vehicle mock-up to record its motion.

To avoid the confusion of the right-hand side of the human body with the left-hand side and to facilitate the motion capture data processing of the motions, two supplementary markers were added on the left upper arm and on the left thigh. The three markers located on the spine (47, 48 and 49) are flexible to cause no embarrassment when the subject is seated in the vehicle mock-up.

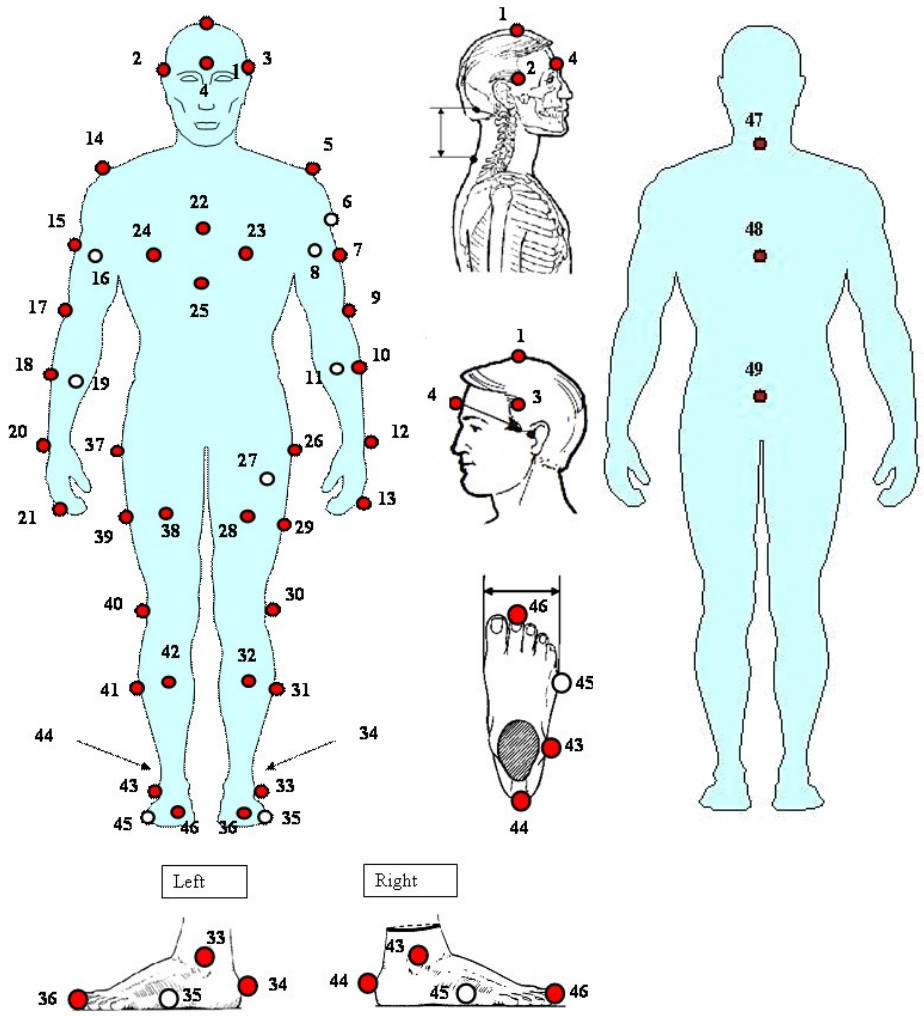

Figure D.2: Markers locations for the vehicle accessibility experiment.

N	Acronym	Body segment	Description
1	TESO	Head	Top of the head
2	TEDR	Head	Right temple
3	TEGA	Head	Left temple
4	FRON	Head	Glabella (flat bone between the eyebrows)
5	EPGA	Left clavicle	Left acromion
6	BRGH	Left upper arm	Left upper arm top
7	BRGA	Left upper arm	Left upper arm
8	BIGA	Left upper arm	Left biceps
9	COGA	Left upper arm	Left lateral humeral epicondyle
10	ABGE	Left forearm	Left forearm exterior

N	Acronym	Body segment	Description
11	ABGA	Left forearm	Left forearm
12	POGA	Left forearm	Left styloid
13	DOGA	Left hand	Left dactylion
14	EPDR	Right clavicle	Right acromion
15	BRDR	Right upper arm	Right upper arm
16	BIDR	Right upper arm	Right biceps
17	CODR	Right upper arm	Right lateral humeral epicondyle
18	ABDE	Right forearm	Right forearm exterior
19	ABDR	Right forearm	Right forearm
20	PODR	Right forearm	Right styloid
21	DODR	Right hand	Right dactylion
22	HAPT	Thorax	Suprasternale
23	PTGA	Thorax	Left thelion
24	PTDR	Thorax	Right thelion
25	STER	Thorax	Substernale
26	TRGA	Left thigh	Left trochanterion
27	CUGH	Left thigh	Left thigh top
28	CUGA	Left thigh	Left thigh
29	CEGA	Left thigh	Left thigh exterior
30	GEGA	Left thigh	Left lateral femoral epicondyle
31	TIGE	Left shank	Left shank exterior
32	TIGA	Left shank	Left shank
33	CHGA	Left shank	Left medial malleolus
34	TAGA	Left foot	Left calcaneous, posterior
35	PEGA	Left foot	Left V metatarsal-phalangeal
36	ORGA	Left foot	Left II digit
37	TRDR	Right thigh	Right trochanterion
38	CUDR	Right thigh	Right thigh
39	CEDR	Right thigh	Right thigh exterior
40	GEDR	Right thigh	Right lateral femoral epicondyle
41	TIDE	Right shank	Right shank exterior
42	TIDR	Right shank	Right shank
43	CHDR	Right shank	Right medial malleolus
44	TADR	Right foot	Right calcaneous, posterior
45	PEDR	Right foot	Right V metatarsal-phalangeal
46	ORDR	Right foot	Right II digit
47	-	Spine	Seventh cervical vertebra. Flexible marker.
48	-	Spine	Sixth thoracic vertebra. Flexible marker.
49	-	Spine	Fifth lumbar vertebra. Flexible marker.

Table D.2: Description of markers location for vehicle accessibility experiment.

D.1.3 DOOR HANDLING

Door handling motions were recorded at 50 Hz with the Vicon motion capture system. Thirty-six markers, mainly placed on the upper limbs, were used to measure the motion. The locations of the markers are described in Figure D.3

and Table D.3. The locations of markers from number 7 to 35 are the same as in the safety belt handling experiment. Only the markers from number 1 to 6 have different locations. Only the description of the markers with different location is included in Table D.3.

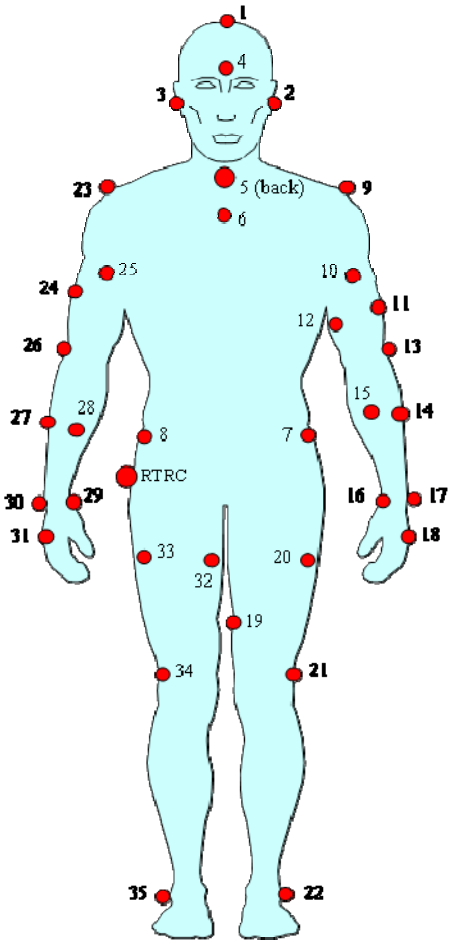

Figure D.3: Markers location for the door handling experiment.

Number	Acronym	Body segment	Description
1	THED	Head	Top of the head
2	LHED	Head	Left Temple
3	RHED	Head	Right Temple
4	FHED	Head	Glabella (flat bone between the eyebrows)
5	VRC7	Thorax	Between C7 and T1
6	CLAV	Thorax	Suprasternale

Table D.3: Description of markers location for door handling experiment

D.1.4 MAXIMAL JOINT ANGLES AND GENERIC ARM REACHING

The motions of this experiment were recorded at 50 Hz with the Vicon motion capture system using ten cameras. Thirty-eight markers and two electromagnetic sensors (Flock of Birds – Ascension Technology Corporation) were used to measure the motion. The locations of the thirty-eight markers and two electromagnetic sensors are described in Figure D.4 and Table D.4. Three markers were placed on the stool and three on the Flock of Birds device. They were used to define the same GCS for every subject.

N	Acronym	Body segment	Description
1	Head_front	Head	Glabella (flat bone between the eyebrows)
2	Head_right	Head	Right temple
3	Head_left	Head	Left temple
4	ac_r	Right clavicle	Right acromion
5	ac_l	Left clavicle	Left acromion
6	sn	Thorax	Suprasternal notch
7	xp	Thorax	Xiphoïd process
8	C7	Spine	Seventh cervical vertebra
9	T4	Spine	Fourth thoracic vertebra
10	T8	Spine	Eighth thoracic vertebra
11	T12	Spine	Twelfth thoracic vertebra
12	L2	Spine	Second lumbar vertebra
13	arm1	Right upper arm	Right upper arm top
14	arm2	Right upper arm	Right upper arm exterior
15	arm3	Right upper arm	Right upper arm interior
16	lhe_r	Right upper arm	Right lateral humeral epicondyle
17	mhe_r	Right upper arm	Right medial humeral epicondyle
18	forearm1	Right forearm	Right forearm top
19	forearm2	Right forearm	Right forearm exterior
20	forearm3	Right forearm	Right forearm interior
21	ls_r	Right forearm	Right lateral styloid process
22	ms_r	Right forearm	Right medial styloid processes
23	smc_r	Right hand	Right dorsal aspect of second metacarpal head
24	vmc_r	Right hand	Right dorsal aspect of fifth metacarpal head
25	lhe_l	Left upper arm	Left lateral humeral epicondyle
26	mhe_l	Left upper arm	Left medial humeral epicondyle
27	ls_l	Left forearm	Left lateral styloid process
28	ms_l	Left forearm	Left medial styloid processes
29	crest_r	Pelvis	Right iliac crest
30	crest_l	Pelvis	Left iliac crest
31	psis_r	Pelvis	Right posterior superior iliac spine
32	psis_l	Pelvis	Left posterior superior iliac spine
33	lfe_r	Right thigh	Right lateral femoral epicondyle
34	mfe_r	Right thigh	Right medial femoral epicondyle
35	lfe_l	Left thigh	Left lateral femoral epicondyle
36	mfe_l	Left thigh	Left medial femoral epicondyle

N	Acronym	Body segment	Description
37	lm_r	Right shank	Right lateral malleolus
38	lm_l	Left shank	Left lateral malleolus
39	index	Right hand	Tip of the right index finger
40	thumb	Right hand	Tip of the right thumb
41	Flock_torso	Thorax	Between the suprasternale and substernale
42	Flock_pelvis	Pelvis	Slightly below the second lumbar vertebra
43	Flock_ori1	-	Marker on the Flock of Birds device used to define a common GCS with Vicon
44	Flock_ori2	-	Marker on the Flock of Birds device used to define a common GCS with Vicon
45	Flock_ori3	-	Marker on the Flock of Birds device used to define a common GCS with Vicon
46	Stool1	Stool	Marker on the stool used to define the GCS
47	Stool2	Stool	Marker on the stool used to define the GCS
48	Stool3	Stool	Marker on the stool used to define the GCS
49	asis_r	Pelvis	Right anterior superior iliac spine
50	asis_l	Pelvis	Left anterior superior iliac spine
51	psis_m	Pelvis	Midpoint between psis_r and psis_l

Table D.4: Description of markers location for maximal joint angles and generic arm reaching experiments. Only markers from 1 to 38 were used in the motion reconstruction

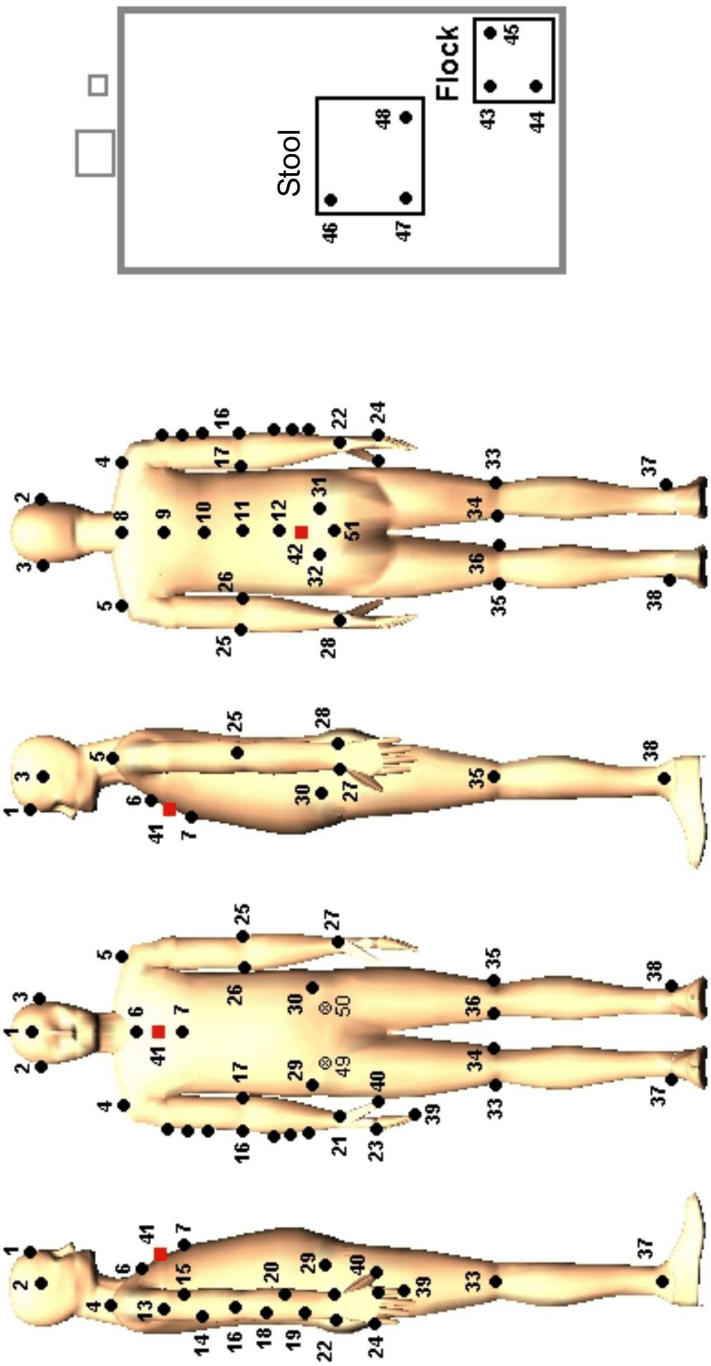

Figure D.4: Markers location for the maximal joint angles and generic arm reaching experiments.

APPENDIX E

PUBLICATIONS

The publications generated so far as a result of the investigations of this thesis are listed below:

Wang, X., Chevalot, N., Monnier, G., Ausejo, S., Suescun, A., Celigüeta, J.T., 2006. Validation of a model-based motion reconstruction method developed in the Realman Project. *SAE 2005 Transactions: Journal of Passenger Cars - Electronic and Electrical Systems*. pp. 873-879. ISBN 0-7680-1693-2.

Ausejo, S., Suescun, A., Celigüeta, J.T., Wang, X., 2006. Robust Human Motion Reconstruction in the Presence of Missing Markers and the Absence of Markers for Some Body Segments. *In Proceedings of the SAE 2006 Digital Human Modeling for Design and Engineering Conference*. July 4-6, Lyon, France.

Wang, X., Chevalot, N., Monnier, G., Ausejo, S., Suescun, A., Celigüeta, J.T., 2005. Validation of a model-based motion reconstruction method developed in the Realman Project. *In Proceedings of the SAE 2005 Digital Human Modeling for Design and Engineering Symposium*. June 14 - 16, Iowa City, Iowa, USA. SAE paper 2005-01-2743

Pérez, M., Ausejo, S., Pargada, J., Suescun, A., Celigüeta J.T., 2003. Application of Multibody System Analysis for the Evaluation of the Driver's Discomfort. *In proceedings of the ECCOMAS Thematic Conference: Multibody Dynamics 2003*. July 1-4, Lisboa, Portugal.

REFERENCES

Ackland, T.R., Blanksby, B.A. and Bloomfield, J., 1988. Inertial Characteristics of Adolescent Male Body Segments. *Journal of Biomechanics* 21, 319-327.

Alexander, E.J. and Andriacchi, T.P., 2001. Correcting for Deformation in Skin-Based Marker Systems. *Journal of Biomechanics* 34, 355-361.

Alvarez, G., Gutierrez, A., Serrano, N., Urban, P. and García de Jalón, J., 1993a. Computer Data Acquisition, Analysis and Visualization of Elite Athletes Motion. *In Proceedings of the Fourth International Symposium on Computer Simulation on Biomechanics*. Paris, France.

Alvarez, G., Serrano, N., Gutierrez, A., Urban, P. and Avello, A., 1993b. Computer Animation of Human Body Motion in Sport, Using Real Captured Data and a "Consistent" Mechanical Model. *In Proceedings of the Second International Symposium on Three-dimensional Analysis of Human Movement*. Parc du Futuroscope, Poitiers, France.

Allard, P., Stokes, I.A.F. and Blanchi, J.P. (Eds.), 1995. *Three-dimensional Analysis of Human Movement*, Human Kinetics.

Anderson, F.C. and Pandy, M.G., 1999. A Dynamic Optimization Solution for Vertical Jumping in Three Dimensions. *Computer Methods in Biomechanics and Biomedical Engineering* 2, 201-231.

Andriacchi, T.P., Alexander, E.J., Toney, M.K., Dyrby, C.O. and Sum, J., 1998. A Point Cluster Method for In Vivo Motion Analysis: Applied to a Study of Knee Kinematics. *Journal of Biomechanical Engineering* 120, 743-749.

Andriacchi, T.P. and Strickland, A.B., 1983. Gait Analysis as a Tool to Assess Joint Kinetics. *In Proceedings of the NATO. Advanced Study Institute Biomechanics of Normal and Pathological Articulating Joints*, pp. 83-103. Lisbon, Portugal.

Apkarian, J., Nauman, S. and Cairns, B., 1989. A three-dimensional kinematic and dynamic model of the lower limb. *Journal of Biomechanics* 22, 143-155.

ARKI Consulting & Development A/S, 2004. CONOPT3. [http://www.conopt.com/].

Baca, A., 1996. Precise Determination of Anthropometric Dimensions by Means of Image Processing Methods for Estimating Human Body Segment Parameter Values. *Journal of Biomechanics* 29(4), 563-567.

Baerlocher, P. and Boulic, R., 2004. An Inverse Kinematic Architecture Enforcing an Arbitrary Number of Strict Priority Levels. *The Visual Computer* 20(6), 402 - 417.

Barker, T.M. and Kirtley, C., 1997. Calculation of Multi-segment Rigid Body Joint Dynamics using MATLAB. *Journal of Engineering in Medicine, Proceedings of the I MECH E Part H* 211, 483-487.

Barnett, N.D., 1996. Measurement and Modelling of Three Dimensional Scapulohumeral Kinematics. Ph.D. Thesis, University of Newcastle upon Tyne, UK.

Bartle, R.G., 1976. *The Elements of Real Analysis.* (2nd ed.), John Wiley & Sons.

Bassett, R.W., Browne, A.O., Morrey, B.F. and An, K.N., 1990. Glenohumeral Muscle Force and Moment Mechanics in a Position of Shoulder Instability. *Journal of Biomechanics* 23, 405-415.

Bell, A.L., Brand, R.A. and Pedersen, D.R., 1989. Prediction of Hip Joint Centre Location from External Landmarks. *Human Movement Science* 8, 3-16.

Bell, A.L., Petersen, D.R. and Brand, R.A., 1990. A Comparison of the Accuracy of Several Hip Centre Location Prediction Methods. *Journal of Biomechanics* 23, 617-621.

Benedetti, M.G., Catani, F., Leardini, A., Pignotti, E. and Gianni, S., 1998. Data Management in Gait Analysis for Clinical Applications. *Clinical Biomechanics* 13(3), 204-215.

Benson, H.Y., Shanno, D.F. and Vanderbei, R.J., 2003. A comparative study of large-scale nonlinear optimization algorithms. In: G. Di Pillo and A. Murli (Eds.), *High Performance Algorithms and Software for Nonlinear Optimization*, pp. 95-128, Kluwer.

Bertsekas, D.P., 1982. *Constrained Optimization and Lagrange Multiplier Method.* Series on Computer Science and Applied Mathematics. New York, Academic Press.

Bertsekas, D.P., 1999. *Nonlinear programming.* (2nd ed.), Athena Scientific.

Biryukova, E.V., Roby-Brami, A., Frolov, A.A. and Mokhtari, M., 2000. Kinematics of Human Arm Reconstructed from Spatial Tracking System Recordings. *Journal of Biomechanics* 33, 985-995.

Bodenheimer, B., Rose, C., Rosenthal, S. and Pella, J., 1997. The Process of Motion Capture: Dealing with the Data. In: D. Thalmann and M. van de Panne (Eds.), *Computer Animation and Simulation '97*. EG Books.

Boggs, P.T. and Tolle, J.W., 1995. Sequential quadratic programming. *Acta Numerica* 4, 1-51.

Bongartz, I., Conn, A.R., Gould, N.I.M. and Toint, P.L., 1995. CUTE: Constrained and Unconstrained Testing Environment. *ACM Transactions on Mathematical Software* 21(1), 123-160.

Bouisset, S. and Pertuzon, E., 1968. Experimental Determination of the Moment of Inertia of Limb Segments. In: J. Wartenweiler, E. Jokl and M. Heggelinck (Eds.), *Biomechanics I*, pp. 106-109. New York, Karger.

Brand, R.A., Crowninshield, R.D., Wittstock, C.E., Pedersen, D.R., Clark, C.R. and van Krieken, F.M., 1982. A Model of Lower Extremety Muscular Anatomy. *Journal of Biomechanical Engineering* 104, 304-310.

Brumbaugh, R.B., Crowninshield, R.D., Blair, W.F. and Andrews, J.G., 1982. An in-vivo study of normal wrist kinematics. *Journal of Biomechanical Engineering* 104, 176-181.

Buchanan, T.S., Moniz, M.J., Dewald, J.P.A. and Rymer, W.Z., 1993. Estimation of Muscle Forces about the Wrist Joint during Isometric Tasks Using an EMG Coefficient Method. *Journal of Biomechanics* 26(4-5), 547-560.

Bush, T.R. and Gutowski, P.E., 2003. An Approach for Hip Joint Center Calculation for Use in Seated Postures. *Journal of Biomechanics* 36(11), 1739-1743.

Buxton, B., Dekker, L., Douros, I. and Vassilev, T., 2000. Reconstruction and Interpretation of 3D Whole Body Surface Images. *In Proceedings of the Scanning 2000*. Paris.

Byrd, R.H., Hribar, M.E. and Nocedal, J., 2000. An interior point algorithm for large scale nonlinear programming. *SIAM Journal on Optimization* 9(4), 877-900.

Cappello, A., Cappozzo, A., La Palombara, P.F., Lucchetti, L. and Leardini, A., 1997. Multiple Anatomical Landmark Calibration for Optimal Bone Pose Estimation. *Human Movement Science* 16, 259-274.

Cappozzo, A., 1984. Gait Analysis Methodology. *Human Movement Science* 3, 27 -54.

Cappozzo, A. and Berme, N., 1990. Subject-specific Segmental Inertia Parameter Determination - a Survey of Current Methods. In: N. Berme and A. Cappozzo (Eds.), *Biomechanics of human movement: applications in Rehabilitation, sports and ergonomics*, pp. 179-185. Worthington, OH, Bertec Corp.

Cappozzo, A., Catani, F., Della Croce, U. and Leardini, A., 1995. Position and Orientation in Space of Bones during Movement: Anatomical Frame Definition and Determination. *Clinical Biomechanics* 10(4), 171-178.

Cappozzo, A., Catani, F., Leardini, A., Benedetti, M.G. and Della Croce, U., 1996. Position and Orientation in Space of Bones during Movement: Experimental Artefacts. *Clinical Biomechanics* 11(2), 90-100.

Caruntu, D.I. and Hefzy, M.S., 2004. 3-D Anatomically Based Dynamic Modeling of the Human Knee to Include Tibio-Femoral and Patello-Femoral Joints. *Journal of Biomechanical Engineering* 126, 44-53.

Cavanagh, P.R. and Gregor, R.J., 1974. The Quick-Release Method for Estimating the Moment of Inertia of the Shank and Foot. In: R.C. Nelson and C.A. Morehouse (Eds.), *Biomechanics IV*. Baltimore, University Park Press.

CEIT, 2001. Compamm HMR user manual. San Sebastian, Spain.

Celigüeta, J.T., 1996. Multibody Simulation of Human Body Motion in Sports. *In Proceedings of the XIV International Symposium on Biomechanics in Sports*, pp. 81-94. Madeira, Portugal, 25-29 June, 1996, Editions FMH.

Clauser, C.E., McConville, J.T. and Young, J.W., 1969. Weight, Volume and Center of Mass Segments of the Human Body. AMRL-TR-69-70. Wright-Patterson Air Force Base, Ohio.

Conn, A.R., Gould, N.I.M. and Toint, P.L., 1992. *LANCELOT, A Fortran Package for Large-Scale Nonlinear Optimization (Release A)*. Series on Computational Mathematics 17. Berling, Springer Verlag.

Conn, A.R., Gould, N.I.M. and Toint, P.L., 1997. Methods for nonlinear constraints in optimization calculations. In: I. Duff and A. Watson (Eds.), *The State of the Art in Numerical Analysis*, pp. 363-390. Oxford, England, Oxford University Press.

Chaffin, D.B., Andersson, G.B.J. and Martin, B.J., 1999. *Occupational Biomechanics*. (3rd ed.), Wiley-Interscience.

Challis, J.H., 1995. A Procedure for Determining Rigid Body Transformation Parameters. *Journal of Biomechanics* 28(6), 733.

Challis, J.H. and Kerwin, D.G., 1996. Quantification of the Uncertainties in Resultant Joint Moments Computed in a Dynamic Activity. *Journal of Sports Sciences* 14, 219-231.

Chandler, R.F., Clauser, C.E., McConville, J.T., Reynolds, H.M. and Young, J.W., 1975. Investigation of Inertial Properties of the Human Body. NTIS No. AD-A016 485. Aerospace Medical Research Laboratory (AMRL TR 74-137). Wright-Patterson Air Force Base, Ohio.

Chao, E.Y. and Morrey, B.F., 1978. Three-dimensional Rotation of the Elbow. *Journal of Biomechanics* 11(1-2), 57-73.

Charlton, I.W. and Johnson, G.R., 2000. An Interactive Musculoskeletal Model of the Upper Limb. *In Proceedings of the Third Conference of the International Shoulder Group*. Newcastle upon Tyne, UK.

Charlton, I.W. and Johnson, G.R., 2001. Application of Spherical and Cylindrical Wrapping Algorithms in a Musculoskeletal Model of the Upper Limb. *Journal of Biomechanics* 34, 1209-1216.

Cheng, C.-K., Chen, H.-H., Chen, C.-S., Lee, C.-L. and Chen, C.-Y., 2000. Segment Inertia Properties of Chinese Adults Determined from Magnetic Resonance Imaging. *Clinical Biomechanics* 15(8), 559-566.

Chevalot, N. and Wang, X., 2004. Experimental investigation of the discomfort of arm reaching movements in a seated position. SAE paper 2004-01-2141. *In Proceedings of the SAE International conference and exposition of Digital Human Modeling for Design and Engineering*. Oakland University, Rochester, Michigan, USA, June 15-17.

Chèze, L., Fregly, B.J. and Dimnet, J., 1995. A Solidification Procedure to Facilitate Kinematic Analyses Based on Video System Data. *Journal of Biomechanics* 28(7), 879-884.

Chiari, L., Croce, U.D., Leardini, A. and Cappozzo, A., 2005. Human movement analysis using stereophotogrammetry: Part 2: Instrumental errors. *Gait & Posture* 21(2), 197.

Churchill, D.L., Incavo, S.J., Johnson, C.C. and Beynnon, B.D., 1998. The Transepicondylar Axis Approximates the Optimal Flexion Axis of the Knee. *Clinical Orthopaedics and Related Research* 356, 111-118.

Daanen, H.A.M. and van der Water, G.J., 1998. Whole Body Scanners. *Displays* 19, 111-120.

Davis, R.B., Ounpuu, S., Tyburski, D. and Gage, J.R., 1991. A Gait Analysis Data Collection and Reduction Technique. *Human Movement Science* 10, 575-587.

de Groot, J.H. and Brand, R., 2001. A Three-Dimensional Regression Model of the Shoulder Rhythm. *Clinical Biomechanics* 16, 735-743.

De Leest, O., Rozing, P.M., Rozendaal, L.A. and van der Helm, F.C.T., 1996. The Influence of Glenohumeral Prosthesis Geometry and Placement on Shoulder Muscles Forces. *Clinical Orthopaedics and Related Research* 330, 222-233.

De Leva, P., 1996a. Adjustments to Zatsiorsky-Seluyanov's Segment Inertia Parameters. *Journal of Biomechanics* 29(9), 1223-1230.

De Leva, P., 1996b. Joint Center Longitudinal Positions Computed from a Selected Subset of Chandler's Data. *Journal of Biomechanics* 29(9), 1231-1233.

De Luca, C.J. and Forrest, W.J., 1973. Force Analysis of Individual Muscles Acting Simultaneously on the Shoulder during Isometric Abduction. *Journal of Biomechanics* 6, 385-393.

Delp, S.L., Loan, J.P., Hoy, M.G., Zajac, F.E., Topp, E.L. and Rosen, J.M., 1990. An interactive graphics-based model of the lower extremity to study orthopaedic surgical procedures. *IEEE Transactions on Biomedical engineering* 37(8), 757-767.

Delp, S.L. and Maloney, W., 1993. Effect of Hip Center Location on the Moment-Generating Capacity of the Muscles. *Journal of Biomechanics* 26(4/5), 485-499.

Della Croce, U., Cappozzo, A. and Kerrigan, D.C., 1999. Pelvis and Lower Limb Anatomical Landmark Calibration Precision and its Propagation to Bone Geometry and Joint Angles. *Medical & Biological Engineering & Computing* 37(2), 155-161.

Dempster, W.T., 1955. Space Requirements of the Seated Operator. Technical report WADC-TR-55-159. Wright-Patterson Air Force Base, Ohio.

Desjardins, P., Plamondon, A., Nadeau, S. and Delisle, A., 2002. Handling missing marker coordinates in 3D analysis. *Medical Engineering & Physics* 24(6), 437.

Dolan, E.D. and Moré, J.J., 2000. Benchmarking Optimization Software With COPS. Technical Memorandum ANL/MSC-TM-246. Argonne National Laboratory, Argonne, Illinois.

Dolan, E.D. and Moré, J.J., 2002. Benchmarking Optimization Software with Performance Profiles. *Mathematical Programming* 91, 201-213.

Drillis, R. and Contini, R., 1966. Body Segment Parameters. Technical Report No. 1166.03. School of Engineering and Science, New York University, New York.

Drud, A.S., 1994. CONOPT: A Large-Scale GRG Code. *ORSA Journal on Computing* 6, 207-216.

Drud, A.S., 2002. On the Use of Second Order Information in GAMS/CONOPT3. *In Proceedings of the SIAM Optimization Meeting*. Toronto, Canada.

Dufour, F., Renard, F., Monnier, G., Wang, X., Doriot, N., Chevalot, N., Zacher, I. and Colinet, O., 2003. Measurement Protocols and Multibody Copies of the Performed Experiments. Internal Report D-2.6. REALMAN project.

Dul, J., 1988. A Biomechanical Model to Quantify Shoulder Load at the Work Place. *Clinical Biomechanics* 3, 124-128.

Dumas, R., Aissaoui, R., Mitton, D., Skalli, W. and de Guise, J.A., 2004. Determination of Personalized Inertial Parameters of Lower Limb by Biplanar Low-dose Radiography. *International Congress Series* 1268, 19-24.

Durkin, J.L. and Dowling, J.J., 2003. Analysis of Body Segment Parameter Differences Between Four Human Populations and the Estimation Errors of Four Popular Mathematical Models. *Journal of Biomechanical Engineering* 125(4), 515-522.

Durkin, J.L., Dowling, J.J. and Andrews, D.M., 2002. The Measurement of Body Segment Inertial Parameters Using Dual Energy X-ray Absorptiometry. *Journal of Biomechanics* 35(12), 1575-1580.

Engin, A.E., 1980. On the Biomechanics of the Shoulder Complex. *Journal of Biomechanics* 13(7), 575-590.

Engin, A.E. and Chen, S.M., 1986a. Statistical Data Base for the Biomechanical Properties of the Human Shoulder Complex -I: Kinematics of the Shoulder Complex. *Journal of Biomechanical Engineering* 108(3), 215-221.

Engin, A.E. and Chen, S.M., 1986b. Statistical Database for the Biomechanical Properties of the Human Shoulder Complex -II: Passive Resistive Properties beyond the Shoulder Complex Sinus. *Journal of Biomechanical Engineering* 108(3), 222-227.

Engin, A.E. and Peindl, R.D., 1987. On the Biomechanics of Human Shoulder Complex - I. Kinematics for Determination of the Shoulder Complex Sinus. *Journal of Biomechanics* 20(2), 103-117.

Engin, A.E., Peindl, R.D., Berme, N. and Kaleps, I., 1984a. Kinematic and Force Data Collection in Biomechanics by Means of Sonic Emitters - II: Force Data Collection and Application to the Human Shoulder Complex. *Journal of Biomechanical Engineering* 106(3), 212-219.

Engin, A.E., Peindl, R.D., Berme, N. and Kaleps, I., 1984b. Kinematic and Force Data Collection in Biomechanics by Means of Sonic Emitters -I: Kinematic Data Collection Methodology. *Journal of Biomechanical Engineering* 106(3), 204-211.

Engin, A.E. and Tümer, S.T., 1989. Three-dimensional Kinematic Modelling of the Human Shoulder Complex - Part I: Physical Model and Determination of Joint Sinus Cones. *Journal of Biomechanical Engineering* 111(2), 107-112.

Erdemir, A. and Piazza, S.J., 1999. Simulation-based Design of a Pointer for Accurate Determination of Anatomical Landmarks. *In Proceedings of the 23rd Annual Meeting of the Americal Society of Biomechanics*, pp. 286-287.

Flaquer, J., Olaizola, J. and Olaizola, J., 2004. *Curso de Álgebra Lineal.* (3ª Edición ed.), EUNSA.

Fletcher, R., 1987. *Pratical Methods of Optimization.* (2nd ed.), Wiley-Interscience.

Fletcher, R. and Leyffer, S., 1998. User manual for filterSQP. Numerical Analysis Report NA\181. Dundee University.

Forsgren, A., Gill, P.E. and Wright, M.H., 2002. Interior methods for nonlinear optimization. *SIAM Review* 44, 525-597.

Frigo, C. and Rabuffetti, M., 1998. Multifactorial Estimation of Hip and Knee Joint Centres for Clinical Application of Gait Analysis. *Gait & Posture* 8, 91-102.

Gamage, S.S.H.U. and Lasenby, J., 2002. New Least Squares Solutions for Estimating the Average Centre of Rotation and the Axis of Rotation. *Journal of Biomechanics* 35, 87-93.

Ganley, K.J. and Powers, C.M., 2004. Anthropometric Parameters in Children: a Comparison of Values Obtained from Dual Energy X-ray Absorptiometry and Cadaver-based Estimates. *Gait & Posture* 19(2), 133-140.

García de Jalón, J. and Bayo, E., 1994. *Kinematics and Dynamic Simulation of Multibody Systems. The Real-Time Challenge.* New-York, Springer-Verlag.

García de Jalón, J., Serna, M.A. and Avilés, R., 1981. A Computer Method for Kinematic Analysis of Lower-Pair Mechanisms. Part I: Velocities and Accelerations and Part II: Position Problems. *Mechanism and Machine Theory* 16, 543-566.

García de Jalón, J., Unda, J. and Avello, A., 1986. Natural Coordinates for the Computer Analysis of Multibody Systems. *Computer Methods in Applied Mechanics and Engineering* 56, 309-327.

García de Jalón, J., Unda, J., Avello, A. and Jiménez, J.M., 1987. Dynamic Analysis of Three-Dimensional Mechanisms in Natural Coordinates. *ASME Journal of Mechanisms, Transmissions and Automation in Design* 109, 460-465.

Garner, B.A. and Pandy, M.G., 1999. A Kinematic Model of the Upper Limb Based on the Visible Human Project (VHP) Image Dataset. *Computer Methods in Biomechanics and Biomedical Engineering* 2, 107-124.

Garner, B.A. and Pandy, M.G., 2000. The Obstacle-set Method for Representing Muscle Paths in Musculoskeletal Models. *Computer Methods in Biomechanics and Biomedical Engineering* 3, 1-30.

Garner, B.A. and Pandy, M.G., 2001. Musculoskeletal Model of the Upper Limb Based on the Visible Human Male Dataset. *Computer Methods in Biomechanics and Biomedical Engineering* 4, 93-126.

Garner, B.A. and Pandy, M.G., 2003. Estimation of Musculotendon Properties in the Human Upper Limb. *Annals of Biomedical Engineering* 31, 207-220.

Giakas, G. and Baltzopoulos, V., 1997. A Comparison of Automatic Filtering Techniques Applied to Biomechanical Walking Data. *Journal of Biomechanics* 30(8), 847-850.

Gill, P.E., Murray, W. and Saunders, M.A., 1997. SNOPT: An SQP Algorithm for Large-scale Constrained Optimization. Report NA 97-2. Department of Mathematics, University of California, San Diego, California.

Gill, P.E., Murray, W. and Saunders, M.A., 2002. SNOPT: An SQP Algorithm for Large-scale Constrained Optimization. *SIAM Journal on Optimization* 12(4), 979-1006.

Glitsch, U. and Baumann, W., 1997. The Three-dimensional Determination of Internal Loads in the Lower Extremity. *Journal of Biomechanics* 30, 1123-1131.

Gonzalez, R.V., Hutchins, E.L., Barr, R.E. and Abraham, L.D., 1996. Development and evaluation of a musculoskeletal model of the elbow joint complex. *Journal of Biomechanical Engineering* 118, 32-40.

Gould, N.I.M. and Leyffer, S., 2003. An introduction to algorithms for nonlinear optimization. RAL-TR-2002-031. CCLRC Rutherford Appleton Laboratory, UK.

Gray, H., 1918. *Anatomy of the Human Body*. Philadelphia, Lea & Febiger. Bartleby.com, 2000. www.bartleby.com/107/.

Gruber, K., Ruder, H., Denoth, J. and Schneider, K., 1998. A Comparative Study of Impact Dynamics: Wobbling Mass Model versus Rigid Body Models. *Journal of Biomechanics* 31(5), 439-444.

Gutierrez, A., 1990. Comportamiento Mecánico del Cuerpo Humano en el Deporte de Alta Competición. PhD Thesis, Applied Mechanics Department, University of Navarra, San Sebastián, Spain.

Hagemeister, N., Yahia, L.H., Duval, N. and de Guise, J.A., 1999. In Vivo Reproducibility of a New Non-invasive Diagnostic Tool for Three-dimensional Knee Evaluation. *The Knee* 6, 175-181.

Halvorsen, K., Lesser, M. and Lundberg, A., 1999. A New Method for Estimating the Axis of Rotation and the Center of Rotation. *Journal of Biomechanics* 32, 1221-1227.

Hanavan, E.P., 1964. A Mathematical Model of the Human Body. AMRL-TR-64-102, AD-608-463. Aerospace Medical Research Laboratories, Wright-Patterson Air Force Base, Ohio.

Happee, R. and van der Helm, F.C.T., 1995. The Control of Shoulder Muscles During Goal Directed Movements: An Inverse Dynamic Analysis. *Journal of Biomechanics* 28(10), 1179-1191.

Hatze, H., 1980. A Mathematical Model for the Computational Determination of Parameter Values of Anthropometric Segments. *Journal of Biomechanics* 13, 833-843.

Hatze, H. and Baca, A., 1992. Contact-Free Determination of Human Body Segment Parameters by Means of Videometric Image Processing of an Anathropomorphic Body Model. *In Proceedings of the Int. SPIE Congr. on Image Processing*. San Diego, USA.

Hefzy, M.S. and Abdel-Rahman, E.M., 2000. Three-Dimensional Dynamic Anatomical Modeling of the Human Knee Joint. In: C.T. Leondes (Ed.), *Biomechanical Systems: Techniques and Applications, Volume III: Musculoskeletal Models and Techniques*, CRC Press.

Herda, L., Fua, P., Plankers, R., Boulic, R. and Thalmann, D., 2001. Using skeleton-based tracking to increase the reliability of optical motion capture. *Human Movement Science* 20(3), 313.

Hinrichs, R.N., 1985. Regression Equations to Predict Segmental Moments of Inertia from Anthropometric Measurements: An Extension of the Data of Chandler et al. (1975). *Journal of Biomechanics* 18(8), 621-624.

Hinrichs, R.N., 1990. Adjustments to the Segment Center of Mass Proportions of Clauser et al. (1969). *Journal of Biomechanics* 23(9), 949-951.

Högfors, C., Karlsson, D. and Peterson, B., 1995. Structure and Internal Consistency of a Shoulder Model. *Journal of Biomechanics* 28(7), 767-777.

Högfors, C., Peterson, B., Sigholm, G. and Herberts, P., 1991. Biomechanical Model of the Human Shoulder - II. The Shoulder Rhythm. *Journal of Biomechanics* 24, 699-709.

Högfors, C., Sigholm, G. and Herberts, P., 1987. Biomechanical Model of the Human Shoulder - I. Elements. *Journal of Biomechanics* 20(2), 157-166.

Holden, J.P. and Stanhope, S.J., 1998. The Effect of Variation in Knee Center Location Estimates on Net Knee Joint Moments. *Gait & Posture* 7, 1-6.

Huang, H.K. and Suarez, F.R., 1983. Evaluation of Cross-sectional Geometry and Mass Density Distributions of Humans and Laboratory Animals Using Computerized Tomography. *Journal of Biomechanics* 16(10), 821-832.

Huang, H.K. and Wu, S.C., 1976. The Evaluation of Mass Densities of the Human Body in Vivo from CT Scans. *Comput. Biol. Med.* 6(4), 337-343.

Inman, V.T., 1976. *The Joints of the Ankle*. Baltimore, Williams & Wilkins.

Inman, V.T., Saunders, J.B. and Abbott, L.C., 1944. Observations on the Function of the Shoulder Joint. *Journal of Bone and Joint Surgery* 26-A, 1-30.

Izmailov, A.F. and Solodov, M.V., 2004. Newton-type Methods for Optimization Problems without Constraint Qualifications. *To appear in SIAM Journal on Optimization*.

Jensen, R.K., 1978. Estimation of the Biomechanical Properties of Three Body Types using a Photogrammetric Method. *Journal of Biomechanics* 11, 349-358.

Jensen, R.K., 1986. Body Segment Mass, Radius and Radius of Gyration Proportions of Children. *Journal of Biomechanics* 19(5), 359-368.

Jensen, R.K., 1989. Changes in Segment Inertia Proportions between 4 and 20 Years. *Journal of Biomechanics* 22(6-7), 529-536.

Johnson, G.R., Spalding, R., Nowitzke, A. and Bogduk, N., 1996. Modelling the Muscles of the Scapula Morphometric and Coordinate Data and Functional Implications. *Journal of Biomechanics* 29(8), 1039-1051.

Kadaba, M.P., Ramakrishnan, H.K. and Wootten, M.E., 1990. Measurement of Lower Extremity Kinematics During Level Walking. *Journal of Orthopaedic Research* 8, 383-392.

Karduna, A.R., McClure, P.W., Michener, L.A. and Sennett, B., 2001. Dynamic Measurements of Three-Dimensional Scapular Kinematics: A Validation Study. *Journal of Biomechanical Engineering* 123, 184-189.

Karlsson, D. and Peterson, B., 1992. Towards a Model for Force Predictions in the Human Shoulder. *Journal of Biomechanics* 25(2), 189-199.

Kecskeméthy, A., Stolz, M., Strobach, D., Saraph, V., Steinwender, G. and Zwick, B., 2003. Improvements in Measure-Based Simulation of the Human Lower Extremity. *In Proceedings of the IASTED Conference on Biomechanics*, pp. 155-160. Rhodes, June 30 - July 2.

Kecskeméthy, A. and Weinberg, A.M., 2003. An Improved Elasto-kinematic Model of the Human Forearm for Biofidelic Medical Diagnosis. *In Proceedings of the Multibody Dynamics 2003*. Lisbon, Portugal, July 1-4.

Kepple, T.M., Sommer III, H.J., Siegel, K.L. and Stanhope, S.J., 1998. A Three-dimensional Musculoskeletal Database for the Lower Extremities. *Journal of Biomechanics* 31, 77-80.

Kingma, I., Toussaint, H.M., De Looze, M.P. and van Dieen, J., 1996. Segment Inertial Parameter Evaluation in Two Anthropometric Models by Application of a Dynamic Linked Segment Model. *Journal of Biomechanics* 29(5), 693-704.

Kirkwood, R.N., Culham, E.G. and Costigan, P., 1999. Radiographic and Non-invasive Determination of the Hip Joint Center Location: Effect on Hip Joint Moments. *Clinical Biomechanics* 14, 227-235.

Klein Breteler, M.D., 1997. Measuring Muscle and Joint Geometry Parameters for a Shoulder Model. *In Proceedings of the First Conference of the International Shoulder Group*, pp. 89-93. Delft, Delft University of Technology, The Netherlands.

Klein Breteler, M.D., Spoor, C.W. and van der Helm, F.C.T., 1999. Measuring Muscle and Joint Geometry Parameters of a Shoulder for Modeling Purposes. *Journal of Biomechanics* 32, 1191-1197.

Kodek, T. and Munih, M., 2004. An Identification Technique for Evaluating Static Body Segment Parameters in the Upper Extremity. *In Proceedings of the IEEE International Conference on Robotics and Automation 2004*, pp. 4747-4752. Piscataway.

Lafortune, M.A., Cavanagh, P.R., Sommer III, H.J. and Kalenak, A., 1992. Three-dimensional Kinematics of the Human Knee during Walking. *Journal of Biomechanics* 25(4), 347-357.

Laporte, S., Skalli, W., de Guise, J.A., Lavaste, F. and Mitton, D., 2003. A Biplanar Reconstruction Method Based on 2D and 3D Contours: Application to the Distal Femur. *Computer Methods in Biomechanics and Biomedical Engineering* 6(1), 1-6.

Le Bras, A., Laporte, S., Bousson, V., Mitton, D., De Guise, J.A., Laredo, J.D. and Skalli, W., 2003. Personalised 3D Reconstruction of Proximal Femur from Low-dose Digital Biplanar Radiographs. *International Congress Series* 1256, 214-219.

Leardini, A., Cappozzo, A., Catani, F., Toksvig-Larsen, S., Petitto, A., Sforza, V., Cassanelli, G. and Giannini, S., 1999. Validation of a Functional Method for the Estimation of Hip Joint Centre of Location. *Journal of Biomechanics* 32, 99-103.

Leardini, A., Chiari, L., Croce, U.D. and Cappozzo, A., 2005. Human movement analysis using stereophotogrammetry: Part 3. Soft tissue artifact assessment and compensation. *Gait & Posture* 21(2), 212.

Lemay, M.A. and Crago, P.E., 1996. A Dynamic Model for Simulating Movements of the Elbow, Forearm and Wrist. *Journal of Biomechanics* 29, 1319-1330.

Lenzi, D., Cappello, A. and Chiari, L., 2003. Influence of Body Segment Parameters and Modeling Assumptions on the Estimate of Center of Mass Trajectory. *Journal of Biomechanics* 36, 1335-1341.

Lorensen, W.E. and Cline, H.E., 1987. Marching Cubes: A High Resolution 3D Surface Construction Algorithm. *Computer Graphics* 21, 163-169.

Lu, T.-W. and O'Connor, J.J., 1999. Bone Position Estimation from Skin Marker Co-ordinates Using Global Optimisation with Joint Constraints. *Journal of Biomechanics* 32, 129-134.

Lucchetti, L., Cappozzo, A., Cappello, A. and Della Croce, U., 1998. Skin Movement Artefact Assessment and Compensation in the Estimation of Knee-Joint Kinematics. *Journal of Biomechanics* 31, 977-984.

Makhsous, M., Högfors, C., Siemienski, A. and Peterson, B., 1999. Total Shoulder and Relative Muscle Strength in the Scapular Plane. *Journal of Biomechanics* 32, 1213-1220.

Martin, P.E., Mungiole, M., Marzke, M.W. and Longhill, L.M., 1989. The Use of Magnetic Resonance Imaging for Measuring Segment Inertial Properties. *Journal of Biomechanics* 22, 367-376.

Maurel, W., 1999. 3-D Modeling of the Human Upper Limb Including the Biomechanics of Joints, Muscles, and Soft Tissues. Ph.D. Thesis, Laboratoire d'Infographie, Ecole Polytechnique Federale de Lausanne, Lausanne, Switzerland.

Maurel, W. and Thalmann, D., 2000. Human Shoulder Modeling including Scapulo-Thoracic Constraint and Joint Sinus Cones. *Computers & Graphics* 24, 203-218.

Maurel, W., Thalmann, D., Hoffmeyer, P., Beylot, P., Gingins, P., Kalra, P. and Magnenat Thalmann, N., 1996. A Biomechanical Musculoskeletal Model of Human Upper Limb for Dynamic Simulation. *In Proceedings of the 7th Eurographics International Workshop on Computer Animation and Simulation*, pp. 121-136. Poitiers, France, Aug 31-Sept 1.

McConville, J.T., Churchill, T.D., Calepis, I., Clauser, C.E. and Cuzzi, J., 1980. Anthropometric Relationships of Body and Body Segment Moments of Inertia. Technical Report AFAMRL-TR-80-119. Wright-Patterson Air Force Base. Aerospace Medical Research Laboratory, Ohio.

Medved, V., 2001. *Measurement of human locomotion*. Boca Raton, USA, CRC Press.

Meskers, C.G.M., van der Helm, F.C.T., Rozendaal, L.A. and Rozing, P.M., 1998. In Vivo Estimation of the Glenohumeral Joint Rotation Center from Scapular Bony Landmarks by Linear Regression. *Journal of Biomechanics* 31, 93-96.

Mittelmann, H.D. and Pruessner, A., 2004. A Server for Automated Performance Analysis and Benchmarking of Optimization Software. *To appear*.

Monnier, G., Wang, X., Dolivet, C., Verriest, J.P., Lino, F. and Dufour, F., 2002. Experimental investigation on the discomfort of safety belt handling. *In Proceedings of the SAE International conference and exposition of Digital Human Modeling for Design and Engineering*. Munich, Germany, June 18-20.

Monnier, G., Wang, X., Verriest, J.P. and Goujon, S., 2003. Simulation of Complex and Specific Task-Orientated Movements - Application to the Automotive Seat Belt Reaching. SAE paper 2003-01-2225. *In Proceedings of the SAE International conference and exposition of Digital Human Modeling for Design and Engineering*. Montreal, Canada, 17-19 June.

Morales, J.L., Nocedal, J., Waltz, R., Liu, G. and Goux, J.-P., 2001. Assessing the Potential of Interior Methods for Nonlinear Optimization. Report OTC 2001/6. Optimization Technology Center, Northwestern University, Illinois, USA.

Moseley, L., Smith, R., Hunt, A. and Gant, R., 1996. Three-Dimensional Kinematics of the Rearfoot during the Stance Phase of Walking in Normal Young Adult Males. *Clinical Biomechanics* 11(1), 39-45.

Muijtjens, A.M.M., Roos, J.M.A., Arts, T., Hasman, A. and Reneman, R.S., 1997. Tracking markers with missing data by lower rank approximation. *Journal of Biomechanics* 30(1), 95.

Mungiole, M. and Martin, P.E., 1990. Estimating Segment Inertial Properties: Comparison of Magnetic Resonance Imaging with Existing Methods. *Journal of Biomechanics* 23(1039-1046).

Murray, W.M., Delp, S.L. and Buchanan, T.S., 1995. Variation of Muscle Moment Arms with Elbow and Forearm Position. *Journal of Biomechanics* 28(5), 513-525.

Murtagh, B.A. and Saunders, M.A., 1998. MINOS 5.5 User's Guide. Report SOL 83-20R. Department of Operations Research, Stanford University.

Nagano, A., Gerritsen, K.G.M. and Fukashiro, S., 2000. A Sensitivity Analysis of the Calculation of Mechanical Output through Inverse Dynamics: A Computer Simulation Study. *Journal of Biomechanics* 33, 1313-1318.

Nagano, A., Komura, T., Himeno, R. and Fukashiro, S., 2004. A Procedure for Adjustment of Body Segmental Parameter Values to Individual Subjects in Inverse Dynamics. *International Journal of Sport and Health Science* 2, 156-162.

Neumaier, A., 2004. Complete Search in Continuous Global Optimization and Constraint Satisfaction. *to apper in: Acta Numerica.*

Nigg, B.M., 1999. Inertial Properties of the Human or Animal Body. In: B.M. Nigg and W. Herzog (Eds.), *Biomechanics of the Musculo-skeletal System*, pp. 376-399. Chichester, John Wiley & Sons.

Nocedal, J. and Wright, S.J., 1999. *Numerical Optimization*. New York, Springer-Verlag.

Norton, J., Donaldson, N. and Dekker, L., 2002. 3D Whole Body Scanning to Determine Mass Properties of Legs. *Journal of Biomechanics* 35, 81-86.

Pain, M.T.G. and Challis, J.H., 2001a. High Resolution Determination of Body Segment Inertia Parameters and Their Variation due to Soft Tissue Motion. *Journal of Applied Biomechanics* 17, 326-334.

Pain, M.T.G. and Challis, J.H., 2001b. The Role of the Heel Pad and Shank Soft Tissue during Impacts: A further Resolution of a Paradox. *Journal of Biomechanics* 34(3), 327-333.

Palmerud, G., Makhsous, M., Sporrong, H., Herberts, P., Högfors, C. and Kadefors, R., 1998. Estimation of the Load Sharing Pattern in the Shoulder - A Comparison Between Electromyographical Measurements and Biomechanical Model Calculations. Biomechanical and Ergonomic Considerations on Shoulder Muscle Load. Ph.D. Thesis, Dept. of Orthopaedics, Institute of Surgical Sciences, Göteborg University, Göteborg, Sweden.

Pataky, T.C., Zatsiorsky, V.M. and Challis, J.H., 2003. A Simple Method to Determine Body Segment Masses in Vivo: Reliability, Accuracy and Sensitivity Analysis. *Clinical Biomechanics* 18, 364-368.

Pearsall, D.J. and Costigan, P.A., 1999. The Effect of Segment Parameter Error on Gait Analysis Results. *Gait & Posture* 9, 173-183.

Pearsall, D.J. and Reid, J.G., 1994. The Study of Human Body Segment Parameters in Biomechanics: An Historical Review and Current Status Report. *Sports Medicine* 18(2), 126-140.

Pearsall, D.J., Reid, J.G. and Livingston, L.A., 1996. Segmental Inertia Parameters of the Human Trunk as Determined from Computed Tomography. *Annals of Biomedical Engineering* 24, 198-210.

Peindl, R.D. and Engin, A.E., 1987. On the Biomechanics of Human Shoulder Complex - II. Passive Resistive Properties beyond the Shoulder Complex Sinus. *Journal of Biomechanics* 20(2), 119.

Pheasant, S., 1986. *Bodyspace: Anthropometry, Ergonomics and Design*. London, Taylor & Francis.

Piazza, S.J. and Cavanagh, P.R., 2000. Measurement of the Screw-home Motion of the Knee is Sensitive to Errors in axis Alignment. *Journal of Biomechanics* 33, 1029-1034.

Piazza, S.J., Okita, N. and Cavanagh, P.R., 2001. Accuracy of the Functional Method of Hip Joint Center Location: Effects of Limited Motion and Varied Implementation. *Journal of Biomechanics* 34, 967-973.

Plagenhoef, S., 1971. *Patterns of Human Motions. A Cinematographic Analysis*. Englewood Cliffs, Prentice-Hall.

Poppen, N.K. and Walker, P.S., 1976. Normal and Abnormal Motion of the Shoulder. *Journal of Bone and Joint Surgery* 58A, 195-201.

Poppen, N.K. and Walker, P.S., 1978. Forces at the Glenohumeral Joint in Abduction. *Clinical Orthopaedics and Related Research* 135, 165-170.

Rab, G., Petuskey, K. and Bagley, A., 2002. A Method for Determination of Upper Extremity Kinematics. *Gait & Posture* 15, 113-119.

Rabuffetti, M., Baroni, G., Ferrarin, M., Ferrigno, G. and Pedotti, A., 2002. Self-marking of anatomical landmarks for on-orbit experimental motion analysis compared to expert direct-marking. *Human Movement Science* 21(4), 439-455.

Reinbolt, J.A., Schutte, J.F., Fregly, B.J., Koh, B.I., Haftka, R.T., George, A.D. and Mitchell, K.H., 2005. Determination of Patient-Specific Multi-Joint Kinematic Models through Two-Level Optimization. *Journal of Biomechanics* 38(3), 621-626.

Renard, F., Lestreli, D., Monnier, G., Trasbot, J., Gaia, E., Wirsching, H.J. and Pappas, M., 2004. Analysis of System Validation Results. Internal Report D-8.2. REALMAN project.

Renard, F., Wang, X., Monnier, G. and Chevalot, N., 2003. Analysis of Test Human Motion Data: Key Parameters and Relative Impacts. Internal Report D-4.1. REALMAN project.

Riley, M., Ude, A. and Atkeson, C.G., 2000. Methods for Motion Generation and Interaction with a Humanoid Robot: Case Studies of Dancing and Catching. *In Proceedings of the AAAI and CMU Workshop on Interactive Robotics and Entertainment 2000*. Pittsburgh, Pennsylvania, USA.

Robinette, K.M. and Daanen, H.A.M., 2003. Lessons Learned from CAESAR: A 3-D Anthropometric Survey. *In Proceedings of the International Ergonomics Association Conference*. Seoul.

Robinette, K.M., Daanen, H.A.M. and Paquet, E., 1999. The CAESAR Project: a 3-D Surface Anthropometry Survey. *In Proceedings of the Second International Conference on 3-D Digital Imaging and Modeling*, pp. 380-386. Ottawa, Canada.

Roux, E., Bouilland, S., Godillon-Maquinghen, A.-P. and Bouttens, D., 2002. Evaluation of the Global Optimisation Method within the Upper Limb Kinematics Analysis. *Journal of Biomechanics* 35, 1279-1283.

Rubí, J., 2002. Cinemática, Dinámica y Control de Robots Redundantes y Robots Subactuados. PhD Thesis, Applied Mechanics Department, University of Navarra, San Sebastián, Spain.

Sarfaty, O. and Ladin, Z., 1993. A Video-Based System for the Estimation of the Inertial Properties of Body Segments. *Journal of Biomechanics* 26(8), 1011-1016.

Schmidt, R., Disselhorst-Klug, C., Silny, J. and Rau, G., 1999. A marker-based measurement procedure for unconstrained wrist and elbow motions. *Journal of Biomechanics* 32, 615-621.

Schneider, K. and Zernicke, R.F., 1992. Mass, Center of Mass, and Moment of Inertia Estimates for Infant Limb Segments. *Journal of Biomechanics* 25(2), 145-148.

Seidel, G.K., Marchinda, D.M., Dijkers, M. and Soutas-Little, R.W., 1995. Hip Joint Center Location from Palpable Bony Landmarks - A Cadaver Study. *Journal of Biomechanics* 28(8), 995-998.

Seireg, A. and Arvikar, R., 1989. *Biomechanical Analysis of the Musculoskeletal Structure for Medicine and Sports*. New York, Hemisphere Publishing.

Seitz, T., Balzulat, J. and Bubb, H., 2000. Anthropometry and Measurement of Posture and Motion. *International Journal of Industrial Ergonomics* 25(4), 447-453.

Seitz, T. and Bubb, H., 1999. Measuring of Human Anthropometry, Posture and Motion. *In Proceedings of the SAE Conference on Human Modelling*. The Hague, The Netherlands, 18-20 May.

Seitz, T. and Bubb, H., 2001. Human-Model Based Movement-Capturing Without Markers for Ergonomic Studies. *In Proceedings of the SAE Conference on Digital Human Modelling*. Washington, D.C., USA, June 26-28.

Serna, M.A., Avilés, R. and García de Jalón, J., 1982. Dynamic Analysis of Plane Mechanisms with Lower-Pairs in Basic Coordinates. *Mechanism and Machine Theory* 17, 397403.

Shan, G. and Bohn, C., 2003. Anthropometrical Data and Coefficients of Regression Related to Gender and Race. *Applied Ergonomics* 34, 327-337.

Silaghi, M., Plaenkers, R., Boulic, R., Fua, P. and Thalmann, D., 1998. Local and Global Skeleton Fitting Techniques for Optical Motion Capture. In: N. Magnenat Thalmann and D. Thalmann (Eds.), *Modelling and Motion Capture Techniques for Virtual Environments, Lecture Notes in Artificial Intelligence, No. 1537*, pp. 26-40, Springer.

Silva, M.P.T., 2003. Human Motion Analysis Using Multibody Dynamics and Optimization Tools. Ph.D. Thesis, Instituto Superior Técnico, Universidade Técnica de Lisboa, Lisboa.

Silva, M.P.T. and Ambrósio, J.A.C., 2002. Kinematic Data Consistency in the Inverse Dynamic Analysis of Biomechanical Systems. *Multibody System Dynamics* 8, 219-239.

Silva, M.P.T. and Ambrósio, J.A.C., 2003. The effect of different physiological cost functions on the solution of the redundant problem in biomechanics. *In Proceedings of the Multibody Dynamics*, Lisbon, Portugal.

Simmons, J.C. and Gardner, M.S., 1960. Self-maneuvering for the Orbital Worker. Technical Report TR-60-748. Wright Air Development Division, Wright-Patterson Air Force Base, Ohio.

Smith, S. and Lasdon, L., 1992. Solving large sparse nonlinear programs using GRG. *ORSA Journal on Computing* 4, 1-15.

Snyder, R.G., Chaffin, D.B. and Schutz, R.K., 1972. Link System of the Human Torso. Technical report AMRL-TR-71-88. Aerospace Medical Research Laboratories, Dayton, Ohio.

Söderkvist, I. and Wedin, P., 1993. Determining the movements of the skeleton using well-configured markers. *Journal of Biomechanics* 26(12), 1473-1477.

Sommer, H.J. and Miller, N.R., 1980. A Technique for Kinematic Modelling of Anatomical Joints. *Journal of Biomechanical Engineering* 102, 311-317.

Spitzer, V.M. and Whitlock, D.G., 1998. The Visible Human Dataset: The Anatomical Platform for Human Simulation. *Anatomical Record* 253, 49-57.

Spoor, C.W. and Veldpaus, F.E., 1980. Rigid Body Motion Calculated from Spatial Co-ordinates of Markers. *Journal of Biomechanics* 13, 391-393.

Stagni, R., Leardini, A., Cappozzo, A., Benedetti, M.G. and Cappello, A., 2000. Effects of hip joint centre mislocation on gait analysis results. *Journal of Biomechanics* 33(11), 1479-1487.

Stijnen, V.V., Williams, E.J., Spaeyen, A.J., Peeraer, L. and Leemputte, M., 1983. A Modified Release Method for Measuring the Moment of Inertia of the Limbs. In: H. Matsui and K. Kobayashi (Eds.), *Biomechanics VIII-B*. Champaign, IL, Human Kinetics Publishers.

Stokdijk, M., Meskers, C.G.M., Veeger, H.E.J., de Boer, Y.A. and Rozing, P.M., 1999. Determination of the optimal elbow axis for evaluation of placement of prostheses. *Clinical Biomechanics* 14, 177-184.

Stokdijk, M., Nagels, J. and Rozing, P.M., 2000. The glenohumeral joint rotation centre in vivo. *Journal of Biomechanics* 33, 1629-1636.

Strang, G., 1988. *Linear Algebra and Its Applications*. (3rd ed.), International Thomson Publishing.

Suescun, A. and Pargada, J., 2003. Reconstruction Method and Multibody model. Internal Report D-2.4. REALMAN project.

Suikerbuik, R., Tangelder, J.W.H., Daanen, H.A.M. and Oudenhuijzen, A., 2004. Automatic Feature Detection in 3D Human Body Scans. *In Proceedings of the SAE Digital human modeling for design and engineering*. Oakland University, Rochester, Michigan, June 15-17.

Tolani, D., Goswami, A. and Badler, N.I., 2000. Real-Time Inverse Kinematics Techniques for Anthropomorphic Limbs. *Graphical Models* 62, 352-388.

Tümer, S.T. and Engin, A.E., 1989. Three-dimensional kinematic modelling of the human shoulder complex - Part II: Mathematical modelling and solution via optimization. *Journal of Biomechanical Engineering* 111(2), 113-121.

Tylkowski, C.M., Simon, S.R. and Mansour, J.M., 1982. Internal Rotation Gait in Spastic Cerebral Palsy in the Hip. *In Proceedings of the 10th Open Meeting of the Hip Society*, pp. 89-125.

Urban, P., 1995. Aplicaciones de la Mecánica Computacional al Análisis del Movimiento del Cuerpo Humano. PhD Thesis, Applied Mechanics Department, University of Navarra, San Sebastián, Spain.

van den Bogert, A.J., Smith, G.D. and Nigg, B.M., 1994. In Vivo Determination of the Anatomical Axes of the Ankle Joint Complex: An Optimization Approach. *Journal of Biomechanics* 27(12), 1477-1488.

van der Helm, F.C.T., 1994a. Analysis of the Kinematic and Dynamic Behavior of the Shoulder Mechanism. *Journal of Biomechanics* 27(5), 527-550.

van der Helm, F.C.T., 1994b. A Finite Element Musculoskeletal Model of the Shoulder Mechanism. *Journal of Biomechanics* 27(5), 551-565.

van der Helm, F.C.T., 1997a. A Standardized Protocol for the Description of Shoulder Motions. International Shoulder Group.

van der Helm, F.C.T., 1997b. A Three-Dimensional Model of the Shoulder and Elbow. *In Proceedings of the First Conference of the International Shoulder Group*, pp. 65-70. Delft, Delft University of Technology, The Netherlands.

van der Helm, F.C.T. and Pronk, G.M., 1994. The Loading of Shoulder Girdle Muscles in Consequence of a Glenohumeral Arthrodesis. *Clinical Biomechanics* 9, 139-148.

van der Helm, F.C.T. and Pronk, G.M., 1995. Three-Dimensional Recording and Description of Motions of the Shoulder Mechanism. *Journal of Biomechanical Engineering* 117, 27-40.

van der Helm, F.C.T., Pronk, G.M., Veeger, H.E.J. and van der Woude, L.H.V., 1989. The Rotation Center of the Glenohumeral Joint. *In Proceedings of the 12th ISB Congress*. Los Angeles, U.S.A.

van der Helm, F.C.T. and Veeger, H.E.J., 1996. Quasi-static Analysis of Muscle Forces in the Shoulder Mechanism during Wheelchair Propulsion. *Journal of Biomechanics* 29(1), 39-52.

van der Helm, F.C.T., Veeger, H.E.J., Pronk, G.M., van der Woude, L.H.V. and Rozendal, R.H., 1992. Geometry parameters of musculoskeletal modelling of the shoulder mechanism. *Journal of Biomechanics* 25, 129-144.

van der Helm, F.C.T. and Veenbass, R., 1991. Modelling the Mechanical Effect of Muscles with Large Attachment Sites: Application to the Shoulder Mechanism. *Journal of Biomechanics* 24(12), 1151-1163.

Vanderbei, R.J., 2001. AMPL models. [http://www.sor.princeton.edu/~rvdb/ampl/nlmodels/].

Vanderbei, R.J. and Shanno, D.F., 1999. An Interior Point Algorithm for Nonconvex Nonlinear Programming. *Computational Optimization and Applications* 13, 231-252.

Vaughan, C.L., Andrews, J.G. and Hay, J.G., 1982. Selection of Body Segment Parameters by Optimization Methods. *Journal of Biomechanical Engineering* 104, 38-44.

Vaughan, C.L., Davis, B.L. and O'Connor, J.C., 1999. *Dynamics of Human Gait*. (2nd ed.), Human Kinetics Publishers.

Veeger, H.E.J., van der Helm, F.C.T., van der Woude, L.H.V., Pronk, G.M. and Rozendal, R.H., 1991. Inertia and Muscle Contraction Parameters for Musculoskeletal Modelling of the Shoulder Mechanism. *Journal of Biomechanics* 24(7), 615-629.

Veeger, H.E.J., Yu, B., An, K.N. and Rozendal, R.H., 1997. Parameters for modeling the upper extremity. *Journal of Biomechanics* 30(6), 647-652.

Veldpaus, F.E., Woltring, H.J. and Dortmans, L.J.M.G., 1988. A least-squares algorithm for the equiform transformation from spatial marker co-ordinates. *Journal of Biomechanics* 21, 356-360.

Wächter, A., 2002. IPOPT: An Interior Point Algorithm for Large-scale Nonlinear Optimization. [http://www-124.ibm.com/developerworks/oss/coin/Ipopt/index.html].

Wang, X., 1996. Construction of Arm Kinematic Linkage from External Surface Markers. *In Proceedings of the 4th International Symposium on 3D Analysis of Human Movement*. Grenoble, France.

Wang, X., Chevalot, N., Monnier, G., Ausejo, S., Suescun, Á. and Celigüeta, J.T., 2005. Validation of a Model-Based Motion Reconstruction Method Developed in the REALMAN Project. *In Proceedings of the SAE 2005 Digital Human Modeling for Design and Engineering Symposium*. Iowa City, Iowa, USA, June 14-16.

Wang, X. and Doriot, N., 2001. Glossary of the REALMAN Project. Internal Report D-1.3. REALMAN project.

Wang, X. and Verriest, J.P., 1998. A Geometric Algorithm to Predict the Arm Reach Posture for Computer-aided Ergonomic Evaluation. *The Journal of Visualization and Computer Animation* 9, 33-47.

Wei, C. and Jensen, R.K., 1995. The Application of Segment Axial Density Profiles to a Human Body Inertia Model. *Journal of Biomechanics* 28(1), 103-108.

Weinberg, A.M., Pietsch, I.T., Helm, M.B., Hesselbach, J. and Tscherne, H., 2000. A New Kinematic Model of Pro- and Supination of the Human Forearm. *Journal of Biomechanics* 33, 487-491.

Whitsett, C.E., 1963. Some Dynamic Response Characteristics of Weightless Man. Technical Report AMRL-TDR-63-18, AD-412-541. Aerospace Medical Research Laboratories, Wright-Patterson Air Force Base, Ohio.

Wicke, J. and Lopers, B., 2003. Validation of the Volume Function within Jensen's (1978) Elliptical Cylinder Model. *Journal of Applied Biomechanics* 19, 3-12.

Winter, D.A., 1990. *Biomechanics and motor control of human movement*. (2nd ed.). Waterloo, Canada, Wiley-Interscience.

Woltring, H.J., 1990. Data Processing and Error Analysis. In: N. Berme and A. Cappozzo (Eds.), *Biomechanics of Human Movement*, pp. 203-237, Bertec Corporation, Worthington.

Wood, J.E., Meek, S.G. and Jacobsen, S.C., 1989a. Quantification of human shoulder anatomy for prosthetic arm control. I. Surface modelling. *Journal of Biomechanics* 22, 273-292.

Wood, J.E., Meek, S.G. and Jacobsen, S.C., 1989b. Quantification of human shoulder anatomy for prosthetic arm control. II. Anatomy matrices. *Journal of Biomechanics* 22, 309-325.

Wooley, C.T., 1972. Segment, Masses, Centers of Mass and Local Moments of Inertia for an Anthropometric Model of Man. In: B. A. Conway, editor, Development of Skylab Experiment T-013, Crew/Vehicle Disturbances. Report D-6584. National Aeronautic and Space Administration, Washington D. C.

Wright, M.H., 2004a. The Interior-Point Revolution in Optimization: History, Recent Developments, and Lasting Consequences. *Bulletin (New Series) of the American Mathematical Society* 42(1), 39-56.

Wright, S.J., 1999. Algorithms and Software for Linear and Nonlinear Programming, *Foundations of Computer-Aided Process Design*. AIChE Symposium Series, CACHE Publications.

Wright, S.J., 2004b. An Algorithm for Degenerate Nonlinear Programming with Rapid Local Convergence. Optimization Technical Report 03-02. Computer Sciences Department, University of Wisconsin, Madison USA.

Wu, G. and Cavanagh, P.R., 1995. ISB recommendations for standardization in the reporting of kinematic data. *Journal of Biomechanics* 28(10), 1257-1261.

Wu, G., Siegler, S., Allard, P., Kirtley, C., Leardini, A., Rosenbaum, D., Whittle, M., D'Lima, D.D., Cristofolini, L. and Witte, H., 2002. ISB recommendation on definitions of joint coordinate system of various joints for the reporting of human joint motion--part I: ankle, hip, and spine. *Journal of Biomechanics* 35(4), 543-548.

Wu, G., van der Helm, F.C.T., Veeger, H.E.J., Makhsous, M., Van Roy, P., Anglin, C., Nagels, J., Karduna, A.R., McQuade, K. and Wang, X., 2005. ISB recommendation on definitions of joint coordinate systems of various joints for the reporting of human joint motion--Part II: shoulder, elbow, wrist and hand. *Journal of Biomechanics* 38(5), 981.

Yamaguchi, G.T. and Zajac, F.E., 1989. A Planar Model of the Knee Joint to Characterize the Knee Extensor Mechanism. *Journal of Biomechanics* 22, 1-10.

Yeadon, M.R., 1990. The simulation of aerial movement-II. A mathematical inertia model of the human body. *Journal of Biomechanics* 23, 67-74.

Yeadon, M.R. and Morlock, M., 1989. The appropriate use of regression equations for the estimation of segmental inertial parameters. *Journal of Biomechanics* 22, 683-689.

Zajac, F.E., 1989. Muscle and tendon: properties, models, scaling, and application to biomechanics and motor control. *Critical Reviews in Biomechanical Engineering* 17(4), 359-411.

Zatsiorsky, V.M., 1998. *Kinematics of human motion*, Human Kinetics Publishers.

Zatsiorsky, V.M., 2002. *Kinetics of Human Motion*, Human Kinetics Publishers.

Zatsiorsky, V.M. and Seluyanov, V.N., 1983. The mass and inertia characteristics of the main segments of the human body. In: H. Matsui and K. Kobayashi (Eds.), *International Series on Biomechanics, Vol. VIII-B*, pp. 1152-1159. Champaign, IL, Human Kinetics.

Zatsiorsky, V.M. and Seluyanov, V.N., 1985. Estimation of the mass and inertia characteristics of the human body by means of the best predictive regression equations. In: D.A. Winter, R.W. Norman, R.P. Wells, K.C. Hayes and A.E. Patla (Eds.), *Biomechanics IX-B*, pp. 233-239. Champaign, IL, Human Kinetics.

Zatsiorsky, V.M., Seluyanov, V.N. and Chugunova, L., 1990a. In vivo body segment inertial parameters determination using a gamma-scanner method. In: N. Berme and A. Cappozzo (Eds.), *Biomechanics of human movement: Applications in rehabilitation, sports and ergonomics*, pp. 187-202. Worthington, OH, Bertec Corporation.

Zatsiorsky, V.M., Seluyanov, V.N. and Chugunova, L., 1990b. Methods of determining mass-inertial characteristics of human body segments. In: G.G. Chernyi and S.A. Regirer (Eds.), *Contemporary Problems of Biomechanics*, pp. 272-291. Massachusetts, CRC Press.

Zhao, J. and Badler, N.I., 1994. Inverse Kinematics Positioning Using Nonlinear Programming for Highly Articulated Figures. *ACM Transactions on Graphics* 13(4), 313-336.

Zheng, Z., Zheng, X., Wang, Y., Wu, Y. and Chen, W., 1990. A New Method to Determine Inertial Parameters of the Segments of the Human Body. *In Proceedings of the Asian Games Scientific Congress*, p. 672. Beijing.